ECCENTRIC GRAVITATIONAL WAVES:

MODELING AND DATA ANALYSIS IMPLICATIONS

by

Blake Carroll Moore

A dissertation submitted in partial fulfillment
of the requirements for the degree

of

Doctor of Philosophy

in

Physics

MONTANA STATE UNIVERSITY
Bozeman, Montana

April, 2020

DEDICATION

To my parents Leslie and James, my siblings Gable, Sean, and Malora, and my best friends Joe & Steve. Without these meaningful relationships and their support, I would not have made it this far.

ACKNOWLEDGEMENTS

I would like to thank my adviser Nicolás Yunes for helping me become a strong researcher, and later an independent researcher. His help and availability has been invaluable to my continued success. I also thank Travis Robson for countless useful conversations throughout my work, David Anderson for help with computing, and both for their company along the way.

TABLE OF CONTENTS

TABLE OF CONTENTS – CONTINUED

TABLE OF CONTENTS – CONTINUED

LIST OF TABLES

LIST OF FIGURES

LIST OF FIGURES – CONTINUED

Figure Page

LIST OF FIGURES – CONTINUED

Figure Page

ABSTRACT

The ground based advanced Laser Interferometer Gravitational wave Observatory (LIGO) has now made numerous detections of compact objects, ushering in an era of gravitational wave astronomy. Soon the Laser Interferometer Space Antenna (LISA) will become operational and allow for even more detections of gravitational waves. With these detections we are able to characterize the physical properties of the sources – the nature of the orbit, the parameters of the individual compact object, and the parameters of the final merged object. Beyond these source measurements, gravitational waves have proven an important test bed for validating General Relativity, as well as testing theoretical astrophysical formation scenarios of these compact binaries. In order to reach these ends, we require accurate and efficient models for the gravitational waves as seen in the detector. While current detections by ground based detectors are consistent with compact binaries in quasi-circular orbits, there are formation scenarios which suggest that some small number of detectable events will be from compact objects in eccentric orbits, and certainly a healthy number of sources detectable by LISA will be in eccentric orbits. We have derived, validated, and explored the data analysis properties of a waveform model for compact objects in eccentric orbits. In the derivation of the waveform we have employed a truncated sum of harmonics, the stationary phase approximation, and a bivariate expansion in eccentricity and orbital velocity. To explore the data analysis implications of this model we have implemented Markov Chain Monte Carlo algorithms to produce the posterior distributions on the waveform parameters. We find that our model is highly accurate for the inspiral phase of compact objects in orbits with eccentricity as high as 0.8, and very computationally efficient – taking only 90ms to evaluate on average. System parameters are best measured when the source eccentricity is about 0.4, sometimes providing two orders of magnitude better measurement than its quasi-circular counterpart, and eccentric signals can provide more stringent constraints on alternative theories of gravity.

INTRODUCTION

The first and second observing run of the advanced Laser Interferometer Gravitational wave Observatory (aLIGO) has seen 11 gravitational wave events from inspiraling compact binaries, and 14 marginal events with false alarm rates less than 1 per 30 days [1]. The ongoing third observing run of aLIGO has already reported 48 candidate events through the `GraceDB`[1] Gravitational-Wave Candidate Event Database at the time of writing this manuscript. The third observing run is improved over the previous runs with detector upgrades as well as the addition of the Virgo detector [2] to the ground-based network. In the coming years we expect even more sensitivity and sky coverage as new ground based detectors are added to our networks and as third-generation detectors move from theory to practice. In addition, the Laser Interferometer Space Antenna (LISA) [3] is set to roughly launch in 2034 making us sensitive to a whole new set of sources. We are thus poised to explore the astrophysical and fundamental physics implications of these events and characterize the sources system parameters.

Integral to the detection and measurements of compact binary systems through their gravitational emission are accurate and efficient waveform models for the theoretical signal which can then be compared to the data. The current detected events have met the expectation that sources emitting in the sensitivity range of ground based detectors should be in quasi-circular orbits, a result of radiation reaction circularizing eccentric orbits drastically over a relatively small decay in orbital separation [4]. However, there are astrophysical formation scenarios which

[1] https://gracedb.ligo.org/

point to the possibility of some small number of compact binaries which will have substantial orbital eccentricity when emitting gravitational waves in the sensitivity band of ground based detectors. Typically these astrophysical scenarios are set in dense stellar environments with higher probability of many body interactions (e.g. the Kozai-Lidov mechanism [5]) which can excite orbital eccentricity in closely bound orbits. Some of the more promising astrophysical scenarios include binaries in globular clusters, with some studies predicting eccentric event rates of ~ 0.5 per Gpc per year for ground based detectors [6–9]. For LISA the numbers increase substantially with projections of about half of binary black hole mergers assembled in globular clusters having measurable eccentricity ($e \geq 0.01$) [10–12].

Given the possibility of eccentric events in ground based detectors, and the probability of these events in space based detectors, it is worth considering whether, and how, source eccentricity affects detection and parameter estimation. It is reasonable to expect that using a circular template to extract parameters from data which truly contains an eccentric signal could lead to a systematic parameter bias. Reference [13] studied this error with an inspiral only model valid for small eccentricities and to 3rd Post-Newtonian (PN[2])) order using a Fisher matrix based approach, developed in [15], to gauge systematic error from mismodeling. They found projected systematic parameter bias exceeding statistical error (at the $1-\sigma$ level) in binary nuetron star systems for eccentricities as small as $\sim 10^{-2}$. Similarly [16] produced a hybrid PN - NR waveform which incorporates a small eccentricity as simulated data, and performed parameter extraction using Markov Chain Monte Carlo with a quasi-circular template to gauge the systematic parameter bias. They found significant bias for eccentricities larger than about 0.1 where the total source

[2]A PN waveform is one constructed assuming small velocities and weak fields. In particular, a 3PN waveform is one which contains relativistic corrections of relative $\mathcal{O}(v^6/c^6)$ with respect to the controlling factor in the expansion [14].

mass was $\sim 65 M_{\odot}$. Beyond systematic parameter bias, assuming circularity in the template banks which are used for detection can lead to a loss in recovered SNR and thus significant loss in detection rate [17–21].

The non-trivial effects of orbital eccentricity in gravitational wave data analysis and detection has lead to a substantial amount of work in recent years towards the development of accurate and efficient waveforms that incorporate eccentricity. Early foundational work by Peters and Matthews produced the energy and angular momentum flux, and the change in orbital elements due to emission of gravitational waves by binaries in elliptical orbits to leading PN order [4, 22]. Wahlquist later derived the appropriate waveform polarization for a binary in an eccentric orbit again to leading PN order [23]. Since then there have been many different techniques aimed at solving these orbital equations and appropriately inputting them into the polarizations to yield fast and accurate waveforms, but the different ways to do so have lead to a family of eccentric waveforms, each valid in different domains, and working in different approximations.

One of the early successful passes at eccentric waveform modeling is the Post-Circular model, introduced to leading PN order in [24], which decomposes the signal into a sum of harmonics of the mean orbital frequency, employs a low eccentricity expansion throughout, inverts the orbital frequency and eccentricity dependence, and is inspiral only. This was later taken to 2PN order and 3PN order in [25] and [26]. It was also computed to leading order in eccentricity while retaining 3PN accuracy in [27]. In [28] the merger and ringdown portion of the signal was added. Spin was added, again in the small eccentricity and spin regime, in Ref [29] and interestingly they explore the effects of spin coupling to the eccentricity. While fast, these models suffers from inaccuracy which we argue in Chapter 1 is due to inverting the relationship between orbital frequency and eccentricity dependence. While these models have been validated through different measures, a rough general conclusion can be drawn that they are valid for eccentricities below about 0.3.

In contrast to the low eccentricity models, there are burst models (named due to the repeated close periastron passes of highly eccentric orbits resulting in a waveform which resembles a series of bursts of emission) which employ expansions working in the high eccentricity limit [30–32]. Since the domain of validity can depend strongly on source properties, we again can only make a rough statement that these models are valid for eccentricities greater than about 0.8. Their computational efficiency varies considerably between models and assumptions, with some useful for data analysis and detection while others are still too slow to be feasible for these uses. There are still more eccentric waveforms where one attempts to extend the highly successful quasi-circular effective one body waveforms (EOB) to include the effects of eccentricity [33–36]. Other waveforms include NR simulations, self-force models which incorporate eccentricity, and phenomenological models [16, 37–39]. These models have varying degrees of validity and are mostly too slow to be used for data analysis purposes (unless one uses a neural-net based approach where the bulk of the computation can be done "offline" [40]).

With these eccentric models in hand some obvious data analysis questions come to mind in the context of gravitational wave emission from eccentric binaries: how do measurements of the system parameters scale with eccentricity, can we do better tests of fundamental physics than in the quasi-circular case, and can we identify those formation scenarios which are predicted to produce these events given a collection of eccentric signals? In [41, 42], the authors use a 1PN valid, but exact in eccentricity, inspiral only model to explore statistical error in source parameter estimation using a Fisher matrix technique. They find that eccentric signals lead to increased accuracy in measurement of the source mass and sky location. They are, however, limited by the low PN order of their model and the Fisher matrix approximation which is employed (as opposed to an MCMC) due to computational expense in the model. Recently in [43], the authors explored the ability of a low-eccentricity model to constrain effects of alternative theories of gravity, finding deteriorated constraints at low eccentricity due to parameter covariance. However their results suggest an improvement in the constraint with higher eccentricities. Studies focused on discriminating between formation scenarios given eccentric signals have found promising abilities given between a handful and tens of eccentric signals [44–46].

In Chapter 1, we derive and develop a Newtonian (0PN) semi-analytic frequency domain model which incorporates the effects of orbital eccentricity. We find, through the use of a harmonic decomposition, the stationary phase approximation, and the use of hypergeometric functions, that at this order there exists exact solutions to the orbital dynamics which lead to a highly accurate waveform model even when eccentricities are as large as 0.9. However this comes at a cost as hypergeometric functions, and an increasingly large number of relevant harmonics, lead to requiring too much computational expense to be useful for parameter estimation. We find however, that through careful truncation of harmonics and a series representation of the hypergeometric functions we are able to retain accuracy and remain efficient for eccentricities near 0.8.

The Newtonian order model is of course limited greatly by neglecting all corrections in velocity beyond leading order, so in Chapter 2 we extend the 0PN model of Chapter 1 to 3PN order ($\mathcal{O}(v^6)$). While this draws heavily on the framework and insights of the model derived in Chapter 1, this derivation is complicated by the physical effect of periastron precession which enters at 1PN order. Beyond this complication the time domain dynamics become much more complicated and no longer admit exact solutions. Even in light of these complications we are able to produce a model that is valid again to eccentricities as high as 0.8 depending on the source system. We point to an increased error (with respect to the quasi-circular case) in the PN approximation for unequal mass binaries as eccentricity is increased. Lastly we isolate and analyze the different approximations which enter our model to guide future improvements.

With this in hand we seek to gauge the data analysis usefulness of our model and explore implications of eccentric signals in Chapter 3. We first employ some computing techniques combined with physically informed optimizations to drive the average time to compute the 3PN model down to about 90ms. Since the model is fast to compute, we are able to explore the data analysis properties of the model using Markov Chain Monte Carlo techniques. We study (with an emphasis on how quantities scale with source eccentricity), statistical errors in source parameters, and systematic parameter error due to neglecting eccentricity and mismodeling in our eccentric signal. Importantly we find systematic errors which are less than the statistical error for eccentricities as high as 0.8 (depending on the source parameters), indicating our model's usefulness for data analysis studies in the future.

Finally in Chapter 4, we probe the ability of eccentric signals to do tests of General Relativity. To achieve these ends we begin by incorporating the effects of two alternative theories of gravity (Einstein-dilaton-Gauss-Bonnet and Brans-Dicke) into our 3PN eccentric model. With this in hand, we characterize the ability of a aLIGO-like detector to constrain these theories through a Bayes factor based analysis obtained via transdimensional reversible jump Markov chain Monte Carlo and confidence interval based constraints through traditional Markov chain Monte Carlo methods. Generally we find constraints that are improved as the eccentricity of the source is increased to about 0.4, after which constraints slowly deteriorate as eccentricity further increases.

Lastly in the Conclusions we summarize this dissertation and discuss future work suggested by the results contained herein. Throughout we use geometric units where $G = c = 1$

CHAPTER ONE

A FOURIER DOMAIN WAVEFORM FOR NON-SPINNING BINARIES WITH ARBITRARY ECCENTRICITY

Contributions of Authors and Co-Authors

Manuscript in Chapter 1

Author: Blake Moore

Contributions: Analytically developed the waveform model. Developed the waveform and analysis code. Wrote the initial draft of the manuscript.

Author: Travis Robson

Contributions: Analytically developed the waveform model, and the code.

Author: Dr. Nicholas Loutrel

Contributions: Advised the project.

Author: Dr. Nicolas Yunes

Contributions: Conceived of design study and Advised the project. Edited the manuscript.

Manuscript Information Page

Blake Moore, Travis Robson, Nicholas Loutrel, Nicolas Yunes

Classical and Quantum Gravity

Status of Manuscript:
____ Prepared for submission to a peer-reviewed journal
____ Officially submitted to a peer-reviewed journal
____ Accepted by a peer-reviewed journal
_X_ Published in a peer-reviewed journal

IOP Publishing
Class. Quantum Grav. Volume 35, Number 23
10.1088/1361-6382/aaea00

Abstract

Although the gravitational waves observed by advanced LIGO and Virgo are consistent with compact binaries in a quasi-circular inspiral prior to coalescence, eccentric inspirals are also expected to occur in Nature. Due to their complexity, we currently lack ready-to-use, analytic waveforms in the Fourier domain valid for sufficiently high eccentricity, and such models are crucial to coherently extract weak signals from the noise. We here take the first steps to derive and properly validate an analytic waveform model in the Fourier domain that is valid for inspirals of arbitrary orbital eccentricity. As a proof-of-concept, we build this model to leading post-Newtonian order by combining the stationary phase approximation, a truncated sum of harmonics, and an analytic representation of hypergeometric functions. Through comparisons with numerical post-Newtonian waveforms, we determine how many harmonics are required for a faithful (matches above 99%) representation of the signal up to orbital eccentricities as large as 0.9. As a first byproduct of this analysis, we present a novel technique to maximize the match of eccentric signals over time of coalescence and phase at coalescence. As a second byproduct, we determine which of the different approximations we employ leads to the largest loss in match, which could be used to systematically improve the model because of our analytic control. The future extension of this model to higher post-Newtonian order will allow for an accurate and fast phenomenological hybrid that can account for arbitrary eccentricity inspirals and mergers.

1.1 Introduction

Eccentric binaries circularize rapidly as their orbital separation shrinks due to the emission of gravitational waves (GWs). Since the target sources of ground-based detectors, such as the Advanced Laser Interferometer Gravitational-Wave Observatory (aLIGO) [47], advanced Virgo (aVirgo) [48], LIGO-India [49], and KAGRA [50], are thought to form at large initial separations, one expects their orbital separation and eccentricity will have decreased considerably by the time they are detectable. As such, the modeling of GWs has focused on quasi-circular binaries, and indeed all current aLIGO/aVirgo detections can be captured well with quasi-circular GW models [51–56].

Several astrophysical scenarios, however, suggest that some small number of binaries could have moderate eccentricities while emitting GWs at frequencies in the sensitivity band of ground-based detectors, and these different formation scenarios can be constrained through detection of eccentric signals [46, 57]. A very small number of weakly eccentric sources emitting detectable GWs are expected to be formed through isolated stellar evolution (field binaries). Kowalska et al. [58] simulated field binary evolution and found typical eccentricities of $\sim 10^{-4}$, with roughly 1% of binaries having eccentricities greater than 0.01 when emitting GWs detectable by ground based networks.

In contrast to binaries formed through isolated stellar evolution, binaries formed in dense stellar regions, such as globular clusters, are significantly more likely to be eccentric due to many-body interactions, such as the Kozai-Lidov mechanism [59–62]. The latter is a form of orbital resonance where oscillations in inclination and eccentricity are induced in a hierarchical triple [5]. Recently, Rodriguez et al. [6] (see also Samsing [7]) incorporated post-Newtonian (PN) effects[1] in orbital dynamics and found that 10% of binaries in globular clusters emitting GWs in the sensitivity band of ground based detectors will have eccentricities greater than 0.1. For more studies

[1]The post-Newtonian approximation is one in which the field equations are solved assuming small velocities and weak gravitational fields in an expansion in powers of $(\frac{v}{c})$, where v is the orbital velocity and c is the speed of light [63]. By nPN order we mean an expansion to order $(v/c)^{2n}$.

which focus on the eccentricity distribution of sources for ground-based detectors see [64–66].

Since there may be some small number of detectable binaries with non-negligible eccentricity, it is natural to consider what error is incurred by neglecting eccentricity in the modeling. Martel and Poisson [17] computed the fitting factor (FF), i.e. the overlap maximized over all parameters of the model, between quasi-circular templates and eccentric signals for a variety of sources at leading PN order. This study showed that as the eccentricity of the signal increases and the total mass decreases, the FF decreases. Since the percent loss in detection rate scales like $1 - FF^3$ [18], neglecting a moderate eccentricity in source modeling can lead to a significant loss in detection rate. Loss in detection rate has also been the focus of several other studies [19–21], which varied the range of masses considered and the PN order, all leading to similar conclusions: for low mass systems, the loss in match due to sub-optimal templates is significant when $e \geq 0.05$, and for higher mass systems when $e \geq 0.1$.

But even if an eccentric signal is detected with quasi-circular templates, the lack of eccentricity modeling will nevertheless lead to an associated parameter bias. Favata [13] showed that the systematic error in the symmetric mass ratio incurred by neglecting eccentricity in the model exceeds the statistical error of aLIGO for initial eccentricities as small as $e \sim 2 \times 10^{-3}$ for a binary neutron star system. For the third-generation Einstein Telescope [67], there is significant parameter error for even smaller orbital eccentricities. Schematically, this is because parameter biases become important when the match (M), i.e. the overlap without maximizing over intrinsic parameters, between quasi-circular templates and eccentric signals drops below $1 - D/(2\rho^2)$ [68], where D is the effective dimensionality of the model and ρ is the signal-to-noise ratio of the detection. Thus, even though the FF may be high, the M may still not be high enough for high signal-to-noise ratio events.

The need for eccentric waveforms has therefore encouraged some research in eccentric modeling. The Post-Circular formalism (PC), introduced at Newtonian order in [24], was one of the first attempts to provide an analytic frequency domain waveform that incorporated eccentricity. The philosophy of this formalism is to expand all relevant quantities in the small eccentricity limit. Tanay, et al. [25] extended this work to 2PN order, and Ref. [27] extended it to 3PN order, but keeping only leading-order in eccentricity corrections. While the PC models are computationally fast, they are not able to handle moderate eccentricities, and so other modeling efforts have combined analytic and numerical methods to arrive at a more accurate model. Pierro et al. [69] solved the equations of motion necessary to build the Fourier domain model of [70] without making a small eccentricity approximation by combining special functions (hypergeometric functions and Bessel functions) with certain numerical inversions. While exact in some regards within the PN approximation, this model is computationally expensive and it has only been extended to 1PN order so far [71].

We here take the first steps toward the construction and validation of a ready-to-use and computationally efficient waveform model in the Fourier domain that is valid to arbitrary eccentricity. The new model combines the accuracy of [69] with the efficiency of the PC models, without requiring the evaluation of costly special functions in the Fourier phase of the frequency response. Instead, the model is constructed by combining elements of the stationary-phase approximation, a truncated sum over harmonics and an analytic representation of hypergeometric functions. Schematically, the Fourier transform of the plus- and cross-polarizations in the new model is

$$\tilde{h}_{+,\times}(f) = \frac{m\eta}{R} \sum_{j=1}^{N} \tilde{\mathcal{A}}^{(j)}_{+,\times}(f)\, e^{i\psi_j(f)} \ . \tag{1.1}$$

where $\tilde{\mathcal{A}}^{(j)}_{+,\times}$ is an analytic, slowly-varying, complex Fourier amplitude and ψ_j is an analytic and real Fourier phase, where j is the harmonic index and N is the truncation index, with m, η and R the total mass, symmetric mass ratio and luminosity distance to the source respectively.

The key of the new model is an analytic prescription for the Fourier amplitude and for the Fourier phase, with the truncation index determined from a match analysis. Although the Fourier phase can be solved for exactly in terms of hypergeometric functions, this representation is not computationally efficient. Instead, we explored different analytic representations of hypergeometric functions, and found that Taylor expansions about small eccentricity do an exceptional job at capturing the exact result. The Fourier amplitude, on the other hand, is not expanded in small eccentricity, and it is instead kept in its exact PN form. The truncation index is determined by requiring that the match between the truncated series and an infinite series be at least 99%. We find in practice that for most initial eccentricity cases the sum need only be taken to the tenth term or less. We then verify that the resulting waveforms are faithful (with matches $\sim 99\%$ to numerical PN waveforms) for aLIGO sources with initial orbital eccentricities as high as 0.9, as shown in Fig. 1.1 for a black hole–neutron star binary (BH-NS). All throughout, we work to leading PN order, focusing mostly on faithfulness measures for the aLIGO detector, but the approach can easily be extended to higher PN order and to other detectors.

Two main byproducts are also generated from this analysis. First, we develop a new method to efficiently maximize the overlap over the time and phase of coalescence

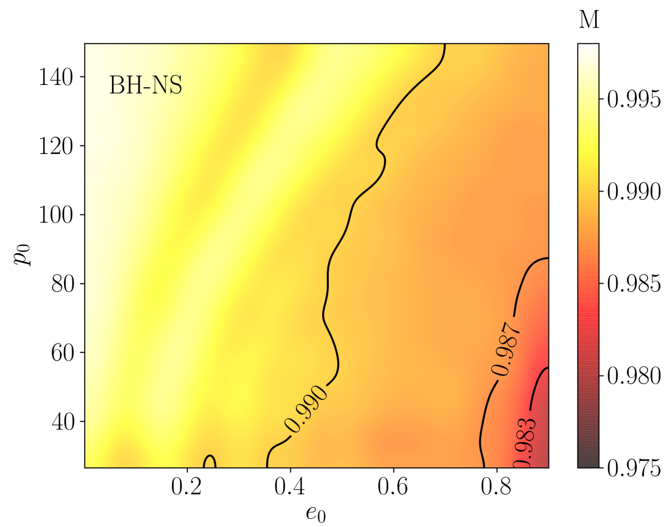

Figure 1.1: Match between our Fourier domain model and a fully numerical PN waveform as a function of initial orbital eccentricity, e_0, and initial dimensionless semilatus rectum, p_0, for a $(10, 1.4)M_\odot$ black hole - neutron star binary (BH-NS). The match is greater than 99% for more than half of the explored parameter space. The decay in match at high initial eccentricity and small initial semilatus rectum is due to finite time effects.

of the new eccentric model. Maximization over these extrinsic parameters is a solved problem for quasi-circular binaries, but the latter must be generalized non-trivially when including several harmonics with comparable power. Second, we investigate which elements of the approximations that make up our new model lead to the largest loss in accuracy. This error analysis therefore allows us to identify which elements should be taken to higher order if a higher match is desired. Due to the analytic control of the waveform model, such extensions to higher order are straightforward.

The remainder of this chapter presents the details of the results described above. Section 1.2 reviews the fundamentals of eccentric GW emission, including the parameterization of the orbit and its time evolution, as well as the decomposition of the signal into a sum of harmonics of the mean orbital frequency. Section 1.3 reviews some basic data-analysis measures to compare waveform models, while presenting the new method to efficiently maximize over the time and phase of coalescence of eccentric templates. Section 1.4 discusses the details of previous models and it introduces the new models we develop in this paper. Section 1.5 studies which of the different approximations used in the new model leads to the largest loss in match. Section 1.6 carries out a faithfulness study of the new analytic model. Section 1.7 concludes and points to future research. Throughout this work we use geometric units ($c = 1 = G$).

1.2 Fundamentals of Eccentric Binary GW Emission

In this section we begin by reviewing the Newtonian parameterization of the Kepler problem in the absence of radiation reaction. We show that the associated time domain GW waveform can be decomposed into a sum of harmonics of the mean orbital frequency. We then review how radiation reaction affects the orbital dynamics and how the application of the stationary phase approximation (SPA) leads to a Fourier response with similar structure to the time domain harmonic decomposition.

1.2.1 Newtonian Emission in the Absence of Radiation Reaction

In the Newtonian treatment of the two-body problem, the dynamics of an elliptical orbit restricted to a plane are described by:

$$r = a(1 - e\cos u), \tag{1.2a}$$

$$\phi - \phi_0 = 2\arctan\left[\left(\frac{1+e}{1-e}\right)^{1/2}\tan\frac{u}{2}\right], \tag{1.2b}$$

$$l = 2\pi F(t - t_0) = u - e\sin u. \tag{1.2c}$$

Here r is the magnitude of the relative separation vector, which we choose to be on the x–y plane $\vec{r} = (r\cos\phi, r\sin\phi, 0)$, ϕ is the orbital phase, e is the orbital eccentricity, m

is the total mass, and F is the mean orbital frequency defined by $F = 1/P$, where P is the orbital period. The semi-major axis, a, is related to the mean orbital frequency via Kepler's third law: $(2\pi F)^2 a^3 = m$. The angles l and u are the mean anomaly and eccentric anomaly, respectively, while the constants t_0 and ϕ_0 arise from integration and specify the initial orientation at some time t_0. From the above equations, one can also easily derive the following differential equations

$$\dot{r} = (2\pi m F)^{1/3} \frac{e \sin u}{(1 - e\cos u)}, \tag{1.3a}$$

$$\dot{\phi} = \frac{2\pi F (1 + e\cos\phi)^2}{(1 - e^2)^{3/2}}. \tag{1.3b}$$

Even in the Newtonian treatment, one is unable to analytically solve for the orbital separation and phase as explicit functions of time. Instead, one is forced to numerically invert Kepler's equation, Eq. (1.2c), in order to obtain the eccentric anomaly as a function of time, and thus the orbital separation and phase as functions of time. Alternatively, one can solve the differential equations presented above to obtain the orbital phase and the separation distance as a function of time.

In General Relativity, the accelerated motion of massive bodies leads to the emission of GWs. Following Martel and Poisson [17], the GW polarizations are given by

$$\begin{aligned} h_+ = -\frac{m\eta}{pR}\Bigg\{ & \left[2\cos(2\phi - 2\beta) + \frac{5}{2}e\cos(\phi - 2\beta) + \frac{1}{2}e\cos(3\phi - 2\beta) + e^2\cos 2\beta\right](1 + \cos^2\iota) \\ & + \left[e\cos\phi + e^2\right]\sin^2\iota\Bigg\}, \end{aligned} \tag{1.4}$$

and

$$h_\times = -\frac{m\eta}{pR}\left[4\sin(2\phi - 2\beta) + 5e\sin(\phi - 2\beta) + e\sin(3\phi - 2\beta) - 2e^2\sin 2\beta\right]\cos\iota \ , \tag{1.5}$$

where R is the luminosity distance and $\eta = m_1 m_2/m^2$ is the symmetric mass ratio, with $m_{1,2}$ the component masses. The angles β and ι are the polar angles describing the polarization axes. The *dimensionless* semilatus rectum, p, is related to the eccentricity and semi-major axis by $a = pm/(1-e^2)$. Following Moreno-Garrido, et al. [72] we decompose the time domain signal into harmonics of the mean orbital frequency such that the signal takes the form

$$h_{+,\times}(t) = -\frac{m\eta}{R}\left(2\pi mF\right)^{2/3}\sum_{j=1}^{\infty}\left[C^{(j)}_{+,\times}\cos jl + S^{(j)}_{+,\times}\sin jl\right] . \tag{1.6}$$

The harmonic coefficients $C^{(j)}_{+,\times}$ and $S^{(j)}_{+,\times}$ are functions of the orbital eccentricity e and the polarization angles (i, β).

We now briefly review how these coefficients are obtained. Making use of the relation $\cos\phi = e^{-1}\left[a(1-e^2)/r - 1\right]$, we express the strain polarizations in Eqs. (1.4) and (1.5) in the form

$$h_{+,\times} = B_1\cos\phi + B_2\left(\frac{a}{r}\right)^2\cos\phi + B_3\sin\phi + B_4\left(\frac{a}{r}\right)^2\sin\phi \ . \tag{1.7}$$

Here the B_i are functions of the orbital eccentricity, mean orbital frequency, and the angles ι and β, which can be found in Appendix A of [72]. Neglecting radiation-

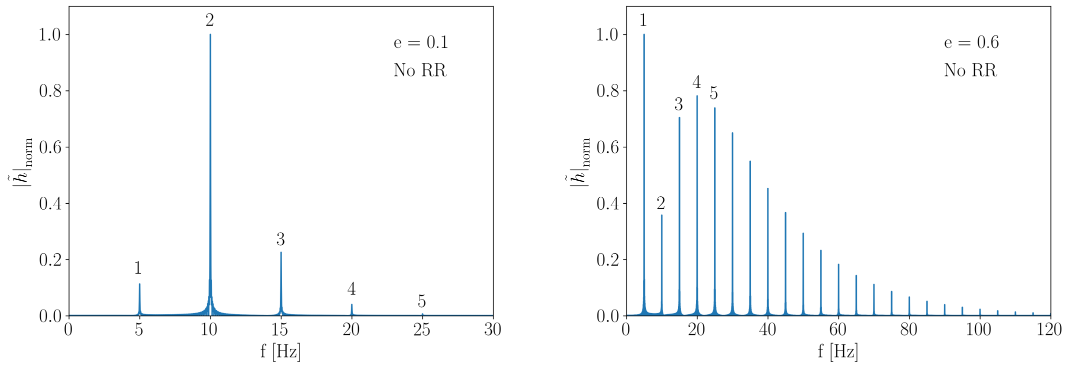

Figure 1.2: The normalized Fourier amplitude of the numerically evolved GW signal in the absence of radiation reaction, obtained by numerically solving Eq. (1.3b) and discretely Fourier transforming Eq. (1.5) for a $(10, 10)M_{\odot}$ binary black hole (BBH) system with a mean orbital frequency of 5 Hz and orbital eccentricity of 0.1 (left) and 0.6 (right). Observe that the Fourier amplitude naturally splits into harmonics of the mean orbital frequency, where we have labeled the first five. For systems with larger orbital eccentricities, there are many harmonics of comparable strength present.

reaction, we have access to the following Fourier series [73],

$$\cos\phi = -e + \frac{2}{e}(1-e^2)\sum_{j=1}^{\infty} J_j(je)\cos jl \ , \tag{1.8a}$$

$$\sin\phi = \sqrt{1-e^2}\sum_{j=1}^{\infty}\left[J_{j-1}(je) - J_{j+1}(je)\right]\sin jl \ , \tag{1.8b}$$

$$\left(\frac{a}{r}\right)^2\cos\phi = \sum_{j=1}^{\infty} j\left[J_{j-1}(je) - J_{j+1}(je)\right]\cos jl \ , \tag{1.8c}$$

$$\left(\frac{a}{r}\right)^2\sin\phi = \sum_{j=1}^{\infty} j\left[J_{j-1}(je) + J_{j+1}(je)\right]\sin jl \ , \tag{1.8d}$$

where $J_j(x)$ are Bessel functions of the first kind. Combining Eqs. (1.7) and (1.8) and rearranging to match the form given in Eq. (1.6) yields the harmonic amplitudes:

$$C_{+}^{(j)} = \frac{2}{e^2}\Big\{c_{2\beta}(1+c_{\iota}^2)e(1-e^2)j(J_{j+1}(je) - J_{j-1}(je))$$

$$- \left[c_{2\beta}(1+c_\iota^2)(e^2-2) + e^2 s_\iota^2\right] J_j(je)\bigg\} \,, \tag{1.9a}$$

$$S_+^{(j)} = \frac{4}{e^2}(1+c_\iota^2)s_{2\beta}\sqrt{1-e^2}\bigg\{eJ_{j-1}(je) - \left[1+(1-e^2)j\right] J_j(je)\bigg\} \,, \tag{1.9b}$$

$$C_\times^{(j)} = \frac{4}{e^2}s_{2\beta}c_\iota\left\{2e(1-e^2)jJ_{j-1}(je) - 2\left[1+(1-e^2)j - \frac{e^2}{2}\right] J_j(je)\right\} \,, \tag{1.9c}$$

$$S_\times^{(j)} = \frac{8}{e^2}c_{2\beta}c_\iota\sqrt{1-e^2}\bigg\{eJ_{j-1} - \left[1+(1-e^2)j\right] J_j(je)\bigg\} \,, \tag{1.9d}$$

with the notation $c_\theta \equiv \cos\theta$ and $s_\theta \equiv \sin\theta$. These expressions are exact, and thus, the waveform in Eq. (1.6) is valid to all eccentricities.

Figure 1.2 shows the normalized amplitude of the Fourier transform of the GW signal in the absence of radiation reaction (i.e. for a system whose mean orbital frequency and eccentricity remain constant). As the figure shows, the Fourier amplitude is composed of harmonics of the mean orbital frequency F. For the small eccentricity case shown on the left panel, the second harmonic is clearly dominant. However, as the eccentricity is increased, as shown on the right panel, the first harmonic of the mean motion dominates and many harmonics are of comparable strength.

Figure 1.2 demonstrates that one *cannot* specify a time domain quantity, such as the orbital eccentricity or the mean orbital frequency at a unique GW frequency. The presence of multiple harmonics demands that at any given time an eccentric binary emits GWs at several different GW frequencies. For example, although the eccentricity of the emitting binary is 0.6 at all times on the right panel of Fig. 1.2, this system emits GWs with significant power at 5, 10, 15, 20 Hz, etc. As such, there is no one-to-one mapping between eccentricity and GW frequency, and one cannot unambiguously define an eccentricity as a signal “enters band.” A much more sensible statement is to refer to the orbital eccentricity at a given value of the mean orbital frequency, which is uniquely defined.

1.2.2 Radiation Reaction and GW Fourier Response

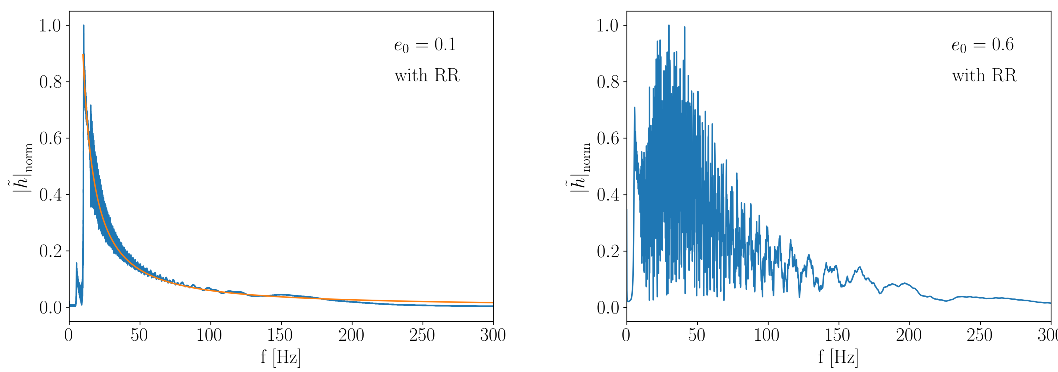

Figure 1.3: The normalized Fourier amplitude of the numerically evolved GW signal in the presence of radiation reaction obtained by numerically solving Eqs. (1.3b), (1.11), and (1.12) for a $(10, 10)M_\odot$ binary black hole (BBH) system with an initial mean orbital frequency of 5 Hz at an initial orbital eccentricity of 0.1 (left) and 0.6 (right). In the low eccentricity case on the left panel, the amplitude is similar to that of a quasi-circular GW (shown in orange), but there is some interference between harmonics above 15 Hz that leads to small oscillations about the quasi-circular spectrum. In the moderate eccentricity case shown on the right panel, the amplitude displays considerable oscillations from the interference of many harmonics of comparable strength.

Let us now consider the effect of radiation reaction on the emitted GWs in the frequency domain. In General Relativity, GWs carry away energy and momentum from the binary, and in response, e and F vary with time. At leading-order in the PN expansion, the equations for r, $\dot{r}$, ϕ, and $\dot{\phi}$, Eqs. (1.2)-(1.3), remain the same, as does Kepler's equation, but the mean anomaly l now obeys

$$l = \int^t 2\pi F(t')dt'. \tag{1.10}$$

The time evolution of the mean orbital frequency and eccentricity were first derived in [4], and are given by

$$\frac{dF}{dt} = \frac{\eta}{2\pi m^2}(2\pi m F)^{11/3}\left(\frac{96+292e^2+37e^4}{5(1-e^2)^{7/2}}\right) \tag{1.11}$$

and

$$\frac{de}{dt} = -\frac{\eta}{m}(2\pi m F)^{8/3} e\left(\frac{304+121e^2}{15(1-e^2)^{5/2}}\right). \tag{1.12}$$

These equations can be combined to form

$$\frac{dF}{de} = -3\frac{F}{e}\left[\frac{96+292e^2+37e^4}{(1-e^2)(304+121e^2)}\right], \tag{1.13}$$

which is separable and easily solved

$$F\sigma(e)^{3/2} = C_0 \tag{1.14}$$

with the definition

$$\sigma(e) = \frac{e^{12/19}}{1-e^2}\left(1+\frac{121}{304}e^2\right)^{870/2299}. \tag{1.15}$$

The constant C_0 is set by the initial conditions $F_0\sigma(e_0)^{3/2} = C_0$, where e_0 is the orbital eccentricity when the mean orbital frequency is F_0.

Applying the stationary phase approximation (SPA), reviewed in Appendix 1.A, to the time domain harmonic decomposition of the GW signal, Eq. (1.6), yields

$$\begin{aligned}\tilde{h}^{\text{SPA}}_{+,\times} = &-\frac{m\eta}{2R}\sum_{j=1}^{\infty}\frac{(2\pi m F(t_j^*))^{2/3}}{\sqrt{j\dot{F}(t_j^*)}}\left[C^{(j)}_{+,\times}(t_j^*) + iS^{(j)}_{+,\times}(t_j^*)\right] \\ &\times e^{i\psi_j}\Theta\left(f - jF_0\right)\Theta\left(jF_{\text{LSO}} - f\right),\end{aligned} \tag{1.16}$$

where the Fourier phase for each harmonic, ψ_j, is given by

$$\psi_j = 2\pi f t_j^* - jl(t_j^*) - \pi/4 \ . \tag{1.17}$$

Here t_j^* is the "stationary" time for the j^{th} harmonic which relates the mean orbital frequency (F) to the Fourier frequency (f) through the stationary phase condition

$$jF(t_j^*) = f \ . \tag{1.18}$$

Equation 1.18 supports the last conclusion of Sec. 1.2.1: an eccentric binary emits GWs at all integer multiples of its mean orbital frequency, and the mapping between time and GW frequency is harmonic dependent, and thus, not one-to-one.

The SPA waveform model of Eq. (1.16) contains a Heaviside function, $\Theta(x)$, because of the finiteness of GW emission in the time domain. A binary that is formed at t_0 will emit GWs until it merges, but the PN model is not valid once the orbital velocities become a non-negligible fraction of the speed of light. As is customary in the GW literature, we thus terminate the time-domain PN waveforms at the eccentric analogue of the innermost stable circular orbit of a point-particle in a Schwarzschild spacetime: the Last Stable Orbit (LSO). The mean orbital frequency at the LSO, F_{LSO}, is defined by [74–76]

$$F_{\text{LSO}} = \frac{1}{2\pi m}\left(\frac{1+e_{\text{LSO}}}{6+2e_{\text{LSO}}}\right)^{3/2} . \tag{1.19}$$

When one computes the Fourier transform of this time-domain PN model in the SPA, the Heaviside function persists, as we review in Appendix 1.A.

Figure 1.3 shows the normalized Fourier amplitude of the GW signal when radiation reaction is included for systems with the same initial condition as shown in

Fig. 1.2. In the low eccentricity case ($e_0 = 0.1$) shown on the left panel, the amplitude is very close to the well known $f^{-7/6}$ trend of quasi-circular GW models. The rapid oscillations appearing past 15 Hz are due to interference between different harmonics. In the high eccentricity case ($e_0 = 0.6$) shown on the right panel, this trend is lost, and instead one finds rapid and large oscillations due to many harmonics of comparable strength interfering with one another. To be clear, by interference here we refer to the oscillation in the amplitude of the Fourier transform which arises from adding the different harmonics, which at any given frequency will, in general, have misaligned phases which differ in their frequency evolution. This does not imply that the different harmonics are not orthogonal in sense of their mutual overlaps. This result makes it clear that a faithful representation of the Fourier transform of eccentric signals must necessarily include several harmonic terms oscillating at different Fourier frequencies.

The harmonic structure of the signal can be more easily appreciated through a Q-transform, as shown for example in Fig. 1.4 for the same BBH system as that used in the right panel of Fig. 1.3. The Q-transform is a wavelet transform where the basis wavelets are Gaussian-windowed complex exponentials. Since these wavelets are localized both in time and frequency, the Q-transform produces a time-frequency representation of the GW signal. A large value of Q localizes the wavelets more in frequency, while a low Q localizes the wavelets more in time, and so in Fig. 1.4 we use a Q of 40. The harmonic structure shown in Eq. (1.16) manifests itself in Fig. 1.4 as several different tracks in time-frequency. At later times, higher harmonics become subdominant as their amplitude is proportional to the orbital eccentricity, which has significantly decayed.

The general structure of the Fourier-domain waveform in Eq. (1.16) is common across all current eccentric models. The main differences arise in how one treats (i) the mean anomaly l and the stationary time t_j^* as functions of frequency, which

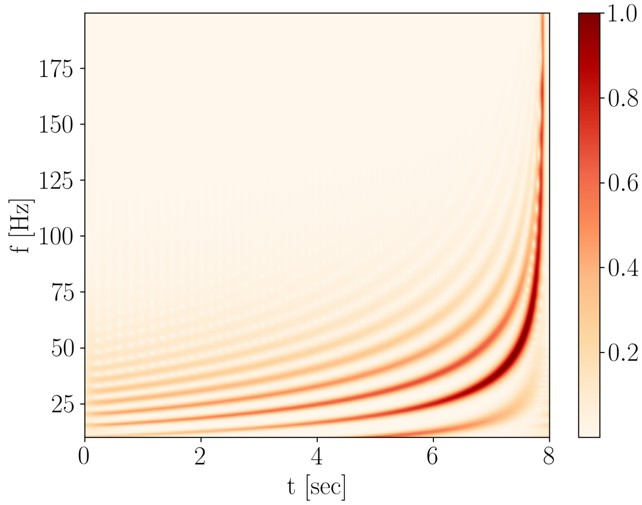

Figure 1.4: The normalized amplitude in a time-frequency representation (Q-transform) of the same system as that used for the right panel of Fig. 1.3. The presence of many harmonics in the signal leads to several tracks in time-frequency space. At later times the higher harmonics have considerably smaller amplitude, as a consequence of eccentricity decay.

appear in the Fourier phase, as well as (ii) the harmonic amplitudes and the choice of truncation of the sum. At higher PN order, other differences arise, such as the precise way in which periastron precession is modeled and the inclusion of modifications to Kepler's equations at 2PN order. As a first step toward the construction of a new, analytic Fourier-domain waveforms for arbitrarily eccentric binaries, we will refrain from going to higher PN order here, but we will review current analytic models in Sec. 1.4.1.

1.3 Measures to Compare Eccentric Waveforms

Before proceeding with a description of current analytic models, and the development of a new one, it will be useful to first describe how to validate and compare different models. A useful data analysis measure to quantify the agreement between two waveforms h_1 and h_2 is through the match

$$M = \max_{t_c, l_c} \frac{(h_1|h_2)}{\sqrt{(h_1|h_1)(h_2|h_2)}} \,. \tag{1.20}$$

This statistic is the normalized inner product between two waveforms, a "signal" h_1 and a "model" h_2, maximized over a time shift t_c and phase shift l_c, which in the models we consider here arise in the phase functions t and l of Eq. (1.17) as constants of integration. The inner products are defined by

$$(h_1|h_2) = 4\mathrm{Re} \int_0^\infty \frac{\tilde{h}_1^* \tilde{h}_2}{S_n(f)} df \,, \tag{1.21}$$

where $S_n(f)$ is the noise power spectral density of the detector and Re is short-hand for the real part. In this paper, we use the design-aLIGO spectral noise density (zero-detuned, high-power) noise curve, which assumes stationary Gaussian noise [77].

When the value of the match is unity, the model perfectly represents the signal to within a time and phase offset, while the more different they are, the lower the match becomes. What value of the match is then high enough for the model to be a "faithful" representation of the signal? To set this threshold, we demand that the systematic error from mismodeling is smaller than the statistical error. Following the detailed discussion in Appendix G of [68], this requirement translates to

$$1 - M < \frac{D}{2\rho^2} \,, \tag{1.22}$$

where D is the (effective) dimension of the model, 10 in our case , and ρ is the signal to noise ratio (SNR) defined by $\rho^2 = (h|h)$.

For quasi-circular GW templates, techniques have been developed to rapidly maximize Eq. (2.64) over a time and phase offset. For eccentric templates, however, this maximization is complicated by the harmonic dependence of the phase offsets arising from l_c. For the remainder of this section, we will thus first review the maximization techniques valid in the quasi-circular limit, and then we will extend them to the case of eccentric templates, assuming the different harmonics are mutually orthogonal. Lastly, we investigate the error incurred using this maximization scheme as we relax our assumption of orthogonality.

1.3.1 Review of Quasi-Circular Match Maximization

For quasi-circular GW templates, only the $j = 2$ harmonic is non-vanishing at leading PN order. Let us then write the template model as $h = \hat{h}e^{i\phi_c - 2\pi i f t_c}$, where $\hat{h}$ is a complex function of frequency and $\phi_c = 2l_c$. Suppose now that we have some data d that is perfectly represented by our model aside from an orbital phase shift and a time shift: $d = \hat{h}e^{i\phi_0 - 2\pi i f t_0}$, where ϕ_0 and t_0 are inherent to the data and we do not have access to their values. Our task is then to develop an algorithm to find the values of (ϕ_c, t_c) that will maximize the overlap between d and h, where in this case we know the solution is simply $(\phi_c, t_c) = (\phi_0, t_0)$.

The inner product we wish to maximize is

$$(h|d) = 4\mathrm{Re}\left[e^{-i\phi_c}\int_0^\infty \frac{|\hat{h}|^2}{S_n(f)} e^{-2\pi i f t_0 + i\phi_0} e^{2\pi i f t_c} df\right]. \tag{1.23}$$

Without specifying t_c or ϕ_c we are able to construct the function

$$\tilde{G}(f) = \frac{|\hat{h}|^2}{S_n(f)} e^{-2\pi i f t_0 + i\phi_0}, \tag{1.24}$$

whose inverse Fourier transform $\mathcal{F}^{-1}[\cdot]$ with respect to t_c,

$$G(t_c) = \mathcal{F}^{-1}[\tilde{G}(f)] = \int_0^\infty \frac{|\hat{h}|^2}{S_n(f)} e^{-2\pi i f t_0 + i\phi_0} e^{2\pi i f t_c} df, \tag{1.25}$$

appears in the above inner product

$$(h|d) = 4\mathrm{Re}\left[e^{-i\phi_c}G(t_c)\right]. \tag{1.26}$$

The quantity $G(t_c)$ is a complex number for any value of t_c and the factor of $e^{-i\phi_c}$ rotates the argument of the real operator in Eq. (1.26) in the complex plane, but does not change the *magnitude* of $G(t_c)$. Thus, we can maximize over ϕ_c by taking the magnitude of $G(t_c)$:

$$\max_{\phi_c}(h|d) = 4|G(t_c)|. \tag{1.27}$$

The overlap maximized over both ϕ_c and t_c, the match M, is found by searching for the maximum value of the array returned by $G(t_c)$ in the inverse Fourier transform over t_c, or simply

$$M = 4\max_{t_c}|G(t_c)|. \tag{1.28}$$

In this method the values of t_c and ϕ_c that maximize the match need not be computed explicitly to evaluate the match, and thus, we refer to this method as *implicit maximization.*

In order to explicitly find the (t_c, ϕ_c) pair that maximizes the match, one can begin by identifying the time corresponding to the value of $t_c = t_{\mathrm{max}}$ that maximizes $|G(t_c)|$. The quantity $G(t_{\mathrm{max}})$ is a complex number that is rotated off the real axis by ϕ_0 (easily verified upon inspection of Eq. (1.25) with $t_c = t_0 = t_{\mathrm{max}}$). Thus we find the value of the ϕ_c that maximizes the inner product (ϕ_{max}) via:

$$\phi_0 = \phi_{\mathrm{max}} = \arctan\left[\frac{\mathrm{Im}(G(t_{\mathrm{max}}))}{\mathrm{Re}(G(t_{\mathrm{max}}))}\right]. \tag{1.29}$$

The pair that maximize the match is then $(t_{\mathrm{max}}, \phi_{\mathrm{max}})$ and one calculates the match explicitly a posteriori. Since in this case t_{max} and ϕ_{max} need to be found explicitly to evaluate the match, we refer to this method as *explicit maximization*.

These two analytic methods to maximize the match are very similar in the quasi-circular case, but as we shall see, this is not the case for eccentric templates. Moreover, the implicit maximization method is computationally faster, as it does not require the evaluation of $t_{\max}$ or $\phi_{\max}$. We shall see next how all of this comes to play for eccentric templates.

1.3.2 Eccentric Match Maximization

The maximization of the match between an eccentric template and an eccentric signal is complicated by the harmonic dependence of the phase offsets arising from the mean anomaly at coalescence. Let us then consider the template h and the data d to be of the form

$$d = \sum_{k=1}^{\infty} \hat{h}_k e^{ikl_0 - 2\pi i f t_0}, \tag{1.30}$$

and

$$h = \sum_{j=1}^{\infty} \hat{h}_j e^{ijl_c - 2\pi i f t_c}. \tag{1.31}$$

Where $\hat{h}_j$ and $\hat{h}_k$ are complex functions of frequency associated with the j^{th} and k^{th} harmonics of mean orbital frequency. We are then tasked with maximizing

$$\begin{aligned}(h|d) &= 4\mathrm{Re}\left[\int_0^{\infty} \sum_{j,k=1}^{\infty} \frac{\hat{h}_j^* \hat{h}_k}{S_n(f)} e^{(ikl_0 - ijl_c)} e^{-2\pi i f t_0} e^{2\pi i f t_c} df\right] \\ &= \sum_{j,k=1}^{\infty} (h_j|d_k)\,. \end{aligned} \tag{1.32}$$

Without making any assumptions, the only way to maximize the above exactly is either through a grid search on t_c and l_c or through another numerical maximization scheme, such as a hill-climber algorithm. These methods are computationally expensive and slower than analytic techniques when the latter exist.

The analytic maximization techniques used in the previous subsection do not immediately extend to maximization of the match for eccentric waveforms, but we generalize them under the assumption that the harmonics are mutually orthogonal. In the absence of radiation reaction, the different harmonics are exactly mutually orthogonal, $(h_j|d_k) = 0$ for $j \neq k$, because they are delta functions centered at integer multiples of mean orbital frequency. In the presence of radiation-reaction, this is not exactly the case any longer, but let us continue to assume it is so, and then check at the end the amount of error introduced by this approximation.

Working in the mutual orthogonal approximation, Eq. (1.32) becomes

$$\begin{aligned} (h|d) &= \sum_{j,k=1}^{\infty} (h_j|d_k) \approx \sum_{j=1}^{\infty} (h_j|d_j) \,, \\ &\approx 4\mathrm{Re}\left[\sum_{j=1}^{\infty} e^{ijl_c} \int_0^{\infty} \frac{|\hat{h_j}|^2}{S_n(f)} e^{-2\pi f t_0 + ijl_0} e^{2\pi f t_c} df\right] . \end{aligned} \tag{1.33}$$

Without specifying t_c or l_c, we are able to construct

$$\tilde{G}_j(f) = \frac{|\hat{h_j}|^2}{S_n(f)} e^{-2\pi i f t_0 + ijl_0} \,, \tag{1.34}$$

whose inverse Fourier transform $\mathcal{F}^{-1}[\cdot]$ with respect to t_c,

$$G_j(t_c) = \mathcal{F}^{-1}\left[\tilde{G}_j(f)\right] = \int_0^{\infty} \frac{|\hat{h_j}|^2}{S_n(f)} e^{-2\pi i f t_0 + ijl_0} e^{2\pi i f t_c} df \,, \tag{1.35}$$

appears in the inner product of Eq. (1.33)

$$(h|d) = 4 \sum_{j=1}^{\infty} \mathrm{Re}\left[e^{ijl_c} G_j(t_c)\right] \,. \tag{1.36}$$

This expression can now be maximized over l_c and t_c in a way analogous to the quasi-circular case. Each individual term in the sum of Eq. (1.36) can be individually maximized on l_c by taking the absolute value of the argument of the real operator because the factor e^{ijl_c} only rotates $G_j(t_c)$ in the complex plane, but leaves its *magnitude* unchanged. Thus we can maximize over l_c by computing

$$\begin{aligned}
\max_{l_c}(h|d) &= 4\sum_{j=1}^{\infty}\max_{l_c}\left\{\mathrm{Re}\left[e^{ijl_c}G_j(t_c)\right]\right\} \\
&= 4\sum_{j=1}^{\infty}|G_j(t_c)|. \qquad (1.37)
\end{aligned}$$

To maximize on t_c we take the maximum value of the array that results from taking the sum of the absolute values of the inverse Fourier transforms appearing above. Again, in this method of maximization one never explicitly calculates $l_{\max}$ to compute the match, and thus, we refer to it as the *eccentric implicit maximization* method. This method runs the risk of *overestimating* the match, as we will show later in Sec. 1.3.3 because of the mutual orthogonality assumption.

Let us now consider the explicit maximization method. In order to explicitly find $l_{\max}$ and $t_{\max}$, we begin by associating $t_{\max}$ with the maximum value of the sum of the absolute values of the inverse Fourier transforms appearing in Eq. (1.37). Inspection of Eq. (1.35) reveals that $G_j(t_{\max})$ is a complex number which is rotated off the real axis by jl_0 (again since $t_c = t_0 = t_{\max}$, the integrand appearing in Eq. (1.35) is purely real aside from the factor of e^{ijl_0}, which rotates it off the real axis). The maximum l_c value is then found using trigonometry:

$$jl_0 = jl_{\max} = \arctan\left\{\frac{\mathrm{Im}[G_j(t_{\max})]}{\mathrm{Re}[G_j(t_{\max})]}\right\}. \qquad (1.38)$$

Unlike in the quasi-circular case, however, the above procedure only produces $jl_{\max}$, which is degenerate with $l_{\max} \to l'_{\max} + 2\pi/j$. One is thus forced to either break this degeneracy by computing Eq. (1.38) explicitly with two different harmonics or try each of the j degenerate guesses for l_{max} (Since the $j = 1$ harmonic is not degenerate, one could just use this harmonic.) In practice, we have found that the most reliable method is to compute Eq. (1.38) for 3 different harmonics ($j = 2, 3, 4$), break the degeneracy, try each l_{max}, and take the one that leads to the best match. As in the quasi-circular case, we here explicitly find the value of $(l_{\text{max}}, t_{\text{max}})$ that maximize the match, and thus, we refer to it as the *eccentric explicit maximization* method. As expected, this method is a bit slower than the implicit maximization, but is better behaved as we relax the assumption of orthogonality between harmonics.

1.3.3 Orthogonality Investigation

Let us begin by examining how much orthogonality is broken when including radiation-reaction by computing the quantity

$$\Delta_{i,j} = \max_{l_c} \frac{(h_i|h_j)}{\sqrt{(h_i|h_i)(h_j|h_j)}}. \tag{1.39}$$

The above inner product between different harmonics h_i and h_j is maximized over any relative phase shift. If the value of $\Delta_{i,j}$ is 0 for all i and j, then the different harmonics are orthogonal and the above approximate methods of maximization are both *exact*. In the numerics that ensue, we use our new eccentric model to evaluate Δ_{ij}, which we refer to as the *Newtonian eccentric Fourier domain* model (NeF) and will be described in detail in Sec. 1.4. The results below, however, should be representative of the orthogonality between harmonics of other PN models as well, as long as they're being evaluated in their domain of validity in eccentricity.

Table 1.1 shows $\Delta_{i,j}$ for the first 5 harmonics of the GWs emitted by a $(10, 10)M_\odot$ binary black hole (BBH) system with a few different initial conditions, where the harmonics are generated with the NeF model. We adopt slightly different frequency

$\Delta_{i,j}$	2	3	4	5
1	0.0035	0.00041	0.00023	0.0043
2	-	0.0013	0.000046	0.00011
3	-	-	0.0010	0.00022
4	-	-	-	0.00039

$\Delta_{i,j}$	2	3	4	5
1	0.0043	0.00074	0.00016	0.0068
2	-	0.0025	0.00024	0.000088
3	-	-	0.000046	0.000083
4	-	-	-	0.00015

$\Delta_{i,j}$	2	3	4	5
1	0.03	0.016	0.011	0.0080
2	-	0.090	0.037	0.022
3	-	-	0.033	0.013
4	-	-	-	0.0077

Table 1.1: The value of $\Delta_{i,j}$ for a $(10, 10)M_\odot$ system with $e_0 = 0.3$ and $F_0 = 3$ Hz (left table), $e_0 = 0.6$ and $F_0 = 3$ Hz (center table) and $e_0 = 0.9$ and $F_0 = 3$ Hz (right table). The first row and column of each table give the values of i and j, respectively. The diagonal terms are 1 and $\Delta_{i,j}$ is symmetric, thus redundant entries have been omitted. The frequency resolution of the inner product appearing in $\Delta_{i,j}$ is $\delta f = 0.0078$ Hz (left), $\delta f = 0.03125$ Hz (center) and $\delta f = 2$ Hz (right). Observe that orthogonality is weakly violated in the low and moderate-eccentricity cases, and less weakly violated in the high-eccentricity case.

resolutions, with choices made to correspond to the resolution of a discrete Fourier transform of a waveform with a period determined by the initial conditions, sampled at 8192Hz in the time domain, and zero-padded such that its length is the nearest power of 2. For the systems with lower eccentricity ($e_0 = 0.3, 0.6$), the values of $\Delta_{i,j}$ are fairly small, of $\mathcal{O}(10^{-4})$. However, for the higher eccentricity system ($e_0 = 0.9$), $\Delta_{i,j}$ is larger with values of $\mathcal{O}(10^{-2})$. This high value is partly due to the low frequency resolution, but it is consistent with the resolution of some of the matches that one would realistically find using waveforms of short duration.

Let us now examine the error incurred by our analytic maximization over t_c and l_c due to the absence of orthogonality. Assuming the maximum inner product is obtained when $t_c = t_0$ and $l_c = l_0$, we find by inspection of Eq. (1.32) that the maximized inner product takes the form

$$M_{\text{exact}} = 4 \sum_{k,j=1}^{\infty} \text{Re} \left[\int_0^\infty \frac{\hat{h}_j^* \hat{h}_k}{S_n(f)} e^{il_0(k-j)} df \right] . \tag{1.40}$$

When we consider the inner product maximized via the eccentric implicit maximization, Eq. (1.37), it is straightforward to show that we are calculating the following in the absence of orthogonality:

$$M_{\text{implicit}} = 4 \sum_{j=1}^{\infty} \text{Abs} \left[\sum_{k=1}^{\infty} e^{ikl_0} \int_0^{\infty} \frac{\hat{h}_j^* \hat{h}_k}{S_n(f)} df \right]. \tag{1.41}$$

Comparing Eqs. (1.41) and (1.40) reveals that the implicit maximization can potentially *overestimate* the value of the match and that it can even become greater than 1. Therefore, in the high eccentricity limit this maximization technique becomes inaccurate, but is still a useful approximation.

Let us now consider the error incurred by using the eccentric explicit maximization. In this case, there is no way to overestimate the match and the overlap is still properly normalized. However, we can still incur an error because the l_{max} derived from the explicit maximization method in Eq. (1.38) assumes mutual orthogonality, and thus, it may not be an accurate estimate of the true l_{max}. Since $G_j(t_{\text{max}})$ appears in Eq. (1.38), it is useful to consider this quantity in the absence of orthogonality:

$$G_j^{\text{exact}}(t_{\text{max}}) = \int_0^{\infty} \frac{|\hat{h}_j|^2}{S_n(f)} e^{ijl_0} df + \sum_{k \neq j}^{\infty} \int_0^{\infty} \frac{\hat{h}_j^* \hat{h}_k}{S_n(f)} e^{ikl_0} df. \tag{1.42}$$

Adopting the notation

$$\alpha_{j,k} = \int_0^{\infty} \frac{\hat{h}_j^* \hat{h}_k}{S_n(f)} e^{ikl_0} df, \tag{1.43}$$

we rewrite Eq. (1.42) as

$$G_j^{\text{exact}}(t_{\text{max}}) = \alpha_{j,j} \left(1 + \sum_{k \neq j}^{\infty} \frac{\alpha_{j,k}}{\alpha_{j,j}} \right). \tag{1.44}$$

We can now identify a small parameter

$$\epsilon \equiv \sum_{k \neq j}^{\infty} \frac{\alpha_{j,k}}{\alpha_{j,j}} \ll 1\,, \tag{1.45}$$

and expand Eq. (1.38) to first order in ϵ to obtain

$$\begin{aligned} j l_{\max}^{\text{exact}} &= \arctan\left[\frac{\mathrm{Im}[G_j^{\text{exact}}(t_{\max})]}{\mathrm{Re}[G_j^{\text{exact}}(t_{\max})}\right] \\ &\approx j l_0 + \sin(j l_0)\cos(j l_0)[\mathrm{Im}(\epsilon) - \mathrm{Re}(\epsilon)]. \end{aligned} \tag{1.46}$$

We then see that the error in $l_{\max}$ using the explicit maximization method is proportional to the difference in the imaginary and real parts of ϵ, which is always much less than unity.

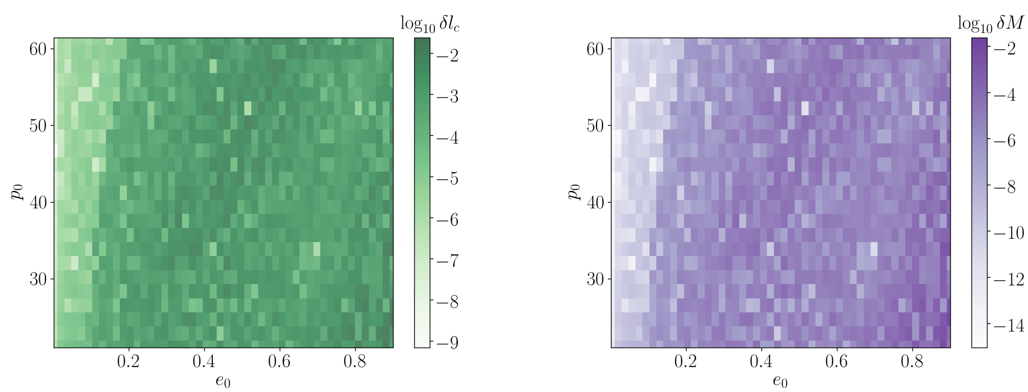

Figure 1.5: The log of the error between the $l_{\max}$ as predicted by Eq. (1.38) and the maximum l_c found by `Mathematica`'s built-in maximization on the left. On the right the error in the match as predicted by the explicit maximization technique and `Mathematica`'s built-in maximization is shown. The system is a BBH binary and the initial conditions are indicated on the x and y axis. The error in the match resulting from explicit maximization is greater as eccentricity increases, but the mean of the error in match is $\sim 10^{-6}$, which is much less than our estimated numerical accuracy.

The left panel of Fig. 1.5 shows the error between $l_{\max}^{\text{explicit}}$, as predicted by the explicit maximization in Eq. (1.38), and $l_{\max}^{\rm exact}$, as predicted by `Mathematica`'s built in maximization routine, while the right panel shows the resulting error in the match. The matches here are between NeF and an "exact" time domain waveform (described in detail in Sec. 1.4.3) obtained by numerically solving the orbital dynamics, given in Eqs. (1.3b), (1.11), and (1.12), and inserting these solutions into the plus and cross GW polarizations given in Eqs. (1.4) and (1.5). For a majority of the initial conditions the explicit maximization is correct to a few (3-5) decimal places. The resulting error in match is also in about the $4^{\rm th}$-$8^{\rm th}$ digit, with a mean error of 10^{-6}. We thus conclude that the explicit method of maximization is highly accurate.

1.4 Eccentric Models

With all of this maximization discussion under control, let us now discuss eccentric waveform models. We begin by reviewing current models in the context of the general Fourier response presented in Eq. (1.16) of Sec. 1.2.2. The main result of this work, the derivation of our *Newtonian eccentric Fourier domain model* (NeF), is presented in Sec. 1.4.2. Lastly, we present the *numerically evolved Newtonian time domain model* (NeT), which we will treat as "exact" for the purpose of comparison with our frequency domain model.

1.4.1 Previous Work

In the Post-Circular formalism (PC), the waveform model is given by Eq. (1.16), but expanding all quantities in a low eccentricity expansion. The functions appearing in the phase, ψ_j, are re-expressed via the chain rule as integrals over mean orbital frequency:

$$t - t_c = \int^{F} \frac{dF'}{\dot{F}(F', e(F'))} \,, \tag{1.47}$$

$$l - l_c = 2\pi \int^F \frac{F'}{\dot{F}(F', e(F'))} dF' \ . \tag{1.48}$$

The subscript c denotes the respective quantity at the time of coalescence. Since the time derivative of the mean orbital frequency appearing in the denominator of the above integrands depends on the orbital eccentricity, one must obtain the orbital eccentricity as an explicit function of frequency, $e(F)$. Equation (1.14) is transcendental for $e(F)$, but it can be inverted in the low eccentricity limit as a bi-variate expansion in e_0 and $\chi = F_0/F$. One then substitutes this inversion in the integrand appearing in Eqs. (1.47) and (1.48) to analytically perform the integration.

In the PC formalism, the amplitudes of each harmonic appearing in Eq. (1.9) are also expanded in the low eccentricity limit. Since the j^{th} harmonic amplitude scales, to leading order in a low eccentricity expansion, as e^{j-2} except for the $j = 1$ harmonic, the number of harmonics kept in the sum appearing in Eq. (1.16) is controlled by the self consistency of the low eccentricity expansion. The end result is an analytic waveform of the form of Eq. (1.16) in which all pieces are series expansions in e_0 and χ. The advantage of such models is their computational efficiency, but the main disadvantage is that they become inaccurate at moderate eccentricities.

The PC formalism has been implemented to several PN orders. The framework was introduced at Newtonian order in Ref. [24], keeping eccentric corrections up to $\mathcal{O}(e_0^8)$, and as a result, the sum in Eq. (1.16) was truncated at $j = 10$. This work was extended to 2PN order in the phasing by [25], with the PN amplitude corrections kept at Newtonian order and the PN phase corrections truncated at $\mathcal{O}(e_0^6)$. A further extension to 3PN in the phasing was done in [27], keeping only the second ($j = 2$) harmonic, the amplitude at Newtonian order in the quasi-circular limit and the PN phase corrections truncated at $\mathcal{O}(e_0^2)$. None of these models ought to be accurate for moderately eccentric systems, although a precise analysis in terms of the match and relative to exact, numerical PN waveforms have not yet been carried out.

Several other extensions of the PC framework also exist. The enhanced PC (ePC) model introduced by [28] leverages the results of [24] and the quasi-circular part of the Fourier phase (known to 3.5PN order) in order to construct a 3.5PN eccentric model. However, this model is not constructed in a PN consistent manner. Recently [29] incorporated spin into a PC-like model, using a semi-analytic approach by computing the phase functions numerically at 3PN order. As such, the Fourier phases are accurate for all eccentricities, but the amplitudes appearing in Eq. (1.16) are computed through a low-eccentricity expansion. As in the more vanilla PC models, these extensions are also valid only for small eccentricities, with e.g. [29] claiming matches greater than 0.99 provided $e_0 \lesssim 0.3$.

One reason for the inaccuracy of all PC models is the low-eccentricity inversion of the orbital eccentricity as a function of mean orbital frequency, with comparison against numerical inversions sometimes used as a rough gauge of the regime of validity of the model. Section 1.5 studies this error quantitatively and in great detail, but let us here summarize the main results. Consider introducing inaccuracies in the exact solutions for $e(F)$ and ψ_j parametrically, and then studying the loss in match as the magnitude of the inaccuracies and the orbital eccentricity is increased. Such a study would reveal that even for mildly eccentric binaries ($e_0 \sim 0.3$), the relative error in $e(F)$ must be below $\sim 10^{-4}$ and the relative error in ψ_j must be below $\sim 10^{-3}$ for the match to remain above 99%. These results strongly suggest that an accurate Fourier domain model must represent $e(F)$ and ψ_j very accurately to avoid a large loss in match.

One potential source of confusion that occurs throughout the literature of the PC models is the interpretation of the parameter $\chi = F/F_0$. In order to evaluate the model at a given GW frequency, χ must be evaluated at the stationary point, $\chi(F(t_j^*))$, via the stationary phase condition $jF(t_j^*) = f$, yielding $\chi = f/(jF_0)$. What is often done is to choose $j = 2$ in this relation so that $\chi = f/f_0$ with $f_0 := 2F_0$ identified as "the frequency when the signal enters band." In reality, this is the GW frequency when the $j = 2$ harmonic enters band, and although this harmonic dominates the entire signal when the eccentricity is truly small, it does not even when $e_0 \sim 0.1$, as shown in Fig. 1.2. This observation strongly suggests that an accurate Fourier domain model must represent the Fourier phase as a function of the harmonic index.

As far as we know, there is only a single alternative to the small eccentricity approximation of the PC framework if one wishes to obtain analytic Fourier waveforms, but it comes at the cost of computational expense. In Ref. [69], the stationary time and the orbital phase in Eq. (1.16) are solved at Newtonian order by changing the integration variable from time to eccentricity ($dt = de/\dot{e}$). The resulting integrals then yield hypergeometric functions which depend on the orbital eccentricity, and to invert these and express eccentricity as a function of orbital frequency, one resorts to numerical methods. Reference [69], however, does not discuss how to truncate the sum appearing in Eq. (1.16) or how a formal model ought to be constructed. Reference [71] extends this method to 1PN order, but a 1PN term in the integral for the time to coalescence is there approximated as unity, when in reality it varies from 1 to 0.94. This leads to a 2% error in $t(e)$, which Section 1.5.1 shows is too large of an error for faithful modeling. Regardless of these issues, these alternative models are computationally expensive because the amplitudes are left exact as infinite sums, and costly hypergeometric functions appear in the Fourier phase.

1.4.2 NeF Model

Let us now introduce the main result of this work: an analytic Fourier-domain waveform model that is valid to eccentricities as high as 0.9 and that we will refer to as the *Newtonian eccentric Fourier domain model* (NeF) throughout this work. This model is defined by the SPA of the harmonically-decomposed time-domain signal in Eq. (1.16), where notice that the amplitude coefficients are *not* expanded in small eccentricity, unlike what is done in the PC model. The model is then fully defined if we can

(i) Provide an accurate analytic representation for the harmonic-dependent Fourier phase $\psi_j(e)$,

(ii) Separately attempt to solve for the orbital eccentricity e as a function of the mean orbital frequency F.

Once we have $\psi_j(e)$ and $e(F)$, we can then express the harmonic-dependent Fourier phase as a function of the GW frequency through the stationary phase condition in Eq. (1.18).

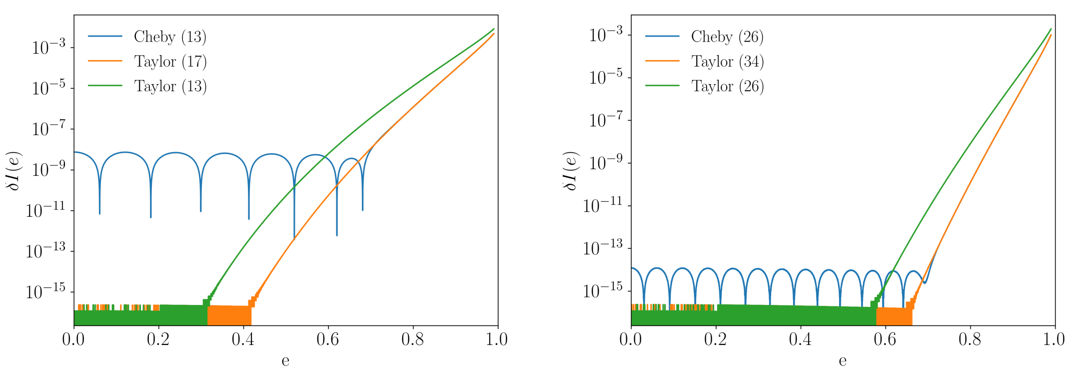

Figure 1.6: The error in $I(e)$ between the exact solution and the Chebyshev resummation, the Taylor expansion which is resummed, and a Taylor expansion which contains as many terms as the Chebyshev resummation. On the left, we keep 13 terms in the Chebyshev expansion, and 17 in the Taylor expansion which is resummed (as indicated in parenthesis in the legend). On the right we double the number of terms kept in both. We can achieve higher accuracy when keeping more terms, however, we find that a 13 term Chebyshev resummation is sufficient for our purposes.

We begin by evaluating the different pieces that make up $\psi_j(e)$ in the SPA, as for example given in Eq. (1.17). Following the work of [69], we use the chain rule $dt = de/\dot{e}$ to write

$$t - t_c = \int_0^e \frac{de'}{\dot{e}(e')} \ , \tag{1.49}$$

$$l - l_c = 2\pi \int_0^e \frac{F(e')}{\dot{e}(e')} de' \ . \tag{1.50}$$

Using the solution for $F(e)$ given in Eq. (1.14), these integrals can be evaluated in closed form and they yield

$$\begin{aligned} t - t_c &= -\frac{m}{\eta} \frac{15}{(2\pi m F_0)^{8/3} \sigma(e_0)^4} \int_0^e \frac{\sigma(e')^4 (1 - e'^2)^{5/2}}{e'(304 + 121 e'^2)} de' \\ &= -\frac{m}{\eta} \frac{15}{304 (2\pi m F_0)^{8/3} \sigma(e_0)^4} I_t(e) \ , \end{aligned} \tag{1.51}$$

and

$$\begin{aligned} l - l_c &= -\frac{30\pi}{(2\pi m F_0)^{5/3} \sigma(e_0)^{5/2}} \int_0^e \frac{[\sigma(e')(1 - e'^2)]^{5/2}}{e'(304 + 121 e'^2)} de' \\ &= -\frac{30\pi}{(2\pi m F_0)^{5/3} \sigma(e_0)^{5/2}} I_l(e) \ , \end{aligned} \tag{1.52}$$

where we have defined

$$I_t(e) = \frac{19}{48} e^{48/19} F_1 \left(\frac{24}{19}; -\frac{1181}{2299}, \frac{3}{2}; \frac{43}{19}; -\frac{121}{304} e^2, e^2 \right) \ , \tag{1.53}$$

$$I_l(e) = \frac{19}{30} e^{30/19} {}_2F_1 \left(\frac{124}{2299}, \frac{15}{19}; \frac{34}{19}; -\frac{121}{304} e^2 \right) . \tag{1.54}$$

Here F_1 in I_t is the ApellF1 hypergeometric function and ${}_2F_1$ in I_l is the generalized hypergeometric function.

The Fourier phase of the j^{th} harmonic is then

$$\psi_j(e) = jl_c - 2\pi f t_c - j\frac{15}{304\eta}\left(\frac{1}{2\pi m F_0}\right)^{5/3}\sigma(e_0)^{-5/2}\left\{\frac{1}{\sigma[e(t_j^*)]^{3/2}}I_t(e) - I_l(e)\right\}. \tag{1.55}$$

We can simplify the Fourier phase using the identity for ApellF1 hypergeometric functions

$$F_1(\alpha;\beta,\beta';\gamma;x,y) = (1-x)^{-\beta}(1-y)^{-\beta'}F_1\left(\gamma-\alpha;\beta,\beta';\gamma;\frac{x}{x-1},\frac{y}{y-1}\right). \tag{1.56}$$

which then yields

$$\psi_j = jl_c - 2\pi f t_c - j\frac{15}{304\eta}\left(\frac{1}{2\pi m F_0}\right)^{5/3}\sigma(e_0)^{-5/2}e^{30/19}I(e)\ , \tag{1.57}$$

where

$$\begin{aligned} I(e) = {} & \frac{19}{48(1+\frac{121e^2}{304})^{124/2299}}F_1\left(1;-\frac{1181}{2299},\frac{3}{2};\frac{43}{19};\frac{121e^2}{304+121e^2},\frac{e^2}{e^2-1}\right) \\ & -\frac{19}{30}\,{}_2F_1\left(\frac{124}{2299},\frac{15}{19};\frac{34}{19};-\frac{121e^2}{304}\right)\ . \end{aligned} \tag{1.58}$$

The above equation for the phase is exact, and thus valid for all eccentricities, but it suffers from the fact that the hypergeometric functions are computationally costly to evaluate, especially F_1. One could of course create a look-up table for these functions to remove the computational cost, but as we shall see, there is a better, analytic approach. After exploring different representations of hypergeometric functions, we find that $I(e)$ is well-approximated by a Chebyshev resummation of a Taylor expansion about small eccentricity. After the collecting of like terms in eccentricity in the Chebyshev resummation, we are able to approximate the frequency dependence of the phase as

$$I(e) \approx \sum_{n=0}^{n=12} C_n e^{2n}, \tag{1.59}$$

where the C_n coefficients and a brief review of Chebyshev resummations is provided in Appendix 1.B. The first few C_n, evaluated to double precision, are

$$C_0 = -0.2375000017589697\ , \tag{1.60a}$$

$$C_1 = -0.3006152896315175\ , \tag{1.60b}$$

$$C_2 = -0.009023468528641264\ , \tag{1.60c}$$

$$C_3 = -0.03715292002990571\ , \tag{1.60d}$$

$$C_4 = -0.01543183701515415\ . \tag{1.60e}$$

Using a simple timing study implemented in `Mathematica`, we find that the resulting approximation is $\sim 10^4$ times faster than evaluating the exact result in Eq. (1.58).

Figure 1.6 shows the relative error between the exact form of $I(e)$ and the Chebyshev resummation keeping 13 terms (left panel) and 26 terms (right panel), and between the exact form and the Taylor series which is Chebyshev resummed or the Taylor series with the same number of terms as what is kept in the Chebyshev resummation. By relative error, we explicitly mean $\delta I(e) = 1 - I_{\text{app}}(e)/I(e)$, where $I_{\text{app}}(e)$ is the approximate solution for $I(e)$, which is the exact solution. Observe that the simple Taylor expansion does surprisingly well at representing the exact function. Observe also that the Chebyshev resummation is capable of representing the exact function in a wider range of eccentricity to a relative accuracy better than 10^{-8} and 10^{-13} in the 13-term and 26-term case respectively. We will see in Secs. 1.5 and 1.6.2 that the level of error in the left panel is tolerable to obtain matches above 99%.

Nonetheless, the method can be easily extended to higher order if higher accuracy is desired for implementation in more sensitive, third-generation detectors.

The Fourier phase in Eq. (1.57) is a function of the orbital eccentricity, but the latter must be mapped to mean orbital frequency F, so that it can be further mapped to GW frequency f via the stationary phase condition $jF[e(t_j^*)] = f[e(t_j^*)]$. Reasonably, one is tempted to invert the transcendental equation for $F(e)$ in Eq. (1.14) in a low eccentricity approximation. However, Section 1.5.2 will show that the low eccentricity inversion of $F(e)$ fails at $e_0 \gtrsim 0.3$, regardless of the number of terms kept. In fact, it is this inversion for $F(e)$ which is probably responsible for the failure of all PC models.

Let us then discuss the analytic inversion of this function. The condition we must invert is

$$\sigma(e) = \zeta\,, \tag{1.61}$$

where recall that $\sigma(e)$ is defined in Eq. (1.15), we have defined $\zeta := (jC_0/f)^{2/3} = \sigma(e_0)(jF_0/f)^{2/3} = \sigma(e_0)(F_0/F)^{2/3}$, and we have used that the constant $C_0 = F_0\sigma(e_0)^{3/2}$ ensures that $F(e_0) = F_0$. Defining the inverse function κ such that $\kappa[\sigma(e)] = e$, the solution is then simply

$$e(f) = \kappa(y) = \kappa\left[\left(\frac{f}{jC_0}\right)^{3/2}\right]. \tag{1.62}$$

Since the inverse function κ is *system-independent*, this function can be obtained once and only once by any means at our disposal.

Let us first discuss analytic inversions. We were able to obtain two analytic representations of $e(\zeta)$ that meet the error tolerance that will be laid out in Sec. 1.5 (relative error of $\mathcal{O}(10^{-6})$). The first is obtained by introducing a $\bar{\sigma}_3(e) \approx \sigma(e)$, whose inverse $\bar{\kappa}_3(\zeta)$ can be found algebraically (the subscript "3" arises from the construction of other approximate $\bar{\sigma}_n$ which are reviewed in Appendix 1.C). The approximate inverse function $\bar{\kappa}_3(\zeta)$ is given by

$$\bar{\kappa}_3(\zeta) = \left\{ -\frac{1}{43923 + 277248\zeta^{19/6}} \left[1824\zeta^{19/6} \left(\frac{283475(2)^{2/3}}{(38)^{1/3}\alpha} - 152 \right) \right.\right. \\ \left.\left. +4\left(18392 - \left(\frac{2}{19}\right)^{1/3} \frac{2225432}{\alpha} - 19^{2/3}\alpha \right) \right] \right\}^{1/2} , \tag{1.63}$$

where we have defined

$$\alpha = \left\{ 2154218176 + 12750\zeta^{19/12}\left(14641 + 92416\zeta^{19/6}\right)\left[51\left(1216 + 11475\zeta^{19/6}\right)\right]^{1/2} \right. \\ \left. -7650\zeta^{19/6}\left(-41031947 + 117830400\zeta^{19/6}\right) \right\}^{1/3} . \tag{1.64}$$

Using this $\bar{\kappa}_3(\zeta)$, we can approximate $e(\zeta)$ to relative error of $\mathcal{O}(10^{-3})$ for sources with e_0 as high as 0.9. In order to further decrease the error we numerically fit the difference using a function of the form

$$e(\zeta) \approx \bar{\kappa}_3(\zeta) \left(1 + \frac{a e^{-b\zeta^{-c}}}{\zeta^d} + \sum_n^{30} H_n L_n(\zeta) \right) , \tag{1.65}$$

where $L_n(\zeta)$ are Legendre polynomials and the constants a, b, c, d, H_n are fitted for and presented in Appendix 1.C.

A second analytic inversion that is faster than the first can be obtained through a piecewise ansatz

$$e(\zeta) \approx \begin{cases} e_{\text{Low}}(\zeta) & \zeta \leq \zeta_{\text{Low}} \\ e_{\text{Mid}}(\zeta) & \zeta_{\text{Low}} < \zeta < \zeta_{\text{High}} \\ e_{\text{High}}(\zeta) & \zeta \geq \zeta_{\text{High}} \end{cases} \tag{1.66}$$

The $e_{\text{Low}}(\zeta)$ and $e_{\text{High}}(\zeta)$ are found by inverting Eq. (1.61) in the $\zeta \ll 1$ and $\zeta \gg 1$

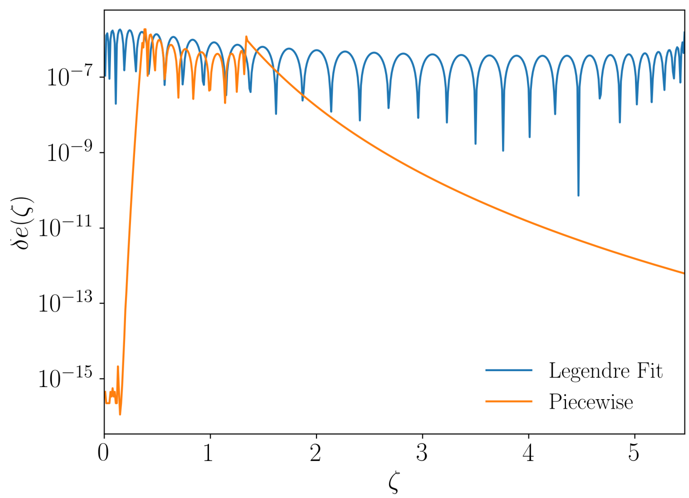

Figure 1.7: The relative error, $\delta e(\zeta)$, between a numerical solution and the Legendre fit presented in Eq. (1.65) (shown in blue) and the piecewise function in Eq. (1.66). The piecewise representation is ~ 30 times faster than the Legendre fit and covers the entire domain of $\zeta \in [0, \infty]$, with less error.

limits through a Taylor expansion, while $e_{\rm Mid}(\zeta)$ is built through a numerical fit. The bounds $\zeta_{\rm Low}$ and $\zeta_{\rm High}$ correspond to the ζ at which the two inversions exceed $\mathcal{O}(10^{-6})$ relative error with an exact solution. The details of the construction of this function and the values of the coefficients are given in Appendix 1.C.

Although these analytic representations are sufficiently accurate for our purposes, they are not the fastest and most accurate solution to the problem. As we indicated above, Eq. (1.61) is system-independent, so any inversion that is accurate and fast will do. In particular, due to the presence of the unit step functions in Eq. (1.16), each harmonic samples $e(f)$ at frequencies $f \in [jF_0, jF_{\rm LSO}]$, and since by the stationary phase condition $f = jF$, any harmonic samples $e(F)$ at orbital frequencies $F \in [F_0, F_{LSO}]$. Thus one only needs to solve for $e(F)$ once, and the result can be used to sample $e(f)$ for any harmonic. A fully-numerical possibility is to either solve de/dF numerically (constructed by differentiating Eqs. (1.11) and (1.12)) or to sample $F(e)$ sufficiently discretely, swapping the columns and then interpolating the result with a cubic spline. Either of these two methods is extremely fast and it can be carried out to double precision.

Figure 1.7 shows the relative error between the numerical solution for $e(\zeta)$, the fit developed in Eq. (1.65), and the piecewise representation of $e(\zeta)$ in Eq. (1.66). Both analytic representations of $e(\zeta)$ maintain a relative error below $\mathcal{O}(10^{-6})$ which is what we will show in Sec. 1.5 is needed for applications in which one is concerned with keeping a high value of the match. However, the evaluation of the Legendre (piecewise) representations is roughly 100 (3) times slower than the evaluation of the numerical solution. For this reason, we employ the numerical solution when constructing the NeF model henceforth due to its computational speed advantages.

1.4.3 NeT Model

The validation of the NeF model requires its comparison to another model that we consider more accurate or exact. We will take this to be an eccentric extension of the quasi-circular TaylorT4 approximant [78], which we will refer to as the *Newtonian eccentric Time domain model* (NeT). This is obtained by numerically solving the set of differential equations in Eqs. (1.3b), (1.11) , and (1.12) for $\phi(t)$, $F(t)$, and $e(t)$, respectively, and then inserting these expressions in the plus and cross polarizations given by Eqs. (1.4) and (1.5). The time-domain polarizations are then discretely Fourier transformed to obtain a representation in the frequency domain.

The integration of the equations of motion is done as follows. We start all numerical integrations with initial conditions $\phi(t_0) = -\pi/2$, $F(t_0) = F_0$, and $e(t_0) = e_0$. This choice is such that binary is initially moving towards and close to pericenter passage. For highly eccentric systems ($e \approx 0.9$), much of the GW power is emitted during pericenter passage, and the eccentricity can decrease significantly between passages if the system is compact enough. Thus, our choice of initial conditions is such that the binary begins emitting GWs with significant power at an initial orbital eccentricity of e_0. For systems with small initial eccentricity or large initial separation (low initial mean orbital frequency) the choice of ϕ_0 becomes less important. We stop our numerical evolution at the last stable orbit (LSO), which is given by Eq. (1.19). Two independent implementations of this integration were developed, one in `Mathematica` with precision and accuracy goals of 13, and one in `C` using the Implicit Bulirsch-Stoer method with a supplied Jacobian for adaptive step-size control. These implementations lead to $h(t)$, $n(t)$, and $e(t)$ that agree to $\sim 10^{-8}$ relative error.

The discrete Fourier transform is done as follows. First, the time-domain functions are sampled at a rate of 8192 Hz, leading to N samples. Then, this discretely sampled time-series is zero padded on both edges with pads of equal length, such that the new time-series is of length 2^p, with p the smallest integer such that $2^p > N$. The new time series is then discrete Fourier transformed.

1.5 Error Analysis of SPA Ingredients

In this section, we investigate the loss in match, maximized via the prescription given in Sec. 1.3, due to errors in the inversion of $F(e)$ and in the calculation of $\psi_j(e)$ to inform analytic models on tolerable errors. We then show that the standard low eccentricity inversion of $F(e)$ leads to a significant loss of match when $e_0 \sim 0.3$ for a BBH system.

In order to investigate the loss in match due to these inaccuracies, we require an exact solution for the analytic Fourier response. To create this exact model we interpolate the eccentricity dependent term of the phase, $I(e)$, given in Eq. (1.58), and we generate a numerical solution for $e(F)$ by numerically solving Eq. (1.14). With

$\log_{10}(\epsilon)$	$e_0 = 0.1$		$e_0 = 0.3$		$e_0 = 0.6$		$e_0 = 0.9$	
-16	0.9877	(0.9877)	0.9847	(0.9847)	0.9825	(0.9825)	0.9828	(0.9828)
-8	0.9877	(0.9877)	0.9847	(0.9847)	0.9825	(0.9825)	0.9828	(0.9828)
-6	0.9877	(0.9877)	0.9847	(0.9847)	0.9825	(0.9825)	0.9824	(0.9825)
-5	0.9877	(0.9877)	0.9847	(0.9847)	0.9820	(0.9822)	0.9743	(0.9761)
-4	0.9872	(0.9876)	0.9844	(0.9846)	0.9765	(0.9790)	0.9046	(0.9134)
-3.5	0.9854	(0.9871)	0.9790	(0.9826)	0.9312	(0.9546)	0.8459	(0.8852)
-3	0.9670	(0.9833)	0.9469	(0.9705)	0.8641	(0.9189)	0.7623	(0.8389)
-2.75	0.9395	(0.9773)	0.9108	(0.9605)	0.8185	(0.8952)	0.7189	(0.8086)
-2.5	0.8776	(0.9639)	0.8500	(0.9447)	0.7614	(0.8682)	0.6532	(0.7783)
-2.25	0.7886	(0.9438)	0.7633	(0.9223)	0.6853	(0.8444)	0.5887	(0.7502)
-2	0.6703	(0.9168)	0.6506	(0.8923)	0.5890	(0.8105)	0.5137	(0.7130)

Table 1.2: Match for different values of ϵ when using e_1 (not in parenthesis) and e_2 (in parenthesis) as approximate inversions. The first column lists the value of ϵ, the other columns list the value of the match for a given e_0. For each of the values shown here, the corresponding system is a BBH system with an initial dimensionless semi-latus rectum of $p_0 = 50$. For large eccentricities, the match begins to decrease as $\epsilon \sim 10^{-5}$.

these solutions in hand, we have an exact (to machine precision), numerical solution for the Fourier response in the SPA, and it is this exact solution that we will use to investigate inaccuracies in ψ_j and $e(F)$. For consistency with our faithfulness study in Sec. 1.6.2, we truncate the the sum over harmonics in Eq. (1.16) at a sufficiently high harmonic index such that the match between it and the NeT model is ~ 0.99, as detailed in Sec.1.6.1 and 1.6.2.

1.5.1 Loss in match due to inaccurate $e(F)$ and ψ_j

To investigate the loss in match due to the inaccurate inversion of $F(e)$, we begin by numerically solving Eq. (1.14) and refer to this solution as $e(F)$. To simulate

$\log_{10}(\epsilon)$	$e_0 = 0.1$		$e_0 = 0.3$		$e_0 = 0.6$		$e_0 = 0.9$	
-16	0.9877	(0.9877)	0.9847	(0.9847)	0.9825	(0.9825)	0.9828	(0.9828)
-8	0.9877	(0.9877)	0.9847	(0.9847)	0.9825	(0.9825)	0.9828	(0.9828)
-6	0.9877	(0.9877)	0.9847	(0.9847)	0.9825	(0.9825)	0.9827	(0.9827)
-5	0.9877	(0.9877)	0.9847	(0.9847)	0.9823	(0.9824)	0.9809	(0.9812)
-4	0.9874	(0.9877)	0.9847	(0.9847)	0.9820	(0.9823)	0.9311	(0.9416)
-3.5	0.9874	(0.9874)	0.9830	(0.9841)	0.9670	(0.9743)	0.8904	(0.9057)
-3	0.9862	(0.9858)	0.9680	(0.9781)	0.9067	(0.9399)	0.8276	(0.8693)
-2.75	0.9655	(0.9825)	0.9431	(0.9695)	0.8647	(0.9202)	0.7714	(0.8459)
-2.5	0.9299	(0.9753)	0.9028	(0.9587)	0.8156	(0.8957)	0.7269	(0.8158)
-2.25	0.8617	(0.9603)	0.8369	(0.9419)	0.7561	(0.8724)	0.6540	(0.7819)
-2	0.7661	(0.9390)	0.7445	(0.9180)	0.6755	(0.8423)	0.5887	(0.7522)

Table 1.3: Match for different values of ϵ when approximating the Fourier phase with I_1 (not in parenthesis) and I_2 in parenthesis. The first column lists the value of ϵ, and the other columns list the value of the match for a given e_0. For each of the values shown here, the corresponding system is a BBH system with an initial dimensionless semi-latus rectum of $p_0 = 50$.

inaccuracies, we construct two different expressions for $e(F)$ using the exact numerical solution:

$$\begin{aligned} e_1 &= e(F)\,(1-\epsilon)\,, \\ e_2 &= e(F)\left[1-\epsilon\left(\frac{e(F)}{e_0}\right)^2\right]\,, \end{aligned} \tag{1.67}$$

with ϵ a constant. In e_1, the relative error with respect to the exact solution is a constant ϵ, while in e_2 it is $\epsilon\;[e(F)/e_0]^2$, decreasing as $e(F)^2$. As before, by relative error we here mean $1-[e_{\rm app}/e(F)]$, where $e_{\rm app} = e_1$ or e_2 is the approximate solution.

We calculate the value of the match for different values of ϵ, given a BBH system with initial dimensionless semi-latus rectum of $p_0 = 50$ and at various different initial eccentricities ($e_0 = 0.1, 0.3, 0.6,$ and 0.9). We increase epsilon to reflect larger values of relative error between the approximate and exact solutions. The values of these matches are shown in Table 1.2. In the e_1 case, the low eccentricity cases begin to show a significant decrease in match when $\epsilon \sim 10^{-3.5}$. This implies that a more accurate inversion of $F(e)$ is required than that quoted by many PC models if one is interested in applications that require such high values of the match, such as parameter estimation. In the moderately eccentric case, the match starts to decrease significantly when $\epsilon \sim 10^{-4}$, while in the large eccentricity case even when $\epsilon \sim 10^{-5}$. In the e_2 case, the trend is similar, but the decrease in match is less sharp for larger ϵ. The match will be more sensitive for systems that are longer lived (lower mass), but these results set roughly tolerable inaccuracy in the inversion of $F(e)$.

We take a similar approach to analyze the loss in match due to inaccuracies in the Fourier phase, $\psi_j(e)$. We interpolate the eccentricity dependent part of the phase appearing in Eq. (1.58) and refer to this as $I(e)$. To simulate inaccuracies, we construct two approximate expressions for $I(e)$ using the exact solution

$$
\begin{aligned}
I_1 &= I(e)(1-\epsilon)\,, \\
I_2 &= I(e)\left[1-\epsilon\left(\frac{e}{e_0}\right)^2\right]\,,
\end{aligned}
\tag{1.68}
$$

with ϵ a constant. In the above, we use a numerical solution for $e(F)$ to isolate inaccuracies in the latter from those in the functional solution for $I(e)$. As in the $e(F)$ case, the relative error in I_1 is a constant ϵ, while that in I_2 decreases as e^2.

Table 1.3 shows the match when using the approximate I_1 and I_2 expressions in the Fourier phase. Observe that the Fourier phase can tolerate more inaccuracy than the inversion of $e(F)$. This is not surprising given that $I(e)$ is multiplied by an overall factor of $e^{30/19}$. In the low eccentricity case, the match begins to decay significantly when $\epsilon \sim 10^{-2.75}$, while in the large eccentricity case, the match deteriorates even when $\epsilon \sim 10^{-4}$. The greater sensitivity to error in the higher eccentricity case can be explained by the appearance of the overall factor of harmonic index j multiplying $I(e)$, and thus, also multiplying the error. As the higher harmonics become more important (i.e. for moderate to large eccentricities), the phase must be approximated more accurately.

1.5.2 Error in the low eccentricity inversion of $F(e)$

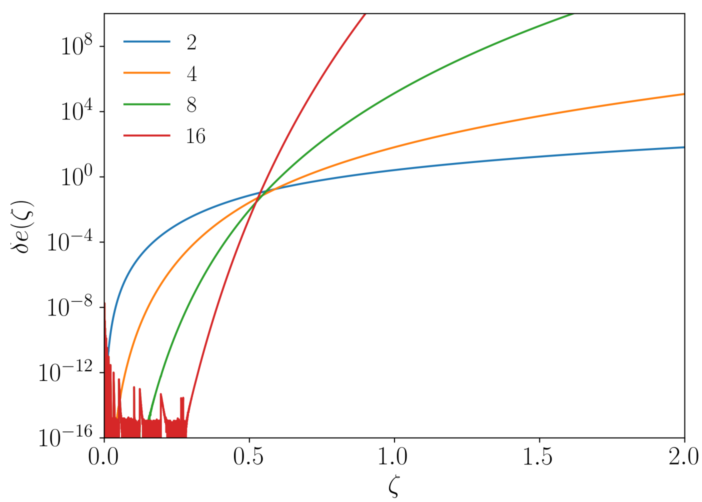

Figure 1.8: The relative error between a numerically solved $e(\zeta)$ and an $e(\zeta)$ obtained by inverting $\zeta(e)$ in the low eccentricity limit. Here $\delta e(\zeta) = 1 - e_{\rm app}(\zeta)/e(\zeta)$, where $e_{\rm app}(\zeta)$ is the approximate inversion of $F(e)$ and $e(\zeta)$ is the exact solution. The different colored lines represent different values of $n_{\rm max}$ (number of terms kept in the Taylor expansion). For $\zeta \sim 0.5$ the error in $e(\zeta)$ becomes considerable which corresponds to $e_0 \sim 0.3$ regardless of the number of terms kept. This suggests that even keeping even more terms in the approximate inversion of $\zeta(e)$ will not increase its domain of validity.

Let us conclude by reviewing the standard low eccentricity inversion of $F(e)$ as given in Eq. (1.14), and investigate its associated loss in match. Our task is then to solve Eq. (1.61) for $e(F)$ perturbatively in $e_0 \ll 1$. We then wish to invert Eq. (1.61) in the limit of small ζ, which corresponds to a low eccentricity and large frequency expansion, since $\zeta \ll 1$ requires $e_0 \ll 1$ and $(F_0/F) \ll 1$. For a system with initial eccentricity e_0, $\zeta \in [\sigma(e_0)(F_0/F_{\rm LSO})^{2/3}, \sigma(e_0)]$. We invert Eq. (1.61) by proposing a solution of the form

$$e(\zeta) \approx \zeta^{19/12} \sum_{n=0}^{n_{\rm max}} M_n \zeta^{19n/6}. \tag{1.69}$$

This proposed solution for $e(\zeta)$ is then substituted into $\sigma(e)$ appearing in Eq. (1.61) and expanded in small ζ. The coefficients, M_n, are determined by demanding that $\sigma[e(\zeta)] = \zeta$.

Figure 1.8 shows the relative error between the solution in Eq. (1.69) with different values of $n_{\rm max}$ and a numerical solution for $e(\zeta)$. Regardless of the number of terms kept in the approximate inversion, the error becomes considerable as $\zeta \sim 0.5$ which corresponds to an initial orbital eccentricity of $e_0 \sim 0.3$. This suggests that the PC models (where all quantities are expanded in low eccentricity) will become unfaithful near $e_0 \sim 0.3$ due to the approximate inversion of $F(e)$. Table 1.4 shows the match when using the low-eccentricity expansion of $e(\zeta)$ for different values of $n_{\rm max}$. Increasing $n_{\rm max}$ mitigates the loss in match until the inversion is pushed past $e_0 = 0.3$, at which point the value of the match drops to nearly 0 in one case as the inversion becomes unphysical. While keeping more terms may increase the accuracy at low ζ, the solution becomes useless for $e_0 \gtrsim 0.35$.

1.6 Faithfulness Analysis of NeF Model

In this section, we will determine the faithfulness of the NeF model by comparing it to the NeT model. All matches in this paper are computed with the response function $h(t) = F_+ h_+(t) + F_\times h_\times(t)$, where the plus and cross polarizations are given

$i_{\max}$	$e_0 = 0.05$	$e_0 = 0.10$	$e_0 = 0.15$	$e_0 = 0.20$	$e_0 = 0.25$	$e_0 = 0.30$	$e_0 = 0.35$
2	0.9911	0.9870	0.9766	0.9531	0.9242	0.8921	0.8527
4	0.9911	0.9877	0.9908	0.9878	0.9799	0.9671	0.9465
8	0.9911	0.9877	0.9908	0.9903	0.9875	0.9806	0.9724
16	0.9911	0.9877	0.9908	0.9904	0.9884	0.9831	0.0057
exact	0.9911	0.9877	0.9908	0.9904	0.9884	0.9841	0.9886

Table 1.4: The value of the match for different values of $i_{\max}$ when inverting $F(e)$ in a low eccentricity approximation. The first column lists the value of $n_{\max}$ (the "exact" in the last row indicates a numerical solution for $e(F)$), and the other columns list the value of the match for a given e_0. For each of the values shown here, the corresponding system is a BBH system with an initial semilatus rectum of $p_0 = 50$. The value of 0.0057 for the 16 term inversion at an e_0 of 0.35 is due to $e(\zeta)$ returning eccentricities less than 0. Presumably, as more terms are kept in the inversion $e(\zeta)$ is very accurate for small ζ and then becomes unusable for $\zeta \sim 0.5$ as indicated in Fig. 1.8 which corresponds to $e_0 \sim 0.3$. The loss in match becomes fairly large for initial eccentricities greater than $e_0 \sim 0.35$ regardless of the number of terms kept in the inversion.

by the different waveform models (either NeF or NeT), while $F_{+,\times}$ are the antenna patterns of the detector

$$F_+(\theta, \Phi, \psi) = \frac{1}{2}(1 + \cos^2\theta)\cos 2\Phi \cos 2\psi - \cos\theta \sin 2\Phi \sin 2\psi, \tag{1.70a}$$

$$F_\times(\theta, \Phi, \psi) = F_+(\theta, \Phi, \psi - \pi/4). \tag{1.70b}$$

Here θ and Φ are the sky angles associated with the orientation of the detector and ψ is the polarization angle that defines the rotation from the wave's polarization basis to that defined by the arms of the detector. All throughout, we choose $\theta = \Phi = \psi = \beta = \iota = 3\pi/7$ as an arbitrary location and source orientation, where recall that β and ι are the polar angles describing the polarization axes.

Before we can study the faithfulness of the NeF model of Sec. 1.4.2, we must first decide the appropriate number of harmonics that ought to be kept in Eq. (1.16).

Section 1.6.1 addresses this in detail. With this at hand, Section 1.6.2 studies the faithfulness of the NeF model with the optimal number of harmonics kept against the NeT model.

1.6.1 Maximum Number of Harmonics Needed

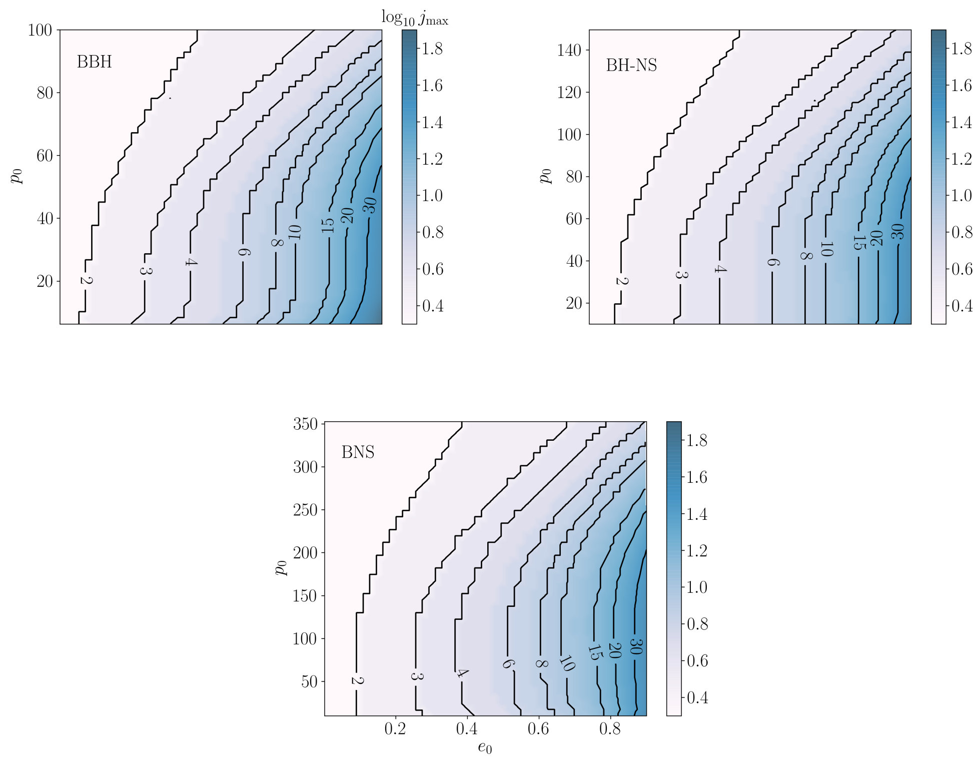

Figure 1.9: The number of harmonics required to achieve a match greater than 0.99 as a function of e_0 and p_0 (the initial orbital eccentricity and dimensionless semilatus rectum) for a BBH (top), BH-NS (middle), and BNS (bottom) system. For systems with initial eccentricities less than ~ 0.6 (and even larger eccentricities at larger initial separations) we only require 10 or less harmonics to achieve a match of 0.99.

We begin by studying the optimal number of harmonics that need to be kept in order for the match to be above 99%. We do so by computing the match between the NeT model (which contains all harmonics) and a harmonically-decomposed time domain model (obtained by solving $\dot{F}$, $\dot{e}$, $\dot{l}$ and using Eq. (1.6)). We then demand that we keep as many harmonics in the latter such that its match against NeT exceeds 0.99. This value of the match ensures the statistical error exceeds the systematic error due to mis-modeling for sources of roughly SNR 20 or less, as discussed in Sec. 1.3.

Figure 1.9 shows the number of harmonics needed in the time domain harmonic decomposition for the match against NeT to exceed 0.99. Results are shown for three different fiducial systems, a $(1.4, 1.4)M_\odot$ binary neutron star (BNS) system, a $(1.4, 10)M_\odot$ neutron star - black hole (BH-NS) system, and a $(10, 10)M_\odot$ binary black hole (BBH) system. For systems with initial eccentricities less than ~ 0.6 (and for even larger eccentricities at larger initial separations), we only require 10 or less harmonics to achieve this threshold match. We thus expect that one need only keep just as many harmonics in the NeF model. This result is very promising as the biggest computational expense of the NeF model is the inclusion of higher harmonics.

Attempts have been made to analytically estimate the number of harmonics that one must keep in order to recover 99% *signal power*. Reference [64] argued that since the power in GWs is peaked near ω_p (orbital frequency at pericenter) and the fractional power in GWs is less than 10^{-3} past $5\omega_p$ [79], one can then approximate the number of harmonics needed to capture 99% of signal power via

$$j_{\rm max} = \frac{5\omega_p}{\omega_{orb}} = 5\frac{(1+e_0)^{1/2}}{(1-e_0)^{3/2}}. \tag{1.71}$$

Reference [80] takes a different approach and uses [4] to calculate the power in a given harmonic. With this at hand, they then compute the harmonic with the most power, $j_{\rm m}$, for a collection of different eccentricities, which they finally fit to obtain

$$j_{\rm m} = 2\frac{(1+e)^{1.1954}}{(1-e^2)^{3/2}}\,. \tag{1.72}$$

Equation (1.72) correctly limits to the $j_{\rm m} = 2$ quasi-circular harmonic as $e \to 0$, while

Eq. (1.71) reduces to $j_{\max} = 5$ in this limit.

Figure 1.10 compares Eq. (1.71) to Eq. (1.72) and to a cross-section of our results for a fixed $p_0 = 20$ and $p_0 = 80$, using a BBH system. Observe that Eq. (1.71) overestimates the number of harmonics needed regardless of initial separation. This is because this equation is derived in the limit of an unbound orbit, and thus, it behaves poorly for moderate eccentricities. Also, this equation is designed to recover 99% of the signal *power*, whereas the match, and the inner product, are weighted by the spectral noise density of the detector; therefore, 99% signal power does not imply a 99% match (the threshold for our choice of $j_{\max}$).

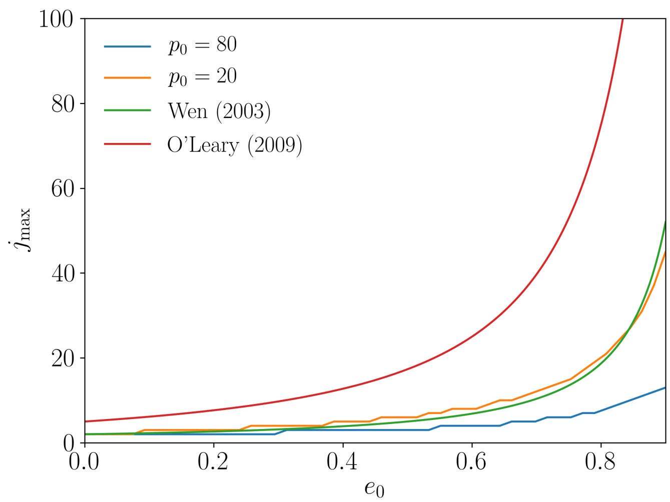

Figure 1.10: Number of harmonics needed as predicted by Eq. (1.71) in red and Eq. (1.72) in green. In orange and blue we plot the number of harmonics needed for a fixed p_0 using the BBH results of Fig. 1.9 for a close initial dimensionless semi-latus rectum (20) and a wider initial dimensionless semi-latus rectum (80). For close initial separation, Eq. (1.72) gives a good estimate for the number of harmonics needed. As the initial separation increases, one needs even less harmonics than predicted by Eq. (1.72). Equation (1.71) overestimates the number of harmonics needed in all cases.

Equation (1.72) does remarkably well at predicting the number of harmonics needed when the initial separation is small. This result is particularly surprising because Eq. (1.72) predicts the harmonic at which the power spectrum peaks, but referring back to Fig. 1.2, although the amplitude peaks at the 4^{th} harmonic, the higher harmonics are still relatively strong. One would therefore reasonably expect that significantly more harmonics should be kept than just the peak harmonic. However, the eccentricity of the binary is rapidly decaying, and as a result, the signal power in higher harmonics also rapidly decays. Coincidentally, the harmonic at which the power spectrum peaks at the initial orbital eccentricity gives a fair estimate for the number of harmonics needed for faithful matches. However, as the initial separation increases, even Eq. (1.72) overestimates the number of harmonics needed. For such large initial separations, the power of the higher harmonics has sufficiently decreased by the time they enter the sensitivity band, and thus, they affect the match even less. It is also worth reiterating that this comparison was done requiring a 0.99 match (which is driven by the desire to reduce systematic biases for signals with roughly SNR 20 or less), but to achieve higher matches (considering sources with higher SNR) one would need to keep more harmonics.

1.6.2 Faithfulness of the SPA

Finally, in this section we estimate the faithfulness and the domain of validity of the NeF model of Sec. 1.4.2. To do so, we truncate the NeF model at the maximum harmonic index found in Sec. 1.6.1. We then compute the match between the NeF and the NeT models. Since the harmonic index at which we choose to truncate our frequency domain model corresponds to the number of harmonics needed to achieve a match of at least 0.99 in the numerical time domain harmonic decomposition, the best match the NeF model can possibly achieve is also 0.99. Of course, this maximum could be improved by keeping more harmonics, but we expect the results we obtain will not qualitatively change.

The NeT and NeF models are discussed in detail in Sec. 1.4.3 and Sec. 1.4.2 respectively, but we go over a few key details here related to the match calculations. Recall that the NeT model is evolved from an initial eccentricity and semi-latus rectum (e_0, p_0) to the LSO, which corresponds to a mean orbital frequency F_0 to F_{LSO}. This time series is then zero padded, such that the length of the new time series is a power of 2, with the result then discrete Fourier transformed. The NeF model, on the other hand, is sampled at the frequencies associated with the discrete Fourier transform of the NeT model. In order to do, so we numerically invert $F(e)$ in order to map the Fourier frequency, f, to the mean orbital frequency, F, which is then further mapped to the orbital eccentricity, e, which appears explicitly in the harmonic amplitudes and phases.

Once both models are sampled we compute the match with all integrals over frequency evaluated as discrete sums from $f \in [0, f_{ny}]$, and then maximized as described in Sec. 1.3. We do not window the NeF model, but we do use a square window for the NeT model. Two independent versions of this code were implemented, one in `Mathematica`, and one in `C` and found to agree in the match to within $\sim 0.1\%$ absolute error. We take this to be an estimate of the numerical error of the match presented here.

Figure 1.11 shows the match for two of the three systems considered in the last section (BNS, BBH, BH-NS), for different initial eccentricities and dimensionless semilatera recta. Figure 1.1 shows the corresponding figure for the BH-NS case. All $\sim 2,500$ matches are Gaussian filtered in order to obtain smooth contours in the figure. In reality, some of the matches presented in Fig. 1.11 may be above or below the value of the corresponding contour, but the contours represent the general features.

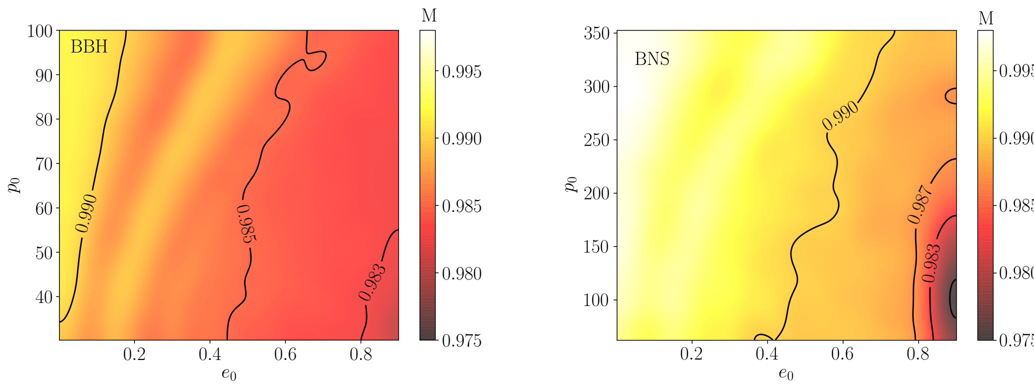

Figure 1.11: Match between the NeT model described in Sec. 1.4.3 and the NeF model as described in Sec. 1.4.2 for a BBH (top) and BNS (bottom) system (a BH-NS case is presented in Fig. 1.1). The match is given as a function of the initial condition (e_0, p_0) on the x and y axis. The maximum match is 0.99, and for a vast majority of the parameter space, NeF very faithfully represents NeT. For the shorter lived source (BBH), the match behaves more poorly than its longer lived counterparts due to finite time effects. The boundaries of the fringes correspond to a boundary where the model demands including more harmonics and thus the match displays a sharp increase as the next harmonic is included.

Observe that the NeF model matches the NeT model extremely well in nearly all cases. As the initial eccentricity increases and the initial semi-latus rectum decreases, however, the match begins to deteriorate from 0.99 (which is nearly perfect due to the truncation of the harmonic sum) to 0.985 and 0.98. This is the result of finite time effects in the DFT of NeT and windowing. Finite time effects result in a loss of match (see [81] and [82]) and this is exacerbated by the fact that eccentric binaries evolve faster than their quasi-circular counterparts (for the same initial mean orbital frequency). This reasoning is supported by the fact that the match is higher for longer lived sources (BH-NS and BNS) than shorter lived ones (BBH) for the same initial eccentricity and mean orbital frequency. If one were interested in a model with a higher value of the match (i.e. one faithful for higher SNR sources), one could include more harmonics in the SPA sum to obtain a higher match than that required in Sec. 1.6.1. One could also attempt to incorporate finite time effects into the SPA itself, as done in [82] or minimize finite time effects by applying the same window functions to both models.

In the BNS system, the match begins to drop steeply to as low as 0.975 near $e_0 \sim 0.85$ even for relatively large initial separations. The loss of match here is not due to finite time effects, but rather it is due to the inaccuracy of the approximation to the Fourier phase in Eq. (1.59). One could improve this match by increasing the number of terms kept in the Chebyshev resummation and in the Taylor expansion. Alternatively, one could choose a different number of terms in the representation of the Fourier phase for sources with different lifetimes, as longer lived sources are more sensitive to error in the representation of the phase. For shorter lived sources, the phase could likely be approximated even more cheaply than done here. We leave a more thorough investigation of such an implementation to future work.

The sudden jumps and drops in the value of the match that appear most prominently near the low eccentricity region of Fig. 1.11 are due to the harmonic nature of the model. For a fixed number of harmonics kept, the value of the match begins to decrease as the initial eccentricity increases. When the model demands the inclusion of another harmonic (informed by the results of Sec. 1.6.1), the value of the match sharply increases. As such, the sudden jumps correspond to the contours of $j_{\max}$ shown in Fig. 1.9.

1.7 Conclusions & Future Work

We have taken the first steps toward the construction of a Fourier domain model that is valid for parameter estimation to arbitrary eccentricity. In particular, we explicitly calculated an efficient analytic frequency domain model to Newtonian order, the NeF model, which we show is faithful to very high initial eccentricity ($e_0 \sim 0.9$)

through match calculations against a numerical time-domain model to Newtonian order, the NeT model (see Fig. 1.1 and 1.11). As byproducts of this analysis, we also derived new techniques to rapidly maximize the match over phase and time at coalescence for eccentric signals, and we analyzed the most important source of errors in the NeF model. Given its analytic features, we have analytic control over the NeF model, which thus allows us to straightforwardly improve it by keeping higher order terms in the analytic expansions.

As a proof-of-concept, we have here presented the NeF model to leading PN order, so it is not yet useful for data analysis. Even once higher PN terms are included, the model as presented here is likely still not accurate enough for a LISA-like detector, which will require a higher match for high signal-to-noise ratio events. Both of these problems, however, can be straightforwardly solved by (i) extending this NeF model to higher PN order and (ii) retaining more terms in the Chebyshev representation of the Fourier phase and more harmonics in the SPA amplitude. All of this future work will make for very interesting extensions of the NeF model.

The least straightforward extension is the inclusion of higher PN order terms. Much of the work required for this, however, already exists. The fluxes and time derivatives of the orbital elements have been computed in [83–86] to 3PN order. The time domain harmonic decomposition becomes troublesome at higher PN order, as Kepler's equation are modified at 2PN order. A method to treat the time domain harmonic decomposition at 3PN, however, is introduced in [87]. Therefore, the extension of the NeF model to higher PN order requires the careful assembly of pieces that are already present in the literature.

With a higher PN waveform in hand, one could in the future conduct many useful studies. For example, one could investigate the ability of aLIGO, LISA, or 3G detectors to measure the parameters and any biases of the model given eccentric signals. Since eccentric binaries are thought to be the result of specific astrophysical scenarios, it could be possible to study whether the detection of eccentric GWs can constrain different formation scenarios by recovering e_0 and F_0.

Another useful future study is to incorporate effects of modified gravity theories into the new model. If a modified gravity theory modifies the eccentricity evolution of a binary, such a theory could be constrained more stringently than with quasi-circular events only. This is because eccentricity excites additional harmonics in the signal, which contain useful information that could be leveraged to break degeneracies and constrain General Relativity. One such approach has already been taken by extending the parameterized post-Einsteinian (ppE) framework [88] to high-eccentricity bursts [89].

Perhaps the most difficult and rewarding goal is an inspiral-merger-ringdown (IMR) type hybrid that incorporates the effects of orbital eccentricity of moderate and large magnitude. Currently, the only IMR model that incorporates orbital eccentricity is that of [90]. This model is constructed in the time domain using PN theory, results of numerical relativity, and a machine learning algorithm to tune the model. It would be interesting to compare that model to this future hybrid model, once one is developed.

Acknowledgments

B.M. was supported by the Joan L. Dalton Memorial Fellowship in Astronomy from Montclair State University. T. R. appreciates the support of the NASA grant NNX16AB98G. N. Y. acknowledges support from NASA grants NNX16AB98G and 80NSSC17M0041. Computational efforts were performed on the Hyalite High Performance Computing system, which is supported by University Information Technology at Montana State University.

1.A Application of the Stationary Phase Approximation

In this Appendix we review the application of the stationary phase approximation (SPA) as applied to the time domain harmonic decomposition of the GW signal given in Eq. (1.6). For a more detailed and general presentation of the approximation see [91]. We begin by considering the time domain GW signal generated by the $j^{\rm th}$ harmonic:

$$h_j(t) = \left[A_j(t)e^{-ijl(t)} + \text{c.c.}\right]\Theta(F(t) - F_0)\Theta(F_{\rm LSO} - F(t))\,, \tag{1.73}$$

where c.c. stands for the complex conjugate and the amplitude is given by

$$A_j(t) = -\frac{m\eta}{2R}(2\pi mF)^{2/3}\left[C^{(j)}_{+,\times}(t) + iS^{(j)}_{+,\times}(t)\right]\,. \tag{1.74}$$

The unit step function, $\Theta(x)$, arises because the binary is assumed to be formed at a time t_0 with mean orbital frequency F_0 and the emission is terminated at the LSO when the binary has mean orbital frequency $F_{\rm LSO}$ (as is customary in the GW literature).

We wish to approximate the Fourier transform of the GW signal given by

$$\tilde{h}_j(f) = \int_{-\infty}^{\infty}\left\{A_j(t)e^{i[2\pi ft - jl(t)]} + A^*_j(t)e^{i[2\pi ft + jl(t)]}\right\}\Theta\left(F(t) - F_0\right)\Theta\left(F_{\rm LSO} - F(t)\right)dt\,. \tag{1.75}$$

In the above integrand, the amplitude varies much more slowly than the mean anomaly ($\dot{A}_j/A_j \ll j\dot{l}$) appearing in the phase. Thus, for most values of t this integrand is rapidly oscillating. However, there exists a time where the phase of the integrand is roughly constant and thus strongly contributes to the integral. This time is called the stationary time (denoted t_j^*) and it occurs when the stationary phase condition is satisfied, i.e. when the first derivative of the argument of the complex exponential vanishes. Thus, the stationary phase condition is

$$2\pi f \mp j\dot{l}(t_j^*) = 0\,, \tag{1.76}$$

where the minus sign corresponds to the stationary phase condition of the first term in the integrand, and the plus corresponds to the second. Since the time derivative of the mean anomaly is proportional to the mean orbital frequency, a positive quantity, the stationary phase condition is never satisfied for the second term in the integrand and so it does not contribute strongly to the integral. The stationary phase condition that is satisfied provides a mapping between the Fourier frequency f and the mean orbital frequency F for the j^{th} harmonic: $f = jF$.

To approximate the integral in Eq. (1.75), we Taylor expand the amplitude to leading order and the phase to first order (as the amplitude is more slowly varying than the phase) about the stationary time and evaluate the unit step functions at the stationary time:

$$\tilde{h}_j(f) \approx A_j(t_j^*) e^{i[2\pi f t_j^* - jl(t_j^*)]} \Theta(f - jF_0)\Theta(jF_{\text{LSO}} - f) \int_{-\infty}^{\infty} \exp\{-ij\frac{\ddot{l}(t_j^*)}{2}(t - t_j^*)^2\} dt\,. \tag{1.77}$$

We carry out the above integral and obtain

$$\tilde{h}_j(f) \approx A_j(t_j^*)\sqrt{\frac{2\pi}{|j\ddot{l}(t_j^*)|}}\, e^{i(2\pi f t_j^* - jl(t_j^*) - \pi/4)}\, \Theta\left(f - jF_0\right) \Theta\left(jF_{\text{LSO}} - f\right)\,. \tag{1.78}$$

Rewriting the above in terms of more familiar quantities we have

$$\tilde{h}_j(f) \approx -\frac{m\eta}{2R}\frac{(2\pi m F(t_j^*))^{2/3}}{\sqrt{j\dot{F}(t_j^*)}}\left[C_{+,\times}^{(j)}(t_j^*) + iS_{+,\times}^{(j)}(t_j^*)\right] e^{i\psi_j}\Theta\left(f - jF_0\right)\Theta\left(jF_{\text{LSO}} - f\right) , \tag{1.79}$$

with

$$\psi_j = 2\pi f t_j^* - jl(t_j^*) - \pi/4. \tag{1.80}$$

To recover the full frequency response due to many harmonics, we simply sum the above over the harmonic index j.

1.B Chebyshev Resummation

In this appendix we review the approximation of the Fourier phase and provide the coefficients of the resulting series in eccentricity to 16 digits of precision. Since the exact coefficients are unwieldy rationals, they are provided in a supplementary notebook. We begin by approximating $I(e)$ in Eq. (1.58) through a Maclaurin series

$$I(e) \approx \sum_{n=0}^{n_{\max}} A_{2n} e^{2n}. \tag{1.81}$$

We use an even basis function for the expansion about small eccentricity because $I(e)$ is even. The coefficients A_n are simply the coefficients of the Taylor expansion, namely

$$A_n = \frac{1}{n!}\left.\frac{d^n I}{de^n}\right|_{e=0} . \tag{1.82}$$

The first seventeen non-zero A_n are given by

$$A_0 = -0.237\,500\,000\,000\,000\,0 \ ,$$

$$
\begin{aligned}
A_2 &= -0.300\,615\,876\,322\,989\,4\ , \\
A_4 &= -0.008\,991\,117\,053\,859\,665\ , \\
A_6 &= -0.037\,851\,834\,031\,183\,92\ , \\
A_8 &= -0.007\,615\,853\,560\,080\,763\ , \\
A_{10} &= -0.009\,769\,540\,332\,607\,544\ , \\
A_{12} &= -0.004\,556\,366\,050\,156\,979\ , \\
A_{14} &= -0.003\,968\,026\,824\,286\,266\ , \\
A_{16} &= -0.002\,630\,835\,486\,794\,598\ , \\
A_{18} &= -0.002\,115\,104\,845\,741\,527\ , \\
A_{20} &= -0.001\,610\,593\,129\,877\,186\ , \\
A_{22} &= -0.001\,304\,358\,739\,038\,224\ , \\
A_{24} &= -0.001\,055\,578\,416\,146\,812\ , \\
A_{26} &= -0.000\,875\,581\,422\,324\,481\,2\ , \\
A_{28} &= -0.000\,732\,963\,908\,943\,822\,6\ , \\
A_{30} &= -0.000\,621\,975\,182\,560\,585\,6\ , \\
A_{32} &= -0.000\,532\,723\,793\,460\,911\,2\ .
\end{aligned}
\tag{1.83}
$$

We then wish to resum this Taylor expansion using Chebyshev polynomials (see [92] for a discussion of the convergence properties of Chebyshev series). The Chebyshev polynomials, $T_n(x)$, are defined for $x \in [-1, 1]$, and thus, to make them a function of the eccentricity and preserve their orthogonality we rescale them as $T_n(s)$ where $s = 2e^2 - 1$, which guarantees $s \in [-1, 1]$ for $e \in [0, 1]$. The first few Chebyshev polynomials are

$$T_0(s) = 1 \ , \tag{1.84a}$$

$$T_1(s) = 2e^2 - 1 \ , \tag{1.84b}$$

$$T_2(s) = 8e^4 - 8e^2 + 1 \ , \tag{1.84c}$$

$$T_3(s) = 32e^6 - 48e^4 + 18e^2 - 1 \ , \tag{1.84d}$$

which can be inverted to find different powers of the eccentricity as functions of Chebyshev polynomials

$$e^0 = T_0(s) \ , \tag{1.85a}$$

$$e^2 = \frac{1}{2}(T_1(s) + T_0(s)) \ , \tag{1.85b}$$

$$e^4 = \frac{1}{8}(T_2(s) + 4T_1(s) + 3T_0(s)) \ , \tag{1.85c}$$

$$e^6 = \frac{1}{32}(T_3(s) + 6T_2(s) + 15T_1(s) + 10T_0(s)) \ . \tag{1.85d}$$

We now seek a resummation of Eq. (1.81) into the form

$$I(e) \approx \sum_{k=0}^{k_{\max}} B_k T_k(s) \, , \tag{1.86}$$

for some set of coefficients B_k. We do so by inserting the monomials of e in terms of the Chebyshev polynomials, Eq. (1.85), into Eq. (1.81) and collecting terms order by order in the Chebyshev polynomials. The first terms for B_k are

$$B_0 = -0.411\,345\,910\,752\,926\,6 \ ,$$

$$B_1 = -0.186\,724\,296\,957\,817\,7 \ ,$$

$$B_2 = -0.016\,970\,870\,078\,114\,17 \ ,$$

$$
\begin{aligned}
B_3 &= -0.005\,185\,894\,691\,512\,303 \ , \\
B_4 &= -0.001\,448\,030\,529\,666\,706 \ , \\
B_5 &= -0.000\,467\,082\,998\,906\,841\,1 \ , \\
B_6 &= -0.000\,146\,724\,477\,933\,540\,0 \ , \\
B_7 &= -0.000\,043\,850\,639\,900\,567\,47 \ , \\
B_8 &= -0.000\,011\,991\,016\,195\,612\,29 \ , \\
B_9 &= -2.925\,622\,159\,845\,224 \times 10^{-6} \ , \\
B_{10} &= -6.210\,389\,911\,462\,248 \times 10^{-7} \ , \\
B_{11} &= -1.117\,172\,525\,811\,035 \times 10^{-7} \ , \\
B_{12} &= -1.649\,269\,175\,725\,618 \times 10^{-8} \ , \\
B_{13} &= -1.913\,379\,819\,810\,920 \times 10^{-9} \ , \\
B_{14} &= -1.632\,587\,267\,118\,429 \times 10^{-10} \ , \\
B_{15} &= -9.096\,722\,174\,897\,557 \times 10^{-12} \ , \\
B_{16} &= -2.480\,688\,474\,424\,701 \times 10^{-13} \ . \qquad (1.87)
\end{aligned}
$$

Clearly if the Maclaurin series is truncated at $n_{\max}$, and the Chebyshev series is truncated at the same order, then the two approximations are identical. However, we find that we can keep less terms in the Chebyshev series than the Maclaurin series to accurately approximate the phase. Specifically, we find that we obtain a sufficiently accurate representation of $I(e)$ if we use a Maclaurin series truncated at $n_{\max} = 16$ and a Chebyshev resummation truncated at $k_{\max} = 12$.

After truncating the Chebyshev series in Eq. (1.86) at $k_{\max} = 12$, it is more computationally efficient to collect like terms in eccentricity when implementing this function, lest one evaluates the same power of eccentricity many times. After collecting the like terms in eccentricity we are left with

$$I(e) \approx \sum_{n=0}^{n=12} C_n e^{2n}. \tag{1.88}$$

We now provide the coefficients $C_{n>5}$ in decimal form to 16 digits:

$$\begin{aligned}
C_5 &= 0.041\,993\,340\,084\,657\,63\ , \\
C_6 &= -0.223\,130\,740\,649\,105\,5\ , \\
C_7 &= 0.608\,665\,210\,424\,159\,5\ , \\
C_8 &= -1.161\,566\,561\,696\,015\ , \\
C_9 &= 1.469\,991\,268\,471\,017\ , \\
C_{10} &= -1.216\,042\,897\,081\,895\ , \\
C_{11} &= 0.595\,816\,296\,413\,753\,2\ , \\
C_{12} &= -0.138\,350\,726\,016\,453\,3\ .
\end{aligned} \tag{1.89}$$

The coefficients $C_{n\in(1,4)}$ were already provided in Eq. (1.60). All of the A_n, B_k, and C_n are provided in their exact rational form in a supplemental notebook.

1.C Inversion of F(e)

Let us review our attempts at inverting

$$\sigma(e) = \zeta, \tag{1.90}$$

where

$$\sigma(e) = \frac{e^{12/19}}{1-e^2}\left(1 + \frac{121}{304}e^2\right)^{870/2299}. \tag{1.91}$$

Recall that $\zeta = \sigma(e_0)(F_0/F)$ and sources with initial conditions (e_0, F_0) will sample values of $\zeta \in [\sigma(e_0)(F_0/F_{\rm LSO}), \sigma(e_0)]$. In Sec. 1.5.2 we invert Eq. (1.90) in the low eccentricity and late frequency regime (i.e. $\zeta \ll 1$) and we find that this inversion leads to a significant loss in match for sources which sample $\zeta \sim 0.5$ which corresponds to sources with $e_0 \sim 0.3$. Since the focus of this work is to provide a model which is useful for parameter estimation (i.e. with matches ~ 0.99) and valid for arbitrary eccentricity, we must investigate other representations of $e(\zeta)$.

Two models for $e(\zeta)$ meet the accuracy goals laid out in Sec. 1.5: (i) a model which is composed of a controlling factor obtained by introducing an approximate $\sigma(e)$ into Eq. (1.90) and algebraically solving and then fitting the remaining error and (ii) a piecewise representation of $e(\zeta)$, which is composed of two Taylor expansions about $\zeta \ll 1$ and $\zeta \gg 1$, and an efficient numerical fit of the function in the range in ζ for which the error in the Taylor expansions is too large for faithful modeling. The piecewise representation is the best of the two methods in speed, accuracy, and domain of validity. All of the coefficients listed in this Appendix are provided in a supplementary notebook.

As a first attempt to solve Eq. (1.90), we introduce

$$\bar{\sigma}(e) = \zeta, \tag{1.92}$$

where $\bar{\sigma}(e)$ is a simpler rational polynomial similar to $\sigma(e)$ which admits an exact solution. Let us define the inverse function $\bar{\kappa}(\zeta)$ such that $\bar{\kappa}[\bar{\sigma}(e)] = e$. We then seek to leverage this inverse function, which we can solve for exactly, to find an approximate solution for $e(\zeta)$ by multiplying by a Taylor series:

$$e(\zeta) \approx \bar{\kappa}(\zeta) \left(\sum_{k=0}^{k_{\max}} D_k (\zeta - \zeta_0)^k \right) . \tag{1.93}$$

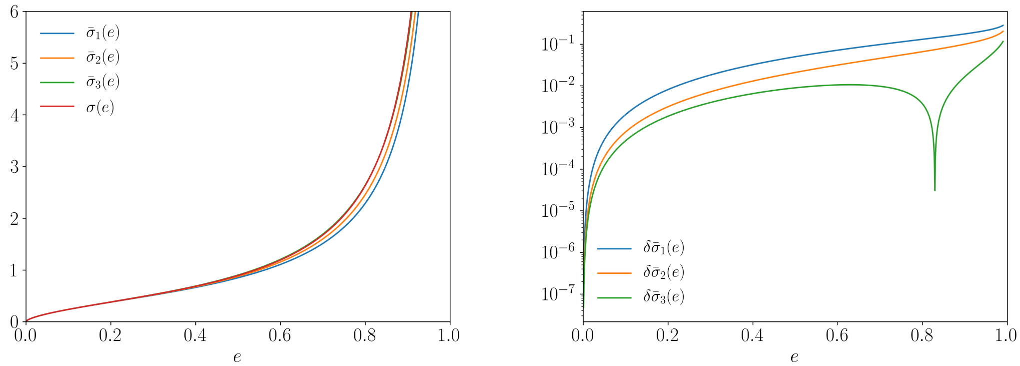

Figure 1.12: The value of $\sigma(e)$, $\bar{\sigma}_1(e)$, $\bar{\sigma}_2(e)$, $\bar{\sigma}_3(e)$ (left), and their relative errors (right). Observe that $\bar{\sigma}_3(e)$ most closely represents $\sigma(e)$.

The factor which is raised to the 870/2299 power in Eq. (1.91) varies from 1 to 1.135, so we first neglect this term. With this term set to 1, we observe that the resulting equation can be solved if the factor of $(1-e^2)$ appearing in the denominator is raised to the power 18/19. We then raise the entire resulting equation to the power 19/6 and we are left with a polynomial equation which can be readily algebraically solved. This corresponds to a $\bar{\sigma}(e)$

$$\bar{\sigma}_1(e) = \frac{e^{12/19}}{(1-e^2)^{18/19}} \,. \tag{1.94}$$

We further note that we can incorporate the factor of $(1+\frac{121}{304}e^2)^{870/2299}$ if we approximate it as $(1+\frac{121}{304}e^2)^{3n/19}$. We generate two more $\bar{\sigma}(e)$ with different choices of n

$$\bar{\sigma}_2(e) = \frac{e^{12/19}}{(1-e^2)^{18/19}} \left(1+\frac{121}{304}e^2\right)^{6/19} \,, \tag{1.95}$$

$$\bar{\sigma}_3(e) = \frac{e^{12/19}}{(1-e^2)^{18/19}} \left(1+\frac{121}{304}e^2\right)^{12/19} \,. \tag{1.96}$$

$$\tag{1.97}$$

In Fig. 1.12 we plot the values of $\sigma(e)$, the approximate $\bar{\sigma}(e)$, and the relative error associated with the $\bar{\sigma}(e)$. Since $\bar{\sigma}_3(e)$ most closely represents $\sigma(e)$, we provide its inverse function in Eq. (1.63) of Sec. 1.4.2. In Fig. 1.13 we plot a numerical solution $\kappa(\zeta)$, $\bar{\kappa}_3(\zeta)$, and the associated relative error for $\zeta \in [0, 5.47]$ which corresponds to systems with e_0 as high as 0.9. As shown in Sec. 1.5, we require relative error of $\mathcal{O}(10^{-6})$ in order to faithfully model sources with arbitrary eccentricity. The relative error between $\bar{\kappa}_3(\zeta)$ and the numerical solution is $\mathcal{O}(10^{-3})$, so we conclude that we must further improve the inversion if we wish to have something accurate enough for our purposes.

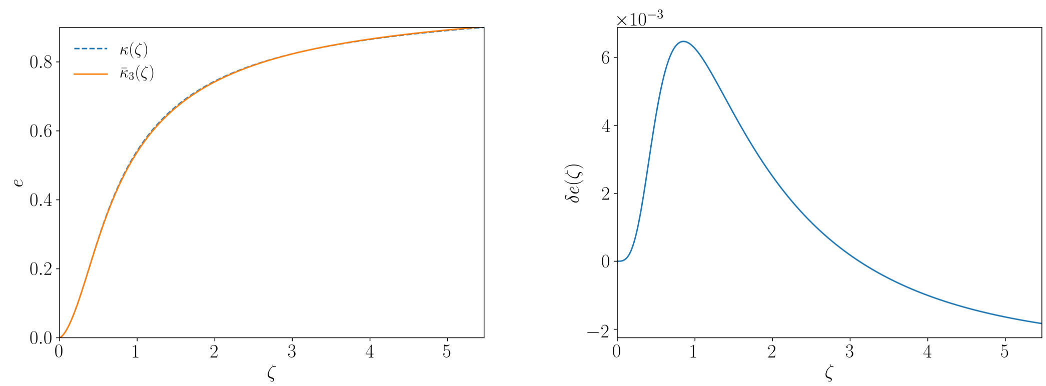

Figure 1.13: The value of a numerical solution for $\kappa(\zeta)$, $\bar{\kappa}_3(\zeta)$ as given in Eq. (1.63) (left), and the relative error between the exact solution and $\bar{\kappa}_3(\zeta)$ (right). We see that the two inversions are nearly indistinguishable by eye, but the relative error is $\mathcal{O}(10^{-3})$.

In order to decrease the relative error further, we multiply $\bar{\kappa}_3(\zeta)$ by a Taylor series as written in Eq. (1.93). The coefficients D_k are determined by substituting this $e(\zeta)$ into $\sigma[e(\zeta)]$ and demanding $\sigma[e(\zeta)] = \zeta$ upon Taylor expansion. After trying many Taylor expansions about different ζ_0, we find that the resulting solution behaves better than $\bar{\kappa}_3(\zeta)$ in a small region near ζ_0, but leads to considerably more error than $\bar{\kappa}_3(\zeta)$ for most of the domain. We conclude that this approach does not lead to an accurate enough inversion of $F(e)$ to be useful for applications that require a high value of the match.

CHAPTER TWO

A 3PN FOURIER DOMAIN WAVEFORM FOR NON-SPINNING BINARIES WITH MODERATE ECCENTRICITY

Contributions of Authors and Co-Authors

Manuscript in Chapter 2

Author: Blake Moore

Contributions: Analytically developed the waveform model. Developed the waveform and analysis code. Wrote the initial draft of the manuscript.

Author: Dr. Nicolas Yunes

Contributions: Conceived of design study and advised the project. Edited the manuscript.

Manuscript Information Page

Blake Moore, Nicholas Loutrel

Classical and Quantum Gravity

Status of Manuscript:
____ Prepared for submission to a peer-reviewed journal
____ Officially submitted to a peer-reviewed journal
____ Accepted by a peer-reviewed journal
__X__ Published in a peer-reviewed journal

IOP Publishing
Classical and Quantum Gravity, Volume 36, Number 18
10.1088/1361-6382/ab3778

Abstract

While current gravitational wave observations with ground based detectors have been consistent with compact binaries in quasi-circular orbits, eccentric binaries may be detectable by ground-based and space-based instruments in the near future. Eccentricity significantly complicates the gravitational wave signal, and we currently lack fast and accurate models that are valid in the moderate to large eccentricity range. In a previous paper, we built a Fourier domain, eccentric waveform model at leading order in the post-Newtonian approximation, i.e. as an expansion in small velocities and weak fields. Here we extend this model to 3rd post-Newtonian order, incorporating the effects of periastron precession and higher post-Newtonian order effects that qualitatively change the waveform behavior. Our 3PN model combines the stationary phase approximation, a truncated sum of harmonics of combinations of two orbital frequencies (an azimuthal one and a radial one), and a bivariate expansion in the orbital separation and the eccentricity. We validate the model through comparisons with a fully-numerical, time domain post-Newtonian model, and find good agreement (matches between $97\% - 99\%$) in much of the parameter space. We estimate in what regions of parameter space eccentric effects are important by exploring the signal to noise ratio of eccentric corrections. We also examine the effects of higher post-Newtonian order terms in the waveform amplitude, and the agreement between different PN-consistent, numerical, time-domain models. In an effort to guide future improvements to the model, we gauge the error in our 3PN model incurred by the different analytic approximations used to construct it. This model is useful for preliminary data analysis investigations and it could allow for a phenomenological hybrid that incorporates eccentricity into an inspiral-merger-ringdown model.

2.1 Introduction

With the multiple detections of gravitational waves (GWs) from binary black hole and neutron star systems by ground based detectors [93–98] and the imminent launch of space based detectors [3], we are now in a position to perform gravitational wave astronomy. With this comes the ability to answer important questions about the physical characteristics of the sources producing those waves, the environments in which they are formed, the validity of General Relativity, and the nature of the universe at large. To answer these questions, we rely heavily on our ability to model these sources, yet still prepare to detect the unknown via un-modeled burst searches [99]. Source modeling was initially focused on binaries in quasi-circular orbits, but in more recent years, there has been much work to model the GWs incorporating the effects of orbital eccentricity.

This work has been motivated by astrophysical studies which suggest that, while quasi-circular binaries dominate potential ground based detector sources, there are a number of scenarios that can produce binaries in eccentric orbits while emitting GWs in the sensitivity band of these detectors. Recently, Rodriguez et al. incorporated PN effects into globular cluster simulations and as a result predicted a merger rate for LIGO/Virgo of 0.5 $\mathrm{Gpc}^{-3}\ \mathrm{yr}^{-1}$ for binaries with detectable eccentricity above 0.1 (with an overall merger rate between 10 and 213 $\mathrm{Gpc}^{-3}\ \mathrm{yr}^{-1}$) [100]. Other promising eccentric formation scenarios include field triples [101], GW capture and triples near supermassive BHs [62, 64]. As a result, the detection of GWs from multiple eccentric sources could help us identify the environment in which they form [46].

Neglecting the effects of eccentricity in source modeling can lead to a loss in detection rate and parameter bias. Several studies have investigated the ability of quasi-circular template banks to recover eccentric signals and found significant loss in detection rate for binaries with eccentricities greater than about 0.1 [19–21]. However, even for eccentricities smaller than 0.1, parameter biases can arise when the eccentricity is neglected in the model and the signal comes from a binary with eccentricity as small as about 10^{-3} [13].

Clearly then, if we wish to recover and perform data analysis on eccentric signals we require models which incorporate the effects of orbital eccentricity, particularly efficient Fourier domain waveforms. The Post-Circular (PC) formalism provides a fully analytic (at Newtonian order) prescription to compute a frequency-domain waveform, while incorporating eccentric effects [24]. This was extended to 2PN order in [25] and recently to 3PN order [102]. In [27], the authors used a circular GW amplitude and incorporated the leading-order eccentric effects in the binary dynamics while working at 3PN order. Recently in [29], spin effects, which couple to the eccentricity, are incorporated into a PC style waveform at 3PN order. These models expand all relevant quantities in small eccentricity and relate the Fourier frequency to the orbital frequency in order to map the model to the Fourier domain. As a result, these models are computationally efficient, but likely only valid in the small eccentricity regime ($e_0 \leq 0.3$) as is demonstrated by investigations of validity in those studies in which the models are derived. We seek to provide a model that is valid for large eccentricities, $e \sim 0.8$.

In Reference [103] (hereafter referred to as paper 1), we built a Fourier domain, eccentric waveform model at leading order in the post-Newtonian (PN) approximation [1]. This Newtonian order model schematically took the form

$$\tilde{h}_{+,\times} \sim \sum_{j=1}^{N} A_{+,\times}^{(j)}(f)\, e^{i\psi_j(f)}\,, \tag{2.1}$$

where $A_{+,\times}^{(j)}$ are the slowly-varying amplitudes and the ψ_j are the rapidly-varying Fourier phases of the j^{th} harmonic of orbital frequency. The multiple harmonics in the Fourier domain arise from the fact that an eccentric signal can be decomposed as a sum over harmonics of the mean orbital frequency in the time domain. We validated this waveform for large eccentricities ($e_0 \leq 0.9$) using the match (a measure of agreement between two models) for advanced LIGO at design sensitivity against a fully-numerical, time-domain model. The key to our Newtonian Fourier-domain model's accuracy and distinction from PC models is an analytic prescription in terms of the orbital eccentricity e for the Fourier phases and the amplitudes, with e then related to the fourier frequency though the stationary phase condition. A similar model to 1PN order is presented in [71].

We here extend the Newtonian model of paper 1 to 3PN order (developing a model similar to TaylorF2 [78] but for eccentric binaries), and we validate it in a large region of initial-separation/initial-eccentricity parameter space. We follow the same procedure as in paper 1, with the most major complication arising from the inclusion of periastron precession due to PN effects. This gives rise to harmonics that are combinations of the two orbital frequencies in the eccentric problem – one related to the radial period and the other related to the azimuthal period. In addition, the Fourier phases do not admit exact solutions in terms of e as was the case in paper 1, where those phases could be expressed exactly in terms of hypergeometric

[1] The PN approximation is one in which the field equations are solved assuming small velocities and weak gravitational fields in an expansion in powers of $(\frac{v}{c})$, where v is the orbital velocity and c is the speed of light [63]. By nPN order we mean an expansion to order $(v/c)^{2n}$.

functions. However, in paper 1 we found that the small eccentricity expansion of those hypergeometric functions were still highly accurate, and so we here employ that same expansion.

Figure 2.1 shows the match between our 3PN Fourier domain model and a fully numerical time-domain PN waveform for a $(1.4, 1.4)M_{\odot}$ binary inspiral for a number of initial separations and initial eccentricities. We see that our model is very faithful to the numerical one in a large region of the parameter space explored. The Fourier and time-domain models begin to disagree for very eccentric binaries that start at very small initial separation, since then their pericenter velocity becomes quite large. The results presented in this figure are representative of systems with other comparable masses. The match, however, deteriorates more rapidly for systems with disparate masses, suggesting that higher PN order models may be needed for these cases.

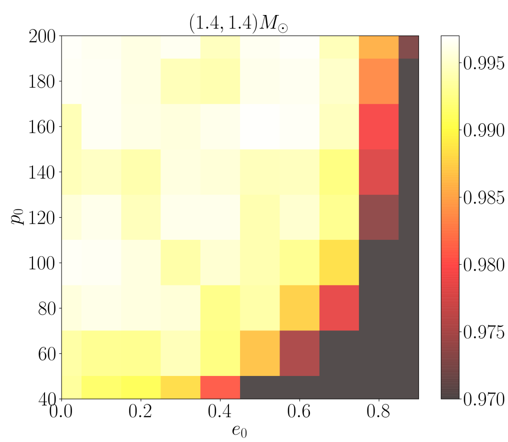

Figure 2.1: Match between our 3PN accurate Fourier domain waveform and a fully numerical PN time domain waveform as a function of the initial eccentricity and initial dimensionless semi-latus rectum for a $(1.4, 1.4)M_{\odot}$ system. The match is greater than 97% for much of parameter space explored.

In order to develop our model and to better understand the features of the model, we produce several byproducts. First, we obtain a 3PN accurate decomposition of the time-domain waveform into an infinite sum of harmonics and we truncate it at a finite order. With this at hand, we then use numerical solutions to the orbital dynamics to validate the truncated model against another model that keeps all harmonics (while being computed at the same PN order as the model which is decomposed into harmonics), so as to determine the loss of faithfulness due to harmonic truncation. Second, we investigate how different PN-consistent ways of solving the orbital dynamics lead to a loss of faithfulness in numerically-solved, time domain models due only to the truncation of the PN series. Third, we produce two Fourier domain waveforms, one with more terms kept in the eccentricity expansions and one with less terms kept, and perform a faithfulness analysis on each in order to understand the error incurred by our expansions in small eccentricity. Lastly, we swap the analytic components of our Fourier domain waveform with numerical solutions in order to get a sense of which of these analytic approximations leads to a dominant loss in faithfulness. Since each of these results isolate a particular approximation made in generating our Fourier domain model, we are able to pinpoint which approximation causes the most error, which can guide future advances aimed at increasing the accuracy of our model.

The organization of the paper is as follows. In Section 2.2 we review the PN dynamics of an eccentric orbit, and in Section 2.3 the time domain GW signal and its decomposition into harmonics of the two orbital frequencies. Section 2.4 presents the GW signal in the Fourier domain, and provides the formalism that we employ to obtain our model. Section 2.5 provides details on the implementation of the Fourier domain model, and carries out a faithfulness study. In Section 4.5 we conclude and point to future work. Throughout this work we use geometric units (c = G = 1).

2.2 Review of Eccentric Orbital Dynamics

In this section we review the orbital dynamics of an eccentric binary. We first begin by reviewing the dynamics at Newtonian order. Then we present the dynamics including effects up to 3PN order in the quasi-Keplerian (QK) formalism presented in [104]. The most notable changes that occur when including higher PN effects is periastron precession (entering at 1PN order), which introduces a second frequency (and thus a second phase angle) into the dynamics, and higher order corrections to Kepler's equation.

2.2.1 Newtonian Order

At Newtonian order the dynamics of an elliptical orbit restricted to a plane are described by

$$r = a(1 - e\cos u)\,, \tag{2.2a}$$

$$\phi = \lambda + W = \lambda + v - u + e\sin u\,, \tag{2.2b}$$

$$\lambda = n(t - t_0) + c_\lambda\,, \tag{2.2c}$$

$$l = n(t - t_0) + c_l = u - e\sin u\,, \tag{2.2d}$$

$$v = 2\arctan\left[\left(\frac{1+e}{1-e}\right)^{1/2}\tan\left(\frac{u}{2}\right)\right]\,. \tag{2.2e}$$

Here r is the magnitude of the relative separation vector, which we choose to be on the $x-y$ plane $\vec{r} = (r\cos\phi, r\sin\phi, 0)$. The angle ϕ is the orbital phase, e the orbital eccentricity, and the angle l is the mean anomaly. The mean motion n is related to the orbital period P by $n = 2\pi/P$, and the semi-major axis via Kepler's third law $n^2a^3 = m$ with m the total mass of the system. We have written ϕ in terms of a linearly increasing phase angle λ, and an oscillatory phase angle W, which accounts for the fact that the rate of change of the orbital phase $\dot{\phi}$ is not constant throughout one orbit. In the absence of radiation reaction, the conservation of energy and angular momentum demands that the orbital eccentricity and semi-major axis remain fixed. To obtain $r(t)$ and $\phi(t)$, a separation and an orbital eccentricity must be specified and then these are used to solve Kepler's equation [Eq. (2.2d)] for $u(t)$ – which can only be exactly solved numerically. This points to a clear complication of eccentric binary modeling – even in the Newtonian treatment and in the absence of radiation reaction, the explicit time domain dynamics require a numerical solution.

In GR, GWs carry away energy and angular momentum from the binary, and in response the orbital eccentricity and mean motion (or alternatively the separations associated with the ellipse) vary in time. Equations (2.2) remain the same with the exception of l and λ, which obey

$$l = \lambda = \int^{t} n(t')dt' \,. \tag{2.3}$$

The time evolution of the eccentricity and mean motion were first derived by Peters and Matthew [4] and is given by

$$\frac{dn}{dt} = \frac{\eta}{m^2}(mn)^{11/3}\left(\frac{96 + 292e^2 + 37e^4}{5(1-e^2)^{7/2}}\right) \,, \tag{2.4a}$$

$$\frac{de}{dt} = -\frac{\eta}{m}(mn)^{8/3}e\left(\frac{304 + 121e^2}{15(1-e^2)^{5/2}}\right) \,. \tag{2.4b}$$

The appearance of the negative sign in $\dot{e}$ implies the well known result that radiation reaction causes a binary to circularize. In paper 1, we solved this coupled set of differential equations exactly for $n(e)$, which in turn allowed us to obtain $t(e)$ and $l(e)$ exactly in terms of hypergeometric functions and the AppelF1 function. We now turn to treat the effects of higher order PN effects in the orbital dynamics.

2.2.2 Inclusion of PN Effects

The quasi-Keplerian formalism (QK) of [104] allows one to describe elliptic motion while including higher order PN effects. Equations (2.2) keep a similar form, with the notable difference being that the orbital angle λ is related to an azimuthal frequency and l is related to a radial one, a distinction caused by periastron precession. Including PN effects causes Eqs. (2.2) to take the form

$$r = a_r(1 - e_r \cos u)\,, \tag{2.5a}$$

$$\phi = \lambda + W\,, \tag{2.5b}$$

$$W = (1+k)(v - l) + (f_{4\phi} + f_{6\phi}) \sin 2\nu + (g_{4\phi} + g_{6\phi}) \sin 3\nu + i_{6\phi} \sin 4\nu + h_{6\phi} \sin 5\nu\,, \tag{2.5c}$$

$$\lambda = (1+k)n(t - t_0) + c_\lambda\,, \tag{2.5d}$$

$$\begin{aligned} l &= n(t - t_0) + c_l \\ &= u - e \sin u + (g_{4t} + g_{6t})\,(\nu - u) + (f_{4t} + f_{6t}) \sin \nu + i_{6t} \sin 2\nu + h_{6t} \sin 3\nu\,, \end{aligned} \tag{2.5e}$$

$$v = 2 \arctan \left[\left(\frac{1 + e_\phi}{1 - e_\phi} \right)^{1/2} \tan \left(\frac{u}{2} \right) \right]. \tag{2.5f}$$

Note that now there are three different eccentricities: the time eccentricity e_t, the radial eccentricity e_r, and the phi-eccentricity e_ϕ. The three eccentricities can be related to one another through PN accurate relations, which can be found in [104,105]. Throughout this work we parameterize the problem in terms of the time eccentricity, e_t, and therefore we will drop the t subscript from hereon out. The functions $g_{n\phi}, g_{nt}, f_{n\phi}, f_{nt}, i_{n\phi}, i_{nt}, h_{n\phi}, h_{nt}$ are $n/2$ PN coefficients that depend on the orbital energy, angular momentum and the masses of the binaries [105].

We adopt a PN parameter y defined by

$$y = \frac{(m(1+k)n)^{1/3}}{\sqrt{1-e^2}} = \mathcal{O}(v). \tag{2.6}$$

Note that in the zero eccentricity limit, y corresponds exactly to the orbital speed v. At Newtonian order, the parameter y is related to the dimensionless semilatus rectum, p, by $y = 1/\sqrt{p}$. This PN parameter is well-behaved even for highly eccentric orbits, since one can think of it as effectively requiring the semi-latus rectum to be large instead of requiring the semi-major axis to be large, which could result in large pericenter velocities.

One of the more pronounced PN effects in eccentric dynamics is the inclusion of periastron precession which enters at 1PN order. This causes two average orbital frequencies to enter the eccentric problem: ω which is related to the 2π angular period and n which is related to the periastron to periastron period. The effect of periastron precession is encoded in the parameter $k = \delta\Phi/(2\pi)$, where $\delta\Phi$ is the advance of periastron over a period. In terms of y at 3PN order

$$\begin{aligned} k = 3y^2 &+ \left[54 - 28\eta + (51 - 26\eta)e^2\right]\frac{y^4}{4} + \Big\{6720 - (20000 - 492\pi^2)\eta + 896\eta^2 \\ &+ [18336 - (22848 - 123\pi^2)\eta + 5120\eta^2]e^2 + (2496 - 1760\eta + 1040\eta^2)e^4 \\ &+ \left[1920 - 768\eta + (3840 - 1536\eta)e^2\right]\sqrt{1-e^2}\Big\}\frac{y^6}{128}. \end{aligned} \tag{2.7}$$

We can use this expression for k to relate the radial orbital angular frequency, n, to the azimuthal orbital angular frequency, $\omega = (1+k)n$.

Another complication arising as a result of considering higher PN effects is the gauge dependence of the eccentricity parameter. Two commonly employed gauges are the Arnowitt-Deser-Misner (ADM) and modified harmonic (MH) ones, which differ at 2PN order; throughout this work, we use the MH gauge. See [84] where the MH gauge is derived for more details about the differences between the gauges. In order to express results in either gauge one needs to relate the time eccentricity in one gauge to another. These relations can be found in [27], but we also list them here:

$$e_t^{\mathrm{ADM}} = e_t^{\mathrm{MH}} \left\{ 1 + \left(\frac{1}{4} + \frac{17}{4}\eta \right) y^4 + \left[\frac{1}{2} + \left(\frac{16739}{1680} - \frac{21}{16}\pi^2 \right)\eta - \frac{83}{24}\eta^2 + \left(\frac{1}{2} + \frac{249}{16}\eta - \frac{241}{24}\eta^2 \right) e_t^2 \right] y^6 \right\} . \quad (2.8)$$

Finally, in order to fully specify the orbital dynamics we must take into account the effects of the emission of GWs which cause the orbital frequency (or alternatively y) and the eccentricity to vary with time. This amounts to solving the following set of coupled ordinary differential equations:

$$\frac{dl}{dt} = n(e,y) = \frac{y^3}{m}(1-e^2)^{3/2} \left\{ 1 - 3y^2 - \frac{1}{4}y^4 \left[18 - 28\eta + e^2\left(51 - 26\eta\right) \right] - \frac{1}{128}y^6 \left[-192 - (14624 - 492\pi^2)\eta + 896\eta^2 + e^2\left(5120\eta^2 - \left(17856 - 123\pi^2\right)\eta + 8544\right) + e^4\left(1040\eta^2 - 1760\eta + 2496\right) + \sqrt{1-e^2}\left(e^2(3840 - 1536\eta) - 768\eta + 1920\right) \right] \right\} \quad (2.9a)$$

$$\frac{d\lambda}{dt} = \omega(e,y) = \frac{y^3}{m}(1-e^2)^{3/2} , \quad (2.9b)$$

$$m\frac{dy}{dt} = (1-e^2)^{3/2}\eta y^9 \left(a_0 + \sum_{n=2}^{6} a_n y^n \right) , \quad (2.9c)$$

$$m\frac{de}{dt} = -\frac{(1-e^2)^{3/2}}{2e}\eta y^8 \left(b_0 + \sum_{n=2}^{6} b_n y^n \right) . \quad (2.9d)$$

where the a_n and b_n can be found in modified harmonic gauge in Appendix C of [29] and $\eta = m_1 m_2/m^2$ is the symmetric mass ratio (see [85] for 3PN equations for all of the orbital elements). The equations for $\dot{y}$ and $\dot{e}$ depend on certain enhancement functions ϕ_y, ϕ_e, ψ_y, ψ_e, ζ_y, ζ_e, κ_y, and κ_e [29], which we have expanded to $\mathcal{O}(e^{50})$. Once the solution to this set of ordinary differential equations is found, one can insert them into Eqs. (2.5) to obtain the evolution of the different orbital quantities (while Kepler's equation must still be solved numerically).

2.3 Eccentric GWs in the Time Domain

In this section we present the GW signal in the time domain. We begin by analyzing the effect of PN corrections to the amplitude of the waveform. This analysis suggests that we can faithfully model signals while restricting to leading PN order in the amplitude. We then obtain and analyze the decomposition of this signal (keeping only leading order PN corrections in the amplitude) into harmonics of the azimuthal and radial orbital frequencies. We validate this decomposition by computing the overlap (a measure of the agreement between two models) between the waveform decomposed into a number of harmonics and one which has not been decomposed into harmonics. Lastly, we discuss different PN consistent ways of solving Eq. (2.9) and the implications this has for modeling eccentric systems. Throughout we provide details on how we obtain the fully numerical model with which we will compare and validate our frequency domain model.

2.3.1 PN Effects in the Amplitude

To 2PN order in the amplitude, the GW polarizations read:

$$h_{+,\times} = \frac{m\eta}{R} y^2 (1-e^2) \left(H^{(0)}_{+,\times} + y H^{(1/2)}_{+,\times} + y^2 H^{(1)}_{+,\times} + y^3 H^{(3/2)}_{+,\times} + y^4 H^{(2)}_{+,\times} \right) \tag{2.10}$$

The lengthy expressions for $H^{(n)}_{+,\times}$ can be found in [106] in ADM gauge and using a PN expansion parameter related to mn where n is the mean motion. Recall that we employ the PN parameter y which is related to $m\omega$ where ω is the angular frequency. The corrections needed to express $H^{(n)}_{+,\times}$ in MH and in terms of y can be found in Appendix 2.A. For reference we list the 0PN polarizations here (which are unaffected by gauge differences or the change of PN parameter between mn and y):

$$H^{(0)}_{+} = \big(P^0_{C2C2}\cos 2W + P^0_{S2C2}\sin 2W\big)\cos 2\bar{\lambda} + \big(P^0_{C2S2}\cos 2W + P^0_{S2S2}\sin 2W\big)\sin 2\bar{\lambda} + P^0\,, \tag{2.11a}$$

$$H^{(0)}_{\times} = \big(X^0_{C2C2}\cos 2W + X^0_{S2C2}\sin 2W\big)\cos 2\bar{\lambda} + \big(X^0_{C2S2}\cos 2W + X^0_{S2S2}\sin 2W\big)\sin 2\bar{\lambda}\,, \tag{2.11b}$$

where we have defined

$$P^0_{C2C2} = \frac{(1+C^2)}{(1-e\cos u)^2}\left[(e\cos u)^2 - e\cos u - 2e^2 + 2\right]\,, \tag{2.12a}$$

$$P^0_{C2S2} = \frac{2(1+C^2)}{(1-e\cos u)^2}\sqrt{1-e^2}\,e\sin u\,, \tag{2.12b}$$

$$P^0 = \frac{S^2}{(1-e\cos u)}e\cos u\,, \tag{2.12c}$$

$$X^0_{C2C2} = -4C\frac{\sqrt{1-e^2}}{(1-e\cos u)^2}e\sin u\,, \tag{2.12d}$$

$$X^0_{C2S2} = \frac{2C}{(1-e\cos u)^2}\{(e\cos u)^2 - e\cos u - 2e^2 + 2\}\,. \tag{2.12e}$$

and where the different orbital parameters entering the polarizations are described in Sec. 2.2, while

$$C = \cos i\,, \qquad S = \sin i\,, \qquad \bar{\lambda} = \lambda - \beta\,. \tag{2.13}$$

with angles β and i polar angles that describe the polarization axes.

Before we can attempt to obtain a Fourier domain model for the GW signal, we must first decide on how many PN corrections to keep in the amplitude of the polarization in Eq. (2.10). In order to do so, we will make use of the overlap, i.e. the normalized inner product in Fourier space, weighted by the spectral noise of the detector. Between two signals h_1 and h_2, the overlap is defined by

$$\mathcal{O}(h_1, h_2) = \frac{(h_1|h_2)}{\sqrt{(h_1|h_1)(h_2|h_2)}}\,, \tag{2.14}$$

where the inner product is defined as

$$(h_1|h_2) = 4\mathrm{Re}\left[\int_{f_1}^{f_2} \frac{\tilde{h}_1^* \tilde{h}_2}{S_n(f)} df\right]\,. \tag{2.15}$$

and $S_n(f)$ is the spectral noise density of the detector. An overlap of unity between two models indicates perfect agreement, while an overlap of -1 indicates models perfectly out of phase, with a vanishing overlap indicating perfect disagreement.

In order to gauge the importance of inclusion of higher order PN corrections to the amplitude we calculate the overlap between two models. One model consists of numerically solving for the orbital parameters (i.e. u, W, l, λ, e, and y) using their evolution equations at 3PN order, and keeping all corrections up to 2PN order in the amplitude. The other consists of again numerically solving for the orbital parameters using their evolution equations at 3PN order, but varying the PN order to which the amplitude of the polarizations in Eq. (2.10) is kept. We also explore the effect of solving for $u(t)$ using the Newtonian version of Kepler's equation.

Before presenting the results of the overlap, let us provide some technical details of how these models are constructed. We begin by numerically solving (using the Bulirsch-Stoer [107] method implemented in `C++` using the `odeint` library [108]) the coupled set of differential equations $(\dot{\lambda}, \dot{l}, \dot{e}, \dot{y})$ provided by Eqs (2.9). We stop the evolution when $y > (3(1+e))^{-1}$, a choice that is explained in detail in Section 2.4.2, but we see that in the circular limit this corresponds to an orbital velocity of a third the speed of light. With the time evolution of these parameters in hand, we must then solve the 3PN Kepler's equation. This is done by adapting Mikkola's method [109], a fast and accurate numerical scheme to solve Kepler's equation at Newtonian (0PN) order. To solve Kepler's equation at higher PN order [Eq. (2.5e)], we first use Mikkola's method on the Newtonian equation, and then use the result as an initial guess to solve Eq. (2.5e) using Mikkola's method again (see [25, 110] for more details). To obtain W, we plug in the solution for u, y, and e into Eq. (2.5f) to obtain the true anomaly v, and then, all of these are substituted into Eq. (2.5c) to obtain W.

The numerical solutions for the orbital elements are plugged into the GW polarization to form $h(t)$ (where we choose to sample all time domain quantities at 8192 Hz). This time series is then zero padded on either side such that its length is the nearest integer power of 2, and we take the discrete Fourier transform using the `FFTW` library implemented in `C++` [111]. The overlaps are computed from $f_1 = 1$Hz to $f_2 = 4096$Hz. We use an interpolation of a set of values of the noise curve corresponding to stationary Gaussian noise in aLIGO at design sensitivity [77]. The integrals appearing in the overlap are evaluated as sums with frequency resolution determined by the frequency resolution of the discrete Fourier transform, which depends on the length of signal, and as a result varies between different initial conditions.

Figure 2.2 presents the value of the overlap between various templates as a function of the initial eccentricity and dimensionless semi-latus rectum. In the equal mass case, the overlaps are not affected past the third decimal place if we keep the amplitude to Newtonian order. We also find that keeping Kepler's equation

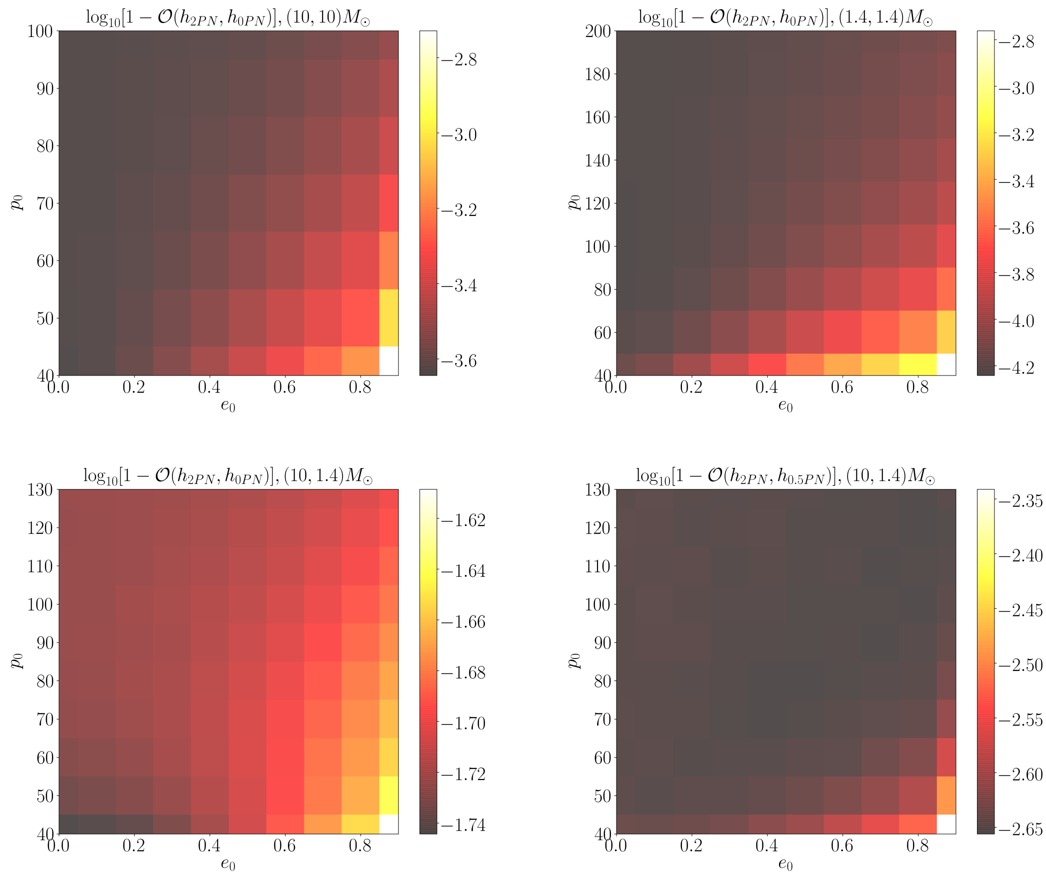

Figure 2.2: $\log_{10}$ of $1-\mathcal{O}$ between a waveform keeping only the leading order corrections and one keeping 2PN corrections in the amplitudes for a $(10,10)M_\odot$ (top left), $(1.4,1.4)M_\odot$ (top right), and $(10,1.4)M_\odot$ (bottom left) system. On the bottom right panel we show the same but between a waveform keeping 0.5PN corrections in the amplitude and one keeping 2PN corrections for the unequal mass case. There is good agreement in the equal mass case, but significant loss in the unequal mass case if we keep only leading order corrections in the amplitude.

at Newtonian order when solving for $u(t)$ only affects the overlaps in the fifth decimal place. This suggests we can keep the amplitude and Kepler's equation to Newtonian order, which considerably simplifies the decomposition of $h(t)$ into a sum over harmonics of l and λ, which in turn is crucial to analytically approximate the Fourier transform. However, half order contributions vanish in the equal mass limit and thus the overlap is affected in the 2nd digit for unequal mass binaries. This amount of loss in overlap may be considerable, depending on the data analysis application one has in mind, and it is not due to solving Kepler's equation at Newtonian order, but rather due to neglecting higher order PN effects in the amplitude. We will return to this loss of accuracy for non-equal mass systems later.

2.3.2 Harmonic Decomposition

Following paper 1, a crucial step in obtaining a Fourier domain waveform is to decompose the time domain signal into a sum over harmonics of the angles related to the mean orbital frequencies n and ω. We carry out such a decomposition here and then verify that it faithfully represents the un-decomposed signal using overlaps. The results of Section 2.3.1, however, indicate that we may retain only the leading order (Newtonian) contributions in the GW amplitude and in Kepler's equation, at least for comparable mass binaries, and thus, we will restrict attention to such a model.

The results of this section rely heavily on the work to analytically solve 3PN accurate Kepler's equation by Boetzel et. al. in [87], which provides a useful decomposition of harmonics of W into an infinite sum of harmonics of l:

$$e^{imW} = \sum_{n=-\infty}^{\infty} \mathcal{P}_n^{mW} e^{inl}. \tag{2.16}$$

Re-expressing the polarizations in Eq. (2.11) in terms of complex exponentials and inserting the above decomposition yields

$$h(t) = \frac{m\eta}{R} y^2 (1-e^2)(F_+ H_+^{(0)} + F_\times H_\times^{(0)}) \,, \tag{2.17}$$

with

$$H_+^{(0)} = P^0 + \frac{P^0_{C2C2} + iP^0_{C2S2}}{2} \sum_{s=-\infty}^{\infty} \mathcal{P}_s^{2W} e^{-i(sl+2\bar{\lambda})} + \text{c.c.} \,, \tag{2.18}$$

$$H_\times^{(0)} = \frac{X^0_{C2C2} + iX^0_{C2S2}}{2} \sum_{s=-\infty}^{\infty} \mathcal{P}_s^{2W} e^{-i(sl+2\bar{\lambda})} + \text{c.c.} \,, \tag{2.19}$$

where c.c. stands for the complex conjugate, and where F_+ and $F_\times$ are the antenna functions of the detector

$$F_+(\theta, \Phi, \psi) = \frac{1}{2}(1+\cos^2\theta)\cos 2\Phi \cos 2\psi - \cos\theta \sin 2\Phi \sin 2\psi \,, \tag{2.20}$$

$$F_\times(\theta, \Phi, \psi) = F_+(\theta, \Phi, \psi - \pi/4) \,, \tag{2.21}$$

with θ and Φ the sky angles associated with the orientation of the detector relative to the source, and ψ the polarization angle that defines the rotation from the wave's polarization basis to that defined by the arms of the detector.

Inspection of Eqs. (2.11) and (2.12) reveals that harmonic decompositions of three additional expressions are required:

$$\chi_0 = \frac{e\cos u}{1-e\cos u} \,, \tag{2.22}$$

$$\chi_1 = -\frac{1}{1-e\cos u}\left[(e\cos u)^2 - e\cos u - 2e^2 + 2\right] \,, \tag{2.23}$$

$$\chi_2 = e\sqrt{1-e^2}\frac{\sin u}{(1-e\cos u)^2} \,. \tag{2.24}$$

The decomposition of χ_0 at 0PN order, which is consistent with our 0PN treatment of Kepler's equation, is very straightforward and we obtain (using Eq.(B13) of [112])

$$\chi_0 = \sum_{s=-\infty}^{\infty} G_s e^{isl}\,, \tag{2.25}$$

with $G_0 = 0$ and $G_{s\neq 0} = J_s(se)$, where $J_s(x)$ are Bessel functions of the first kind. With a little more work, we further obtain

$$\chi_1 = \sum_{s=-\infty}^{\infty} I_s e^{isl}\,, \tag{2.26}$$

with the definitions

$$I_0 = (e^2-1)2A_0^2\,, \tag{2.27a}$$

$$I_{s\neq 0} = J_s(se) + (e^2-1)A_s^2\,, \tag{2.27b}$$

where the A_j^s are given by Eq. (42b) of [87]. Lastly, for χ_2 we have

$$\chi_2 = i\sum_{s=-\infty}^{\infty} L_s e^{isl} \tag{2.28}$$

where we have defined

$$L_s = e\sqrt{1-e^2}\left[J_s'(se)A_0^1 + \frac{1}{2}K_{|s|}\right]\,, \tag{2.29a}$$

$$K_s = \sum_{j=1}^{s-1} A_j^1 J_{s-j}'[(s-j)e] - \sum_{j=s+1}^{\infty} A_j^1 J_{j-s}'[(j-s)e] + \sum_{j=1}^{\infty} A_j^1 J_{j+s}'[(j+s)e]\,. \tag{2.29b}$$

We can combine all of these results to find the harmonic decomposition of the waveform. First, we find that

$$P^0_{C2C2} + iP^0_{C2S2} = -(1 + C^2) \sum_{s=-\infty}^{\infty} M_s e^{isl} \,, \tag{2.30a}$$

$$X^0_{C2C2} + iX^0_{C2S2} = -2iC \sum_{s=-\infty}^{\infty} M_s e^{isl} \,, \tag{2.30b}$$

where we have defined $M_s = I_s + 2L_s$, and we note that $M_s = M_{-s}$. With this, we then have the full decomposition of $H^{(0)}_{+,\times}(t)$ into harmonics of l and λ:

$$H^{(0)}_{+} = S^2 \sum_{s=-\infty}^{\infty} G_s e^{isl} - \frac{(1 + C^2)}{2} \sum_{j=-\infty}^{\infty} N_j e^{-i(jl+2\bar{\lambda})} + \text{c.c.} \tag{2.31a}$$

$$H^{(0)}_{\times} = -iC \sum_{j=-\infty}^{\infty} N_j e^{-i(jl+2\bar{\lambda})} - \text{c.c.} \,, \tag{2.31b}$$

where we have defined

$$N_j = \sum_{s=-\infty}^{\infty} \mathcal{P}^{2W}_s M_{j-s} \,. \tag{2.32}$$

The N_j coefficients scale as $e^{|j|}$ to leading PN order. In this work, we represent N_j as the first 20 terms in a low-eccentricity expansion past leading order and at 3PN in the contributions from W (keeping only 0PN contributions from the solution to Kepler's equation) with $j = [-15, 15]$.

Putting the above together to form the GW strain we then have

$$h(t) = \mathcal{A} \left(F_+ S^2 \sum_{s=-\infty}^{\infty} G_s e^{isl} + Q \sum_{j=-\infty}^{\infty} N_j e^{-i(jl+2\lambda)} + \text{c.c.} \right) \tag{2.33}$$

where Q is the complex function of the antenna functions and sky location

$$Q = -\left(F_+ \frac{1+C^2}{2} + iCF_\times\right) e^{i2\beta}\,, \tag{2.34a}$$

and $\mathcal{A} = \frac{m\eta}{R} y^2(1-e^2)$. Notice that in the circular limit the first term in Eq. (2.33) is not present, as it scales as $G_s = \mathcal{O}(e^{|s|})$.

We are now in a position to check if the low eccentricity expansion of the N_j and G_s can be used to faithfully reconstruct the signal. In order to do so, we compute the overlap between the harmonically decomposed waveform keeping $j = [-15, 15]$ and $s = [-15, 15]$ harmonics in Eq. (2.33), and a waveform where trigonometric functions of u and W have not been harmonically decomposed. Figure 2.3 shows these overlaps for a $(10, 10)M_\odot$, $(10, 1.4)M_\odot$, and $(1.4, 1.4)M_\odot$ binary. We see that for a majority of the parameter space considered, the overlap is above 0.98.

For very high initial eccentricities ($e_0 > 0.7$) and small dimensionless initial separations ($p_0 < 50$), however, the overlap decreases sharply (below the minimum value shown) to values as low as 0.93. This is due to a combination of spectral truncation (i.e. not enough harmonics have been kept in Eq. (2.33) to faithfully reconstruct the full signal) and inaccuracy of the harmonic amplitudes, as they have been expanded in low eccentricity. Since Bessel functions appear all throughout the harmonic amplitudes with the form $J_s(se)$, and expansions of Bessel functions are known to converge very slowly as their argument is near their index, we conclude that the faithful modeling of this small subset of the parameter space would require a considerably higher number of terms in the eccentric expansions of the amplitudes, as well as more harmonics in the sum of Eq. (2.33).

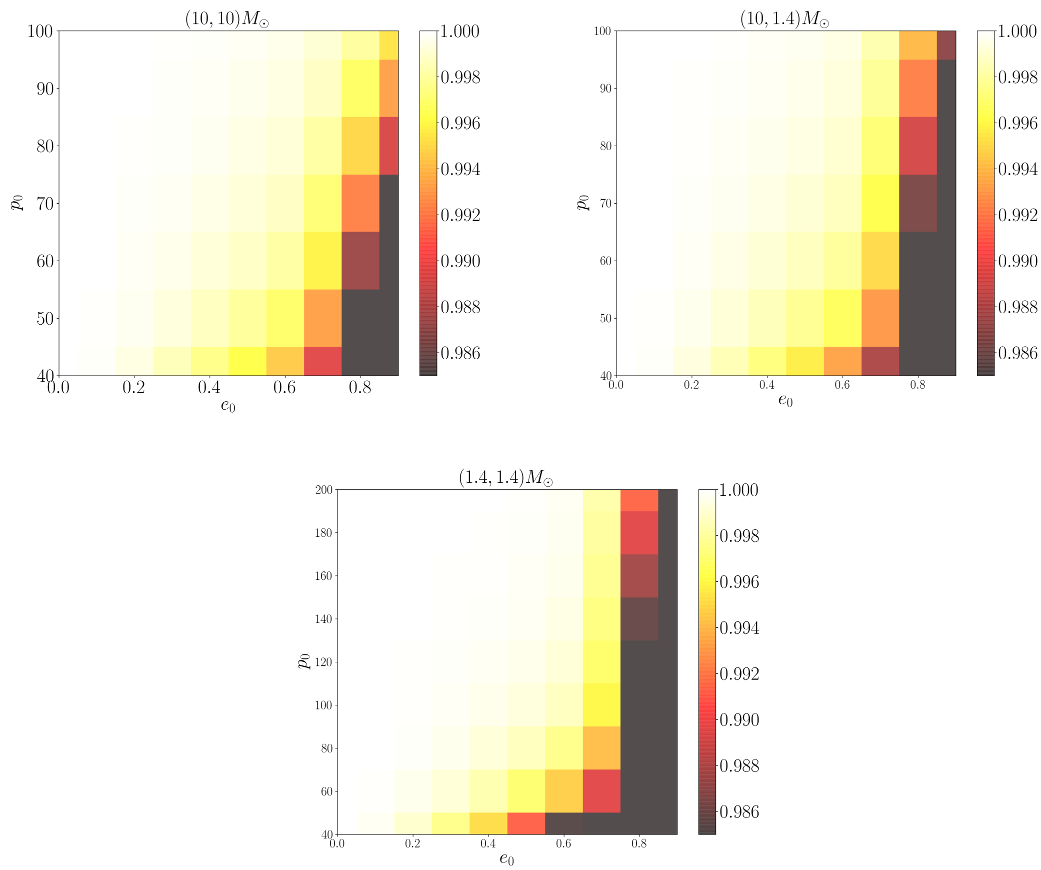

Figure 2.3: Overlap between the harmonic decomposed signal of Eq. (2.33) with $s = [-15, 15]$ and $j = [-15, 15]$ harmonics and the non-decomposed signal of Eq. (2.11). The overlap is above 0.985 for much of the parameter space.

2.3.3 Qualitative Analysis of Eccentric Signals

Let us now develop a sense of the relative strength of the harmonics and the structure of the Fourier domain signal before moving on to explicitly deriving such a Fourier-domain waveform. We achieve this through a few different methods. First, we examine the structure of the Fourier response without including the effects of radiation reaction. This reveals the relative strength of the different harmonics and the mapping between the orbital frequencies, n and ω, and the Fourier frequency, f. Second we examine the structure of the Fourier response with radiation reaction using both the Fourier transform and a time frequency representation of the signal. Lastly we investigate the relative strength of the N_j by plotting their values as function of j and e. Knowing which amplitudes are the strongest is key if one wishes to make the model more efficient by careful truncation or selection of which harmonics to include in Eq. (2.33).

Let us first inspect the Fourier response of a steady state system (i.e. in the absence of radiation reaction so that $\dot{e} = \dot{y} = 0$). As a result the orbital angles l and λ are given by $l = n(t - t_0)$ and $\lambda = \omega(t - t_0)$. The Fourier transform of the signal as written in Eq.(2.33) is then trivial: the sum of the product of the harmonic amplitude N_j or G_s and delta functions centered at $sn/(2\pi)$ or $\pm(jn + 2\omega)/(2\pi)$, where s and j are the indices of the sums in Eq. (2.33). We proceed by taking the discrete Fourier transform of the numerical un-decomposed time domain signal in order to get a sense of the distribution of strength of the harmonics, as well as to verify that the result is consistent with Eq. (2.33).

The left panel of Fig. 2.4 shows the amplitude of the discrete Fourier transform of the numerically evolved (at 3PN order in the dynamics, keeping only leading PN order contributions in the amplitude) time-domain signal as written in Eq. (2.11). As predicted, we see spectral lines appearing at Fourier frequencies that are combinations of the two orbital frequencies. In the case of the signals with modest initial eccentricities, we have labeled a number of frequency positions of the different harmonics. The subscript on the index j indicates whether the plus or minus has been taken in the location of the jth harmonic given by $\pm(jn+2\omega)/(2\pi)$. In the high eccentricity case, there are too many closely spaced harmonics to clearly indicate which is which. The harmonics of index j_+ tend to be dominant, followed by the harmonics of s, and the harmonics of index j_- are clearly subdominant. We choose all sky angles to be $3\pi/7$, and have verified that the results do not qualitatively change much with the choice of sky angle (other than the fact that the harmonics of s vanish in the $\iota \to 0$ limit).

When we allow the binary to inspiral due to radiation reaction, the orbital eccentricity and the two orbital frequencies change with time. As a result, the Fourier transform is not a simple sum of spectral lines any longer. Since the amplitude is slowly varying compared to the complex exponentials, we can expect the spectral lines of the left panels of Fig. 2.4 to sweep with the orbital frequencies as the latter increase, forcing different harmonics to overlap and to interference. The right panel of Fig. 2.4 shows the Fourier spectrum when the effects of radiation reaction are included. We see that the amplitude oscillates rapidly due to harmonic interference as expected.

Since the amplitude is so rapidly oscillating when radiation-reaction is included, it is more enlightening to look at a time-frequency representation of the GW signal. Figure 2.5 shows the Q-transform of the GW signals considered in the right panel of Fig. 2.4. A Q-transform is one in which the basis functions are sine-Gaussians with quality factor Q, such that a low (high) value of Q localizes the basis more in time (frequency). With this representation of the signal, we can clearly see the behavior of the different harmonics. Each harmonic takes a distinct track in time-frequency

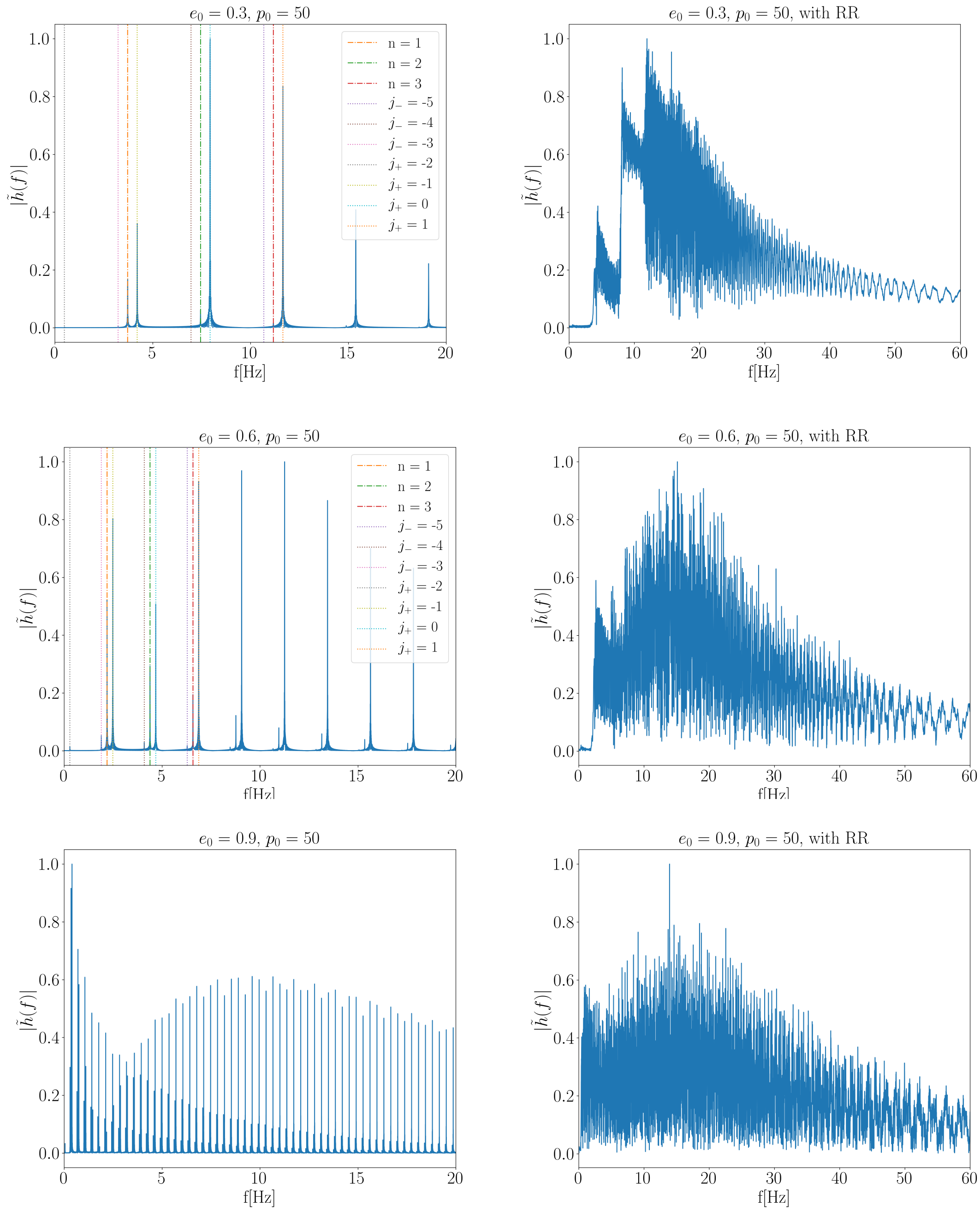

Figure 2.4: DFT of the the numerically evolved time domain signal as written in Eq. (2.11) without (left) and with (right) radiation-reaction effects for a BBH system with different initial conditions. When radiation-reaction is absent, the signal is split into harmonics of combinations of the orbital frequencies, with harmonic index as appearing in Eq. (2.33) labeled. When radiation-reaction is present, the harmonics now sweep in frequency and interfere with once another producing a rapidly varying amplitude.

space, as a result of the orbital frequencies increasing in time. We also see that harmonics, besides the $j = 0$ one (the only non-vanishing harmonic in the circular limit), decay with time and very rapidly with frequency. The lower left panel shows the time frequency evolution for the high eccentricity case ($e_0 = 0.9$). Although at late times the harmonic structure is clear, this is not so at early times, which is an artifact of the particular choice of Q we made in this figure (a choice of $Q = 150$ does well at capturing the oscillatory nature of the late signal since it is more localized in frequency). At early times the signal consists of a series of bursts. In the lower right panel we have plotted the Q-transform of some of the early signal with $Q = 20$, to appreciate how much more localized in time the signal is at early times.

Figure 2.6 presents the value of N_j as a function of the index j and the eccentricity e at which they are being evaluated, keeping 20 terms in eccentricity past leading (left) and 16 terms past leading (right). We have set $\eta = 0.25$ in these results, but verified that setting $\eta = 0.1$ changes the result negligibly. We have set y such that the results correspond to a dimensionless semilatus rectum of 50. In the low eccentricity limit, the $j = 0$ harmonic dominates as expected as it is the only non-vanishing harmonic in the circular limit. As the eccentricity is increased, the harmonics become more comparable in strength with the $j > -1$ harmonics clearly dominating. For large eccentricities, there is considerable strength in the larger negative j harmonics. We see that at such high eccentricity there are visibly different features between the two panels suggesting that the eccentricity expansions are beginning to break down.

2.3.4 Different Time Domain Approximants

Given the increase in the number of relevant ODEs and parameters in the eccentric problem, there are a number of different and new PN-consistent ways to

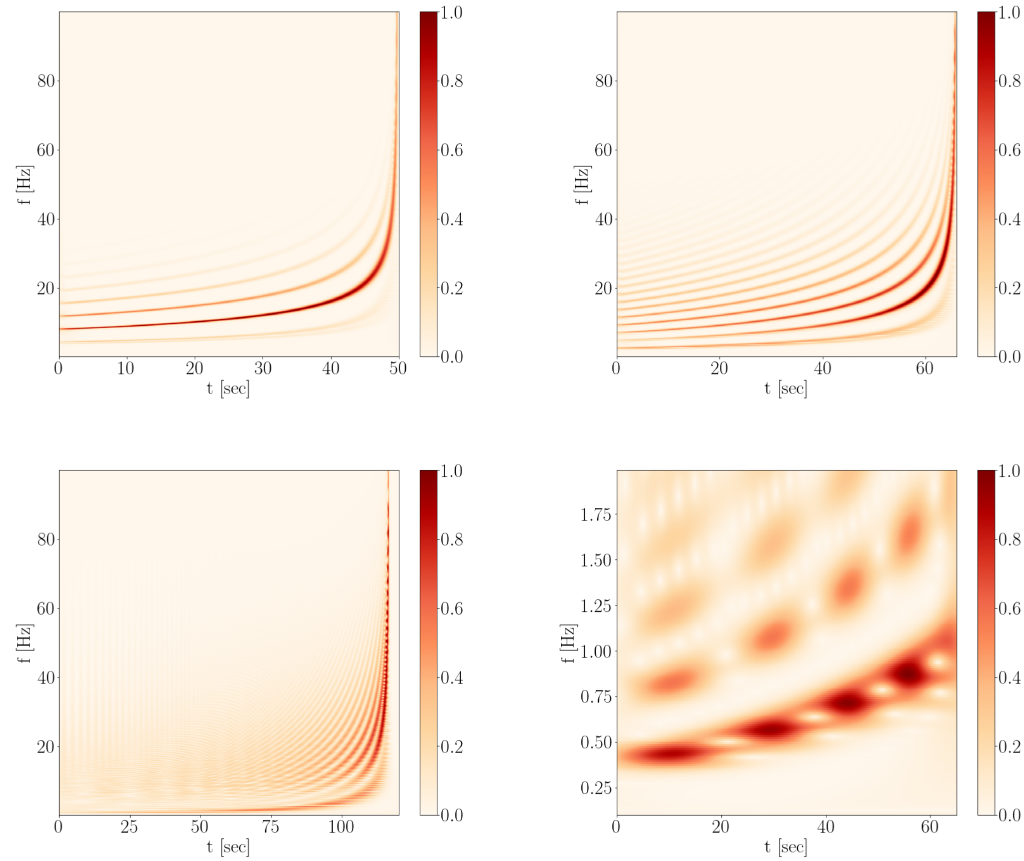

Figure 2.5: A time frequency representation of the numerically solved eccentric signal for a BBH system all with a $p_0 = 50$, $e_0 = 0.3$ (top left), $e_0 = 0.6$ (top right), $e_0 = 0.9$ (bottom left). The bottom right is a zoomed in view of the high eccentricity case. We clearly see in time frequency space that the signal is composed of different harmonics which increase in frequency as time increases. The bursty nature of highly eccentric signals is encapsulated by the bottom right panel. Power rapidly decays from higher harmonics as frequency is increased, suggesting that they may be negligible past certain frequencies.

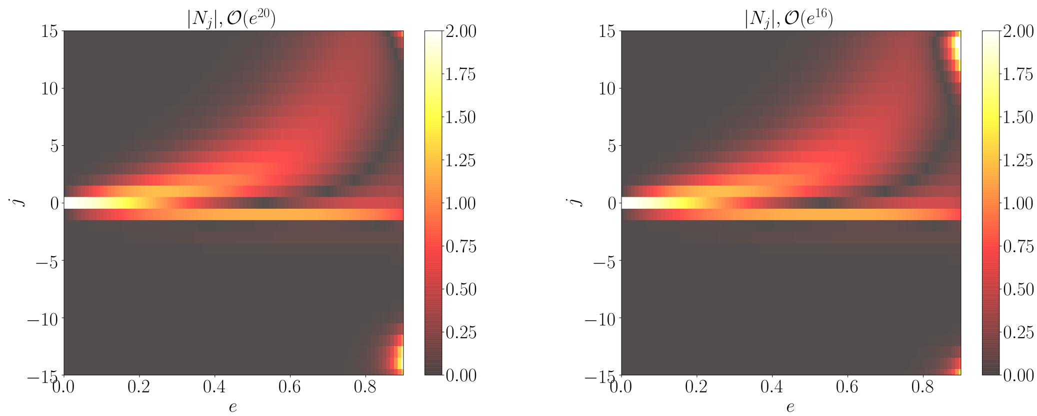

Figure 2.6: Absolute value of N_j with fixed $\eta = 0.25$ and $p_0 = 50$, keeping 20 terms in eccentricity past leading order (left) and 16 terms past leading (right). Most of the power is concentrated in the $j > -1$ harmonics as eccentricity is increased. For large eccentricities, we see that differences arise between the two panels suggesting that perhaps more eccentric corrections are needed to evaluate the harmonics accurately at such large eccentricities.

solve the orbital dynamics beyond what is possible in the circular limit. In order to introduce these, let us begin by reviewing the circular TaylorT4 approximant (for a more in-depth discussion of the different circular PN approximants, see Sec. III of [78]). In the circular TaylorT4 approximant, one numerically solves the set of ODEs:

$$\frac{dv}{dt} = \frac{32}{5}\frac{\eta}{M}v^9\left[1 - \left(\frac{743}{336} + \frac{11}{4}\eta\right)v^2 + ... + \mathcal{O}(v^7)\right] \tag{2.35a}$$

$$\dot{\phi} = \frac{v^3}{M} \tag{2.35b}$$

The numerical solutions to these are then substituted into a circular GW polarization and a DFT can then be taken to obtain a Fourier-domain waveform.

In the eccentric case, however, there are several different ways of solving the relevant orbital dynamics presented in Eq.(2.9), and each of them is consistent in a PN sense. Given this, we introduce here 3 different time-domain approximants that extend the circular TaylorT4 approximant to eccentric inspirals: TaylorT4t, TaylorT4y, and TaylorT4e. Each of these is constructed by numerically solving a set of ODEs, with the difference being the independent variable t, y, or e used to parameterized the solution.

The TaylorT4t approximant is obtained by using time t as the independent variable when numerically solving the set of ODEs $(\dot{l}, \dot{\lambda}, \dot{e}, \dot{y})$ for $[\lambda(t),\ l(t),\ e(t), y(t)]$. The resulting solutions are then inserted into the appropriate expressions for the full orbital dynamics (Eq. (2.5)) to obtain $\phi(t)$, and the result of this is then inserted into the expression for $h(t)$ in Eq. (2.11). Finally, we take a DFT to obtain a Fourier domain waveform.

The TaylorT4e approximant is obtained by using the eccentricity e as the independent variable when solving the orbital dynamics equations. This implies we must first express the ODEs of TaylorT4t in terms of the eccentricity and then numerically solve $(d\lambda/de, dl/de, dt/de, dy/de)$ for $[\lambda(e), l(e), t(e), y(e)]$. This re-writing is obtained via the chain rule and the subsequent re-expansion of the resulting expressions to the appropriate PN order. For example, to obtain dy/de, we use $dy/de = \dot{y}/\dot{e}$, where the ratio is re-expanded to 3PN order in y. The numerical solution to these ODEs can then be expressed as functions of time by numerically inverting $t(e)$ for $e(t)$. With these substitutions done, one finds $h(t)$ through Eq. (2.11) and applies a DFT to find the Fourier-domain representation.

The TaylorT4y approximant is obtained by using the PN variable y as the independent variable when numerically solving the set of ODEs $(d\lambda/dy, dl/dy, dt/dy, de/dy)$ for $[\lambda(y), l(y), t(y), e(y)]$. Again in each of these ODEs, any ratio of PN expressions arising due to the use of the chain rule is re-expanded to the appropriate PN order. With solutions for the orbital elements in terms of y in hand, one then numerically inverts $t(y)$ for $y(t)$, and this is used to construct $h(t)$ via Eq. (2.11) before taking a DFT to find the Fourier-domain representation.

Each of these different ways to solve for the orbital elements is equally valid in the PN approximation, but each solution is slightly different due to the truncation of this series in the ODEs and the subsequent use of numerical solvers. Since our Fourier domain waveform will later rely on the differential equations of the TaylorT4e approximant, it is important to know how faithful TaylorT4e is relative to the TaylorT4t approximant. Such an analysis will reveal the PN limitations of our frequency domain waveform model. We choose to compare TaylorT4e to TaylorT4t because, at least in the circular limit, the latter have been shown to be the most faithful against EOB waveforms [78].

Figure 2.7 shows the overlap maximized over a time offset and overall phase offset between the TaylorT4e and the TaylorT4t approximants for a $(10, 10)M_{\odot}$, a $(10, 1.4)M_{\odot}$, and a $(1.4, 1.4)M_{\odot}$ binary for a variety of different initial conditions (e_0 and p_0). In the equal-mass cases, we see that as the two models agree with each other in most of the initial parameter space, with disagreements only arising at sufficiently large initial eccentricity or small initial separation. To be clear, there has been no small eccentricity expansion or approximations between these two models, with the only source of disagreement coming from the truncation of the PN series when reformulating the ODEs in terms of t or e. Both models are obtained purely numerically and without any harmonic decomposition.

In the unequal mass case, the disagreement between the TaylorT4e and TaylorT4t approximants is much more pronounced. This is because of the well-known fact that the PN expansion is poorly behaved for unequal masses [113], but this feature seems to become enhanced for even moderate initial eccentricities. Since the Fourier-domain model we will develop later solves for the orbital dynamics as formulated in the TaylorT4e approximants, we expect that it will also disagree with TaylorT4t to the level displayed in Fig. 2.7.

We have not explored the agreement of the TaylorT4y approximant with the others as the main goal of this work is to obtain a frequency domain waveform, but we expect a similar level of disagreement between the TaylorT4y approximant and the others. We reiterate that all 3 of these approximants are equally valid under the PN approximation. In order to investigate which of these is the best one would ideally need to compare with NR waveforms.

2.4 Eccentric GWs in the Fourier Domain

In this section we begin by reviewing the Fourier domain model that was derived in paper 1. Following the prescription laid out there, we extend the model to 3PN order in the Fourier phase. Lastly we describe how other frequency domain approximants could be derived in analogy to the different time domain approximants discussed in Section 2.3.4.

2.4.1 Review of Newtonian model

In paper 1 we computed the Fourier response via the SPA of a time domain signal whose time domain harmonic decomposition took the general form:

$$h_{+,\times} = \sum_{j=-\infty}^{\infty} A_j e^{ijl} + \text{c.c.} \tag{2.36}$$

Here the amplitudes A_j are functions of eccentricity and vary on a slower timescale (the radiation reaction timescale) than the orbital angle l (which varies on the orbital timescale). This makes it appropriate for the application of the stationary phase approximation (SPA) which is described in detail in [91]. The time domain signal in

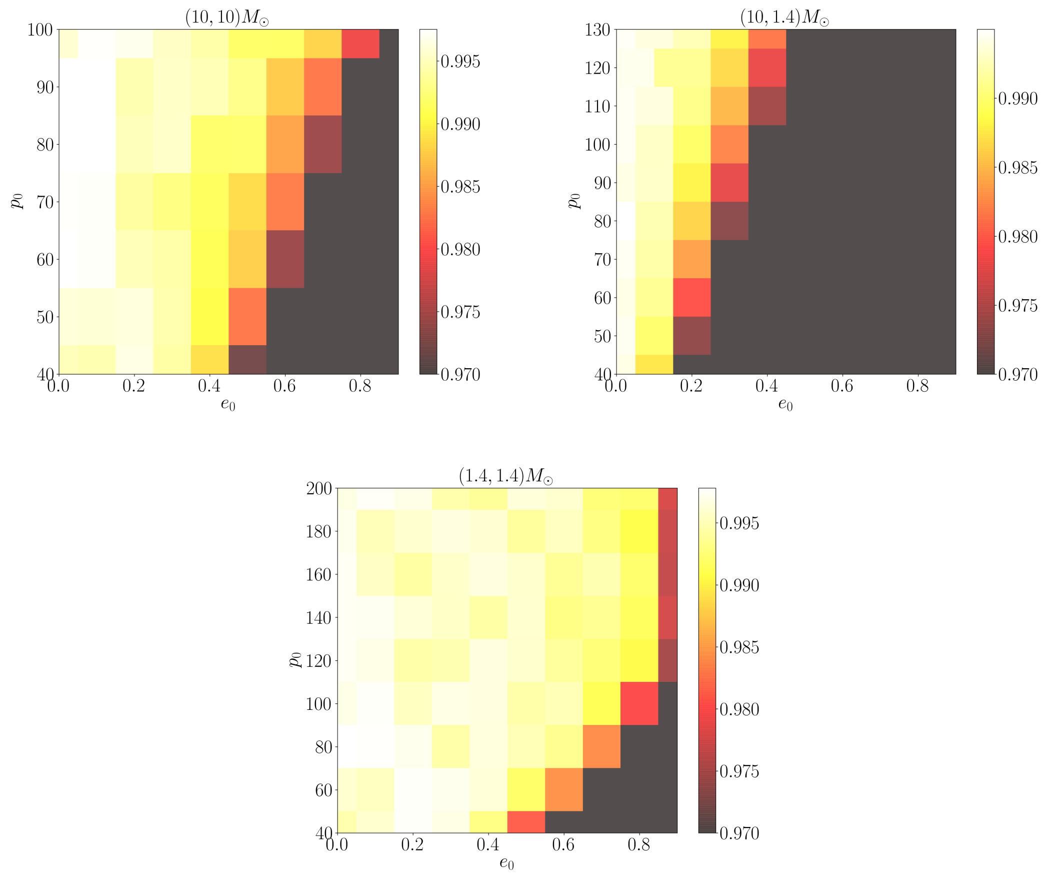

Figure 2.7: Maximized overlap between the TaylorT4t and TaylorT4e approximants for three different systems with different initial conditions. In the equal-mass case, there is good agreement between the two models until the initial eccentricity is large enough or the initial separation is small enough. In the unequal-mass case, however, the disagreement becomes considerable even for small eccentricities. Note that we do not plot values below 0.97, as the value of the overlap drops considerable below this value in the close and highly eccentric cases.

Eq. (2.36) is composed entirely of harmonics of l because at Newtonian order $\lambda = l$, a result of periastron precession effects entering at 1PN order. Application of the SPA to the above signal yields

$$\tilde{h}_{+,\times}(f) = \sum_{j=1}^{\infty} A_j(t_j^*) \sqrt{\frac{2\pi}{j\ddot{l}(t_j^*)}} e^{i\psi_j} \,, \tag{2.37}$$

where the Fourier phases are given by

$$\psi_j = 2\pi f t_j^* - j l(t_j^*) - \pi/4 \,. \tag{2.38}$$

The stationary phase condition relates the Fourier frequency, f, to time domain quantities through

$$2\pi f = j\dot{l}(t_j^*) \,. \tag{2.39}$$

Clearly then, it is necessary to express the functions t_j^* and l that appear in the Fourier phases in terms of some time domain quantity to evaluate the model at any given frequency. In paper 1, we chose to use the orbital eccentricity as that time domain quantity, because the orbital dynamics at Newtonian order can be solved exactly in terms of this quantity, i.e. one is able to exactly solve the Newtonian order dn/de equation to obtain $n(e)$. This solution can then be used in the integrals that define the phase functions

$$t(e) = \int \frac{de'}{\dot{e}[n(e'), (e')]} \tag{2.40}$$

$$l(e) = \int \frac{n(e')}{\dot{e}[n(e'), (e')]} de' \,, \tag{2.41}$$

which admit exact solutions in the form of hypergeometric functions. Evaluation of these functions, however, is computationally expensive, and thus, in paper 1 we used a simple Taylor expansion of those hypergeometric functions about small eccentricity, which we found was sufficient to faithfully model the Fourier phases, even to eccentricities as high as ~ 0.9. The last step to evaluate the model at a given frequency was to numerically invert the stationary phase condition written in Eq.(2.39) to find $e(n)$. The stationary phase condition can be more suggestively written (using $\dot{l} = n$) as

$$2\pi f = jn(e) \,. \tag{2.42}$$

Thus relating the Fourier frequency f to eccentricity amounts to inverting $n(e)$ for $e(n)$, and this is a relatively cheap inversion because the solution is clearly independent of j and, in the Newtonian limit, also system independent.

The key result which allows for the model to be readily extended to 3PN order is that the Taylor expansions in orbital eccentricity of the hypergeometric functions appearing in the phase were generally sufficient to faithfully represent the signal even for large eccentricities. Only the inversion of $n(e)$ behaves very poorly for even moderate eccentricities. Thus, the route for extension to higher PN is clear:

(i) solve for the frequency evolution as a function of eccentricity in an expansion in both a PN parameter and the orbital eccentricity,

(ii) use this solution to express the integrands appearing in the phase functions as expansions of those same parameters and integrate the series in eccentricity,

(iii) numerically invert the stationary phase condition to relate frequency to the eccentricity.

2.4.2 Eccentric 3PN Fourier Domain Model

Let us now derive the Fourier domain model to 3PN order, which we will call TaylorF2e as it closely follows the quasi-circular TaylorF2 model, and corresponds to solving the orbital dynamics where the independent variable is e.

Following the general scheme laid out in paper 1, we begin by applying the SPA to the harmonic decomposition, which was derived in Eq. (2.33) of Sec.2.3.2. We reiterate the harmonic decomposition here, explicitly writing out the complex conjugate term:

$$h(t) = \mathcal{A}\left\{F_+ S^2 \sum_{s=-\infty}^{\infty} G_s e^{isl} + \left[Q \sum_{j=-\infty}^{\infty} N_j e^{-i(jl+2\lambda)} - Q^* \sum_{j=-\infty}^{\infty} N_j e^{i(jl+2\lambda)}\right]\right\} . \tag{2.43}$$

Applying the SPA to each of the oscillating terms separately (see Appendix A of paper 1 for a brief description of the SPA as applied to individual harmonics of the orbital phases), we find

$$\mathcal{F}\left[N_j e^{-i(jl+2\lambda)}\right] \approx N_j \sqrt{\frac{2\pi}{|j\ddot{l} + 2\ddot{\lambda}|}} e^{i\psi_j^-} , \tag{2.44a}$$

$$\psi_j^- = 2\pi f t_j^- - (jl + 2\lambda) - \frac{\pi}{4} , \tag{2.44b}$$

$$2\pi f = j\dot{l}(t_j^-) + 2\dot{\lambda}(t_j^-) , \tag{2.44c}$$

for the first term,

$$\mathcal{F}\left[N_j e^{i(jl+2\lambda)}\right] \approx N_j \sqrt{\frac{2\pi}{|j\ddot{l} + 2\ddot{\lambda}|}} e^{i\psi_j^+} , \tag{2.45a}$$

$$\psi_j^+ = 2\pi f t_j^+ + (jl + 2\lambda) - \frac{\pi}{4} , \tag{2.45b}$$

$$2\pi f = -j\dot{l}(t_j^+) - 2\dot{\lambda}(t_j^+) , \tag{2.45c}$$

for the second term and

$$\mathcal{F}\left[G_s e^{isl}\right] \approx G_s \sqrt{\frac{2\pi}{|s\ddot{l}|}} e^{i\psi_s}\,, \tag{2.46a}$$

$$\psi_s = 2\pi f t_s^* - sl - \frac{\pi}{4}\,, \tag{2.46b}$$

$$2\pi f = s\dot{l}(t_s^*)\,, \tag{2.46c}$$

for the last term.

The stationary phase condition reveals which terms in the sum contribute to the Fourier transform. In the case of harmonics of $\dot{l}$, only positive s terms contribute as $\dot{l} > 0$. However, in Eqs.(2.44) and (2.45), the appearance of $(j\ddot{l} + 2\ddot{\lambda})$ in the denominator could lead to catastrophes (instances where the amplitude diverges at a subset of frequencies) in the event that this term vanishes. To determine which terms could possibly lead to these catastrophes, we re-express the term appearing in the denominator of the amplitudes as

$$j\ddot{l} + 2\ddot{\lambda} = \dot{n}\left(j + 2 + 2k + 2n\frac{\dot{k}}{\dot{n}}\right)\,. \tag{2.47}$$

We can rearrange the above to find the j for which there are catastrophes,

$$j = -2\left[1 + k(1 + \chi(e))\right] \tag{2.48}$$

where

$$\chi(e) = \frac{n}{\dot{n}}\frac{\dot{k}}{k} = -\frac{8\left(7e^4 + e^2 - 8\right)}{37e^4 + 292e^2 + 96}. \tag{2.49}$$

Are there catastrophes in the SPA? Figure 2.8 shows $\chi(e)$, which clearly varies from 2/3 at $e = 0$ to about 0.05 at $e = 0.9$. If we bound the 1PN pericenter precession quantity k to $0 < k < 1/2$, we see that it is possible to have a catastrophe in the $j = -3$ case when the binary is sufficiently close (i.e. when $k \sim 1/2$) and circular ($\chi(e) \sim 2/3$). However, since accuracy in the amplitude is less important than accuracy in the phase for GW data analysis, we proceed by keeping only the leading PN order corrections in $\ddot{l}$ and $\ddot{\lambda}$. At leading PN order, $\ddot{l} = \ddot{\lambda}$, and clearly, there are only catastrophes when $j = -2$. But this harmonic corresponds to a low-frequency contribution that has a negligible amplitude contribution, as we can see from the stationary phase condition and Figure 2.6. In fact, neglecting this harmonic altogether affects the matches shown in Fig. 2.3 negligibly, so henceforth we neglect the $j = -2$ harmonic, which ensures our model never hits catastrophes.

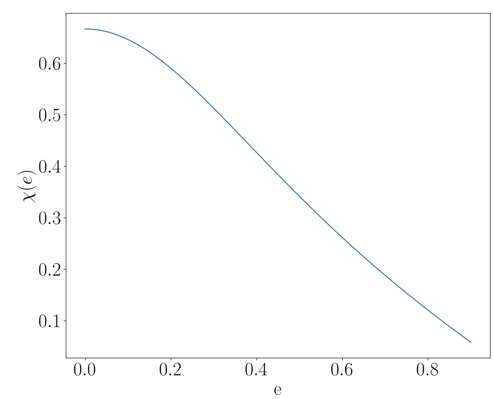

Figure 2.8: The value of $\chi(e)$ as a function of e.

But exactly which j indices contribute to the Fourier transform? Inspection of the stationary phase conditions (Eqs. (2.45c) and (2.44c)) does not clearly reveal the answer to this question. In order to find the j indices that do contribute, let us begin by rearranging the stationary phase conditions to set a condition on j for which f is positive:

$$j > -2(1 + k(t_j^-)), \tag{2.50a}$$

$$j < -2(1 + k(t_j^+)), \tag{2.50b}$$

where we have used $\dot{l} = n$ and $\dot{\lambda} = n(1+k)$. We see that as long as $k \leq 1/2$ then the stationary point corresponding to the "-" superscript is satisfied when $j > -2$ and that corresponding to the "+" superscript when $j < -3$.

Clearly then, in order to understand which indices j contribute to the Fourier transform, we must first determine which values of k are reasonable within the PN approximation. To do so, let us compare two constraints that we might impose on our waveforms:

(i) that the periastron velocity be small $v_p < 1/3$,

(ii) that the rate of periastron advance be slow $k < 1/2$.

Each of these constrains the final separation of the binary, but since our results are typically quoted in terms of initial dimensionless semi-latus rectum, p, it is natural to consider what lower limit on p each of the above constrains implies. Constraining the periastron velocity ($v_p < 1/3$) leads to $p > 9(1+e)^2$ [or equivalently $y < (3(1+e))^{-1}$], while constraining the advance of periastron ($k < 1/2$) leads to $p > 6$. Since the periastron velocity constraint is more stringent, henceforth we use it to stop our waveform evolution. Semi-latus recta below this number would incur into a regime were the PN approximation may be inaccurate [113].

Restricting $v_p < 1/3$ ensures that $k < 1/2$, and thus, we see that the stationary phase condition of Eq. (2.44c) is satisfied only when $j > 2$, while that of Eq. (2.45c) is satisfied when $j < -2$ (with the understanding that we have dropped the $j = -2$ harmonic). In practice, we have found that the stationary phase condition for the $j = -3$ harmonic can become double valued, instead of adding more complication by treating this harmonic with more care, we simply neglect it as we have verified that it does not affect the results of Fig. 2.3. Putting everything together then we have a frequency response in the SPA given by:

$$\tilde{h}(f) = \mathcal{A}\left[F_+ S^2 \sum_{s=1}^{\infty} G_s \sqrt{\frac{2\pi}{|s\ddot{l}|}} e^{i\psi_s} + Q \sum_{j=-1}^{\infty} N_j \sqrt{\frac{2\pi}{|j+2|\ddot{l}}} e^{i\psi_j^-} + Q^* \sum_{j=-\infty}^{-4} N_j \sqrt{\frac{2\pi}{|j+2|\ddot{l}}} e^{i\psi_j^+}\right] \tag{2.51}$$

where

$$\ddot{l} = \frac{\eta}{5m^2}(1-e^2)^2(96+292e^2+37e^4)y^{11}\,. \tag{2.52}$$

Following paper 1 and with this in hand, we now seek solutions to express the functions appearing in the phase (t, l, λ) in terms of the orbital eccentricity.

Let us begin by seeking a relation between the orbital frequency and the eccentricity. Since either of the two orbital frequencies (n or ω) can be expressed in terms of the PN parameter y, this amounts to seeking the mapping $y(e)$. Composing dy/de using the chain rule (i.e. $dy/de = \dot{y}/\dot{e}$) and expanding to 3PN order in y yields

$$\frac{dy}{de} = y\left[c_0(e) + \sum_{n=2}^{6} c_n(e) y^n\right]\,, \tag{2.53}$$

whose PN solution is

$$y(e) = y_0\left[d_0(e) + \sum_{n=2}^{6} d_n(e) y_0^n\right]\,, \tag{2.54}$$

for certain functions $d_n(e)$. Inserting Eq. (2.54) into Eq. (2.53) and expanding to 3PN order (now an expansion in the parameter y_0) gives a set of coupled ordinary differential equations for the $d_n(e)$ functions, namely

$$d_0'(e) = c_0 d_0 \,, \tag{2.55a}$$

$$d_2'(e) = c_0 d_2 + c_2 d_0^3 \,, \tag{2.55b}$$

$$d_3'(e) = c_0 d_3 + c_3 d_0^4 \,, \tag{2.55c}$$

$$d_4'(e) = c_0 d_4 + c_4 d_0^5 + 3c_2 d_0^2 d_2 \,, \tag{2.55d}$$

$$d_5'(e) = c_0 d_5 + c_5 d_0^6 + 3c_2 d_0^2 d_3 + 4c_3 d_0^3 d_2 \,, \tag{2.55e}$$

$$d_6'(e) = c_0 d_6 + c_6 d_0^7 + 3c_2 (d_0^2 d_4 + d_0 d_2^2) + 4c_3 d_0^2 d_4 + 5c_4 d_0^4 d_2 \,, \tag{2.55f}$$

$$d_{6l}'(e) = c_0 d_{6l} + c_{6l} d_0^7 \,, \tag{2.55g}$$

where we have split the 3PN contribution into a component that is proportional to the natural logarithm of y_0 and one that is not proportional to it, such that the 3PN part of the solution to $y(e)$ takes the form $(d_6 + d_{6l} \ln y_0) y_0^6$.

Given that

$$c_0 = \frac{12}{304} \frac{8 + 7e^2}{e(1 + \frac{121}{304} e^2)} \,, \tag{2.56}$$

we see that solving any of Eqs. (2.55) amounts to solving a differential equation of the form

$$\frac{df}{de} = \frac{12}{304} \frac{8 + 7e^2}{e(1 + \frac{121}{304} e^2)} f(e) + g(e) \,, \tag{2.57}$$

for some functions $g(e)$. The above differential equation has the solution

$$f(e) = \frac{1}{e^{6/19}(1 + \frac{121}{304} e^2)^{435/2299}} \left(C + \int g(e) e^{6/19} (1 + \frac{121}{304} e^2)^{435/2299} de \right) \,, \tag{2.58}$$

for some constant C. The constants arising from solving for any of the coefficients d_n are determined by requiring that at each PN order $y(e_0) = y_0$. Clearly, in solving for

d_0, $g(e) = 0$ and the solution is simply

$$d_0(e) = \frac{e_0^{6/19}(1 + \frac{121}{304}e_0^2)^{435/2299}}{e^{6/19}(1 + \frac{121}{304}e^2)^{435/2299}}\,. \tag{2.59}$$

The solutions for the higher PN coefficients d_n are not so simple as the form that $g(e)$ takes becomes a more complicated function of eccentricity. In order to solve the equations, we then expand Eq. (2.58) in eccentricity, which allows us to integrate the series analytically.

With the solution of $y(e)$ in hand, we are now in a position to solve for the phase functions $t(e), \lambda(e)$, and $l(e)$. We begin by substituting the solution above for $y(e)$ into the integrands for each of the phase functions

$$t(e) - t_c = \int^e \frac{de'}{\dot{e}[y(e'), e']}\,, \tag{2.60}$$

$$l(e) - l_c = \int^e \frac{n[y(e'), e']}{\dot{e}[y(e'), e']} de'\,, \tag{2.61}$$

$$\lambda(e) - \lambda_c = \int^e \frac{\omega[y(e'), e']}{\dot{e}[y(e'), e']} de'\,. \tag{2.62}$$

In order to carry out the integration above we expand the integrand to 3PN in y_0. We then expand the coefficients at each order in y_0 to a given order in e. Note that there is no restriction on the order to which we expand any PN coefficient (coefficients of y_0 in each of the integrands) in eccentricity other than the order to which we have obtained $y(e)$. We could, for example, keep $\mathcal{O}(e^{100})$ terms in each coefficient, but with the inclusion of so many terms the model would become very computationally inefficient to evaluate. On the other hand, if we keep too few eccentric corrections, the model becomes inaccurate. In Section 2.5.1 we introduce a scheme to pick the order in eccentricity to which we keep the expansions of each y_0 coefficient, and then show in Section 2.5.2 how the eccentricity expansion affects the validity of the waveform for systems with different initial eccentricities.

After carrying out the integration, we have the phase functions in terms of the orbital eccentricity,

$$\lambda(e) = \frac{1}{y_0^5\eta}[\lambda^{(0)}(e) + y_0^2\lambda^{(1)}(e,\eta) + y_0^3\lambda^{(1.5)}(e,\eta) + y_0^4\lambda^{(2)}(e,\eta) + y_0^5\lambda^{(2.5)}(e,\eta) + y_0^6\lambda^{(3)}(e,\eta,\ln y_0)]\,, \tag{2.63a}$$

$$l(e) = \frac{1}{y_0^5\eta}[l^{(0)}(e) + y_0^2 l^{(1)}(e,\eta) + y_0^3 l^{(1.5)}(e,\eta) + y_0^4 l^{(2)}(e,\eta) + y_0^5 l^{(2.5)}(e,\eta) + y_0^6 l^{(3)}(e,\eta,\ln y_0)]\,, \tag{2.63b}$$

$$t(e) = \frac{m}{y_0^8\eta}[t^{(0)}(e) + y_0^2 t^{(1)}(e,\eta) + y_0^3 t^{(1.5)}(e,\eta) + y_0^4 t^{(2)}(e,\eta) + y_0^5 t^{(2.5)}(e,\eta) + y_0^6 t^{(3)}(e,\eta,\ln y_0)]\,, \tag{2.63c}$$

where the functions $t^{(n)}, l^{(n)}$ and $\lambda^{(n)}$ are series in eccentricity (and also depend on the constants of integration appearing in $y(e)$), which are provided in the supplemental material. With these solutions in hand, the phases in Eq. (3.1) are functions of only the orbital eccentricity. The final step then is to numerically invert the appropriate stationary phase condition to relate the Fourier frequency to the orbital eccentricity. The specifics of the evaluation of TaylorF2e are described in Sec. 2.5.1. Section 2.5.2 shows that this waveform model is as faithful to TaylorT4t as the TaylorT4e model is, giving good agreement for even moderate eccentricities.

2.4.3 Alternative Frequency Domain Models

In Section 2.3.4 we laid out different possible time domain models based on the independent variable appearing in the set of ODEs that one solves numerically to specify the orbital dynamics of the system. In the frequency domain model derived in the previous section, we solved the set of ODEs with the eccentricity e as the independent variable, and thus, the Fourier domain TaylorF2e model corresponds to the SPA version of the TaylorT4e time domain approximant. In this section, we wish to explore schematically how one would go about obtaining other frequency domain approximants related to the other two time domain approximants TaylorT4t and TaylorT4y.

TaylorF2y would be obtained by first solving the set of ODEs (dl/dy, $d\lambda/dy$, dt/dy, de/dy) analytically within the PN approximation (and possibly in a low-eccentricity expansion). With this at hand, one would then invert $y(e)$ as given in Eq. (2.54) to obtain $e(y)$, which would be a series in both y and y_0. This solution would then be plugged into the integrands that define the phase functions and integrated to give $l(y)$, $\lambda(y)$, and $t(y)$. The different stationary phase conditions could be numerically inverted to relate y to the Fourier frequency f; one could attempt to invert the stationary phase condition perturbatively as well, but the error incurred would have to be investigated with the waveform in hand. We expect, however, that the resulting TaylorF2y approximant would have only limited validity in e, because even at Newtonian order the inversion of $y(e)$ is transcendental and very poorly behaved even for eccentricities as low as 0.3 (see Appendix C of paper 1 where we investigated this inversion at length at Newtonian order).

TaylorF2t would be obtained by first solving the set of ODEs $(\dot{l}, \dot{\lambda}, \dot{e}, \dot{y})$ analytically within the PN approximation (and possibly in a low-eccentricity expansion) to find both $e(t)$ and $y(t)$. With this at hand, one would express the integrals for l and λ in terms of only the t variable, but to obtain both, one would first have to invert the solutions found in TaylorF2e and TaylorF2y to obtain $t(y)$ and $t(e)$, or else come up with some scheme to solve $\dot{e}$ and $\dot{y}$ analytically. Upon substitution of these solutions into $\dot{l}$ and $\dot{\lambda}$, one would integrate to obtain $l(t)$ and $\lambda(t)$ analytically. Again, the stationary phase condition would be numerically solved to find $t(f)$ for any given

j or s harmonic index, or alternatively one could try to perturbatively invert the stationary phase condition, but this could incur too much error and would have to be investigated with the approximant in hand.

2.5 Implementation and Validation

In this section we validate the TaylorF2e model introduced in in Sec. 2.4 against the TaylorT4e model. To quantify the agreement between two models h_1 and h_2 it is customary to introduce the match

$$M = \max_{t_c, l_c, \lambda_c} \mathcal{O}(h_1, h_2)\,, \tag{2.64}$$

which is nothing but the overlap between two waveforms maximized over the extrinsic parameters t_c, l_c, and λ_c. Note that this differs from the match in the quasicircular case, which is only maximized over ϕ_c and t_c, because in the eccentric case there is an extra phase angle associated with pericenter precession. We employ the implicit maximization scheme developed in Section 3 of Paper 1 in order to maximize over these parameters.

2.5.1 Implementation

Let us begin by clearly describing how theTaylorF2e model is generated and implemented. As explained in Sec. 2.4, the TaylorF2e model can be deployed in slightly different ways, which in essence depend on the following choices:

(i) The order of the eccentricity expansion of each of the coefficients appearing in the phase functions of Eqs. (2.63).

(ii) The technique by which we invert the stationary phase condition to relate the orbital eccentricity to the Fourier frequency.

(iii) The method of obtaining the eccentricity dependence on the orbital frequency.

Let us begin by addressing item (i). The expansion of the phase functions in small eccentricity introduces an error in our waveform model, and thus, we wish to determine the optimal expansion order such that the resulting waveform is accurate enough to lead to sufficiently high matches against a TaylorT4e model. Let us then begin by introducing the following notation for our ODEs $(dl/de, d\lambda/de, dt/de)$ that lead to Eqs. (2.63):

$$\frac{d\lambda}{de} = \frac{1}{y_0^5}\left[\lambda'_0(e) + \lambda'_2(e)y_0^2 + ...\lambda'_6(e)y_0^6\right] , \tag{2.65a}$$
$$\frac{dl}{de} = \frac{1}{y_0^5}\left[l'_0(e) + l'_2(e)y_0^2 + ...l'_6(e)y_0^6\right] , \tag{2.65b}$$
$$\frac{dt}{de} = \frac{M}{y_0^8}\left[t'_0(e) + t'_2(e)y_0^2 + ...t'_6(e)y_0^6\right] . \tag{2.65c}$$

In each of the PN coefficients appearing above $[\lambda'_i(e), l'_i(e), t'_i(e)]$, we have substituted in our solution for $y(e)$, which is valid to order $\mathcal{O}(e^{40})$ past leading, but we have not yet expanded these coefficients in eccentricity. We now wish to determine the order in eccentricity to which we should expand each of these coefficients.

Let us then introduce the following measure of error in each of the PN coefficients

$$\gamma_n^\lambda(e) = \text{Abs}\left(1 - \frac{\lambda'_n(e)}{\bar{\lambda}'_n(e)}\right) , \tag{2.66a}$$
$$\gamma_n^l(e) = \text{Abs}\left(1 - \frac{l'_n(e)}{\bar{l}'_n(e)}\right) , \tag{2.66b}$$
$$\gamma_n^t(e) = \text{Abs}\left(1 - \frac{t'_n(e)}{\bar{t}'_n(e)}\right) , \tag{2.66c}$$

where the overhead bar stands for the Taylor expansion in small eccentricity to a given order. This is analogous to the Newtonian-order measure of error introduced in paper I

$$\epsilon = 1 - \frac{\psi_{\rm exact}}{\psi_{\rm err}}\,, \tag{2.67}$$

where $\psi_{\rm exact}$ was our exact (in eccentricity) phase and $\psi_{\rm err}$ had a fixed amount of error introduced through ϵ via the above equation. We found that for moderately eccentric systems, the match began to drop for values of $\epsilon \sim 10^{-5}$, as shown in Table III of paper I.

Returning to our measures of error in Eq. (2.66), we must now choose a tolerance for $\gamma_n^{\lambda,l,t}$ that is acceptable for our model, i.e. that leads to a sufficiently small loss of match. Guided by the error investigation of paper 1, one may be tempted to set a uniform tolerance of 10^{-5}. One may expect, however, that more error could be tolerated in the coefficients appearing at higher PN order, since they are multiplied by the small parameter y_0. Thus, at each PN order we impose a maximum error tolerance $\gamma_n^{\lambda,l,t}(e) \leq \epsilon_n$, where

$$\epsilon_n = \epsilon\,(y_0)^{-n}\,, \tag{2.68}$$

for some constant ϵ. The factor of (y_0) allows for more error to be accumulated by coefficients at higher PN order, since their contribution to the phase is scaled by the small parameter y_0.

The tolerance condition described above clearly depends on y_0 (or p_0), η, e_0, and the constant ϵ. We have investigated two different constraints, one in which we set $\epsilon = 10^{-5.5}$, $\eta = 0.25$, $p_0 = 12$, and $e_0 = 0.7$, and one in which we set $\epsilon = 10^{-5}$, $\eta = 0.25$, $p_0 = 18$, and $e_0 = 0.4$. The first set of conditions forces us to keep more terms in eccentricity than the second set, which we may then consider a conservative choice. With these choices, we then generate two waveforms, one with more terms kept in eccentricity (TaylorF2e+) and with less terms kept (TaylorF2e-), and then we investigate the effects in the match. Figure 2.9 shows $\gamma_n^{\lambda,l,t}$ as a function

n	$\lambda'_n(e)$	$t'_n(e)$
0	10 (4)	36 (12)
2	240/19 (8)	620/19 (202/19)
3	208/19 (4)	512/19 (170/19)
4	278/19 (126/19)	26 (164/19)
5	246/19 (132/19)	468/19 (182/19)
6	14 (94/19)	328/19 (100/19)

Table 2.1: Eccentricity order to which each of the coefficients in Eq. (2.65) is expanded past leading order for the TaylorF2e+ model and the TaylorF2e- model in parenthesis. We keep the same number of terms in $l'_n(e)$ as in $\lambda'_n(e)$

of eccentricity for the conservative choice. We see that $\gamma_n^{\lambda,l,t}$ is at least nearly bounded by the threshold imposed by Eq. (2.68) (the spikes correspond to zero-crossings on a logarithmic scale). In Table 2.1 we list the maximum order past leading to which each of our coefficients are expanded in eccentricity for TaylorF2e+ and TaylorF2e-. Note that while many terms have been kept in each of the phase functions, one can collect the resulting expression in like powers of eccentricity. For example, after such a collection, there are only 26 terms in eccentricity to be evaluated for $\lambda(e)$ in the TaylorF2e- case.

To address item (ii), let us first recall the different stationary point inversions that we must achieve to relate f to e. The equations that must be inverted are

$$2\pi f = j\dot{l} \pm 2\dot{\lambda} = jn \pm 2\omega \tag{2.69a}$$

$$2\pi f = s\dot{l} = sn(e) \tag{2.69b}$$

where the sign in the first equation depends on the index j as detailed in Sec. 2.4.

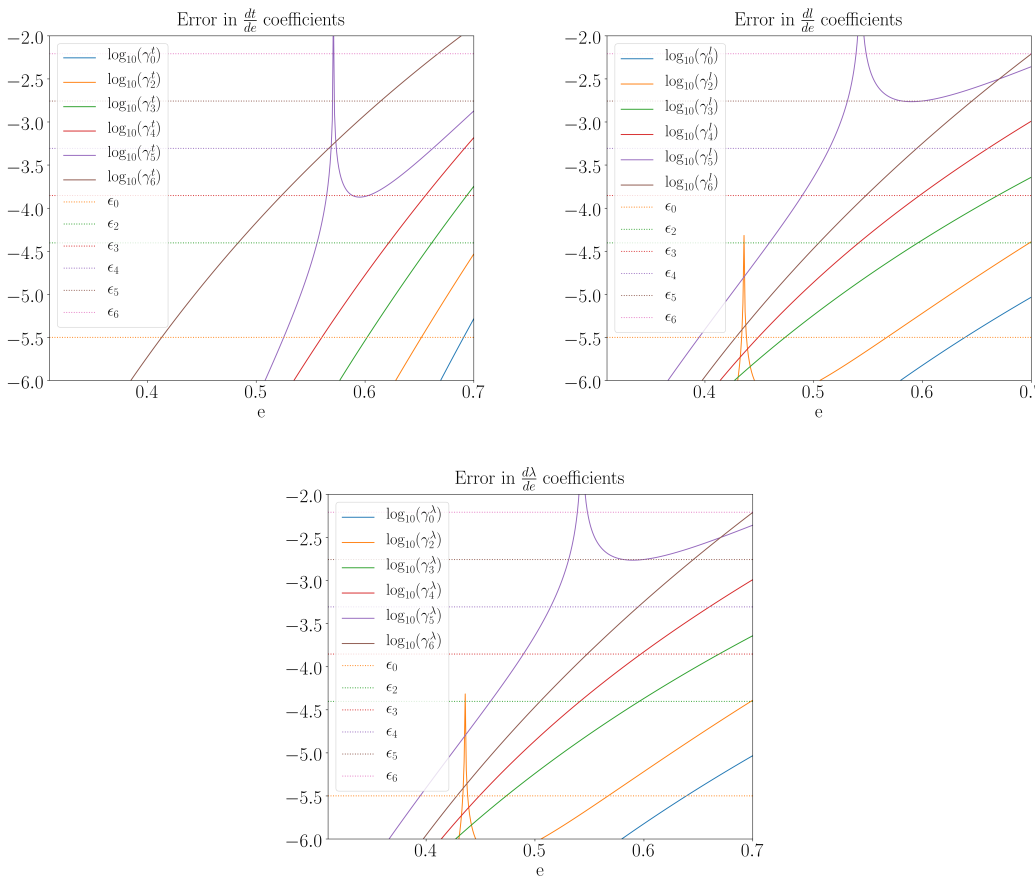

Figure 2.9: Error in the coefficients appearing in Eq. (2.65) given by Eq. (2.66). The horizontal dashed lines are the rough error tolerances that we impose on the coefficients to select the different orders of eccentricity expansion that occur in the phase functions.

The second equation is particularly simple to solve since it only requires the inversion of $n(e)$. That is, defining the inverse function κ such that $\kappa[n(e)] = e$, one can relate f to e for the s indices via

$$e_b(f) = \kappa\left[\frac{2\pi f}{s}\right]. \tag{2.70}$$

Of course, the inverse function κ must be obtained numerically, but this formulation has the advantage that once κ is obtained, it can be used for any index s. The inversion of the equation for the j harmonics is more complicated. First, let us rewrite the stationary condition as

$$2\pi f = jn \pm 2(1+k)n = \pm(j+2)n \pm kn\,. \tag{2.71}$$

We then employ the secant method [107] to numerically solve Eq. (2.71), where we recognize that the term kn is of higher PN order than $\pm(j+2)n$ and we leverage this to specify the approximate initial guess $e_j(f)^{\rm guess} = \kappa[2\pi f/\pm(j+2)]$. Indeed, this initial guess makes the secant method typically converge after 4 iterations to an accuracy of 10^{-8}. We expect that this error tolerance could be relaxed.

Let us conclude this subsection by discussing item (iii), which in any case is required to invert the stationary phase conditions, as it needs a solution for $y(e)$. We obtain this solution by solving $\dot{y}$ and $\dot{e}$ and interpolating these solutions to compose $n(e)$ and $\omega(e)$. Given that we have obtained $y(e)$ numerically, this is then in turn used in the various harmonic amplitudes, which enter the SPA (in $\mathcal{A}$, N_j, and $\ddot{l}$). While somewhat computationally costly, we estimate that there are considerable speedups to be gained through numerical techniques and careful truncation of the sum appearing in Eq. (3.1). We leave a thorough investigation of computational cost to future work. Alternatively we could use the solution found in Eq. (2.54), which is purely analytical. However, in the interest of being consistent with paper 1, we chose here to solve $\dot{y}$

and $\dot{e}$ numerically instead.

2.5.2 Validation

In this subsection we validate the TaylorF2e model by computing the match between it and the TaylorT4t model, which was introduced in Sec. 2.3. Figure 2.10 shows the match for a $(10, 10)M_\odot$, $(10, 1.4)M_\odot$, and a $(1.4, 1.4)M_\odot$ binary, with TaylorF2e+ on the left and TaylorF2e- on the right. In these match calculations there are three main sources of loss in match:

(i) the truncation of the summations in Eq. (3.1) (explored in Fig. 2.3),

(ii) the PN disagreement between models obtained through solving different PN valid sets of ODEs (explored in Fig. 2.7), and

(iii) the truncation of the eccentricity expansions in the phase functions.

Let us discuss each of these potential sources of error in turn.

In order to address item (i), let us return to Fig. 2.3, which shows the overlap between two numerically calculated time-domain models (both TaylorT4t) with one model kept to all harmonics and the other restricted to $j = [-15, 15]$ and $s = [1, 15]$. Comparison of that figure to Fig. 2.10 reveals that spectral truncation is not the main source of loss in match between TaylorT4t and TaylorF2e. The loss in match due to spectral truncation (as shown in Fig. 2.3) occurs for much greater initial eccentricities and smaller initial semi-latus recta than the loss in match that is seen between TaylorF2e and TaylorT4t (as shown in Fig. 2.10).

When we compute the match between TaylorF2e+ and TaylorT4t we nearly exactly recover the results of taking the match between TaylorT4t and TaylorT4e. This is not a surprising result as TaylorF2e is built by solving the ODEs formulated with e as the independent variable, as is done in TaylorT4e. This suggests that, at least when keeping many terms in eccentricity, the dominant source of loss in match is due to the PN differences between the ODEs governing the orbital dynamics, when re-expressing them in terms of a different independent variable. This result suggests that a more faithful model would require PN ODEs at higher PN order for the orbital dynamics.

Let us now return to item (iii). When comparing the left and right panels of Fig. 2.10, we see that for the $(10, 10)M_{\odot}$ and $(1.4, 10)M_{\odot}$ systems, there is nearly no change in the match whether we use TaylorF2e+ or TaylorF2e-. However, in the $(1.4, 1.4)M_{\odot}$ case, there is significant loss in match as the initial eccentricity exceeds 0.5. This suggests that for less massive systems, it is important to keep more terms in the eccentricity expansions. This conclusion is also supported by Fig. 2.11, which shows again the match between TaylorF2e+/- (left/right) and TaylorT4t but this time for a $(5, 5)M_{\odot}$ system. In this case, the loss in match due to truncation of the eccentricity expansions becomes considerable for close initial separations and initial eccentricities around 0.6.

The matches appearing in Fig. 2.10 misleadingly suggest that the model is unfaithful for a significant amount of the parameter space, but this is only an artifact of the particular parameter space region we chose to calculate the match over. For initial semi-latus recta that are larger than those considered here, the model is very faithful with matches larger than 0.98. Let us then study if eccentric corrections to the model matter at larger initial separations than those considered in Fig. 2.10. In order to roughly determine which combinations of mass, initial eccentricity, and initial semi-latus recta lead to significant eccentric corrections, we employ a signal-to-noise ratio (SNR) measure, defined by

$$\mathrm{SNR}^2 = (h_1|h_1)\,. \tag{2.72}$$

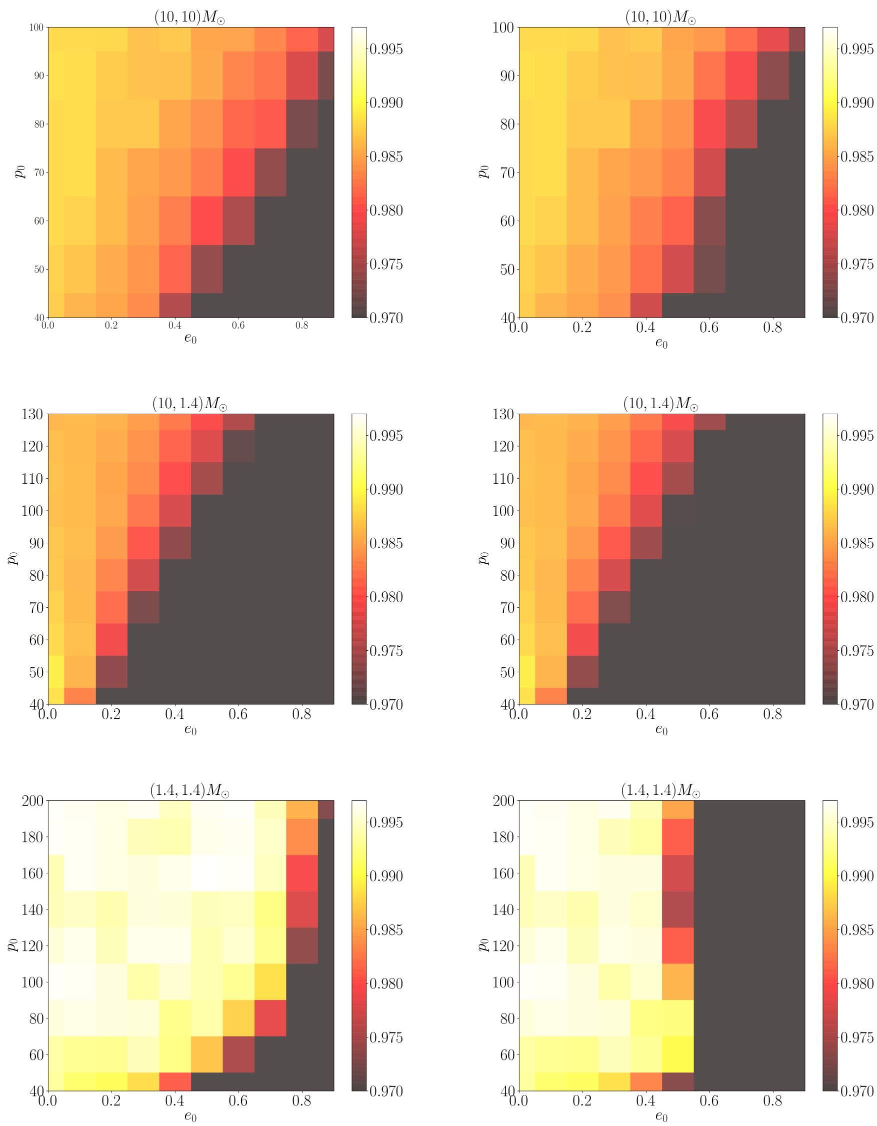

Figure 2.10: Match between TaylorF2e+ (left) or TaylorF2e- (right) against TaylorT4t for a $(10, 10)M_\odot$ (top), $(10, 1.4)M_\odot$ (middle), and a $(1.4, 1.4)M_\odot$ (bottom) binary. Note that we do not plot values below 0.97, as the value of the match drops considerable below this value in the close and highly eccentric cases.

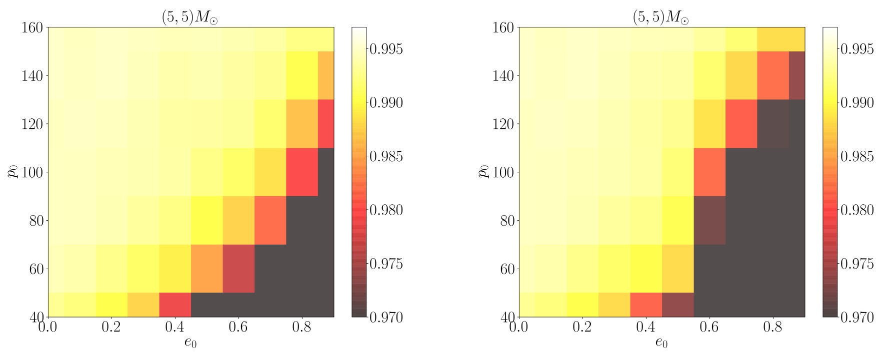

Figure 2.11: Match for a $(5,5)M\odot$ system, with more terms kept in eccentricity (left), and less terms kept (right). The loss in match due to the truncation of the eccentricity expansions appearing in the phase functions suggests that more terms must be kept for less massive systems.

Figure 2.12 shows the SNR normalized by the largest SNR present in the parameter space explored for the three systems considered in Fig. 2.10. We see that particularly in the less massive case there is significant SNR for systems with larger initial semi-latus recta than those considered in Fig. 2.10. This suggests that our TaylorF2e model is useful for systems in a larger parameter space than considered in Fig. 2.10. To be clear, we are not suggesting that the SNR is a measure of validity, instead we are illustrating that eccentric effects are significant (via a noticeably different SNR) at higher initial separations than explored in Fig. 2.10. By inspecting Fig. 2.10 we see that the model performs well at such large initial separations. We leave a more thorough investigation of the region of parameter space in initial eccentricity and semi-latus recta where eccentric effects matter to future work.

2.5.3 Error Analysis in Different Components of TaylorF2e

In this section we wish to investigate which of the major analytic components which enter the TaylorF2e contribute to the most error in match. Namely we wish to know which of the functions which appear in the phase ($\lambda(e)$, $l(e)$, and $t(e)$) give

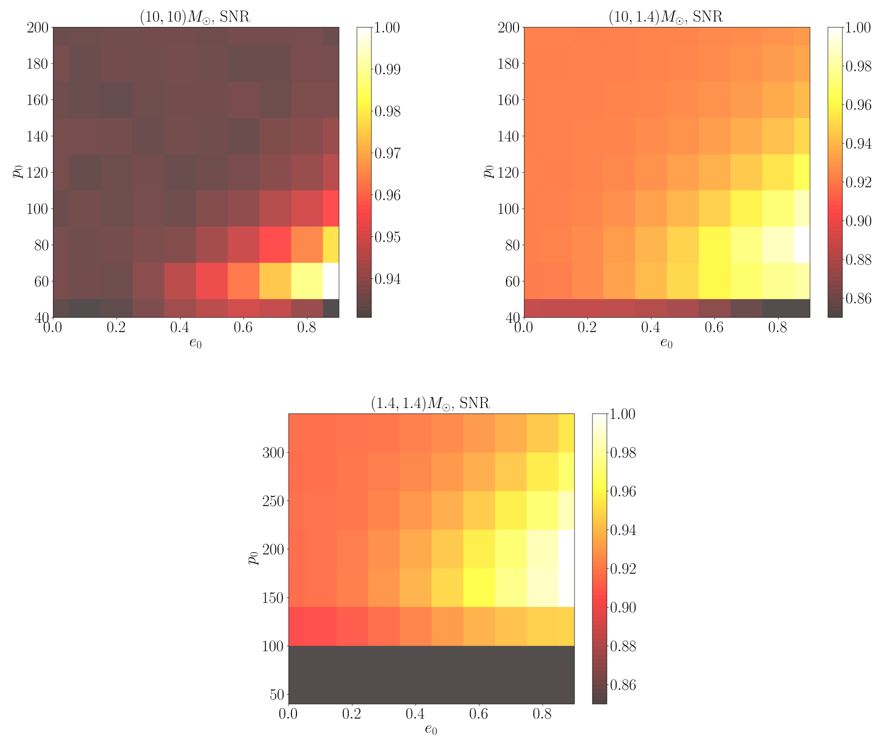

Figure 2.12: The SNR (normalized by the largest SNR present) as a function of mass and initial orbital eccentricity and semi-latus rectum. In the less massive case there is still significant SNR even for initial semi-latus recta greater than 300, a region where our model works well.

the most loss in match, so that if one wished to improve the model they would have some guidance as to where to start. In order to do so we obtain numerical solutions for the phase functions by numerically solving $\dot{\lambda}$, $\dot{l}$, $\dot{y}$, and $\dot{e}$. With these solutions in hand we invert $e(t)$ to obtain $t(e)$ and use this to map λ and l to the eccentricity domain which allows them to be used in our TaylorF2e model.

In Figure 2.13 we show the value of the match for a $(10, 10)M_{\odot}$ system where we have kept the phase functions all numerical, or just one of any of them numerical. We see, as expected, when all of the phase functions are numerical we recover the result of Figure 2.3. The error in match is due to the truncation of harmonics in Eq.(3.1). The best increase in match (besides keeping all phase functions numerical) occurs when $l(e)$ is computed numerically. Interestingly, the match when $\lambda(e)$ is kept numerical is slightly worse than had the analytic expression for $\lambda(e)$ been used. This is because there is cancellation in error between the analytic expression for $t(e)$ and $\lambda(e)$.

2.6 Conclusions & Future Work

We have extended the eccentric Fourier-domain Newtonian model of paper 1 to 3PN order. This model combines a harmonic decomposition of the time domain signal, the stationary phase approximation, and PN theory. We have thoroughly validated the model and shown that it is faithful to very high initial orbital eccentricities ($e_0 \sim 0.7$), but of course this depends on the particular system and the initial separation at which the initial eccentricity is defined. We expect that the model is valid to even higher eccentricities in relevant regions of (e_0, p_0) parameter space.

In addition to this main result, we have validated the harmonic decomposition of the eccentric time-domain signal in terms of a sum of harmonics of the two orbital frequencies with amplitudes that are expanded in small eccentricity. We also

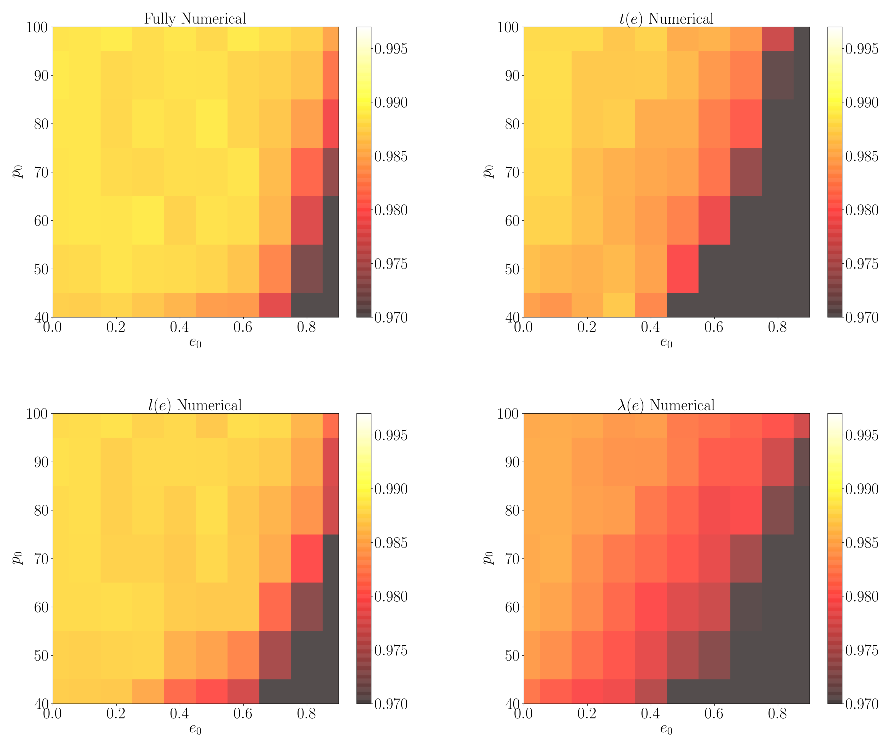

Figure 2.13: The match between TaylorF2e and TaylorT4t where we have kept all phase functions ($\lambda(e)$, $l(e)$, and $t(e)$) numerical (top left), just $t(e)$ numerical (top right), just $l(e)$ numerical (bottom left), and just $\lambda(e)$ numerical (bottom right). The largest improvement (besides using all numerical phase functions) in match occurs when $l(e)$ is kept numerical.

investigated the importance of higher PN corrections in the overall amplitude of the time domain model, and we investigated the agreement of different PN consistent time domain approximants. We found that the harmonic decomposition presented here is valid for very large initial eccentricities ($e_0 \sim 0.9$), and that in the equal mass case the effects of higher PN corrections in the amplitude are negligible. Interestingly, we found that different PN consistent ways of solving for the orbital dynamics lead to time-domain approximants that disagree at moderate initial eccentricities and relatively close initial separation – an effect which is enhanced in the unequal mass limit. However, we expect that this result only excludes faithful modeling in a small region of the relevant parameter space.

A useful extension of this model would be the inclusion of compact object spin. Such an extension could be achieved using the framework provided in [29] which incorporates spin into a low eccentricity waveform model. Since spin effects couple to the orbital eccentricity, it is possible that neglecting spin can incur considerable error in waveform faithfulness and thus error in parameter estimation (perhaps more than in the circular case), and with such a waveform in hand one could quantify that error.

Given our model's 3PN accuracy, we believe it is sufficient for preliminary data analysis applications. However, first we must address the efficiency of the model. In this work we sought to validate the model, but we did not implement it in the fastest possible way. We expect that through a careful evaluation of the Fourier phase, the inversion of the stationary phase condition, and neglecting certain low SNR harmonics, the model can retain its accuracy and become very efficient.

With such an efficient and 3PN accurate eccentric model we could seek to answer some important questions about eccentric inspirals using Bayesian techniques. We plan to investigate the region of (M, η, p_0, e_0) parameter space where eccentric corrections to the signal are important (i.e. where in this parameter space we could differentiate between a quasi-circular signal and an eccentric one). We also plan to investigate the ability to measure parameters and any biases of the model.

We also expect that, using our model, we can constrain certain modified theories of gravity. If such a modified theory of gravity modifies the eccentricity evolution of a binary, these corrections could be incorporated into the model presented here. With these corrections due to a modified theory present in the model, we could investigate the ability of detectors to constrain these corrections and test General relativity perhaps more stringently than possible with a quasi-circular model.

Lastly, in order to fully model an eccentric signal we require the incorporation of effects due to the merger and the ringdown. The model presented here could be used to create an inspiral-merger-ringdown (IMR) type hybrid model. The only IMR model which incorporates orbital eccentricity is that of [90]. It will be useful to have several IMR type models with which to extract signals in the future for validation purposes, as is the case for quasi-circular coalescences. In addition to modeling the merger and ringdown, it is possible to extend the GW amplitudes to contain tail contributions and memory effects at 3PN using the results of [114] and [115].

Acknowledgments

B. M. was supported by the Joan L. Dalton Memorial Fellowship in Astronomy from Montclair State University. B. M. and N. Y. also acknowledge support from NSF Grant No. PHY-1759615, as well as NASA grants NNX16AB98G and 80NSSC17M0041. We thank Antoine Klein for useful conversations and providing us with the expressions for the tail terms. We also thank Travis Robson and Alejandro Cárdenas-Avendaño for useful conversations. Computational efforts were performed on the Hyalite High Performance Computing system, which is supported by University

Information Technology at Montana State University.

2.A 2PN Polarizations in Modified Harmonic Gauge

Here we provide the necessary corrections in order to obtain Eq.(2.10) using the expressions in [106]. In the latter reference, the authors list the amplitude corrections as

$$h_{+,\times} = \frac{m\eta}{R}\xi^{2/3}\left(\bar{H}^{(0)}_{+,\times} + \xi^{1/3}\bar{H}^{(1/2)}_{+,\times} + \xi^{2/3}\bar{H}^{(1)}_{+,\times} + \xi\bar{H}^{(3/2)}_{+,\times} + \xi^{4/3}\bar{H}^{(2),\mathrm{ADM}}_{+,\times}\right) \tag{2.73}$$

where $\xi = mn$ and we have introduced an overbar to differentiate these amplitudes from those listed in Eq.(2.10). Because gauge differences arise at 2PN order, only the 2PN amplitude contains differences due to gauge. First, we must re-express the above in terms of y. At 2PN order, y and ξ are related by

$$\xi = y^3(1-e^2)^{3/2}\left\{1 - 3y^2 + \frac{1}{4}y^4\left[-18 + 28\eta + e^2(-51+26\eta)\right]\right\} \tag{2.74}$$

Inserting the above into the expressions for $h_{+,\times}$ in Eq. (2.73), expanding to 2PN order in y, and collecting like terms in y such that it takes the form

$$h_{+,\times} = \frac{m\eta}{R}y^2(1-e^2)\left(H^{(0)}_{+,\times} + yH^{(1/2)}_{+,\times} + y^2H^{(1)}_{+,\times} + y^3H^{(3/2)}_{+,\times} + y^4H^{(2),\mathrm{ADM}}_{+,\times}\right) \tag{2.75}$$

gives the unbarred amplitudes as a function of the barred ones

$$H^{(0)}_{+,\times} = \bar{H}^{(0)}_{+,\times} \tag{2.76a}$$

$$H^{(1/2)}_{+,\times} = (1-e^2)^{1/2}\bar{H}^{(1/2)}_{+,\times} \tag{2.76b}$$

$$H^{(1)}_{+,\times} = (1-e^2)\bar{H}^{(1)}_{+,\times} - 2\bar{H}^{(0)}_{+,\times} \tag{2.76c}$$

$$H^{(3/2)}_{+,\times} = (1-e^2)^{3/2}\bar{H}^{(3/2)}_{+,\times} - 3(1-e^2)^{1/2}\bar{H}^{(1/2)}_{+,\times} \tag{2.76d}$$

$$H^{(2),\text{ADM}}_{+,\times} = (1-e)^4\bar{H}^{(2),\text{ADM}}_{+,\times} - 4(1-e^2)\bar{H}^{(1)}_{+,\times} + \frac{1}{6}\left[-24+28\eta+e^2(-51+26\eta)\right]\bar{H}^{(0)}_{+,\times} \tag{2.76e}$$

In order to express these results in MH gauge we must substitute Eq.(2.8) into the expression for $\bar{H}^{(0)}_{+,\times}$. This will produce 2PN corrections that when added to $\bar{H}^{(2),\text{ADM}}_{+,\times}$ yields $\bar{H}^{(2),\text{MH}}_{+,\times}$. We have then

$$\bar{H}^{(2),\text{MH}}_{+} = \bar{H}^{(2),\text{ADM}}_{+} + \Lambda_{+} \tag{2.77a}$$

$$\bar{H}^{(2),\text{MH}}_{\times} = \bar{H}^{(2),\text{ADM}}_{\times} + \Lambda_{\times} \tag{2.77b}$$

where the $\Lambda_{+,\times}$ are given by

$$\Lambda_{+} = \frac{1+17\eta}{4(e\cos u-1)^3}e\Big[-(1+C^2)(3\cos u-4e+\cos^2 u)\cos(2\bar{\lambda}+2W) - S^2\cos u(1-e\cos u)$$
$$-2\sin u(1+C^2)\frac{(1+e\cos u-2e^2)}{\sqrt{1-e^2}}\sin(2\bar{\lambda}+2W)\Big] \tag{2.78a}$$

$$\Lambda_{\times} = C\frac{1+17\eta}{4(e\cos u-1)^3}e\Big[\frac{\sin u}{\sqrt{1-e^2}}(1+e\cos u-2e^2)\cos(2\bar{\lambda}+2W)$$
$$-(3\cos u-4e+e\cos^2 u)\sin(2\bar{\lambda}+2W)\Big] \tag{2.78b}$$

We these expressions, we now have all that we need to express the polarization in MH gauge and in terms of the parameter y.

CHAPTER THREE

DATA ANALYSIS IMPLICATIONS OF MODERATELY ECCENTRIC GRAVITATIONAL WAVES

Contributions of Authors and Co-Authors

Manuscript in Chapter 3

Author: Blake Moore

Contributions: Wrote and ran code which produced data analysis deliverables. Analyzed results.

Author: Dr. Nicolas Yunes

Contributions: Conceived of design study and advised the project. Edited the manuscript.

Manuscript Information Page

Blake Moore, Nicolas Yunes

Classical and Quantum Gravity

Status of Manuscript:
____ Prepared for submission to a peer-reviewed journal
____ Officially submitted to a peer-reviewed journal
_X_ Accepted by a peer-reviewed journal
____ Published in a peer-reviewed journal

IOP Publishing
Accepted February 24th, 2020

Abstract

While the expectation is that the majority of gravitational wave events observable by ground-based detectors will be emitted by compact binaries in quasi-circular orbits, the growing number of detections suggests the possibility of detecting waves from binaries with non-negligible orbital eccentricity in the near future. Several gravitational wave models incorporate the effects of small orbital eccentricities ($e \lesssim 0.2$), but these models may not be sufficient to analyze waves from systems with moderate eccentricity. We recently developed an inspiral only gravitational wave model that faithfully accounts for eccentric corrections in the moderate eccentricity regime ($e \lesssim 0.8$ for certain source masses) at 3rd post-Newtonian order. Here we consider the data analysis implications of this particular waveform model by producing and analyzing posteriors via Markov Chain Monte Carlo methods. We find that the accuracy to which eccentricity and source masses can be measured can increase by 2 orders of magnitude with increasing eccentricity of the signal. We also find that signals with low eccentricity can be confidently identified as eccentric as soon as their eccentricity exceeds 0.008 (0.05) for low (high) mass systems, suggesting eccentric detections are likely to come first from low-mass systems. We complete our analysis by investigating the systematic (mismodeling) error inherent in our post-Newtonian model, finding that for signals with a signal-to-noise ratio of 15, the systematic error is below the statistical error for eccentricities as high as 0.8 (0.5) for low (high) mass systems. We also investigate the systematic error that arises from using a model that neglects eccentricity when the signal is truly eccentric, finding that the systematic error exceeds the statistical error in mass for eccentricities as small as 0.02. As a byproduct of this work we also present some new measures of the accuracy of our model, and investigate the efficiency of the model. We also show that

the model is efficient enough to be useful for data analysis provided we are in a mass range in which an inspiral only model is valid. In the higher mass cases, this work points to the importance of developing IMR models.

3.1 Introduction

We have now entered an era where gravitational wave (GW) detection is routine, enough so to compose a catalog of the 11 confirmed events [1] (including a very recent potential binary nuetron star detection [116]) and explore the properties of populations of compact binaries [117], such as mass and spin distributions. These GW detections provide information about the compact objects that emit them, but also they can be used to shed light on their formation scenarios, which helps further our knowledge of astrophysics and the universe at large. Currently only the masses, spins, distance, and sky orientation are modeled and measured, but there has been much work in producing and analyzing models that incorporate orbital eccentricity [26, 27, 29, 32, 33, 39, 118–123].

The traditional expectation is that gravitational wave observations with ground-based detectors should correspond to binaries in quasicircular orbits, because GW emission causes an eccentric binary to circularize. Recent studies [124–126] have searched for eccentric signals in the LIGO data and concluded that all of the current detections are consistent with binaries in quasicircular orbits. However, this is not completely inconsistent with the expectations of astrophysical scenarios, which suggest that there will be some small number of eccentric signals seen by ground-based detectors. With the GW catalog expected to expand considerably in the coming months and years, it is possible we will see at least one such event.

For binaries with detectable eccentricities emitting in the sensitivity range of ground-based detector networks, the main formation channels are dense stellar regions, such as globular clusters (GC) and the environment near supermassive black holes (SMBHs). Several recent works have incorporated post-Newtonian (PN) effects in population synthesis studies, focusing on binary formation in GCs and finding an increased number of binaries with eccentricity, with rates between 0.5 and 0.7 eccentric events per Gpc per year, and about 5% of all GWs in GCs having $e > 0.1$ when detectable by ground-based networks [6–9]. About 0.5% of events near SMBH binaries with detectable mergers are expected to have $e > 0.5$ [62, 64, 127]. For the space based Laser Interferometer Space Antenna (LISA), the expected number of eccentric sources considerably increases as they have not yet circularized due to GW emission [10–12, 128].

With these distinct formation channels that can potentially assemble compact binaries in eccentric orbits comes the ability to constrain the formation mechanisms given a number of observations of eccentric events. In [44], the authors claim that given tens of observations by LIGO one could discriminate between formation by the Kozai-Lidov mechanism and gravitational capture in GC. For LISA, only a handful of observations are needed to distinguish a population of events formed near SMBHs, and tens of events to distinguish between a population of binaries formed in the field versus in GCs [45, 46]. Given the rich science potential of eccentric signals and the increasing likelihood of detecting such events, it is important to begin to investigate the data analysis implications and feasibility of models that incorporate eccentricity.

Several studies have considered some of the data analysis implications of eccentric gravitational waves. In [13], the authors study the systematic parameter error due to using quasi-circular templates to recover parameters from an eccentric signal using a Fisher analysis. Also recently in [16], the authors produce hybrid eccentric PN-NR waveforms and again study the systematic error in parameter extraction from using circular templates on eccentric signals with a Bayesian methodology. The former found significant parameter error for low mass systems for signals with eccentricities near 10^{-2}, and the latter found significant parameter error for higher mass systems for signals with eccentricities larger than 10^{-1}. In [41, 42], the authors characterize some of the statistical errors associated with the various parameters of moderate and highly eccentric signals using a 1PN valid model and a Fisher analysis.

Previous studies were limited either by the computational expense or the accuracy of the eccentric model used. Here we carry out a fully Bayesian analysis of eccentric signals using Markov Chain Monte Carlo to produce the posterior distributions for the various parameters of eccentric systems. The key to this analysis is the use of the TaylorF2e model derived in [119], which has been slightly modified to increase efficiency while retaining model accuracy. The model is inspiral only, valid to 3PN in the phasing, while keeping only the leading-order amplitude corrections. As in [119], we also illustrate that this model is accurate to eccentricities of ~ 0.8 for certain masses, and we also demonstrate that it is highly computationally efficient (∼90ms per waveform evaluation).

With this model in hand, we create simulated data using TaylorF2e and study the ability of a LIGO detector to recover parameters in both the moderate and low eccentricity regime. Generally, as the eccentricity of the signal is increased from 0.1 to > 0.4, the accuracy to which we can measure the eccentricity in the model improves by a factor of 10^2, leading to statistical uncertainties on this parameter of order 10^{-5} (10^{-3}) for low (high) mass systems. We also find that the statistical uncertainty on the extraction of the chirp mass decreases by a factor of 10 as the eccentricity of the signal increases. In the low eccentricity regime ($e < 0.1$), the eccentricity of the model becomes detectable when the eccentricity of the signal reaches values of about $\gtrsim 0.008$ ($\gtrsim 0.05$) for low (high) mass systems. This suggests that we might expect a larger number of statistically significant measurements of eccentricity from low mass compact binaries, unless these do not exist in Nature.

In addition to characterizing the measurement error sourced by detector noise, we also study the systematic error due to mismodeling in two different cases. We first study the recovery of parameters when fitting a circular waveform model to an eccentric signal. We find that there is significant error in the extraction of parameters when the eccentricities of the signal is as small as 0.01 (0.08) for low (high) mass systems. This underscores the importance of using eccentric models even when the eccentricity of the signal is expected to be very small. We then also studied the parameter error induced by inaccuracies in our eccentric model, such as that due to the truncation of expansions at a finite order. This error is studied by estimating the parameters in the frequency-domain, TaylorF2e model when the signal is a fully numerically-solved, 3PN, time-domain waveform. We here find that our model incurs parameter error that is smaller that the statistical error for eccentricities of at least $\lesssim 0.8$ in the low mass case, and $\lesssim 0.5$ in the high mass cases. This again points to the faithfulness of the model for parameter estimation in the moderate eccentricity regime. We, however, note that restriction to 3PN accuracy and inspiral only can potentially lead to significant parameter biases especially for higher mass systems in the case of the latter. This work would be well complimented by development of an IMR model and higher PN corrections to the waveform, which could be used to point to the magnitude of systematic error as a function of source eccentricity.

The organization of the paper is as follows: Section 3.2 presents the model we use for our analysis, presenting its validity and efficiency. Section 3.3 reviews the Bayesian techniques we use in this work, and Section 3.4 presents and analyses parameter estimation in the high eccentricity regime, while Section 3.5 treats the low eccentricity regime. Sections 3.6.1 and 3.6.2 study systematic parameter error from neglecting eccentricity and inaccuracy in our eccentric model, respectively. Section 4.5 presents conclusions and points to areas to improve this study and possible interesting extensions. Throughout this work, we use geometric units (c = G = 1).

3.2 Eccentric Model

In this section we summarize the inspiral only, 3PN-accurate, Fourier domain model that incorporates effects of periastron precession developed in [103,119]. This is the model that we will use to carry out our Bayesian analysis of binaries with moderate eccentricities. We implement minor modifications to this model that increases its computational efficiency, and so we also re-validate it against a fully numerical time-domain PN model. Lastly, we discuss the computational efficiency of generating the model, which has been recently added to the open-source `PyCBC` GW analysis package as `TaylorF2e`. See Figures 3.1, 3.11, and 3.12 for metrics that point to the validity of the model in the quasi-circular limit and as a function of increasing orbital eccentricity.

The model that we use for our Bayesian analysis is an optimized version of the TaylorF2e model derived and presented in [119]. In that paper we wrote our semi-analytic frequency-domain model schematically as

$$\tilde{h}(f) = A\left[F_+ S^2 \sum_{s=1}^{\infty} G_s \sqrt{\frac{2\pi}{|s\ddot{l}|}} e^{i\psi_s} + Q \sum_{j=-1}^{\infty} N_j \sqrt{\frac{2\pi}{|j+2|\ddot{l}}} e^{i\psi_j^-} + Q^* \sum_{j=-\infty}^{-4} N_j \sqrt{\frac{2\pi}{|j+2|\ddot{l}}} e^{i\psi_j^+}\right] \tag{3.1}$$

where Q is a function of the binary orientation relative to the detector frame, A is an overall amplitude depending on the masses and distance to source, the G_s and N_j are amplitudes which control the strength of the different harmonics appearing in the sums that scale as $e^{|s|}$ and $e^{|j|}$ respectively (where here $e = e_t$ is the temporal

PN eccentricity). In investigating techniques to optimize the model we found that we could neglect a significant number of harmonics appearing in the infinite sums of Eq. (3.1) without losing much accuracy in the regions where the model was shown to be faithful to a fully numerical TaylorT4 model.

Let us now make the parameter dependence and our optimizations more explicit. We neglect several harmonics in Eq.(3.1), and rewrite the model in the form of

$$\tilde{h}(f) = 10\pi\mathcal{A}\frac{\mathcal{M}_c}{\eta^{1/5}}\sum_{j=-1}^{15} N_j \sqrt{\frac{y^{-7}}{(j+2)(96+292e^2+37e^4)}}e^{i\psi_j^-} , \tag{3.2}$$

where $\mathcal{A}$ is an overall amplitude that depends on the sky angles, polarization angle and distance to source, $\eta = m_1 m_2/M^2$ and $\mathcal{M}_c = M\eta^{3/5}$ are the symmetric mass ratio and chirp mass respectively, with M the total mass, and m_1 and m_2 the component masses, and $y = \mathcal{O}[(Mn)^{1/3}]$ is our PN expansion parameter, with $n = 2\pi/P$ the mean motion and P the orbital period. The phases, ψ_j^-, are analytic functions of eccentricity given by

$$\psi_j^- = 2\pi f\,[t(e) - t_c] - j\,[l(e) - l_c] - 2\,[\lambda(e) - \lambda_c] - \frac{\pi}{4} , \tag{3.3}$$

where λ and l are angles associated with the orbit and $t - t_c$ is the time to coalescence. These phase functions depend on the masses and mass ratio, and are series expansions in e. In this work, we use both the version of the waveform that keeps more terms in eccentricity in these phase functions (TaylorF2e+), and the version which keeps less terms (TaylorF2e-). For a summary of how many terms each keeps, see Table I of [119].

In order to compute the model at a given frequency, one must numerically invert the stationary phase condition given a Fourier frequency for the corresponding eccentricity, which is then used in the model. The stationary phase condition reads

$$2\pi f = j\dot{l}(e) + 2\dot{\lambda}(e)\,, \tag{3.4}$$

where an overdot denotes the time derivative. For much more detail on the model derivation, see [119].

A further optimization that we implement is an adaptive scheme to sample the different j harmonics appearing in the sum in Eq. (4.1) in frequency. Any given harmonic j begins emitting at a lower frequency $f_{0,j}$ obtained through Eq.(3.4) as $2\pi f_{0,j} = j\dot{l}(e_0) + 2\dot{\lambda}(e_0)$. Here e_0 is the eccentricity at an initial time and separation, where recall that we cannot assign e_0 to a single initial GW frequency because the signal is composed of many harmonics. Any given harmonic j ends emission at $2\pi f_{\rm fin,j} = j\dot{l}(e_{\rm fin}) + 2\dot{\lambda}(e_{\rm fin})$, where $e_{\rm fin}$ is chosen to correspond to some truncation condition. We truncate our waveforms when the periastron velocity reaches one-third the speed of light. Thus, higher harmonics emit in a wide frequency band, but inspection of the N_j reveals that they rapidly tend to zero as e decreases (see Fig. 6 of [119]). As a result, it is inefficient to waste computational resources computing the higher harmonics once their contribution to the signal becomes negligible. We choose to stop sampling the $j^{\rm th}$ harmonic when e satisfies $e \leq (j-1)/28$ or $e < e_{\rm fin}$, whichever is satisfied first (a choice that can be made by inspection of Fig. 6 of [119]). We translate this condition on the eccentricity into a starting and ending frequency for each harmonic using Eq.(3.4).

We must be careful in the way that we parameterize the orbital eccentricity in our model. In [119], we parameterized the model in terms of e_0 and p_0, which were to be understood as the eccentricity and semi-latus rectum at some initial time. This choice was made because we were taking the Fourier transform of a time-domain

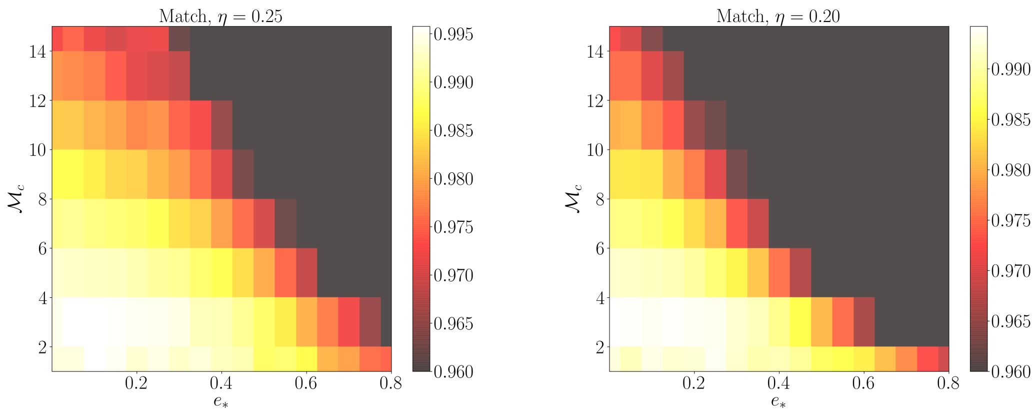

Figure 3.1: The match between the TaylorF2e+ model and a fully numerical, time-domain model as a function of the chirp mass and e_* for $\eta = 0.25$ (left) and $\eta = 0.2$ (right). Values below 96% are excluded. As the mass becomes unequal, the match deteriorates. The model is more faithful for lower mass systems. Figure 3.11 shows the same when using the less accurate TaylorF2e- model, and Figure 3.12 shows the fitting factor between the TaylorF2e+ model and the time domain TaylorT4-like model.

signal, and subsequently using it to validate an approximate frequency-domain model. The time-domain signal had to be started at a given initial time t_0 with some initial eccentricity e_0 and semi-latus rectum p_0. Each harmonic of the GW signal would then emit in some frequency range that depended on the harmonic index j, as described above. However, these choices came with the physical interpretation that the binary had to spontaneously begin emitting at t_0, and there was no emission before this time. In reality, binary systems are likely to have been around long before the fiducial time t_0 that we chose, and thus, all harmonics should have been emitting significantly from initial frequencies much lower than the lower frequency cutoff of ground-based detectors. Thus, this time around, we would like to construct the model in such a way that we choose some reference eccentricity and reference separation, and then compute all the relevant GW emission self-consistently, some of which will likely come from earlier times when the orbit had a higher eccentricity and a larger separation.

What is the best way to choose this reference eccentricity and separation? What is commonly done is to choose the "eccentricity at a GW frequency of 10Hz". However, this description is problematic because, at any given time and eccentricity, an eccentric binary emits GWs at multiple frequencies. What is typically meant by the previous statement is that one chooses the "eccentricity at an orbital frequency of 5 Hz," since the only harmonic that is non-vanishing in the circular limit emits at twice the orbital frequency. This amounts to fixing the eccentricity at some reference semi-major axis by Kepler's third law. While this is a sensible choice for small eccentricities, for large eccentricities this choice becomes troublesome. While the semi-major axis may be large, for large eccentricities the corresponding pericenter distance can be very, very small, and sometimes so small than the PN approximation should not be trusted. For example, if we fix the reference semi-major axis to be $50M$ (corresponding to a reference orbital frequency of about 5 Hz for a $(10, 10)M_{\odot}$ system) and increase the orbital eccentricity from 0.1, to 0.3, 0.6, and 0.9, the reference pericenter distance becomes $45M$, $35M$, $20M$, and $5M$.

This way of choosing a reference eccentricity is clearly inappropriate, since it can correspond to an orbit with such small pericenter distances that the PN approximation breaks down. Instead, we here choose to parameterize our model by *specifying the eccentricity at the semi-latus rectum that corresponds to the separation of a circular binary emitting GWs at 10 Hz.* With this choice, if we now fix the semi-latus rectum to be $50M$ and increase the orbital eccentricity from 0.1, to 0.3, 0.6, and 0.9, then the corresponding pericenter distances are $45M$, $38M$, $31M$, and $26M$. This choice has the advantage that we are not specifying orbits outside the PN regime of validity, and as the eccentricity is decreased, this choice will nearly match the conventions of early models. We will refer to this reference eccentricity parameter as e_{*}.

Given this new parameterization, we must now re-validate the model against a fully numerical, time-domain signal. In order to achieve this, we generate a time-domain model whose initial conditions (e_0, p_0) are determined by the separation and eccentricity sampled by our TaylorF2e's highest harmonic at 10 Hz. This time-domain model and our techniques for calculating the match are described in detail in [119]. Figure 3.1 shows the match between our frequency-domain model TaylorF2e+ and the fully numerical, time-domain model as a function of the chirp mass and e_*. The match deteriorates as the mass and eccentricity is increased, and as η is decreased. In Appendix 3.B, we present plots of the fitting factors as well as match for the model that keeps less terms in the eccentric expansions in the phase TaylorF2e-. There is a significant difference in the regime of validity between the two frequency-domain models when the mass is low and the eccentricity is high.

We conclude this section with a note about the computational performance of the model. In order to gauge the speed of generating our model, we draw parameters from uniform random variables. We draw the chirp mass from $U[0.8, 15]$, η from $U[0.15, 0.25]$, e_* from $U[10^{-6}, 0.8]$, and $\mathcal{A}$ from $U[10^{-16}, 10^{-20}]$. We make 10^6 draws and calculate the corresponding frequency response with a frequency resolution of 0.015625Hz. The average time to compute the waveform in the parameter space described above is 61.4ms per TaylorF2e- waveform evaluation and 94.8ms per TaylorF2e+ waveform evaluation. This timing study was carried out on a 2.20GHz Intel Xeon E5-2630 v4 CPU.

3.3 Bayesian Framework

In this section we provide a short summary of the technical details and techniques used to investigate the data analysis implications of moderately eccentric GWs. We use an MCMC algorithm to produce samples of the posterior given advanced LIGO at design sensitivity, assuming a single detector, and maximizing the likelihood over

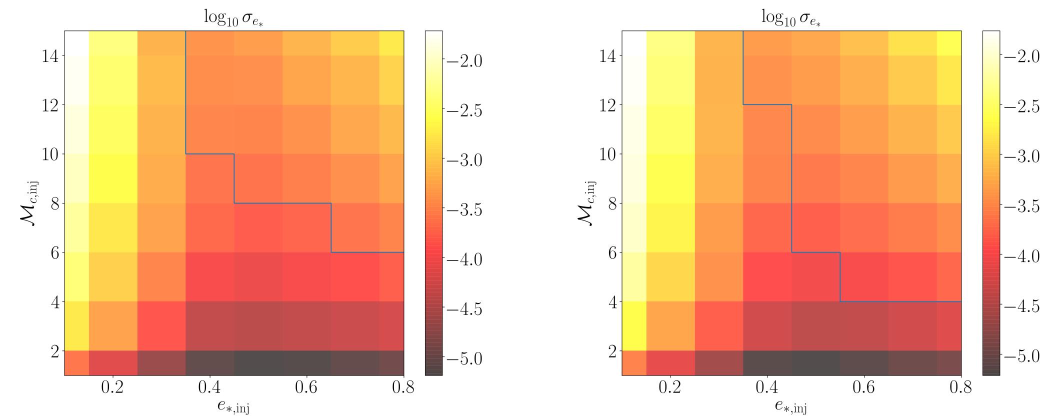

Figure 3.2: Log base 10 of the standard deviation of the marginalized posterior of eccentricity for different injected eccentricities ($e_{*,\mathrm{inj}}$) and chirp masses ($\mathcal{M}_{c,\mathrm{inj}}$), with $\eta_{\mathrm{inj}} = 0.25$ on the left panel and 0.20 on the right panel, and with an SNR of 15. To the right of the blue line on the left panel the systematic error from mismodeling exceeds σ_{e*}. Observe that the accuracy to which the eccentricity can be measured can exceed 10^{-5} for moderately eccentric and low mass systems.

extrinsic parameters. The maximization of the likelihood over the source parameters can potentially shift the peak of the posteriors and lead to a tighter constraints than would occur had we marginalized over these parameters. However, we don't expect this effect to affect our main result, the dependence of various measurements on the source eccentricity, qualitatively.

In order to answer questions about how well we can recover the parameters of the waveform model described in Section 3.2, we employ Bayesian inference and obtain the posterior distribution $p(\theta|\mathbf{d}, M)$. The posterior is the probability of the parameters (θ) given the data ($\mathbf{d}$) and the model (M). This probability distribution is used to glean information about the recovered parameters, such as credible intervals, the mode, mean, and median. In order to work with and visualize the posterior in terms of a single parameter, we often work with the marginalized posterior, given by

$$p(\theta^j) = \int p(\theta|\mathbf{d}, M) \prod_{k\neq j} d\theta^k \,. \tag{3.5}$$

In our case, we have reduced the model to four intrinsic parameters and three extrinsic parameters, $\theta = \{\ln M_c, \eta, e_*, \ln \mathcal{A}, \lambda_c, l_c, t_c\}$, because we assume the binary is non-spinning, and because we consider a single detector with which it is not possible to obtain sky localization information.

In order to obtain the posterior distribution we have written our own Markov Chain Monte Carlo (MCMC) algorithm [129]. In short the MCMC is a stochastic process whose random walk in parameter space produces the posterior distribution. In order to take steps, the MCMC requires the computation of the likelihood $\mathcal{L}(\mathbf{h})$, given by

$$\mathcal{L}(\mathbf{h}) \sim \exp\left\{-\frac{1}{2}(\mathbf{d}-\mathbf{h}|\mathbf{d}-\mathbf{h})\right\}\,, \tag{3.6}$$

where the inner product between a signal $h_1(t)$ and $h_2(t)$ is given by

$$(h_1|h_2) = 4\mathrm{Re}\int \frac{\tilde{h}_1^*(f)\tilde{h}_2(f)}{S_n(f)} df\,, \tag{3.7}$$

which also defines the signal to noise ratio (SNR) of a signal h:

$$\mathrm{SNR}^2 = (\mathbf{h}|\mathbf{h})\,. \tag{3.8}$$

In Eq. (3.7), Re stands for the real operator, $*$ denotes complex conjugation, the overhead tilde stands for the Fourier transform, and $S_n(f)$ is the spectral noise density of the detector. In this work we use spectral noise of aLIGO at designed sensitivity (zero-detuned, high-power), and assume stationary, Gaussian noise [77] when computing the likelihood. We consider one detector with no noise injection. In addition, we maximize the inner product appearing in the likelihood over the parameters λ_c, l_c, and t_c which arise in the phases shown in Eq. (4.2) as harmonic dependent phase shifts and an overall time shift. This maximization procedure differs from the analogous procedure in the circular case, and was derived and explained in Sec. III of [103].

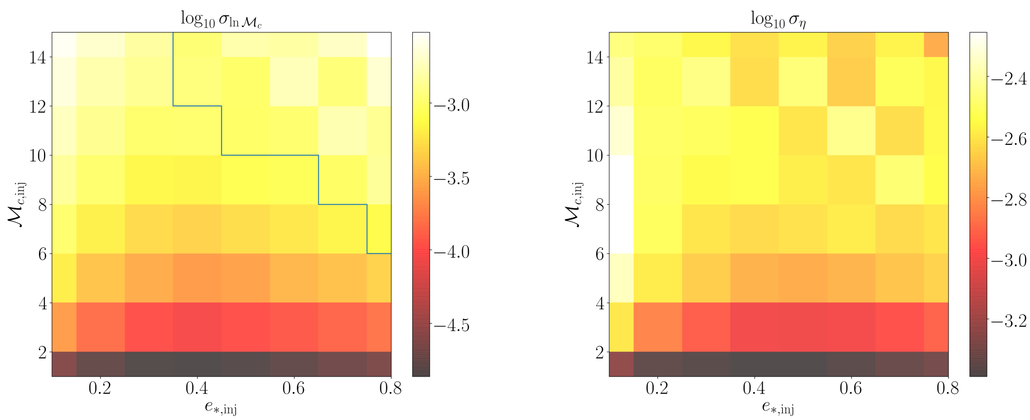

Figure 3.3: Same as Fig. 3.2 but for the $\ln\mathcal{M}_c$ (top) and η (bottom) parameter. Observe that the accuracy to which both the chirp mass and reduced mass ratio can be measured improves for moderately eccentric signals.

In order to complete the description of our MCMC algorithm, we must still specify the priors and the proposal distribution from which we draw in order for the algorithm to propose steps in parameter space. Our prior distributions are uniform flat on all parameters: $\ln\mathcal{M}_c \in [-0.223, 2.708]$, $\eta \in [0.15, 0.25]$, $e_* \in [10^{-6}, 0.8]$, and $\ln A \in [-36.8414, -46.0517]$. The choice of priors in chirp mass corresponds to the type of sources we explore here. Our restrictive choice of lower bound on the prior for η is a consequence of eccentric models suffering from inaccuracy as η becomes small (see Figure 3.1 and Figures 7 and 10 of [119]). Likewise our choice of upper bound on e_* represents the highest eccentricity we expect the model to be faithful for

(for certain masses). Our proposal distribution consists of a mixture of Fisher matrix proposals, draws from the prior, and differential evolution [130]. Additionally, we use parallel tempering to ensure that the entire parameter space is explored and efficiently sampled. We have checked and ensured that the hottest chains are exploring the entire parameter space. In order to determine convergence of the chains, we have verified that producing more samples of the posterior does not qualitatively affect our results.

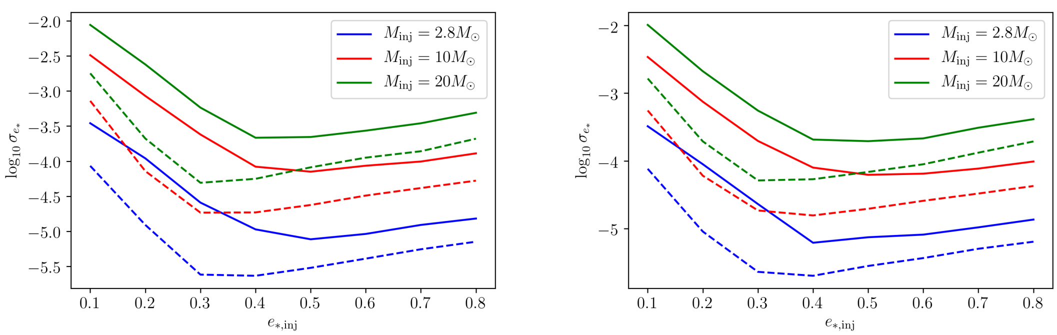

Figure 3.4: Log base 10 of the standard deviation of the marginalized posterior of eccentricity, σ_{e_*} for different injected eccentricities holding the injected total mass ($M_{\rm inj}$) fixed. The signal SNR is 15 (solid) and 30 (dashed), while $\eta_{\rm inj}$ is 0.25 (left panel) and 0.20 (right panel). Observe that the accuracy to which the eccentricity can be measured improves with the injected eccentricity of the signal, but it reaches a saturation point at moderate injected eccentricities due to covariances (see Fig. 3.5).

3.4 How Well Can We Measure Large Eccentricities?

In this section we explore how well we can estimate the eccentricity of the model when the eccentricity of the injected signal is larger than 0.1. We consider two sources of parameter estimation error. There is a statistical error in parameter estimation due to covariances between model parameters and detector noise – an error that will obviously depend on the SNR. There is also a systematic error in parameter estimation

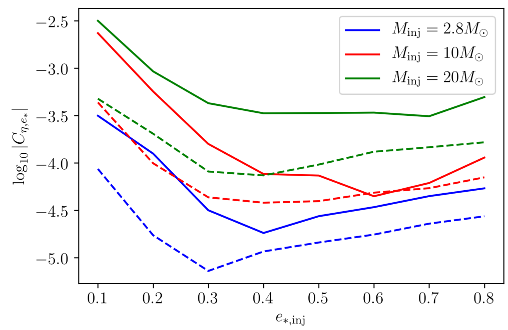

Figure 3.5: Log base 10 of the absolute value of the covariance between η and e_* for various total masses as a function of the injected eccentricity. The signal SNR is 15 (solid) and 30 (dashed). Observe that the covariance between these parameters improves with the injected eccentricity of the signal, until it saturates at moderate injected eccentricity, presenting a patter similar as that found for the variance of the eccentricity in Fig. 3.4.

due to the template not being an exact representation of the true signal – an error that will be independent of the SNR. We here seek to explore the measurement of eccentricity in the context of both errors. In producing statistical errors, we employ our TaylorF2e- model and have verified that the results are qualitatively unchanged when using the TaylorF2e+ model. However, to gauge systematic error we require a more faithful model and instead use the TaylorF2e+ model.

In the figures that appear later in this section, we explore the ability to measure system parameters for systems with mass as large as $\mathcal{M}_c = 15M_\odot$. With such large masses being explored, it is worth making a statement about systematics due to the neglect of merger and ringdown. Without explicitly constructing the IMR extension of this eccentric model, it is not possible to exactly explore this systematic. However, we can look to the quasi-circular limit to inform the region where these effects become significant (in the quasi-circular limit, our TaylorF2e model recovers TaylorF2 identically). Reference [131] found that using inspiral models incur systematic parameter biases larger than the associated statistical error for

$M > 17M_\odot$ ($\mathcal{M}_c > 7.4M_\odot$ for equal mass) when assuming a signal SNR of 20. Here we explore results for an SNR 15 source so that criteria could likely be relaxed slightly. This does point to the need for the development of an IMR model that extends the waveform used in this paper, especially for higher masses. However, our analysis of the inspiral portion of such signals still points to valid data analysis implications from that phase of the waveform.

Figure 3.2 shows σ_{e_*} (i.e., the standard deviation in the samples of the marginalized posterior on the parameter e_*) as a function of the injected chirp mass ($\mathcal{M}_{c,\mathrm{inj}}$) and eccentricity ($e_{*,\mathrm{inj}}$). We present results for two different mass ratios and all signals have an SNR of 15. In the top panel, we have added a line which indicates that, to the right (for larger injected eccentricities), the systematic error from mismodeling is greater than σ_{e_*}. Our technique for obtaining this systematic error is explained in Sec. 3.6.2, where we also provide analogous plots for this error. If we assume that the marginalized posterior in terms of eccentricity is Gaussian (an appropriate approximation according to the posteriors plotted in Fig. 3.10), then the 1-sigma region indicates a region of 68% confidence. Thus, when the systematic error exceeds 1-sigma, our systematic error causes the measurement to be outside of this 68% confidence region. Although not shown in this figure, as the SNR is increased, the statistical error also decreases, and thus, we will eventually require more faithful modeling for higher mass systems with large eccentricities and higher SNRs.

Let us now make note of some of the features of the statistical error shown in Fig. 3.2. Overall, the eccentricity can be extracted to better than 10%, with typical values that go down all the way to 10^{-5} for low mass systems. The fact that as the injected chirp mass decreases, σ_{e_*} becomes smaller is sensible. The signal contains more GW cycles for lower mass systems, and thus, the likelihood is more sensitive to changes in model parameters. While the difference in σ_{e_*} is nearly indistinguishable by eye when $\eta_{\rm inj}$ is changed from 0.25 to 0.20 (from the left to the right panel), we have verified that σ_{e_*} typically has a fractional difference of about 0.06 between the two cases.

Figure 3.3 shows the standard deviation of the marginalized posterior of $\ln \mathcal{M}_c$. Again, the blue line indicates the threshold for when the systematic error exceeds 1-sigma. This line is slightly less restrictive than the systematic error in eccentricity. We see that, as the injected eccentricity is increased, the standard deviation decreases compared to the low eccentricity case. This suggests that moderately eccentric signals could provide better constraints on the chirp mass of the emitting system. The result for the unequal mass case is nearly indistinguishable by eye, so we do not include it here. We also include in Fig. 3.3 an analogous plot for the dependence of the statistical uncertainty in the symmetric mass ratio, η, as a function of injected chirp mass and eccentricity. For the low mass sources, this uncertainty decreases by about half an order of magnitude as the injected eccentricity is increased. For $\ln \mathcal{A}$, there is no trend in the statistical error with respect to eccentricity.

Figure 3.4 plots again $\log_{10} \sigma_{e_*}$, but this time holding the injected total mass fixed and changing the SNR from 15 (solid lines) to 30 (dashed lines). As expected, σ_{e_*} decreases as the SNR is increased. However, we notice a counterintuitive result: σ_{e_*} initially decreases as $e_{*,\rm inj}$ is increased, but hits a certain value of $e_{*,\rm inj}$, and then begins to slowly increase as $e_{*,\rm inj}$ continues to increase. One explanation for this behavior is that a covariance between η and e_* follows a similar trend. Figure 3.5 shows $\log_{10} |C_{\eta,e_*}|$ for the same case as the top panel of 3.4. This covariance forces the statistical error on the marginalized posteriors of eccentricity to widen.

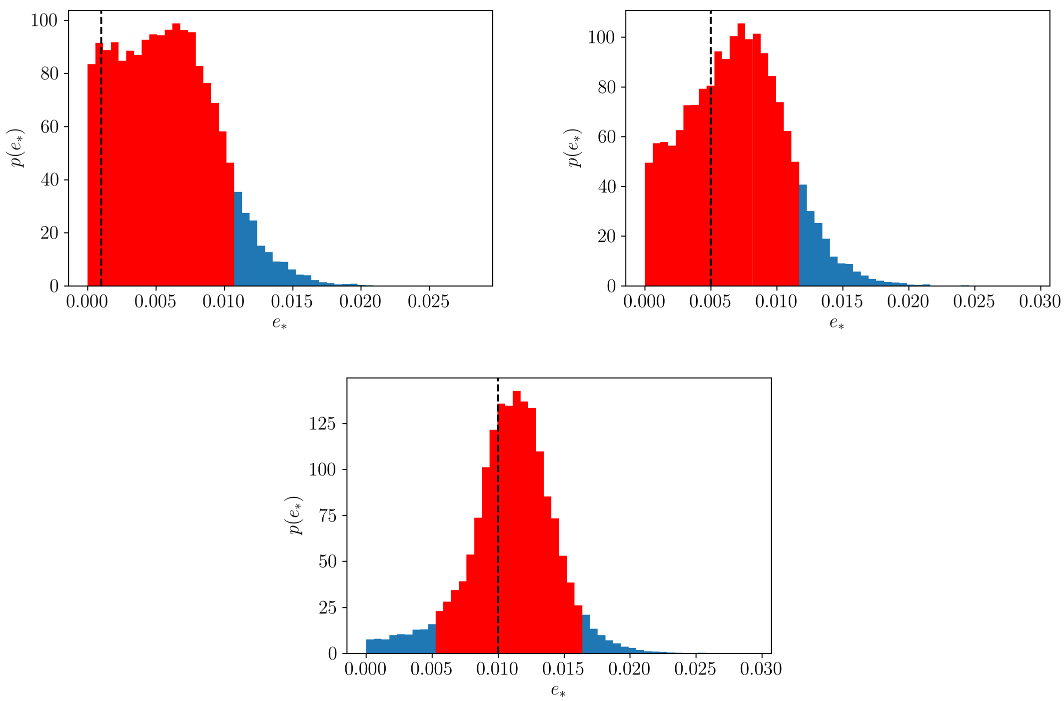

Figure 3.6: Marginalized posteriors on eccentricity for an SNR 15, $(1.4, 1.4)M_{\odot}$ mass injection with injected eccentricity of 0.001 (top), 0.005 (middle), and 0.01 (bottom). In red we have over-plotted the 90% confidence region, with the dashed line indicating the injected value of eccentricity. In the lowest eccentricity injection, we see that, in the region near zero eccentricity, the posterior is effectively sampling the flat prior. By 0.005 eccentricity, the posterior is beginning to have a more defined peak away from zero, and by 0.01 eccentricity, there is an even more well defined peak with zero eccentricity excluded from the 90% confidence region.

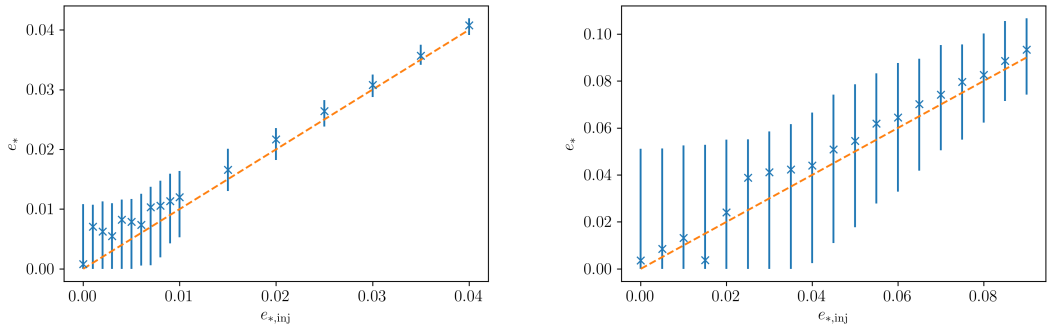

Figure 3.7: A characterization of the marginalized posterior of eccentricity, $p(e_*)$, when injected eccentricity is small. The vertical line indicates the 90% minimal area confidence interval, and the "x" indicates the peak of the marginalized posterior. The dashed line indicates where $e_{*,\mathrm{inj}} = e_*$. We show results for a $(1.4, 1.4)M_\odot$ mass injection (left) and a $(10, 10)M_\odot$ mass injection (right) (in all cases the SNR is 15). For the low (high) mass injection, the 90% confidence interval begins to exclude 0 eccentricity around $e_* = 0.008\,(0.05)$.

3.5 How Well Can We Measure Small Eccentricities?

In this section we study the ability to measure the eccentricity parameter of our model when the injected eccentricity of the signal is small. The most rigorous method to determine whether one can distinguish an eccentric model from a circular model is to compute the Bayes factor or Odds ratio. As the main focus of this work is to characterize measurement in the high eccentricity regime, we instead choose to investigate the small eccentricity regime more qualitatively, by characterizing the marginalized posteriors of eccentricity when the injected eccentricity is small. In particular, we compute the 90% confidence interval of the marginalized posterior of eccentricity to discern at what value of the injected eccentricity the marginalized posteriors transition from clustering mostly near zero to clustering away from zero without considerable support at zero.

Let us describe the confidence interval that we will use in our results. We here work with the minimum volume confidence interval which is obtained by defining a threshold probability (p_*) and integrating those regions where the probability density exceed this limit. This limit is lowered until the total probability reaches the desired amount. This minimum volume confidence interval is given by

$$\int [p(x) \geq p_*] dx = \alpha \,, \tag{3.9}$$

where α is the desired credible interval.

Figure 3.6 shows some of the marginalized posteriors obtained for a $(1.4, 1.4)M_\odot$ signal with various eccentricities, as well as their 90% confidence interval, and the value of the injected eccentricity. In the low eccentricity case, the posterior is effectively producing samples of the uniform flat prior in the regime where eccentricity is very small ($e_* \leq 0.07$), but excludes higher eccentricities. Had we used a prior that was uniform on $\ln e$, the recovery of the prior in the small eccentricity regime would have produced smaller upper limits, which we sought to avoid with our choice of a uniform-in-e prior. This leads to the lack of structure in the peaks of the posterior at low injected eccentricity. As the injected eccentricity is increased, the posterior still includes zero in the 90% confidence interval, but there is a more defined peak and the distribution begins to take on a Gaussian shape whose peak is shifted from zero. Finally, as the injected eccentricity is raised high enough, there is little support for zero eccentricity, and the posterior takes on a Gaussian shape with a well defined peak near the injected value (the peak does not lie directly on the injected value due to marginalization along other covariant parameters).

Figure 3.7 shows the maximum of the marginalized posterior (denoted with an"x") of e_* for a $(1.4, 1.4)M_\odot$ system (left) and a $(10, 10)M_\odot$ system (right), together with vertical error bars constructed from the 90% minimal area confidence intervals (shown e.g., in Fig. 3.6 for the NS binary case). In the low and high mass cases, the 90% confidence begins to exclude zero eccentricity at $e_{*,\mathrm{inj}} = 0.008$ and at $e_{*,\mathrm{inj}} =$ (0.05), respectively. These results suggest that we could in principle be detecting even very small eccentricities with advanced LIGO at design sensitivity, if such systems exist in Nature. For lower mass sources, like a neutron star binary, LIGO could measure eccentricities as low as $e_* \sim 0.01$ and for higher mass systems $e_* \sim 0.05$. Of course this also is dependent on the SNR of the signal, which here is assumed to be 15. We could also possibly provide a better measurement given an eccentric model that incorporates merger and ringdown effects in the waveform.

3.6 Systematic Parameter Error from Mismodeling

In Section 3.4, we presented the statistical error in measuring the eccentricity and chirp mass of our model given eccentric signals, and tempered these results with the systematic error due to model inaccuracy. In the following sections, we expand on that discussion of systematic error by considering two sources of this error from model inaccuracy: error from neglecting orbital eccentricity altogether in our models when recovering parameters from an eccentric signal, and the error introduced by model inaccuracy in our eccentric model.

We study systematic error by assuming that the signal is described by an "exact" model, given by $h_{\mathrm{EX}}(\theta^i)$, and it is fitted by an approximate model, given by $h_{\mathrm{AP}}(\theta^i)$. The model that best fits the signal for a given set of injected parameters is the one that maximizes the likelihood, or by appropriately replacing **d** and **h** in Eq.(3.6) minimizes the quantity $(h_{\mathrm{EX}}(\theta^i_{\mathrm{inj}}) - h_{\mathrm{AP}}(\theta^i)|h_{\mathrm{EX}}(\theta^i_{\mathrm{inj}}) - h_{\mathrm{AP}}(\theta^i))$. We refer to the parameters of the model, θ^i, which minimize this quantity as the "best-fit parameters" θ^i_{bf}, and the injected parameters of the "exact" signal as θ^i_{inj}. The systematic parameter error is the difference between the parameters of the signal, and the best-fit parameters of the approximate model, i.e.,

$$\delta\theta^i = \theta^i_{\text{inj}} - \theta^i_{\text{bf}}\,, \tag{3.10}$$

Clearly then, to study this parameter error and obtain θ^i_{bf} we require a very precise estimate of the maximum likelihood (which is identical to finding the best fit in our analysis) when injecting an "exact" signal and recovering with an approximate model. In order to obtain this very accurate maximum likelihood estimation, we use our MCMC algorithm with a signal injected at a very large SNR, so that the likelihood, as a function of the parameters of the approximate model θ^i, is very narrowly peaked. We employ many chains so that the coldest chain can effectively explore the very narrowly peaked likelihood. After several thousands of iterations with no new maximum found, we end the search.

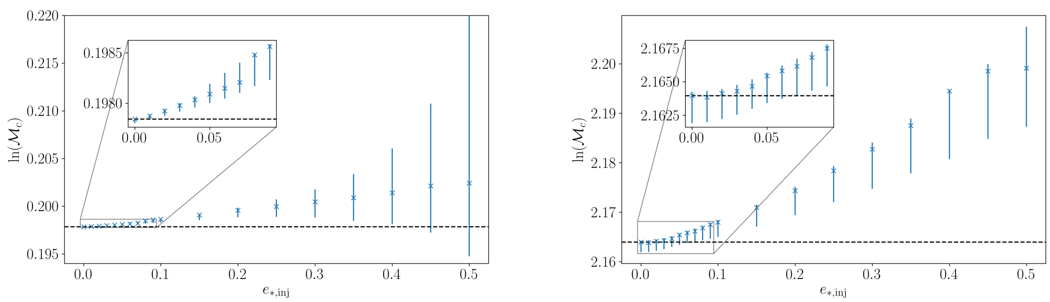

Figure 3.8: Best-fit value of $\ln\mathcal{M}_c$ ("x"), as a function of injected eccentricity, together with a measure of the statistical error in the extraction of this parameter, when using a circular template to recover an eccentric signal. The vertical error bar represents the 90% confidence interval in the extraction of $\ln\mathcal{M}_c$. The dashed line indicates the injected value of $\ln\mathcal{M}_c$. The left panel corresponds to a $(1.4, 1.4)M_\odot$ mass injection and the right corresponds to a $(10, 10)M_\odot$ mass injection, while the SNR of the injected signal is fixed at 15. Observe that the best-fit parameter diverges away from the injected value at injected eccentricities as low as 0.02 (0.08) for the less (more) massive binary.

3.6.1 What Systematic Error is Incurred by Neglecting Eccentricity in Waveform Modeling?

In this subsection we study the systematic parameter error which results from neglecting the effects of eccentricity in the model. In order to do so, we inject an eccentric signal and recover it using our model with the eccentricity fixed to zero[1], i.e.,$h_{\rm EX}(\theta^i)$ is the TaylorF2e+ model, while $h_{\rm AP}(\theta^i)$ is the circular limit of the TaylorF2e+ model. We employ both the method mentioned above to estimate the best-fit parameter values which gauge systematic error, as well as our MCMC algorithm to produce posteriors and extract confidence intervals which gauge statistical error, as we will explain below. We then explore how using the circular model given an eccentric signal leads to biases in the recovery of $\ln \mathcal{M}_c$ exploring both systematics and increase in statistical error.

Figure 3.8 shows the best-fit value of $\ln \mathcal{M}_c$ (as an "x") as a function of injected eccentricity, together with the 90% central confidence interval in the marginalized posterior on $\ln \mathcal{M}_c$ (vertical error bar). We show results for a $(10, 10)M_\odot$ and $(1.4, 1.4)M_\odot$ system. The central confidence interval is computed by integrating the posterior toward its maximum value from each side until the appropriate amount of probability has been collected. Thus, to find the bounds $x_{\rm min}$ and $x_{\rm max}$ of the central confidence interval of size α for a probability distribution $p(x)$ one uses

$$\int^{x_{\rm min}} p(x)dx = \int_{x_{\rm max}} p(x)dx = \frac{\alpha - 1}{2}\,. \tag{3.11}$$

In each case shown in Figure 3.8, the best-fit mass (whose difference from the injected value represents the systematic error) increases and is larger than the injected

[1] In reality the model requires a solution for how the eccentricity changes with orbital separation so we have used a very small eccentricity of 10^{-10}, which is effectively circular.

value, while the confidence region grows, as the injected eccentricity is increased. The bias toward higher mass is, at least in part, due to the fact that an eccentric system inspirals faster than its circular counterpart (depending on the length that is held fixed while taking the circular limit), and more massive systems inspiral faster. For the lower mass system, the 90% confidence interval in $\ln \mathcal{M}_c$ does not contain the injected value for eccentricities larger 0.02, and for the more massive case for eccentricities larger than 0.08. In each case, the best-fit value of the mass differs from the injected value by the time the eccentricity of the signal reaches $e_* \sim 0.02$. However, in the low mass case the injected value does begin to fall in the confidence interval for very large eccentricities – a result of that interval becoming very large.

This suggests that eccentricity should be considered when carrying out parameter estimation even in cases where the signal could be very nearly circular ($e_* \sim 0.02$) in order to avoid systematic bias. The value of the injected eccentricity of the signal at which this systematic bias becomes important is unsurprisingly close to the value at which eccentricity becomes measurable, as shown in Sec. 3.5. Obviously, the degree to which the systematic error exceeds the statistical error will depend on the signal SNR (as systematic error is independent of SNR and statistical error decays as SNR^{-1}), which in these studies was fixed at 15. We also note that these investigations should also be carried out in the future with a model that incorporates merger and ringdown, when the later is developed, as this could affect some of the quantitative details of the conclusions presented above.

3.6.2 What Systematic Error is Incurred by Inaccuracies in the Modeling of Eccentric Binaries?

In this subsection, we illustrate the systematic parameter error in the estimation of the eccentricity induced by mismodeling in our eccentric waveform. In the most ideal situation, we would have access to a catalog of numerical relativity waveforms with eccentricities as high as $e_* = 0.8$ and durations consistent with our TaylorF2e+ waveform. Unfortunately, these numerical waveforms are costly to compute and very few exist that incorporate eccentricity. However, we do have access to our TaylorT4-like waveform, which is obtained by numerically solving the PN binary dynamics, plugging these into the appropriate PN expression for $h(t)$, and then taking a discrete Fourier transform numerically. Thus, we will treat this numerically-solved, PN model as exact, use it as our true model, and find the TaylorF2e+ that fits it best, i.e., $h_{\rm AP}(\theta^i)$ is the TaylorF2e+ model, while $h_{\rm EX}(\theta^i)$ is the TaylorT4-like model described above. This provides the best estimate of the systematic error from model inaccuracy of TaylorF2e+ that is currently available to us. As a byproduct of this study, we produce the fitting factor as a function of chirp mass and eccentricity, which is presented in Appendix 3.B.

It is in order, then, to carefully discuss which approximations we are probing the systematics of. In going from the time-domain equations for the binary dynamics and waveform to our fast, frequency-domain waveform, we have employed a number of approximations. In principle, there are infinite harmonics of mean motion in the eccentric signal that we have truncated for speed of evaluation. We have also employed the stationary phase approximation, PN expansions, and series expansions in eccentricity throughout. It is systematics due to these approximations that we are probing here. There are also systematics due to mismodeling, stemming from the validity of the PN approximation and the neglect of the merger and ringdown. To carefully explore the former we would at least require the next order PN corrections, and for the latter we would require an IMR waveform that uses our inspiral signal to isolate the systematics only from the merger and ringdown. Lacking such ingredients, we focus our analysis here only to systematics induced by the approximations we have implemented in the inspiral, relegating a more complete analysis of systematics to future work.

Figure 3.9 shows δe (i.e., the systematic error in the estimation of the eccentricity as defined by Eq. 3.10) as a function of the injected eccentricity and chirp mass. To the right of the blue line, this error exceeds σ_{e_*} for a SNR 15 signal. Generally as the injected eccentricity increases, the systematic error increases which is consistent with the match calculations in [119] as well as the matches shown in Figure 3.1. As the system becomes less massive, the systematic error decreases but our ability to constrain eccentricity increases, so we still require more faithful templates even for these low mass systems. This is especially true as the SNR is increased, because our ability to constrain parameters will also increase, but the systematic error from model inaccuracy will be independent of SNR. We also see that the error is increased for unequal mass systems (as expected from Figure 3.1).

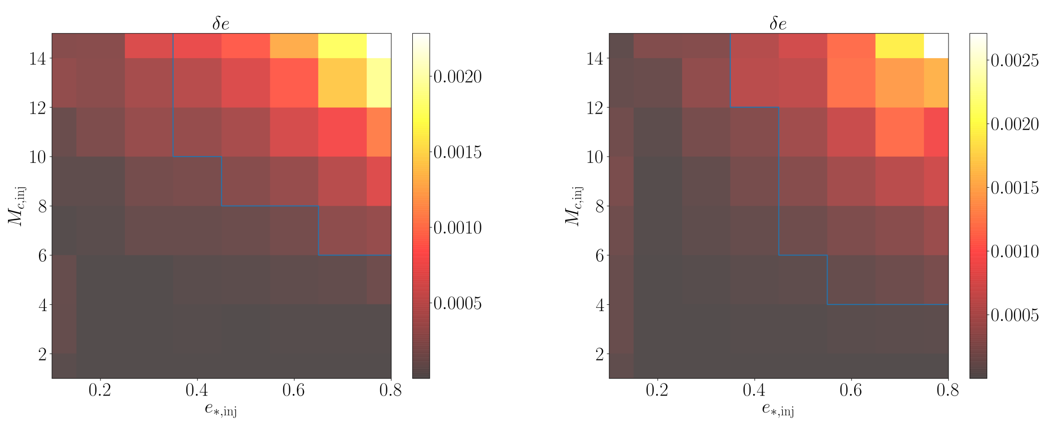

Figure 3.9: The systematic error described by Eq. (3.10). To the right of the blue line, the systematic error is larger than σ_{e_*} for an SNR 15 signal. Results for $\eta_{\rm inj} = 0.25$ (top) and 0.20 (bottom) are shown.

The parameter error seen here suggests that we require better modeling to accurately measure eccentricity, especially for more eccentric signals. In [119] we showed results that strongly suggest that the error in match between our TaylorF2e+ model and the fully numerical time-domain model are sourced by PN differences (and not eccentric series expansions). Moreover, this error was seen to become exacerbated by decreasing η and increasing eccentricity. This error in the match is what sources the systematic error we see here [68]. This was ultimately illustrated by computing the match with different equally PN valid time-domain waveforms. The results of this portion of our study supports the conclusion of that work: we require higher PN order corrections, or a different and more accurate PN-based model, to faithfully model eccentric sources and extract parameters when the eccentricity becomes large and systems have significantly unequal masses.

3.7 Conclusions & Future Work

We have explored the ability of aLIGO at design sensitivity to measure eccentricity in both the moderate and small eccentricity regime using our recently developed inspiral only, 3PN valid, eccentric waveform TaylorF2e. Generally, as the eccentricity of the signal increases, so does our ability to measure it with σ_{e_*} increasing from $\mathcal{O}(10^{-2})$ for small eccentricities ($e_* \sim 0.2$) to about $\mathcal{O}(10^{-4})$ for moderate eccentricities ($e_* \sim 0.6$). The accuracy to which the chirp mass can be measured ($\sigma_{\ln \mathcal{M}_c}$) also sees nearly a factor of ten improvement as the eccentricity of the signal increases from 0.1 to 0.4. For nearly-circular signals ($e_* \leq 0.05$), the eccentricity model parameter begins to become measurable already when $e_* \sim 0.008$, but this strongly depends on system mass, with lower mass systems having smaller detectable eccentricity thresholds.

Importantly, we discern regions of the $(\mathcal{M}_c, e_*)$ parameter space where the systematic error becomes larger than the statistical error. For low mass systems, the systematic error in our model is sufficiently low even when the eccentricity of the signal is as high as 0.8 (extrapolation of Figure 3.2 suggests that the model could be faithful out to eccentricities as high at 0.9 for a binary neutron star type system). As the signal-emitting system becomes more massive, the systematic error becomes large for eccentricities around 0.5 suggesting more faithful modeling in that regime is required. As the masses of the emitting binary becomes unequal, the systematic error also increases. In [119] we presented results that very strongly suggest that the source of this error is ultimately PN disagreement between otherwise equally valid waveforms. Thus, in order to decrease the systematic error in eccentric modeling, a better PN model is required.

As a result of the changes to model parameterization and approximation in the interest of model efficiency, we explored the model's validity in $(\mathcal{M}_c, e_*)$ in terms of the match and fitting factor. We have a model that is very faithful for moderate eccentricities, while still being highly efficient ($\sim$90ms per waveform evaluation). This means our model is realistically useful for data analysis techniques that require the computation of the likelihood many millions of times.

One large assumption of this work, the neglect of compact object spin, could qualitatively change our results. In the future, inclusion of spin in moderately eccentric waveforms should be considered. In addition, modeling of the merger and ringdown would complete the model and provide a more complete picture of our ability to constrain parameters by making the covariances between all parameters clearer. Without the full IMR model in hand, the model is not yet useful for data analysis purposes for the majority of the total masses seen in current detections. We have also assumed a single detector in this work and, as a result, we have merged source orientation parameters into a single overall amplitude. Further work should consider a network of detectors and investigate the effect of orbital eccentricity on sky localization.

Another important future study would investigate the convergence of all of the current eccentric gravitational wave models. Several independent groups have developed eccentric gravitational wave models to different levels of complexity in modeling the full signal. Many of the different existing waveforms use different approximations to get their final waveform, much like in circular, Taylor approximant family, but complicated by the effects of an extra parameter and periastron precession. Each of these waveforms have been studied with different metrics to gauge their validity, ranging from the match between itself and a model keeping one less term in the eccentric expansion, the match between a different eccentric model, and simple dephasing studies. The Simulating eXtreme Spacetimes (SXS) collaboration has recently introduced some NR simulations that include orbital eccentricity – albeit limited by the duration of signal and the ability to extract eccentricity from NR simulations. It is therefore high time to produce an exhaustive study that gauges the validity of all of these eccentric gravitational wave models with respect to one another to study the convergence of such models with a common metric of validity, like the match. This could be complimented with a study of how they match to current NR simulations, although due to the difficulty in extracting eccentricity in those simulations, one would likely need to compute the fitting factor instead.

An interesting extension of this work would be to extend the results of [43], where they incorporated leading-order eccentricity effects due to a particular scalar-tensor theory of gravity. The effect of eccentricity coupling to this theory leads to improved constraints on the particular theory, however that model was only valid in the small eccentricity regime. Incorporation of those effects into our model which is valid for larger eccentricities could yield an avenue for better constraints on that theory, given moderately eccentric detections.

Lastly, with the Laser Interferometer Space Detector (LISA) set to launch in the near future and other 3G detectors planned, and the expectation that these detectors will see many eccentric sources, it is highly important to gauge the validity and viability of this eccentric model for such detectors. It is plausible to expect that given these detectors increased sensitivities and diverse frequency bands, we might require even more accurate models, but also an improved ability to measure eccentricity.

Acknowledgments

B. M. was supported by the Joan L. Dalton Memorial Fellowship in Astronomy from Montclair State University. B. M. and N. Y. also acknowledge support from NSF PHY-1759615 and NASA ROSES grant 80NSSC18K1352. We thank Travis Robson and Neil Cornish for very useful conversations. Computational efforts were performed on the Hyalite High Performance Computing system, which is supported by University Information Technology at Montana State University.

3.A Corner Plots

In this appendix, we present a few select corner plots to get a complete picture of the results of other sections, which use the results of 100s of posteriors to paint a general picture of the likelihood surface. On the diagonal of the corner plots is the marginalized posterior, and on the off diagonals are the 2-D joint posteriors, which show the covariances between parameters.

Figure 3.10 presents the posteriors for a $(10, 10)M_{\odot}$ mass injection with injected eccentricities of 0.3 (top left), 0.6 (top right), and 0.8 (bottom left). Also shown in the bottom right is a a $(1.4, 1.4)M_{\odot}$ mass injection with injected eccentricity of 0.3. Each has a SNR of 15. We see that (with all else held fixed), as the eccentricity of the signal is increased, the posterior on $\ln \mathcal{A}$ is unchanged. This suggests that

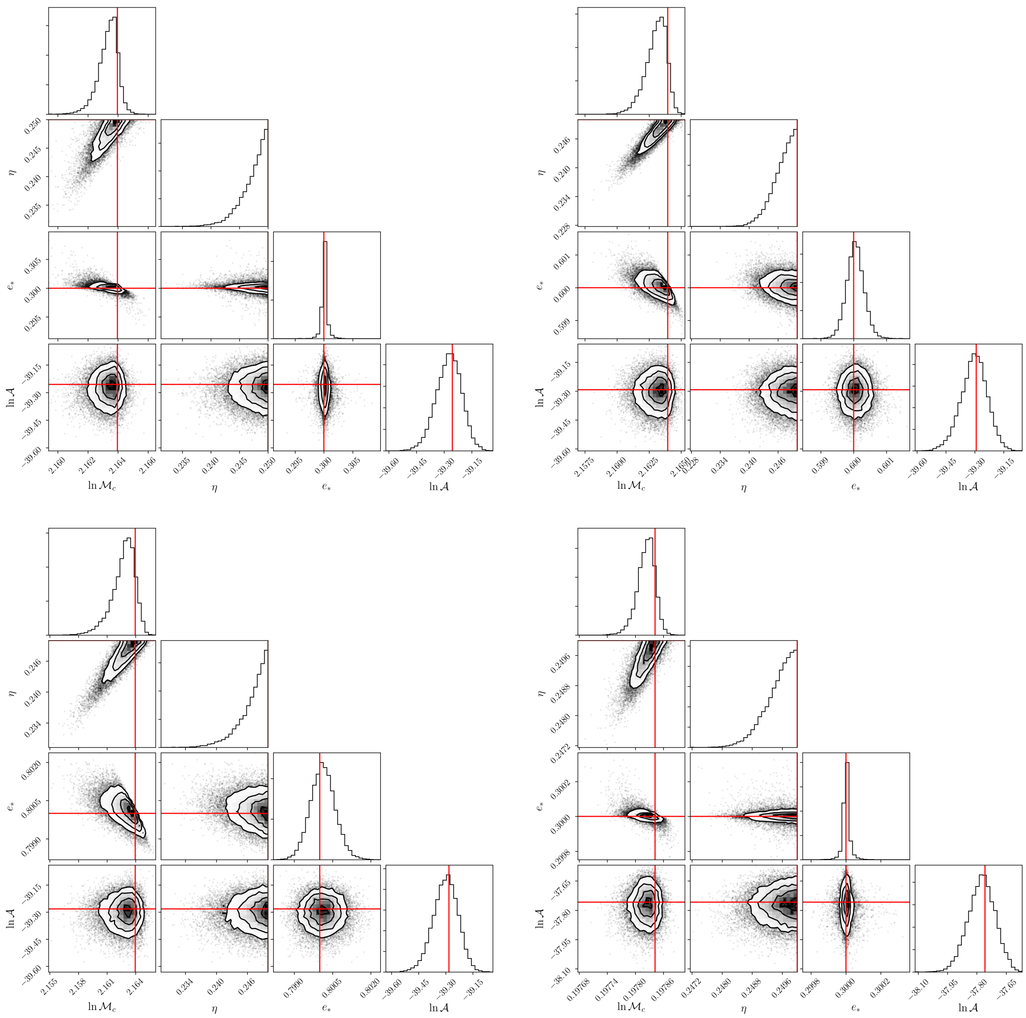

Figure 3.10: Posteriors for a SNR 15 signal with (1.4,1.4)$M_\odot$ (bottom right) and (10,10)$M_\odot$ (top, bottom left) masses. The red lines indicate injected values. Observe that most of the marginalized posterior appear fairly Gaussian in shape. As the injected eccentricity is increased, a stronger covariance between eccentricity and mass ratio develops. All posteriors are more closely clustered on the injected values in the low mass case.

measurement of the overall amplitude is mostly independent of eccentricity, though it is worth noting that this study only considers one detector. It is possible that with many detectors, eccentric effects could improve sky localization. As expected from the results of Sec. 3.4, the marginalized posteriors on eccentricity become more constraining as the eccentricity of the signal is increased, as well as when the mass is decreased. Interestingly, as the eccentricity of the signal increases, there is an increased covariance with chirp mass and eccentricity, as well as covariance with reduced mass ratio and eccentricity.

3.B Matches and Fitting Factors

In this appendix, we provide a few more measures of faithfulness for our two Fourier domain eccentric waveforms: TaylorF2e+ and TaylorF2e-, which are discussed in Sec. 3.2. We present the match and the fitting factor. The match is the waveform overlap maximized over extrinsic parameters. The fitting factor (FF) is the overlap maximized over all parameters (this is computed using the method to estimate maximum likelihood presented in Section 3.6).

Figure 3.11 shows the match between TaylorF2e- (our Fourier domain model which keeps less terms in the eccentric expansions appearing in the phases) and a fully numerically solved TaylorT4-like PN model. We see that this model has a match similar to the analogous result for the TaylorF2e+ model (which keeps more terms in eccentric expansions) as shown in Fig. 3.1. However, as the mass becomes small, TaylorF2e- is much less faithful, valid only for about half the eccentricities of the TaylorF2e+ model. This suggests that the TaylorF2e+ model should be used if trying to detect or measure parameters for low mass sources.

Figure 3.12 shows the fitting factor between the TaylorF2e+ model and our fully numerically-solved, time-domain PN model. We see that the fitting factor is

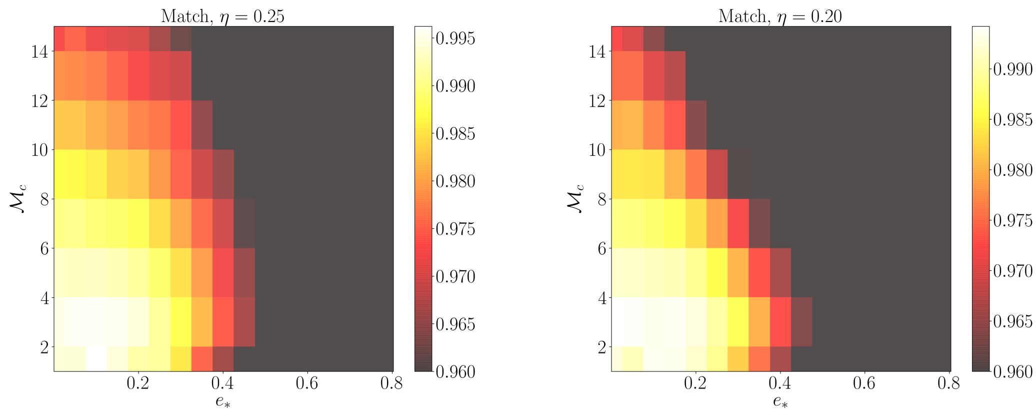

Figure 3.11: The match between the TaylorF2- model and a fully numerical time-domain model as a function of the chirp mass and e_* for $\eta = 0.25$ (left) and $\eta = 0.2$ (right). Values below 96% are excluded. Observe that in the low mass cases ($\mathcal{M}_c < 6$), this version of the model performs significantly worse than its TaylorF2e+ counterpart (which keeps more terms in various expansions in eccentricity) as shown in Figure 3.1.

particularly high even for very large eccentricities, provided that the system is low mass. Interestingly, there is little difference between the equal and unequal mass case (unlike in the match). The low fitting factors for high mass and eccentricity again points to the need for more accurate templates in this regime.

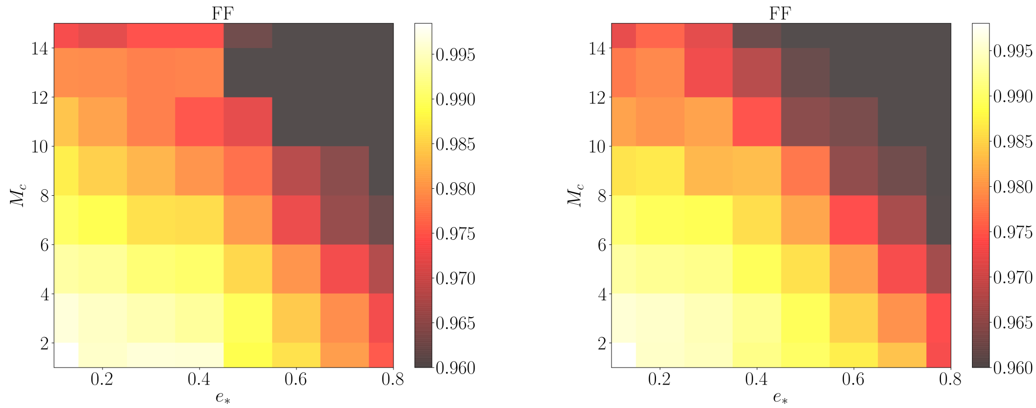

Figure 3.12: The fitting factor (FF) between the TaylorF2+ model and a fully numerical time-domain model as a function of the chirp mass and e_* for $\eta = 0.25$ (left) and $\eta = 0.2$ (right). Values below 96% are excluded. Observe that there is little difference in fitting factor between the equal and unequal mass cases. The fitting factor is greater than 97% for much of the explored parameter space.

CHAPTER FOUR

CONSTRAINING GRAVITY WITH ECCENTRIC GRAVITATIONAL WAVES: PROJECTED UPPER BOUNDS AND MODEL SELECTION

Contributions of Authors and Co-Authors

Manuscript in Chapter 4

Author: Blake Moore

Contributions: Wrote and ran code which produced data analysis deliverables. Analyzed results.

Author: Dr. Nicolas Yunes

Contributions: Conceived of design study and advised the project. Edited the manuscript.

Manuscript Information Page

Blake Moore, Nicolas Yunes

Classical and Quantum Gravity

Status of Manuscript:
____ Prepared for submission to a peer-reviewed journal
__X__ Officially submitted to a peer-reviewed journal
____ Accepted by a peer-reviewed journal
____ Published in a peer-reviewed journal

IOP Publishing
Submitted February 13th 2020

Abstract

Gravitational waves allow us to test general relativity in the highly dynamical regime. While current observations have been consistent with waves emitted by quasi-circular binaries, eccentric binaries may also produce detectable signals in the near future with ground- and space-based detectors. We here explore how tests of general relativity scale with the orbital eccentricity of the source during the inspiral of compact objects up to $e \sim 0.8$. We use a new, 3rd post-Newtonian-accurate, eccentric waveform model for the inspiral of compact objects, which is fast enough for Bayesian parameter estimation and model selection, and highly accurate for modeling moderately eccentric inspirals. We derive and incorporate the eccentric corrections to this model induced in Brans-Dicke theory and in Einstein-dilaton-Gauss-Bonnet gravity at leading post-Newtonian order, which suggest a straightforward eccentric extension of the parameterized post-Einsteinian formalism. We explore the upper limits that could be set on the coupling parameters of these modified theories through both a confidence-interval- and Bayes-factor-based approach, using a Markov-Chain Monte Carlo and a trans-dimensional, reversible-jump, Markov-Chain Monte Carlo method. We find projected constraints with signals from sources with $e \sim 0.4$ that are one order of magnitude stronger than that those obtained with quasi-circular binaries in advanced LIGO. In particular, eccentric gravitational waves detected at design sensitivity should be able to constrain the Brans-Dicke coupling parameter $\omega \gtrsim 3300$ and the Gauss-Bonnet coupling parameter $\alpha^{1/2} \lesssim 0.5$ km at 90% confidence. Although the projected constraint on ω is weaker than other current constraints, the projected constraint on $\alpha^{1/2}$ is 10 times stronger than the current gravitational wave bound.

4.1 Introduction

The Laser Interferometer Gravitational-Wave Observatory (LIGO), its Italian counter-part Virgo, and other soon to be operational ground based gravitational wave (GW) detectors are positioned to probe the validity of general relativity (GR) and modified theories of gravity in the dynamical and non-linear strong field regime [132, 133]. Indeed with the growing number of current detections [1], we have been able to constrain the mass of the graviton, generic parameterized post-Einsteinian (ppE) deviations in the waveform, and the number spacetime dimensions to name a few effects [134–136]. As we add new types of detectors and observe different types of sources, our ability to constrain modified gravity will only improve, as the strength of constraints depends heavily on the system observed.

A particularly powerful source to test GR would be eccentric compact binary inspirals, but can we observe these signals with ground-based detectors? All current observations are consistent with GWs produced by binaries in quasi-circular orbits [124, 125]. However, there are a number of astrophysical channels by which we expect a small number of eccentric observations. Most of these scenarios rely on many-body interactions, such as scattering or the Kozai-Lidov mechanism in dense stellar regions. The most promising dense stellar environments for eccentric binary formation are globular clusters and regions near supermassive black holes. Rough estimates show that from globular clusters we could expect around ~ 0.15 eccentric events per Gpc per year with advanced LIGO (aLIGO) at design sensitivity [6–9]. For the events around SMBH, about 0.5% are expected to have eccentricities greater than 0.1 when emitting GWs detectable by ground based detectors [62, 64, 127].

Even if one were able to observe GWs from eccentric compact binary inspirals, one may still wonder precisely what one gains from observing these signals as compared to observing quasi-circular inspirals. GWs from eccentric inspirals contain amplitude and phase modulations induced in part by precession that are typically absent in their quasi-circular counterparts. These modulations contain information that, if extracted properly, can lead to a more accurate and robust estimation of the parameters of the system. For example, eccentric signals can provide a factor of 1-2 improvement in sky localization [137, 138], and factors of 10 or more increase in accuracy of measurement of the source parameters [42, 139]. Naturally, following from the argument that eccentric binaries are formed in specific stellar regions, an ensemble of eccentric detections can provide constraints on formation scenarios with as little as tens of observations [44–46].

Eccentric signals could be an optimal source for validating GR and constraining alternative theories of gravity given the promising results in terms of sky localization and parameter measurement. References [140, 141] studied how projected constraints on several modified theories of gravity depend on eccentricity using space-based detectors. These papers, however, only considered weakly-eccentric (and weakly-spinning) compact binary inspirals, and thus, they ignored eccentric corrections to non-GR terms in the waveform model. This was because if the non-GR effect is assumed to be small, and if the eccentricity is assumed to be small, then eccentric corrections to non-GR terms are a second order effect, which was ignored in those papers. Reference [43] lifted this later assumption, calculating and incorporating eccentric corrections in the non-GR sector of the waveform explicitly. This paper confirmed that, at low eccentricity, covariances between non-GR and GR parameters in the waveform model deteriorate our ability to constrain GR; nonetheless, when the eccentricity of the signal is large enough, then these covariances begin to break, suggesting the constraints on non-GR effects could recover and become stronger than quasi-circular constraints for sufficiently eccentric observations. The study of

Ref. [43], however, was limited to mildly eccentric inspirals because the waveform model used became highly inaccurate of eccentricities larger than $e \sim 0.1$–0.2.

From the above summary, it should be clear that all previous studies have been limited to the small eccentricity regime because no model existed that was shown to be valid to high eccentricities, while remaining fast enough to carry out parameter estimation studies. In Ref. [119], we recently developed a 3 post-Newtonian (PN[1]) accurate waveform, TaylorF2e, to model the eccentric inspiral of compact binaries, which has been validated through a parameter bias and overlap study for eccentricities as high as ~ 0.8. Moreover, this waveform model is fast enough for use in parameter estimation studies, which employ Markov Chain Monte Carlo (MCMC) methods [139]. This model, therefore, provides the foundations on which to build non-GR eccentric waveforms and study how well we can test GR with moderately eccentric signals.

In this paper, we begin by deriving non-GR corrections to TaylorF2e due to leading PN order effects in (massless) Brans-Dicke (BD) and in Einstein-dilaton-Gauss-Bonnet (EdGB) theory. In BD theory, a dynamical scalar field couples to the physical (Jordan frame) metric to modify how massive (strongly self-gravitating) bodies move, thus violating the strong equivalence principle [132]. In EdGB theory[2], a dynamical scalar field couples to the curvature, also introducing violations to the strong equivalence principle [132]. In both of these theories, the dynamical scalar field introduces a -1PN modification to the rate of change of the orbital energy and angular momentum, which in turn changes the orbital dynamics and the GWs emitted.

With these corrections derived, we turn to analyzing the ability of a single

[1]A PN waveform is one constructed assuming small velocities and weak fields. In particular, a 3PN waveform is one which contains relativistic corrections of relative $\mathcal{O}(v^6/c^6)$ with respect to the controlling factor in the expansion [14].

[2]EdGB gravity defines a class of theories in which a dynamical scalar field couples non-minimally to the Gauss-Bonnet invariant in the action through a coupling function. We here study EdGB gravity with a linear coupling function, which is sometimes also referred to as scalar-Gauss-Bonnet gravity.

aLIGO detector (at design sensitivity) to constrain either theory. This is explored with two different techniques. One technique is to synthesize a GR signal injection and to attempt to recover it with a non-GR waveform template or model through an MCMC exploration of the likelihood function in Bayesian parameter estimation. After such an exploration, we can estimate an upper limit on the non-GR coupling parameter by explicitly calculating the confidence intervals from its marginalized posterior distribution. This is similar to a Fisher matrix analysis, except that the latter one assumes a Gaussian posterior and uses the standard deviation of that posterior to estimate confidence intervals. Another approach is to carry out a Bayes factor analysis to investigate at which value of the coupling parameter the effects of the alternative theory are significant enough such that the data supports the alternative theory over GR. Since such a study can be heavily influenced by the priors, we also explore how different priors can affect our results.

This work has led to two main results. First, in Eqs.(4.22) and (4.19) we provide the analytic expressions that are necessary to construct the Fourier transform of the GW response function in the TaylorF2e model for both BD theory and EdGB gravity. Interestingly, we find that the corrections due to both theories can be very simply mapped to one another through a relation between their coupling parameters. This suggests that a general formalism for eccentric waveforms where different theories can be mapped to the same set of corrections, like in the ppE formalism in [88], must exist. We also find that although previous studies found deteriorated constraints on alternative theories of gravity when including eccentricity, this is likely due to only working in the small eccentricity regime, as Ref. [43] hinted at. At higher eccentricities, the strong covariances between parameters, which sourced the deteriorated constraint, are broken, and the ability to constrain EdGB and BD increases by about one order of magnitude as the eccentricity of the signal is increased from 0 to ~ 0.4.

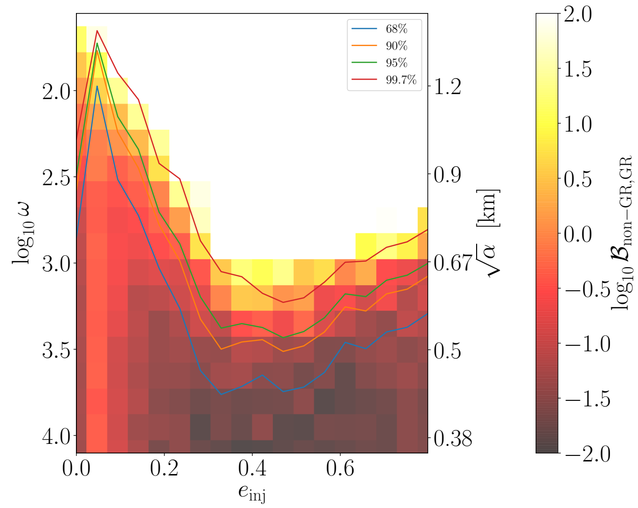

Figure 4.1: A heat plot of the Bayes factor in favor of the non-GR model as a function of injected eccentricity and injected non-GR coupling parameter on the y-axis for a $(10, 1.4)M_{\odot}$ system with SNR 30. Values above 2 and below -2 have been excluded. We have overplotted the upper bounds on the non-GR parameters obtained through requiring different confidence regions as indicated in the legend. In both the upper bounds from the confidence interval analysis and Bayes Factor analysis we see nearly an order of magnitude increased constraint on GR in Brans Dicke (ω) and about a factor of 2 in EdGB ($\sqrt{\alpha}$).

Figure 4.1 shows the projected (log-10)Bayes factor as a function of the injected coupling parameter of BD theory ω and EdGB gravity $\alpha^{1/2}$, and as a function of the orbital eccentricity of the signal for a source with component masses $(10, 1.4)M_{\odot}$ and SNR 30. This figure also shows upper bounds (confidence intervals) on the coupling parameters obtained through a Bayesian parameter estimation study. Observe that confidence limit constraints are consistent with the Bayes factor constraint, with a 3σ bound (99.7% confidence interval) corresponding roughly to a Bayes factor of 10. Observe also that our analysis suggests the best constraints come from the inspiral of compact binaries with orbital eccentricities of $e \sim 0.4$, leading to constraints on $\alpha^{1/2} \lesssim 0.6$ km and $\omega \gtrsim 10^3$ at 3σ; due to historical reasons, the GR limit is recovered when

$\omega \to \infty$. This deterioration of the constraint past eccentricities of 0.4 is consistent with the number of phase cycles in the signal. The latter initially increases as the number of harmonics of mean motion in the signal increases, because each harmonic contributes its own number of phase cycles. As the eccentricity is increased past ~ 0.4, the number of phase cycles begins to decrease because eccentric binaries inspiral faster.

How do these projected constraints compare to other current bounds on EdGB gravity and BD theory? The most robust and most stringent current bound on the EdGB coupling parameter $\alpha^{1/2}$ comes from a recent analysis of GW170608, which set a 90% bound of $\alpha^{1/2} \lesssim 5.6$ km [142]. This is to be compared with a projected 90% bound in Fig. 4.1, namely $\alpha^{1/2} \lesssim 0.5$ km for a signal with $e \sim 0.4$, which is about one order of magnitude stronger. On the other hand, the most stringent constraint currently placed on the BD coupling parameter ω comes from measuring the frequency shift of radio photons as they passed near the Sun to and from the Cassini spacecraft, which sets $\omega \gtrsim 40,000$ [143] at 95% confidence. Our projected constraints in Figure 4.1 are not a strong as the Cassini bound ($\omega \gtrsim 2700$) at 95% confidence, even when the GW constraint is boosted by the effects of orbital eccentricity in the signal.

The paper is organized as follows. In Section 4.2 we derive the EdGB and BD eccentric corrections to the orbital dynamics and frequency response. Section 4.3 presents the Bayesian framework for our analysis, the notation used, and derives some useful approximations. The results of our model selection and confidence interval based approaches to exploring the ability of eccentric signals to constrain EdGB and BD are presented in Section 4.4. Lastly we point to interesting future extensions suggested by this work and general conclusions in Section 4.5. Throughout we have set $c = G = 1$.

4.2 Modified Gravity Corrections to Eccentric Signals

In this section, we present the incorporation and derivation of the effects of EdGB and BD gravity into our existing 3PN GR eccentric waveform. We will not provide here a detailed description of BD or EdGB theory, but instead refer the interested reader to [132]. Each of these theories introduce a dynamical scalar field in the Einstein-Hilbert action, which in BD is sourced by the matter stress energy tensor, while in EdGB by a curvature-squared invariant. In turn, these theories both admit dipole radiation, which adds corrections to the energy and angular momentum flux of the binary, and therefore, changes to the gravitational waveform. We work to leading PN order in the non-GR corrections while retaining the 3PN accuracy in the GR sector of our eccentric model derived in [119] and optimized in [139]. We find here that because the non-GR corrections take a similar form at this order it is simple to map the corrections induced by the two theories to one another.

In order to obtain the eccentric non-GR corrections to the frequency response, we follow the prescription laid out in [119] and optimizations laid out in [139]. The 3PN valid eccentric model schematically takes the form:

$$\tilde{h}(f) = \mathcal{A} \sum_{j=-1}^{15} N_j \sqrt{\frac{y^{-7}}{(j+2)(96+292e^2+37e^4)}} e^{i\psi_j} \,, \tag{4.1}$$

where the j^{th} Fourier phase is given by

$$\psi_j = 2\pi f t(e) - j l(e) - 2\lambda(e) - \frac{\pi}{4} \,. \tag{4.2}$$

In the above, $\mathcal{A}$ is an overall amplitude term which depends on the masses, distance to source, and source orientation. The N_j are harmonic amplitudes which control the contribution of each harmonic and scale as $e^{|j|}$. Our post-Newtonian expansion parameter y is related to the semi-latus rectum (p) and orbital frequency (ω) by:

$$y = \sqrt{\frac{M}{p}} = \frac{(M\omega)^{1/3}}{\sqrt{1-e^2}} \,. \tag{4.3}$$

Here and above we work with the time-eccentricity $e_t = e$, ω is the azimuthal orbital frequency and M is the total mass of the system. To specify each of the Fourier phases we must model the different phase functions appearing in Eq.(4.2): the time to coalescence $t(e)$, the mean anomaly $l(e)$, and $\lambda(e)$, which is an orbital angle related to the azimuthal orbital frequency ω. Since, at 1PN order, eccentric orbits undergo periastron precession, there are two comparable orbital scales. One is related to the azimuthal period (P_ϕ), and the other is related to the radial period, related to the periastron to periastron period (P_r). These two differing scales give rise to the orbital angles $\lambda(e)$ and $l(e)$ respectively, and the orbital frequencies ω and n.

Our strategy is to specify all of the functions appearing in Eq. (4.1) analytically in terms of the eccentricity. This can succinctly be seen as solving the following set of equations:

$$y(e) = \int^e \frac{dy}{de'} de' \,, \tag{4.4a}$$

$$t(e) = \int^e \frac{dt}{de'} de' \,, \tag{4.4b}$$

$$\lambda(e) = \int^e \omega(e') \frac{dt}{de'} de' \,, \tag{4.4c}$$

$$l(e) = \int^e n(e') \frac{dt}{de'} de' \,. \tag{4.4d}$$

In the above, the two orbital frequencies n and ω as well as dt/de are originally functions of both y and e, so first $y(e)$ must be specified (i.e. Eq. (4.4a) must be solved first). Then, $y(e)$ is substituted into the integrands of the phase functions in Eqs. (4.4b)-(4.4d), and the integrands are expanded in eccentricity and finally integrated. We then map Fourier frequency to the eccentricity using the stationary phase condition. For much more detail in deriving these corrections and computing the Fourier response, see [119].

In order to solve Eqs. (4.4a)-(4.4d) with the non-GR corrections, we introduce a small parameter κ that vanishes in the GR limit and takes a small, but non-zero value in the non-GR theory. We then expand to leading order in κ and to leading PN order in the corrections that are proportional to κ. The theories we work with here are already constrained to the level that higher PN order corrections will not change the conclusions of our work (see e.g. Appendices A and B in [144] for the effect of higher PN order terms in inspiral waveforms for tests of GR). The integrands in Eqs. (4.4a)-(4.4d) are then given as a series in κ and e. This will then provide a set of non-GR corrections that are linearly proportional to κ: $y_\kappa(e)$, $t_\kappa(e)$, $l_\kappa(e)$, and $\lambda_\kappa(e)$, from which we can specify the full function to be used in the frequency response as $y(e) = y_{\rm 3PN,GR}(e) + y_\kappa(e)$ and so forth for the other necessary functions. We use the 3PN accurate functions for the GR corrections given in [119]. In Sec. 4.2.1 we compute in more detail the non-GR corrections to $\dot{e}$ and $\dot{y}$ required to form the integrands in Eqs. (4.4a)-(4.4d). In Sec. 4.2.2 we solve Eqs. (4.4a)-(4.4d) and give the explicit functional forms of $y_\kappa(e)$, $t_\kappa(e)$, $l_\kappa(e)$, and $\lambda_\kappa(e)$ that are used in our analysis.

4.2.1 Orbital Dynamics

Here we derive the differential equations $\dot{y}$ and $\dot{e}$ that are used to express the integrands in Eqs. (4.4a)-(4.4d) in terms of only e and constants in both EdGB and BD. In order to derive these equations we start with the expressions for the binding energy, E, and the angular momentum, L, of the binary and their time derivatives.

In BD theory, the binding energy and (the $\hat{z}$ component of the) angular momentum at leading PN order are left unchanged from GR, and are thus given by:

$$E_{\rm GR} = \frac{M\eta}{2}(e^2-1)y^2\,, \tag{4.5a}$$
$$L_{\rm GR} = \frac{M^2\eta}{y}\,. \tag{4.5b}$$

The rate of change of these two quantities, however, is modified in BD theory, and in our notation they take the form $\dot{E} = \dot{E}_{\rm GR} + \dot{E}_{\rm BD}$ and $\dot{L} = \dot{L}_{\rm GR} + \dot{L}_{\rm BD}$, where the GR fluxes are [31]

$$\dot{E}_{\rm GR} = -\frac{1}{15}\eta^2 y^{10}(1-e^2)^{3/2}(96+292e^2+37e^4)\,, \tag{4.6a}$$
$$\dot{L}_{\rm GR} = -\frac{4}{5}M\eta^2 y^7(1-e^2)^{3/2}(8+7e^2)\,, \tag{4.6b}$$
$$\tag{4.6c}$$

and the BD corrections are

$$\dot{E}_{\rm BD} = -\frac{32}{5}\eta^2 b y^8(1-e^2)^{3/2}\left(1+\frac{e^2}{2}\right)\,, \tag{4.7a}$$
$$\dot{L}_{\rm BD} = -\frac{32}{5}M\eta^2 b y^5(1-e^2)^{3/2}\,. \tag{4.7b}$$

to leading order in κ and to leading PN order. The BD corrections here follow the conventions of [145], where $b = 5\mathcal{S}_{\rm BD}^2/48\omega_{\rm BD}$, $\mathcal{S}_{\rm BD}$ is the sensitivity difference of the two objects ($\mathcal{S}_{\rm BD} = s_1 - s_2$), and $\omega_{\rm BD}$ is the BD coupling parameter, which goes to infinity in the GR limit. In this theory, black holes have $s_{\rm BH} = 0.5$, and neutron stars have sensitivities of $s_* \sim 0.15$, depending on their equation of state.

With this at hand, we can now compute $\dot{y}$ and $\dot{e}$ in terms of y and e. To do so, we use implicit differentiation, $\dot{y}$ and $\dot{e}$ in terms of $\dot{E}$ and $\dot{L}$ through Eqs. (4.5), then substitute $\dot{E}$ and $\dot{L}$ with Eqs. (4.7). The result is then expanded to leading order in a $b \ll 1$ expansion. We are also considering the GR terms up to 3PN order for our later analysis, but for readability and simplicity of deriving the non-GR terms, we will here omit the GR higher order PN terms here. We then have $\dot{y} = \dot{y}_{\rm GR} + \dot{y}_{\rm BD}$ and $\dot{e} = \dot{e}_{\rm GR} + \dot{e}_{\rm BD}$, where the GR terms are

$$\dot{y}_{\rm GR} = \frac{4}{5}\frac{\eta}{M} y^9 (1-e^2)^{3/2}(8+7e^2)\,, \tag{4.8a}$$
$$\dot{e}_{\rm GR} = -\frac{1}{15}\frac{\eta}{M} y^8 e (1-e^2)^{3/2}(304+121e^2)\,, \tag{4.8b}$$

and the BD corrections re

$$\dot{y}_{\rm BD} = \frac{32}{5}\frac{\eta}{M} b y^7 (1-e^2)^{3/2}\,, \tag{4.9a}$$
$$\dot{e}_{\rm BD} = -\frac{48}{5}\frac{\eta}{M} b y^6 e (1-e^2)^{3/2}\,. \tag{4.9b}$$

The BD corrections enter at -1PN order relative to the GR terms, which suggests their effect may be large enough to be constrainable. With this in hand, we are now in a position to solve Eqs. (4.4) to prescribe the Fourier response, but let us first derive similar corrections in the orbital dynamics for EdGB gravity.

As in BD theory, the binding energy and (the $\hat{z}$ component of the) angular momentum in EdGB gravity are not modified to leading PN order [31]. This then means that these quantities can be approximated by their GR expressions, which at leading PN order were given in Eq. (4.5). The fluxes of energy and angular momentum, however, are modified in EdGB gravity to $\dot{E} = \dot{E}_{\rm GR} + \dot{E}_{\rm EdGB}$ and $\dot{L} = \dot{L}_{\rm GR} + \dot{L}_{\rm EdGB}$ [31], where $\dot{E}_{\rm GR}$ and $\dot{L}_{\rm GR}$ are given in Eqs. (4.6), while

$$\dot{E}_{\rm EdGB} = -\frac{\eta^2}{3}\mathcal{S}^2_{\rm EdGB} y^8 (1-e^2)^{3/2}\left(1+\frac{e^2}{2}\right)\,, \tag{4.10a}$$

$$\dot{L}_{\rm EdGB} = -\frac{M\eta^2}{3}\mathcal{S}^2_{\rm EdGB}y^5(1-e^2)^{3/2}\,, \tag{4.10b}$$

where $\mathcal{S}_{\rm EdGB} = \zeta_1^{1/2} - \zeta_2^{1/2}$ and $\zeta_{1,2} = \xi/m_{1,2}^4$ are dimensionless deformation parameters, with $\xi = 16\pi\alpha^2$ and α the EdGB coupling parameter with units of length squared. If one of the objects is a neutron star, its associated ζ_n vanishes, and modifications to the fluxes of energy and angular momentum enter at higher PN order.

As in the BD theory case, we can use implicit differentiation to solve the system of equations for $\dot{y}_{\rm EdGB}$ and $\dot{e}_{\rm EdGB}$. The GR corrections were given in Eqs. (4.8a)-(4.8b) already, so here we only list the corrections due EdGB gravity:

$$\dot{y}_{\rm EdGB} = \mathcal{S}^2_{\rm EdGB}\frac{\eta}{3M}y^7(1-e^2)^{3/2}\,, \tag{4.11a}$$

$$\dot{e}_{\rm EdGB} = -\mathcal{S}^2_{\rm EdGB}\frac{\eta}{2M}y^6 e(1-e^2)^{3/2}\,. \tag{4.11b}$$

By inspection of Eqs. (4.9) and (4.11) we realize that there is a simple mapping between the equations $\dot{y}$ and $\dot{e}$ between the two theories: $96b = 5\mathcal{S}^2_{\rm EdGB}$. This suggests that we ought to parameterize $\dot{y}$ and $\dot{e}$ in terms of a small parameter κ which can be mapped to either theory via $\kappa = 96b$ to map to BD theory or $\kappa = 5\mathcal{S}^2_{\rm EdGB}$ to map to EdGB provided

$$\dot{y}_\kappa = \kappa\frac{\eta}{15M}y^7(1-e^2)^{3/2}\,, \tag{4.12a}$$

$$\dot{e}_\kappa = -\kappa\frac{\eta}{10M}y^6 e(1-e^2)^{3/2}\,. \tag{4.12b}$$

Moving forward we present phasing results in terms of κ, as it is very simple to convert the results to either of the theories through the above mapping.

In what regime in κ are we justified in treating the corrections introduced by the modified theories as a small deformation of the PN dynamics? This region is defined by requiring that the non-GR corrections to the orbital dynamics $(\dot{y}, \dot{e})$ be smaller than the GR PN dynamics. The most conservative estimate of where our expansions in κ are valid can be found from

$$\dot{y} = \frac{32}{5}\frac{\eta}{M}\left(y^9 + \kappa\frac{y^7}{96}\right), \tag{4.13}$$

where we have assumed circularity for simplicity. Inspection of the above equation suggests that our expansion is valid provided $\kappa \ll 96y^2$. Assuming circularity again, we can define the region in which the expansion in κ is valid to be

$$\kappa \ll 0.06 \left(\frac{M}{M_\odot}\right)^{2/3}\left(\frac{f_{\rm low}}{1\text{ Hz}}\right)^{2/3}, \tag{4.14}$$

where in the above $f_{\rm low}$ is the lower frequency cutoff of the detector. For a $(10,10)M_\odot$ or $(1.4,1.4)M_\odot$ system with a detector lower frequency cutoff of 10Hz, this translates to $\kappa \ll 2.04$ and 0.550 respectively, while for a system with $M = 10^6 M_\odot$ and a detector with $f_{\rm low} = 10^{-5}$Hz, Eq. (4.14) implies $\kappa \ll 0.276$. If we take the more conservative of the bounds for the aLIGO-like sources, we can then set $\omega \gg 0.182$ (assuming $\mathcal{S}_{\rm BD} \sim \mathcal{O}(10^{-1})$). Current constraints place us well within this small κ limit, and our region of interest for our Bayesian analysis will lie within this limit.

The mapping between κ and α depends strongly on the mass difference and whether one of the objects is a neutron star. In this paper we explore an optimal system with component masses $(1.4,10)M_\odot$. The expansions in κ are then valid when $\alpha^{1/2} \ll 4$ km when we assume $f_{\rm low} = 10$ Hz and that the NS is not (monopolarly) charged under the scalar field (as is the case in EdGB gravity). Reference [142] used GW170608 to place a 90% constraint on EdGB of $\alpha^{1/2} < 5.6$ km using the GWs emitted by quasi-circular binary; for such a binary, this constraint is at the edge of the region of validity of the small coupling approximation. Do note, however, that

$\alpha^{1/2}$ scales as $\kappa^{1/4}$ so an order of magnitude difference in $\alpha^{1/2}$ scales as 2 orders of magnitude in κ. Thus, we could be working just below these limits and still be well within the limit on κ. In our Bayesian analysis we place an upper limit on the prior on κ which ensures we are working well within the limit where our expansions in κ can be treated as a deformation of the PN GR dynamics.

Let us now make some general comments regarding the above modified gravity modifications to the rate of change of the PN parameter y and the eccentricity e. Since both y and e are dimensionless, on general grounds we would expect $\dot{e}_\kappa$ and $\dot{y}_\kappa$ to be proportional to M^{-1}. Moreover, since we assume the deformation from GR possesses a continuous GR limit, and the deformation is small (in the sense that we can linearize about the GR background), then both of these rates of change must be linear in κ. Furthermore, since the modifications to the energy and angular momentum fluxes we are considering are both of -1PN order relative to GR, we then expect $\dot{y}_\kappa \sim y^7$ and $\dot{e}_\kappa \sim y^6$. Whether general principles can be used to deduce the η, and especially the e dependence of $\dot{y}_\kappa$ and $\dot{e}_\kappa$ requires further study. Either way, the above analysis suggests that a ppE generalization of the TaylorF2e model is possible.

4.2.2 Frequency Response

Let us proceed by using the expressions for $\dot{y}_\kappa$ and $\dot{e}_\kappa$ to produce the non-GR corrections to the functions required to compute the frequency response set forth in Eqs. (4.4): y_κ, t_κ, l_κ, λ_κ. For compactness we will often not give the GR expressions for these functions as they can be found in [119] and [103]. Let us first derive an analytic solution for the frequency evolution as a function of eccentricity, $y(e)$. This is obtained by direct integration of $dy/de = \dot{y}/\dot{e}$, employing expansions in $\kappa \ll 1$ throughout.

Expanding dy/de to leading order in κ and integrating yields an exact solution:

$$y(e) = \sqrt{\frac{C_1}{e^{12/19}(304+121e^2)^{870/2299}} - \kappa\left[\frac{396720}{1429(304+121e^2)} - \frac{3230{}_2F_1(\frac{84}{121},1;\frac{25}{19};-\frac{121}{304}e^2)}{4287}\right]}, \tag{4.15}$$

where ${}_2F_1(a,b;c;z)$ is the ordinary hypergeometric function. The constant of integration, C_1, is determined by requiring that $y(e_0) = y_0$:

$$C_1 = e_0^{12/19}(304+121e_0^2)^{870/2299}\left\{y_0^2 - \kappa\left[\frac{396720}{1429(304+121e_0^2)} - \frac{3230{}_2F_1(\frac{84}{121},1;\frac{25}{19};-\frac{121}{304}e_0^2)}{4287}\right]\right\}. \tag{4.16}$$

After plugging in this constant into Eq. (4.15) and expanding to leading order in κ we have

$$y_{\rm GR}(e) = \frac{e_0^{6/19}\left(121e_0^2+304\right)^{435/2299}y_0}{e^{6/19}\left(121e^2+304\right)^{435/2299}} \tag{4.17}$$

$$\begin{aligned} y_\kappa(e) = 5\kappa &\left\{5168\left(\frac{121e^2}{304}+1\right)^{1429/2299} e_0^{12/19}\left(\frac{121e_0^2}{304}+1\right){}_2F_1\left(\frac{84}{121},1;\frac{25}{19};-\frac{121e_0^2}{304}\right)\right. \\ &-5168e^{12/19}\left(\frac{121e^2}{304}+1\right)\left(\frac{121e_0^2}{304}+1\right)^{1429/2299}{}_2F_1\left(\frac{84}{121},1;\frac{25}{19};-\frac{121e^2}{304}\right) \\ &\left.+6264\left[\left(\frac{121e^2}{304}+1\right)^{1429/2299} e_0^{12/19} - e^{12/19}\left(\frac{121e_0^2}{304}+1\right)^{1429/2299}\right]\right\} \\ &\times\left[20851968e^{6/19}\left(\frac{121e^2}{304}+1\right)^{1864/2299} e_0^{6/19}\left(\frac{121e_0^2}{304}+1\right)^{1864/2299}y_0\right]^{-1} \end{aligned} \tag{4.18}$$

While the above equation is exact, the sampling of the hypergeometric functions can become costly and we found in [103] that these special functions could very faithfully be represented, even to high eccentricities, in a low eccentricity expansion without keeping a computationally prohibitive number of terms. To be consistent, we choose to also expand all other terms in eccentricity as well. What results for the expanded

κ correction to y is the sum of two Taylor series with different controlling factors,

$$
\begin{aligned}
y_\kappa(e) = &-\frac{5\kappa e^{6/19}}{1824 e_0^{6/19}\left(\frac{121e_0^2}{304}+1\right)^{435/2299} y_0}\left(1-\frac{17163e^2}{72200}+\frac{72226161e^4}{917459840}\right.\\
&\left.-\frac{447503490791e^6}{15897744107520}+\frac{79594709788763e^8}{7652114163752960}-\frac{69877537192796697791e^{10}}{1785623900957418717 1840}\right)\\
&+\frac{5\kappa e_0^{6/19}\left[646\left(\frac{121e_0^2}{304}+1\right){}_2F_1\left(\frac{84}{121},1;\frac{25}{19};-\frac{121e_0^2}{304}\right)+783\right]}{2606496 e^{6/19}\left(\frac{121e_0^2}{304}+1\right)^{1864/2299} y_0}\\
&\times\left(1-\frac{435e^2}{5776}+\frac{594645e^4}{33362176}-\frac{997616095e^6}{192699928576}+\frac{1828630302135e^8}{1113034787454976}-\frac{3522307687972437e^{10}}{6428888932339941376}\right).
\end{aligned}
\tag{4.19}
$$

We keep the hypergeometric function which is a function of the initial eccentricity e_0 unexpanded as this need only be evaluated once per entire waveform generation so its cost is negligible. Note that although the second term above scales as e^{-6}, it obviously does not diverge faster as $e \to 0$ than the GR term, which as we can see in Eq. (4.17) diverges at the same rate.

With $y(e)$ now in hand, we seek the phase functions $t(e)$, $l(e)$, and $\lambda(e)$ which were introduced in Eqs. (4.4). For simplicity we will only list the non-GR contributions $t_\kappa(e)$, $l_\kappa(e)$, and $\lambda_\kappa(e)$. Since we are working at leading PN order in the non-GR terms and periastron precession is a 1PN effect we have then that

$$
l_\kappa(e) = \lambda_\kappa(e) = \int^e \left[\frac{y(e')^3(1-e'^2)^{3/2}}{M}\frac{dt}{de'}\right]_\kappa de' \,, \tag{4.20}
$$

where $[\quad]_\kappa$ is shorthand notation for the expansion of the term within the brackets in $\kappa \ll 1$ and taking only the term which scales as κ (as the term which scales as κ^0 is the GR term which has already been derived in the literature). Likewise for $t_\kappa(e)$

then

$$t_\kappa(e) = \int^e \left[\frac{dt}{de'}\right]_\kappa de' \,, \tag{4.21}$$

where in Eqs. (4.20) and (4.21) it is understood that we have substituted Eq. (4.17) into the integrands in order to obtain them as functions of the eccentricity and constants only. Some of the terms which appear in these integrands can be integrated directly giving rise to AppellF1 functions and more ${}_2F_1$ hypergeometric functions; however, since we intend to series expand these expressions in $e \ll 1$, and since series expansion and integration commute in our case (due to the uniform nature of the expansions), it is generally simpler to expand the integrands in eccentricity first, and then integrate the result. These integrations yield a similar structure to that of Eq. (4.19):

$$\begin{aligned}
l_\kappa(e) = {} & -\frac{5\kappa e^{42/19}}{25536 e_0^{42/19}\left(\frac{121e_0^2}{304}+1\right)^{3045/2299}\eta y_0^7}\left(1-\frac{132027e^2}{1848320}+\frac{293611227e^4}{21652052224}\right.\\
& \left.-\frac{2213979348413e^6}{661346154872832}+\frac{2223905948814193e^8}{2375216236428918784}-\frac{1867393272311822254223e^{10}}{6628235920353938278187008}\right)\\
& +\frac{25\kappa e^{30/19}\left(646\left(\frac{121e_0^2}{304}+1\right){}_2F_1\left(\frac{84}{121},1;\frac{25}{19};-\frac{121e_0^2}{304}\right)+783\right)}{83407872 e_0^{30/19}\left(\frac{121e_0^2}{304}+1\right)^{4474/2299}\eta y_0^7}\\
& \times\left(1-\frac{465e^2}{49096}+\frac{1126695e^4}{884097664}-\frac{295569655e^6}{1156199571456}+\frac{889369091895e^8}{14469452236914688}\right.\\
& \left.-\frac{290112197776149e^{10}}{17679444563934838784}\right) \,,
\end{aligned} \tag{4.22a}$$

$$\begin{aligned}
t_\kappa(e) = {} & -\frac{31\kappa e^{60/19} M}{116736 e_0^{60/19}\left(\frac{121e_0^2}{304}+1\right)^{4350/2299}\eta y_0^{10}}\left(1+\frac{526002e^2}{548359}+\frac{83906652315e^4}{96700267136}\right.\\
& \left.+\frac{25781287733225e^6}{32481981710592}+\frac{2381368804696359 65e^8}{324449640543125504}+\frac{2371064777915453655463 21e^{10}}{345964630810499876454400}\right)+\\
& \frac{25\kappa e^{48/19}\left(646\left(\frac{121e_0^2}{304}+1\right){}_2F_1\left(\frac{84}{121},1;\frac{25}{19};-\frac{121e_0^2}{304}\right)+783\right)M}{83407872 e_0^{48/19}\left(\frac{121e_0^2}{304}+1\right)^{5779/2299}\eta y_0^{10}}
\end{aligned}$$

$$\times\left(1+\frac{29535e^2}{31046}+\frac{216378255e^4}{258556864}+\frac{181644301 95e^6}{24087491072}\right.$$
$$\left.+\frac{1920648415789053e^8}{2782586968637440}+\frac{611977649049927940 77e^{10}}{95629722868556627968}\right). \tag{4.22b}$$

Now, since the functions $y_\kappa(e)$, $t_\kappa(e)$, $l_\kappa(e)=\lambda_\kappa(e)$ have been determined analytically in terms of e, we are able to simply add them to the already-computed (and validated in [119]) expressions for $y_{\rm 3PN,GR}(e)$, $t_{\rm 3PN,GR}(e)$, $l_{\rm 3PN,GR}(e)$, and $\lambda_{\rm 3PN,GR}(e)$. For details on the efficient generation of the model see [139].

4.3 Bayesian Framework

In this section, we review the techniques we use for our Bayesian statistical analysis of the non-GR terms. We wish to gauge when the non-GR terms are detectable and what constraints we can place on these theories and their parameters. These two questions are subtly different. In gauging when the non-GR terms are detectable, we would like to avoid assuming which model (GR or non-GR) is true *a priori*, and instead, let the data decide. To investigate this question, we can then inject synthetic non-GR signals with varying strengths of the non-GR coupling parameter, and attempt to recover them with both a GR and a non-GR model. A trans-dimensional RJMCMC exploration of the likelihood surface then allows us to compute the Bayes factor in favor of the GR model relative to the non-GR model (or viceversa), given the injected data. Such a study then reveals the value of the coupling parameter at which one would be able to tell that a non-GR effect is present in the data. Alternatively, we can investigate what constraints we can place on the coupling parameters of a non-GR theory, if the signals detected are determined to be consistent with GR. For such a study, we can simulate various GR injections and then carry out a parameter estimation study with a non-GR model. An MCMC exploration of the likelihood surface then allows us to compute the marginalized posterior on the non-GR coupling parameter, and from this extract a projected constraint in terms of a confidence region.

Let us describe each of these approaches in more detail, starting with the calculation of projected constraints in terms of confidence regions. In producing confidence intervals, we first obtain the full joint posterior, $p(\boldsymbol{\theta}|d, M)$, which is the probability of the set of parameters ($\boldsymbol{\theta}$) in a model to reproduce the given the data (d) with the model (M). For our non-GR model, the parameters are $\boldsymbol{\theta} = \{M_c, \eta, e_*, \mathcal{A}, \kappa\}$ where M_c is the chirp mass, η is the dimensionless mass ratio, $\mathcal{A}$ is an overall amplitude depending on source orientation and distance to source, and κ is the non-GR parameter introduced in Sec. 4.2, which can be mapped to either the BD or EdGB theory. The eccentricity parameter e_* sets both e_0 and p_0 (or equivalently e_0 and y_0). This parameter is defined to be the eccentricity when the binary has a semilatus rectum corresponding to that of a circular binary emitting GWs at 10Hz. An eccentric signal is composed of many harmonics emitting at several Fourier frequencies at any given time, so a single eccentricity cannot be identified with a single Fourier frequency for all harmonics. As a result, we choose to parameterize our model in terms of e_*, which specifies a reference ellipse from which we can compute the relevant frequency response for each harmonic. For more discussion on the parameter e_* see [139].

An MCMC algorithm produces samples of the joint posterior, $p(\boldsymbol{\theta}|d, M)$, via a random walk through parameter space. Proposed "steps" for the sampler are drawn from a proposal distribution. The proposed jump is accepted based on a transition kernel, which depends on the prior distribution and the likelihood evaluated both at the current location in parameter space and at the proposed location. Here the likelihood is designed to be consistent with Gaussian noise when evaluated at the correct model that reproduces the signal exactly [146]:

$$\mathcal{L}(\theta) \sim \exp\left\{-\frac{1}{2}(d-h(\theta)|d-h(\theta))\right\}\,, \tag{4.23}$$

where the inner product between signals is given by

$$(h_1|h_2) = 4\mathrm{Re}\int \frac{\tilde{h}_1^*\tilde{h}_2}{S_n(f)}df\,. \tag{4.24}$$

In the above "Re" stands for the real part operator, the overhead tilde stands for the Fourier transform, and $S_n(f)$ is the spectral noise density of the detector. In this work we use spectral noise of aLIGO at designed sensitivity (zero-detuned, high-power), and assume stationary, Gaussian noise when computing the likelihood. We also maximize the likelihood over time and phase constants (t_c, l_c, λ_c). The signal to noise ratio (SNR) of a signal h is given by $\mathrm{SNR}^2 = (h|h)$.

In order to produce a one dimensional posterior, which represents the probability that a given parameter θ^i in a given model can reproduce the data $(p(\theta^i))$, we marginalize the joint posterior over all other parameters,

$$p(\theta^i) = \int p(\boldsymbol{\theta}|d, M)\prod_{k\neq i} d\theta^k\,. \tag{4.25}$$

In order to produce confidence intervals that set an upper limit on a parameter θ^i we integrate the probability density, $p(\theta^i)$ from $\theta^i = 0$ to an upper bound $\theta^i = \theta^i_*$ which is determined by requiring a cumulative probability Δ:

$$\int_0^{\theta^i_*} p(\theta^i) = \Delta\,, \tag{4.26}$$

where Δ is the desired probability interval (e.g. for a 90% confidence interval, $\Delta =$

0.9).

Given all of this machinery, we can now explain how we obtain our confidence intervals to estimate projected constraints on a non-GR parameter. First, we use a signal, d, synthesized within GR ($\kappa = 0$), and use an MCMC to explore the parameters of a non-GR model ($\kappa \neq 0$). This exploration leads to a joint posterior distribution, from which we can compute the marginalized posterior on κ, $p(\kappa)$. This marginalized posterior will be centered at zero, and we can then use it to produce upper bounds via confidence intervals through Eq. (4.26). Confidence-interval constraints on κ can then be mapped to projected constraints on the BD and EdGB coupling parameters. This is a standard technique to produce upper limits on modified gravity theories [43, 147] (though this is often done with a Fisher analysis in place of a full MCMC implementation and analysis).

In producing our confidence intervals we use a MCMC which we have written from scratch in `C++`. Our proposal distribution consists of a mix of draws from the prior distributions, Fisher jumps, and differential evolution jumps. We also employ parallel tempering to ensure efficient and complete exploration of the posteriors by the MCMC sampler. We start the MCMC at the maximum likelihood solution, so in principle there is no burn in phase, but we still choose to discard the first 1000 samples. We have verified that the MCMC has converged by taking different subsets of samples and verifying the the end results do not change. Since the MCMCs are run for a set period of time on our computing cluster as opposed to a set number of iterations, the total number of iterations can vary from run to run. Generally they generate a total of $\sim 200,000$ samples (~ 1000 independent samples) of the posterior, which we have ensured is more than enough for the chains to have converged.

In the above analysis, we assume that the signal is described by GR, but use a non-GR model to extract it, so as to determine how large the non-GR effects can be,

$\log_{10}\mathcal{B}_{1,2}$	$\mathcal{B}_{1,2}$	Evidence
0 - 1/2	1 - 3.2	Inconclusive
1/2 - 1	3.2 - 10	Substantial
1 - 2	10 - 100	Strong
> 2	> 100	Decisive

Table 4.1: Bayes factors and their associated level of evidence in favor of Model 1.

while remaining consistent with statistical noise. We now also want to investigate a separate question: how large of a non-GR deviation is needed in the signal so that the data itself supports a non-GR model over a GR model. To investigate this question, so we must consider the ratio of the probability of the two models given the data. From Bayes' Theorem, the probability of model i given the data is related to the likelihood via

$$p(M_i|d) = \frac{p(M_i|I)p(d|M_i)}{p(d)} \tag{4.27}$$

where $p(d|M_i)$ is the likelihood for model i, $p(d)$ is the evidence, and $p(M_i|I)$ is the prior. The ratio of probabilities of two models is the odds ratio, namely

$$\mathcal{O}_{1,2} = \frac{p(M_1|I)}{p(M_2|I)}\frac{p(d|M_1)}{p(d|M_2)} = \frac{p(M_1|I)}{p(M_2|I)}\mathcal{B}_{1,2}\,, \tag{4.28}$$

where in the ratio the model evidences have canceled out. The quantity $\mathcal{B}_{1,2}$ is the Bayes factor, which in this work will be equal to the odds ratio as we assume that the prior probability for either model is the same. The Bayes factor represents the level of evidence for model 1 versus model 2. Different values for the Bayes factor represent different levels of belief in either model 1 or 2, as shown in Table 4.1.

To better understand the Bayes factors, we invoke a standard derivation, presented for example in [148], wherein we write the global likelihood as

$$
\begin{aligned}
p(d, M_i) &= \int p(\boldsymbol{\theta}|M_i, I)p(d|\boldsymbol{\theta}, M_i)d\boldsymbol{\theta} \\
&= \int p(\boldsymbol{\theta}|M_i, I)\mathcal{L}(\boldsymbol{\theta})d\boldsymbol{\theta} \approx \mathcal{L}(\hat{\boldsymbol{\theta}})\frac{V_{\sigma,\theta}}{V_\theta}
\end{aligned}
\tag{4.29}
$$

where we see in the first two equalities that the global model likelihood is just the likelihood evaluated at the best-fit parameters, weighted by the priors. In the last equality, we have approximated the priors are uniform, and thus, given rise to a factor of the prior volume V_θ. We have also approximated the likelihood for the model parameters to be a multivariate Gaussian, leading to the factor of the likelihood evaluated at its maximum, $\mathcal{L}(\hat{\boldsymbol{\theta}})$, and $V_{\sigma,\theta}$ which is the 1-sigma posterior volume (since the priors are assumed to be flat, the 1-sigma posterior volume is equivalent to the 1-sigma likelihood volume). It is then straightforward to approximate the Bayes factor from Eq. (4.28) using the above, where we assume that we have a nested model with model 1 including an extra parameter κ to specialize to the case we consider in this work,

$$
\mathcal{B}_{1,2} \approx \frac{\mathcal{L}(\hat{\boldsymbol{\theta}}_1)}{\mathcal{L}(\hat{\boldsymbol{\theta}}_2)}\frac{\delta\kappa}{\Delta\kappa}\,, \tag{4.30}
$$

where $\delta\kappa$ is a characteristic width of the marginalized posterior of κ and $\Delta\kappa$ is the prior volume of the prior on κ. We note that since model 1 contains model 2 as a special case, the first factor can never be less than unity, i.e. the ratio of maximum parameter likelihoods will always favor the more complicated model. However the second factor, called the "Occam factor," penalizes the more complicated model for "wasted" parameter space. The consequence of Eqs. (4.30) and (4.29) is that the Bayes factor is sensitive to the prior volume and shape.

While the above form is a useful approximation to understand the main features that affect the Bayes factor, we choose to compute the Bayes factor via a trans-dimensional reversible jump MCMC [149]. Within a given model, we use Fisher jumps, draws from the prior distribution, and differential evolution. For trans-dimensional jumps between models, we use draws from a log flat distribution on κ (or whichever modified theory parameter is being explicitly jumped in). Parallel tempering is used to ensure a complete and efficient exploration of the posteriors; we find that most of the trans-dimensional jumps in the $T = 1$ chain are from parallel tempering. Our prior distributions are as follows: $\log \mathcal{M}_c \sim \mathrm{U}[-0.22, 2.3]$, $\eta \sim \mathrm{U}[0.08, 0.25]$, $e_* \sim \mathrm{U}[0, 0.805]$, and $\log \mathcal{A} \sim \mathrm{U}[-46, -37]$. As we have made clear that the prior on the alternative theory parameter can affect the Bayes factor heavily, we explore two different priors in the next section: a flat prior on κ and a flat prior on α^2 as this is what enters the waveform linearly (a flat prior on κ implies a non-trivial prior on α^2 and vice versa).

4.4 Results

In this section we present the results of our upper bound analysis on the modified theory coupling parameter, along with our Bayes factor analysis. In our Bayes factor analysis, we grid the (κ, e_*) parameter space and inject signals on this grid assuming a $(m_1, m_2) = (1.4, 10)M_\odot$ inspiral with an SNR of 30. In our upper bound analysis, we inject data that is consistent with a GR waveform ($\kappa = 0$) and conduct parameter estimation with a non-GR model to estimate the marginalized posterior on κ for eccentric inspirals with the same eccentricities used in the Bayes factor analysis. We then translate our marginalized posteriors on κ to posteriors on the BD parameters (b, $\omega_{\rm BD}$) and the EdGB parameters ($\mathcal{S}^2_{\rm EdGB}$, α). In relating b to $\omega_{\rm BD}$ we have assumed that the $1.4M_\odot$ object is a neutron star with a sensitivity $s = 0.171$, which is what one would find for an APR equation of state [150, 151]. We also assume the $10M_\odot$

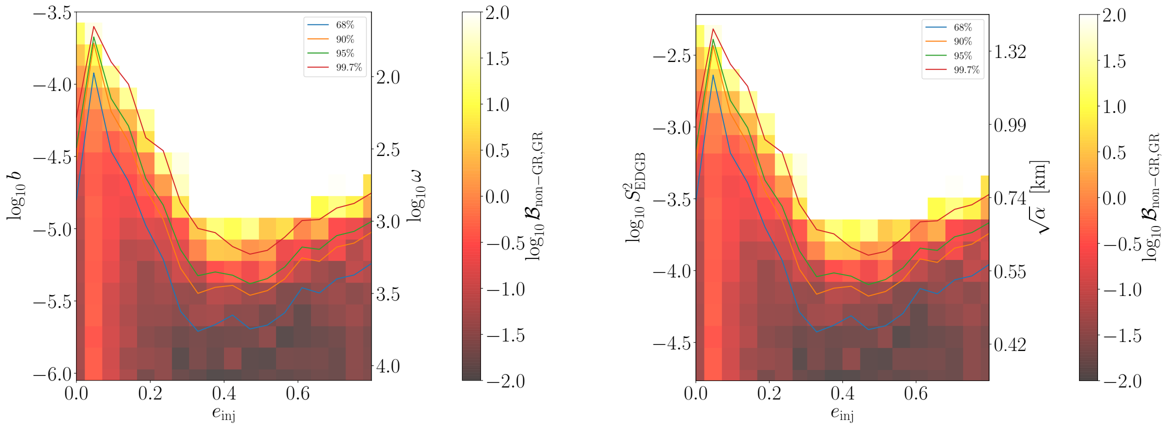

Figure 4.2: The left (right) panel shows the Bayes factor in favor of the Brans-Dicke (EdGB) model over the GR model as a function of injected eccentricity and coupling parameter, using a flat prior on κ. The lines indicate upper limits on the coupling parameter for the 68%, 90%, 95%, and 99.7% confidence regions. In the Bayes factor analysis, we see an enhancement of about a factor of $10^{3/2}$ in the sensitivity to the coupling parameter. In the confidence interval analysis, we see an enhancement of of a little under 10 in the ability to constraint the coupling parameter.

object is a black hole with $s = 0.5$ by the no hair theorems [152]. In the EdGB case, we again assume the binary is composed of a neutron star and a black hole, and thus, we have that $\mathcal{S}^2_{\text{EdGB}} = \xi/m^4_{\text{BH}} = 16\pi\alpha^2_{\text{EdGB}}/m^4$.

4.4.1 What constraints can we put on non-GR theories with eccentric signals?

In Figure 4.2 we present both the Bayes factor as a function of the values of the injected modified theory parameter indicated on the y-axes and the injected eccentricity. We also overplot contours that represent the upper bound on the modified theory parameter given certain confidence intervals as a function of the injected eccentricity. As the injected eccentricity is raised from $e_{\text{inj}} = 0$ to $e_{\text{inj}} \sim 0.4$, the region in coupling parameter where the Bayes factor begins to provide significant support for the modified theory model is lowered by a factor of about $10^{3/2}$. To be clear, by e_{inj} we here mean the injected value of e_* in the signal. In the confidence interval curves, we see that for small eccentricities ($e_{\rm inj} \leq 0.2$) the upper bound on the coupling parameter is less stringent or about as stringent as in the circular case. Still however, as the eccentricity is raised to $e_{\rm inj} \sim 0.4$, the constraint improves by about an order of magnitude.

We can now compare these projected constraints to current constraints. Recall from Sec. 4.1 that the current constraint on EdGB gravity from the GW170608 observation is $\sqrt{\alpha} < 5.6$km at 90% confidence, while the current constraint on BD theory from the Cassini mission is $\omega > 40,000$ at 95% confidence. Taking the minimum of the appropriate confidence interval from Fig. 4.2 suggests that one could obtain GW constraints as good as $\sqrt{\alpha} \lesssim 0.5$km at 90% confidence and $\omega \gtrsim 2700$ at 95% confidence. This is an improvement of roughly an order of magnitude in the EdGB case, but it does not improve the current constraint on the BD coupling parameter. In this analysis, we have assumed a uniform prior on the coupling parameter $\kappa \sim {\rm U}[0, 0.034]$; our constraints would be even more stringent if we have chosen a uniform prior on the logarithm of the coupling parameter, as this would put more wait around GR values.

Although this projected constraints are interesting, it is important to remember that the analysis here assumes an SNR of 30 in the inspiral only (whereas GW170608 had an SNR of 13 for the entire waveform). Such an increase in SNR will be possible once LIGO reaches designed sensitivity for a sufficiently nearby source. More dangerous perhaps is the use of a significantly reduced set of parameters, importantly neglecting spin effects. The modifications we consider here, however, are -1PN order, while spin effects start at +1.5PN order in the waveform phase. For this reasons, covariances between the modified gravity effects we consider here and spin effects should be very weak and not affect our conclusions significantly.

There does, however, arise a complication in the mapping between $\mathcal{S}^2_{\rm EdGB}$ and

$\sqrt{\alpha}$ (and thus between κ and $\sqrt{\alpha}$) when spins are considered. As discussed extensively in [144, 153] (see e.g. Appendix D in [144]), the spin dependence of $\mathcal{S}^2_{\rm EdGB}$ makes it impossible to constrain $\sqrt{\alpha}$ unless the spins are well measured. This is because there are values of the spins and the masses for which $\mathcal{S}^2_{\rm EdGB}$ vanishes identically irrespective of the value of $\sqrt{\alpha}$. Therefore, if the masses and spins cannot be constrained well enough to disallow this possibility, then $\sqrt{\alpha}$ cannot be constrained. This effect can be mitigated by future detectors which will be able to resolve the spin of the compact objects better than current detectors.

Our projected BD constraint is stronger than what one finds in the quasi-circular limit, but still not stronger than current constraint from the Cassini spacecraft. This suggests that in order to obtain a better constraint, even with the most optimal system configuration, we will likely need to wait for more sensitive ground based detectors. For example, in Fig. 5 of [43], a Fisher matrix analysis is used to project constrain on ω using GWs from from binaries with small eccentricity. Their work suggests that Cosmic Explorer and Einstein telescope could supersede the current constraint on BD, especially if their results are extrapolated to our moderate eccentricity results.

Why does the constraint on the non-GR parameter deteriorate for eccentricities past 0.4? Recall from Eq. (4.30) that the Bayes factor scales as the ratio of the maximum likelihoods for either model times the ratio of the characteristic width of the posterior on the non-GR parameter to the prior width. As the eccentricity is increased from 0.4 to 0.8, the ratio of the maximum likelihoods decreases in magnitude at the same rate as the Bayes factor decreases. By Eq. (4.30), this suggests that as the eccentricity is increased from 0.4 to 0.8, the width of the posterior on the non-GR parameter remains roughly constant, which implies the likelihood is less sensitive to the modified theory parameter; note that this effect can also be seen in the other system parameters, as shown e.g. in [139]. This would also explain the deteriorated constraint from the confidence intervals.

But what is happening to the waveform and the likelihood to cause this effect? As the inner product that enters likelihood calculation, $(d - h(\theta)|d - h(\theta))$, is highly sensitive to phase differences between the data (d) and the template (h), the overall number of phase cycles is a useful metric to understand how sensitive the likelihood can be to the system parameters. If there are many phase cycles, then we might expect that a small change in parameters could (over these many cycles) cause a significant dephasing. However, if the number of phase cycles is small then a change in the parameters of the model may not lead to enough dephasing to significantly affect the inner product entering the likelihood.

Since eccentricity enhances energy and angular momentum loss, it increased eccentricity forces the binary to inspiral faster, and thus, to produce less cycles of phase. However, the higher the eccentricity, the more important higher harmonics are, and the latter can produce even more cycles of phase, as they emit at higher multiples of the orbital frequency. Thus we expect that there is some interplay between these two contributions to the number of phase cycles, and ultimately, this quantity should be computed in order to understand the loss in likelihood sensitivity to parameter changes.

To do so, we first extend the circular calculation of the number of cycles of phase to the case of many harmonic applicable to eccentric inspirals. In the circular case, the number of phase cycles is given by [154]

$$\Delta N_{\psi} = \frac{1}{2\pi}\left[\psi(f_2) - \psi(f_1) + (f_1 - f_2)\left.\frac{d\psi}{df}\right|_{f=f_1}\right] , \tag{4.31}$$

where f_1 is the initial frequency, f_2 is the final eccentricity, and the derivative term ensures that ΔN_{ψ} and its frequency derivative vanish at f_1. In the eccentric case, the presence of many harmonics complicate calculations of the *overall* phase, so it is preferable to work with the individual phases of each harmonic, ψ_j. Each harmonic j contributes some number of phase cycles:

$$\Delta N_{\psi_j} = \frac{1}{2\pi}\left[\psi_j(f_2) - \psi_j(f_1) + (f_1 - f_2)\frac{d\psi_j}{df}\bigg|_{f=f_1}\right]. \tag{4.32}$$

In order to find the total number of phase cycles we choose to weight each harmonic contribution by its fractional SNR. Thus, for the total number of phase cycles we now have

$$\Delta N_{\psi} = \frac{1}{(h|h)^{1/2}}\sum_j (h_j|h_j)^{1/2}\Delta N_{\psi_j}\,. \tag{4.33}$$

Here h is the full signal given by Eq. (4.1), and the individual harmonics, h_j, are given by individual terms in the sum on j in Eq. (4.1). Note that this reduces to Eq. (4.31) in the circular limit.

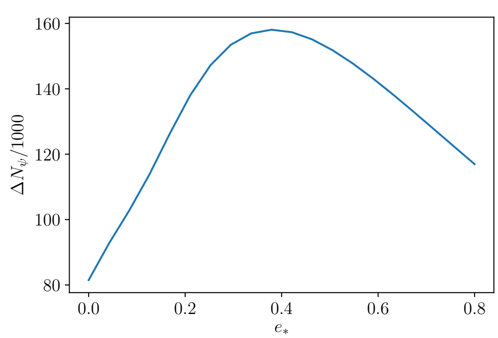

Figure 4.3: The number of phase cycles as given by Eq. (4.33) as a function of the eccentricity. Initially, the number of phase cycles increases until eccentricities ~ 0.4 at which point they begin to decrease.

In Figure 4.3 we plot the weighted phase cycles (Eq (4.33)) as a function of the eccentricity. Note that as suspected, we see that there is an interplay between the binary inspiraling faster and producing less phase cycles, and the increasing

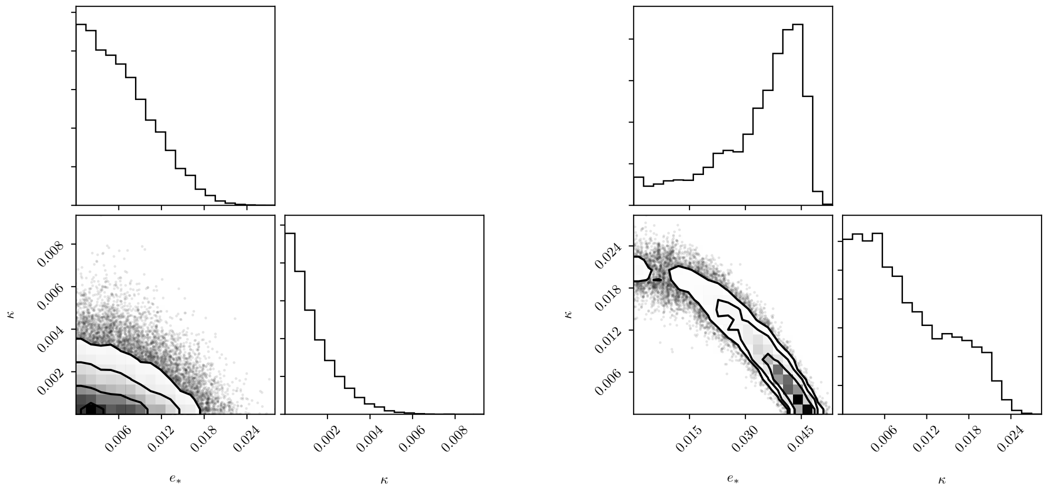

Figure 4.4: Corner plots for the posteriors on e_* and κ when injecting a GR signal and recovering with a modified theory model. The injected eccentricity is 0 (left) and 0.047 (right). For small eccentricities, a large negative covariance arises.

number of harmonics contributing more phase cycles. Up until eccentricities near 0.4, the number of cycles increases, but then for higher eccentricities the number of phase cycles decreases. The (inverted) shape is nearly identical to the shape of the confidence interval constraints on Fig. 4.2. This is strong evidence that the source of the likelihood's decreased sensitivity to parameters is the decreasing number of phase cycles. This in turn sources a deterioration of the constraints on the non-GR parameters, as well as on the source parameters as pointed out in [139], as the eccentricity is increased above ~ 0.4.

4.4.2 Disagreement at circularity

Interestingly the upper bound produced by the confidence interval very closely follows contours of the Bayes factor, except in the circular case. In order to understand this behavior, it is helpful to look at the covariance between e_* and κ, as well as the marginalized posterior in κ. Figure 4.4 shows the covariance between these parameters, as well as their marginalized posterior for the $e_{\rm inj} = 0$ and $e_{\rm inj} = 0.047$ cases. We see that for small eccentricities there arises a strongly negative covariance between these parameters. In turn, this covariance leads to the exploration of much larger values of the modified theory coupling parameter, giving a less stringent bound on the parameter when $e_{\rm inj} = 0.047$. This covariance is sensible as the eccentricity and the non-GR parameter *both* lead to a similar physical effect: an increased rate of energy and angular momentum loss by the binary, and therefore a faster inspiral. As the injected eccentricity becomes large, however, this covariance disappears, likely because the effect of eccentricity begins to introduce considerable more power in higher harmonics, which cannot be duplicated by the modified theory parameter.

In the case of the Bayes factors, we do not see an increased constraint at circularity. The key to this feature is that, unlike in the confidence interval analysis, the signal has a non-zero value of the non-GR parameter. As such, even when $e_{\rm inj} = 0$, the GR model is free to explore higher eccentricities along the covariance between κ and e_*. In exploring that covariance, the GR model can achieve a higher maximum likelihood and thus inflate the denominator in Eq. (4.30) leading to smaller Bayes factors. To summarize, in the confidence interval analysis, the covariance between e_* and κ is small when both injected values are zero, however in the Bayes factor analysis even when $e_{\rm inj} = 0$ the injected value of the non-GR parameter is nonzero, so the effects of this covariance "turning on" are not seen.

4.4.3 How sensitive are the results to the priors?

Since the Bayes factor is sensitive to the prior volume as well as the shape of the prior (see e.g. Eqs. (4.29) and (4.30)) especially when in lower SNR regimes, it is worth exploring what the prior looks like when converted from κ to the modified theory coupling constant. In Fig. 4.2 we chose a uniform prior on κ, i.e. $\kappa \sim \mathrm{U}[0, 0.034]$,

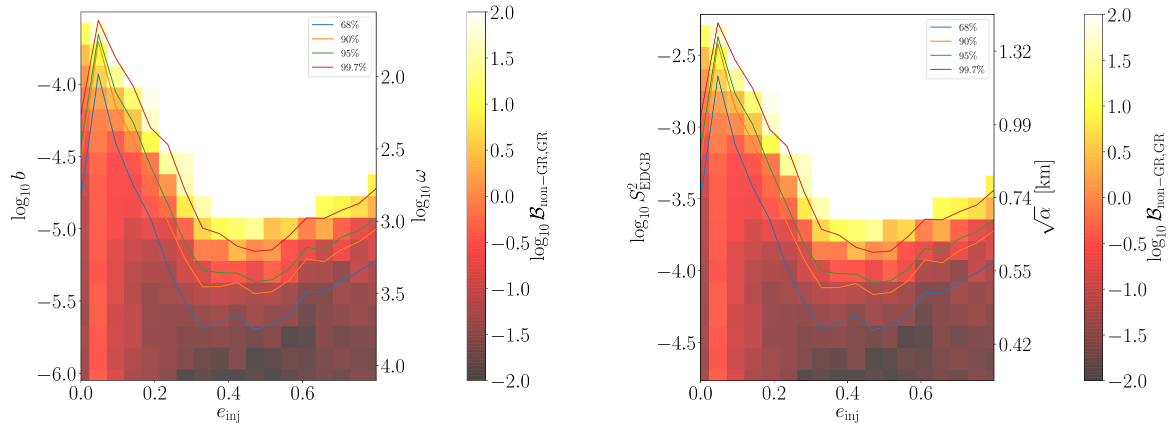

Figure 4.5: Same as Figure 4.2, but here we have used a flat prior in α^2

so let us explore how this translates to a prior on the EdGB parameter $\sqrt{\alpha}$, which we show in Fig. 4.6. Clearly, a uniform prior on κ leads to a non trivial prior on $\sqrt{\alpha}$. We also show a flat prior on α^2 whose upper bound is consistent with the upper bound obtained with a uniform prior on κ (assuming the same injected mass). We choose here to compare against a uniform prior on α^2, instead of a uniform prior on $\sqrt{\alpha}$, because α^2 enters the phase functions linearly (while $\sqrt{\alpha}$ is ultimately what is to be constrained). We are then forced to wonder if the results of our Bayes factor analysis would be greatly affected if we explicitly used uniform priors on the coupling parameter α^2. This is particularly important because often the widely used ppE parameters do not map linearly to coupling parameters in different theories. A flat prior in those generic corrections in the ppE formalism could imply non-trivial prior on the coupling parameter that is ultimately being constrained. See for example the posteriors on $\sqrt{\alpha}$ obtained through analysis of GW170808 in [142] where a prior much like the one shown in Fig. 4.6 enforces nearly zero support in the posterior at $\sqrt{\alpha} = 0$. We have verified that we obtain a similar result in the posterior of $\sqrt{\alpha}$ when using a flat prior on κ.

In Figure 4.5 we show the Bayes factors and confidence intervals, as in Fig. 4.2,

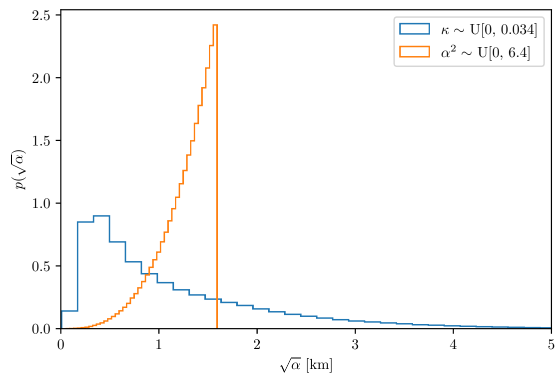

Figure 4.6: The prior probability distributions for $\sqrt{\alpha}$ when the prior on κ is flat (blue) and when the prior on α^2, which enters the phasing linearly, is flat (orange).

but now assuming a uniform prior on α^2: $\alpha^2 \sim \mathrm{U}[0, 6.4]$. We see that despite the differently shaped priors, the Bayes factors barely differ quantitatively, and virtually suffer no qualitative differences. We have verified numerically that they are, in fact, slightly different. This is reassuring, since it implies that provided the bounds of the priors are consistent, we see a consistent Bayes factor in this case; the Bayes factors change considerably if we increase our prior volume, but this is a well-known feature of any Bayes factor analysis. We can conclude that it is sufficient to have one parameter estimation or model selection run with a single κ coefficient, which can then meaningfully be translated to various coupling parameters, regardless of the non-linearity of the mapping between them implying non trivial priors. This, however, will not always be the case, and the robustness of the calculation will depend on the functional form of the mapping between the ppE parameter and the coupling constant of the theory. For example, Ref. [144] showed in detail (see Appendix D in that paper) that a well-constrained value of the ppE parameter leads to a wide number of allowed values of $\sqrt{\alpha}$ due to unconstrained spins in the mapping between $\sqrt{\alpha}$ and the ppE parameter[3].

4.4.4 Uncertainty in Bayes Factor

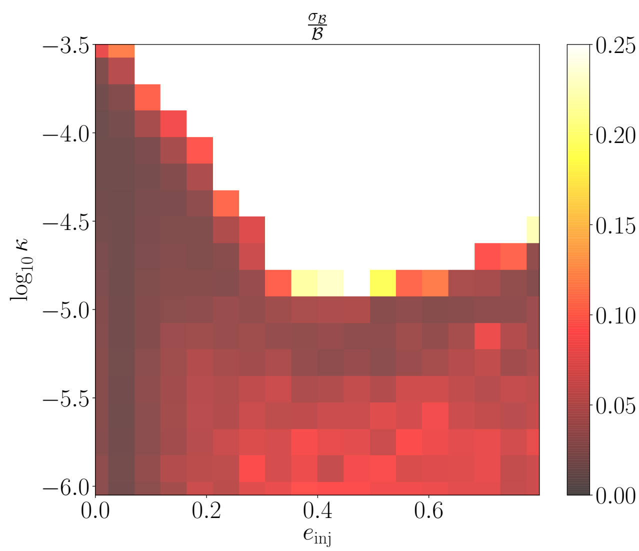

Figure 4.7: Standard deviation of the Bayes factor scaled by the Bayes factor as a function of the injected eccentricity and the non-GR parameter. For the regions of parameter space of interest, the uncertainty in Bayes factor is small enough and our reported Bayes factors are robust.

Here we seek to quantify the uncertainty in the Bayes factors shown throughout this work. The brute force method to calculate the uncertainty in the Bayes factor generated by an RJMCMC is to run identical algorithms with different seeds for the random number generator, which is used to draw jumps from the proposal distributions. This requires an excessive amount of computational resources. Instead, here we use a metric developed in [155] to assess the error in the Bayes factor calculation. In that paper, the authors model the joint likelihood of observing the possible transitions of the RJMCMC, N_{ij}, where N_{ij} are the number of transitions from state i to state j of the RJMCMC. This allows them to compute the variance

[3]Particularly, see their Figure 15 where GW150914 is shown to place limits between $\sqrt{\alpha} \sim 0$ and $\sqrt{\alpha} < 40$km depending on the values of the (unconstrained) spins.

of the Bayes factor. In terms of the standard deviation, this reads:

$$\sigma_{\mathcal{B}_{1,2}} = \mathcal{B}_{1,2}\left[\frac{(N_1 - N_{12})}{N_1 N_{12}} + \frac{(N_2 - N_{21})}{N_2 N_{21}}\right]^{1/2}, \tag{4.34}$$

where N_i is the number of iterations the RJMCMC algorithm spends in model i.

In Figure 4.7 we show the values of the standard deviation of the Bayes factor scaled by the Bayes factor as a function of the non-GR parameter and the eccentricity of the signal. We have removed any value above 0.25, as those regions with larger uncertainties have already been omitted in previous figures. We see that the standard deviation is mostly much below 0.25, and the result shows that we can be confident in our reported Bayes factors in the regions of injected parameter space of interest.

4.5 Conclusions & Future Work

In this work we have derived and implemented corrections from Brans Dicke and Einstein-dilaton-Gauss-Bonnet theories of gravity into an eccentric waveform model which is valid in the moderate eccentricity regime. This is done by specifying the phase functions from these theories in terms of the orbital eccentricity which can than be trivially incorporated into the already existing TaylorF2e model [119, 139]. We then carry out a comprehensive study of the data analysis implications of these alternative theories of gravity as a function of the eccentricity of the source. We set projected upper limits on the coupling parameter of BD and EdGB given an eccentric signal and employ a Bayes factor analysis exploring at what values of the injected alt theory parameter the non-GR model is favored. We also explore how non-trivial priors due to non-linear mapping between parameters can affect the results of these analyses.

As a main result we find that regardless of the model selection or parameter estimation technique employed we find that moderately eccentric signals provide a more stringent constraint on the alternative theory of gravity than a circular signal with all other parameters held equal. When we assume the signal is consistent with GR we can set constraints on the coupling parameter about 10 times as stringent as in the circular case when the eccentricity is ~ 0.4. However, due to strong covariances with eccentricity at low eccentricities the constraint actually initially worsens for low eccentricity signals. The Bayes factor analysis is insensitive to this covariance and shows about a factor of $10^{3/2}$ increase in constraint of the alternative theory as the eccentricity is increased to ~ 0.4.

We also set projected constraints on the coupling parameters assuming an ideally eccentric signal with high SNR. We find a projected constrain for the EdGB parameter of $\sqrt{\alpha} < 0.5$ km which is an order of magnitude better than current constraints. A more conservative constraint is that given an eccentric detection which is otherwise comparable to current circular detections, we may be able to place a constraint that is a factor of 2 more stringent than provided by the circular signal. In the case of BD we are able to place a projected constraint of $\omega > 2700$ which is an order of magnitude less than the current constraint on ω. Examination of Figure 5 of [43] which explores the constraint of ω for low eccentricity signals through a fisher analysis for several ground based detectors suggests that Cosmic Explorer or Einstein Telescope could provide a more stringent constraint than the current best especially for a moderately eccentric signal.

In deriving the eccentric corrections to the GW waveform we found that there is a simple mapping between the coupling parameters of the BD and EdGB theories of gravity in the way they affect the waveform. That is, the BD coupling parameter is related to the EdGB parameter by a constant factor. This simple mapping between the effects of alternative theories of gravity on the waveform suggests that a simple extension of the widely used ppE formalism exists for eccentric binaries. Given this work demonstrates that eccentric signals provide enhanced constraints on the alternative theories like EdGB and BD, if an extension to the PPE formalism does exist for eccentric signals its derivation would maximize the science that could be done with eccentric signals.

This works underscores the importance of eccentric modeling and analysis. We have seen that eccentric signal not only increases our ability to validate GR but also lead to better measurement of source parameters [139]. They also help complete our picture of how black hole binaries are formed due to their assembly being dependent of dynamic processes particular to certain astrophysical settings. We still require even more accurate models which are suitable for future detectors with the ability to incorporate the effects of several alternative theories of gravity to maximize the science potential of current and future detectors.

Acknowledgments

B. M. was supported by the Joan L. Dalton Memorial Fellowship in Astronomy from Montclair State University. B. M. and N. Y. also acknowledge support from NSF PHY-1759615 and NASA ROSES grant 80NSSC18K1352. We thank Travis Robson and Neil Cornish for very useful conversations. Computational efforts were performed on the Hyalite High Performance Computing system, which is supported by University Information Technology at Montana State University.

CONCLUSION

In this work we, in Chapter 1, derive a leading order framework in which to handle the frequency response of a LIGO-like detector to a gravitational wave signal generated by compact binaries with significant orbital eccentricity. As a byproduct of that work we develop a novel method to maximize the match over an orbital phase and time shift for a signal with many harmonics. Using this statistic, we validate our model for eccentricities as high as $e \sim 0.9$ depending on the mass of the system and the separation at which the binary has this eccentricity. We also point to the components of previous models which lead to considerable error in order to guide other improvements in the eccentric waveform modeling community. In chapter 2, we extend this model to 3rd Post-Newtonian order (the highest order for which the necessary energy and angular momentum fluxes have been derived). At higher PN order complications arising from periastron precession and highly coupled differential equations in the binary dynamics lead to solutions in the signal which require more approximations than in the Newtonian case. Once again we investigate sources of error in the waveform match and find that the most egregious source of error is likely due to the PN approximation breaking down, especially for binaries with unequal masses.

In chapter 3 we present some speedups in the waveform which include coding best practices, clever evaluation of harmonics in the signal, and a fast scheme to numerically invert relations between orbital elements. After this implementation we find that on average our waveform takes about 90ms to evaluate. With this fast and accurate model in hand we explored the data analysis implications of the model. We find that eccentric signals provide a better estimate for the source eccentricity and mass over their quasi-circular counterparts by over a factor of 10.

Likewise we characterize the region in which the waveform mismodeling, present from the approximate nature of our waveform, leads to systematic errors larger than the statistical error finding that in the low mass cases, our waveform is valid for eccentricities as high as ~ 0.8. In the higher mass cases it is valid to lower eccentricities of about ~ 0.4.

Lastly in chapter 4 we introduce the effects of alternative theories of gravity into our waveform in order to gauge how ground based detector's ability to do fundamental physics will scale with the orbital eccentricity of the source. We consider EdGB and BD theories of gravity, and in deriving their corrections to the waveform we find a simple mapping between the coupling parameters in each theory to one another which is independent of the dynamical variables in the problem. This suggests that similar mappings might exist in other theories which could reduce the theoretical and computational expense of testing these theories. With these corrections derived we explore how well we can place constraints on the coupling parameters of the theories. Importantly, we find about an order of magnitude improved constraint as the orbital eccentricity of the source is raised from quasi-circular to 0.4. At higher eccentricities the constraint starts to break down – a result of the binary inspiraling faster as the eccentricity becomes large.

Perhaps the most impactful extension of this work is inclusion of the merger and ringdown corrections to the waveform to form a so called inspiral-merger-ringdown (IMR) model. As the model is currently inspiral only, it is only useful for lighter systems where the inspiral portion of the waveform dominates, for higher mass systems neglecting the merger and ringdown can result in loss of detection as well as parameter error. A simple way to incorporate these effects would exploit the very small (potentially nearly vanishing) eccentricity that the binary has by the time it reaches merger. With such an IMR model in hand, it would be very useful to study the agreement between the numerous current eccentric waveforms in the literature. Each waveform has been derived independently and uses their own unique set of approximations and techniques to validate them, and as such is it unclear how the waveforms agree when compared to each other with respect to an equal metric. This would be well complimented by a number of numerical relativity waveforms which incorporate eccentricity and last well into the inspiral phase. Simulations of this nature have yet to be realized.

In terms of future improvements to the inspiral phase of this waveform, deriving the PN corrections beyond 3PN order and the incorporation of spin would be useful. Either task would be difficult – in the former, the energy and angular momentum fluxes have yet to be derived to higher than 3PN order for eccentric binaries and, for the latter, spin couples non-trivially to the eccentricity in the orbital dynamics and introduces yet more harmonics. A simpler interesting extension would involve exploring how corrections from different theories of gravity map to eccentric signals. We found a simple mapping between two theories in the eccentric case, if this is a general property it would allow for an extension of the ppE formalism to the eccentric case. Such an extension could provide useful for tests of fundamental physics.

In our data analysis studies we have assumed that the binary formed at some time before emitting gravitational waves in the sensitivity band of ground based detectors. In doing so we only specify the eccentricity at a certain orbital separation, and calculate the entire frequency response from each harmonic starting from the lower frequency cutoff of the detector to the upper frequency limit of the waveform. If, instead, the binary were to truly form in the sensitivity band of ground based detectors (which could likely be the case for detectors with smaller lower frequency cutoffs like Einstein Telescope), the harmonics in the signal would "turn on" at different frequencies in the detector. It would be interesting to study at what separations, eccentricities, and signal-to-noise, the distinction could be confidently made between a binary forming in band and one that formed long before emitting detectable gravitational waves.

REFERENCES CITED

[1] The LIGO Scientific Collaboration and the Virgo Collaboration 2018 *arXiv e-prints* arXiv:1811.12907 (*Preprint* `1811.12907`)

[2] VIRGO `www.virgo.infn.it`

[3] LISA `www.esa.int/science/lisa`, `lisa.jpl.nasa.gov`

[4] Peters P C and Mathews J 1963 *Physical Review* **131** 435–440

[5] Kozai Y 1962 AJ **67** 591

[6] Rodriguez C L, Amaro-Seoane P, Chatterjee S and Rasio F A 2018 *Physical Review Letters* **120** 151101 (*Preprint* `1712.04937`)

[7] Samsing J 2018 Phys. Rev. D **97** 103014 (*Preprint* `1711.07452`)

[8] Samsing J, MacLeod M and Ramirez-Ruiz E 2014 ApJ **784** 71 (*Preprint* `1308.2964`)

[9] Zevin M, Samsing J, Rodriguez C, Haster C J and Ramirez-Ruiz E 2019 ApJ **871** 91 (*Preprint* `1810.00901`)

[10] Samsing J and D'Orazio D J 2018 *Mon. Not. Roy. Astron. Soc.* **481** 5445–5450 (*Preprint* `1804.06519`)

[11] Kremer K *et al.* 2019 *Phys. Rev.* **D99** 063003 (*Preprint* `1811.11812`)

[12] Samsing J, Hamers A S and Tyles J G 2019 *Phys. Rev.* **D100** 043010 (*Preprint* `1906.07189`)

[13] Favata M 2013 *ArXiv e-prints* (*Preprint* `1310.8288`)

[14] Blanchet L 2006 **9** 4 (*Preprint* `gr-qc/0202016`)

[15] Cutler C and Vallisneri M 2007 Phys. Rev. D **76** 104018 (*Preprint* `0707.2982`)

[16] Ramos-Buades A, Husa S, Pratten G, Estellés H, García-Quirós C, Mateu M, Colleoni M and Jaume R 2019 *arXiv e-prints* arXiv:1909.11011 (*Preprint* `1909.11011`)

[17] Martel K and Poisson E 1999 *Phys. Rev. D.* **60** 124008 (*Preprint* `gr-qc/9907006`)

[18] Ajith P 2008 *Classical and Quantum Gravity* **25** 114033 (*Preprint* `0712.0343`)

[19] Huerta E A and Brown D A 2013 *Phys. Rev.* **D87** 127501 (*Preprint* `1301.1895`)

[20] Brown D A and Zimmerman P J 2010 *Phys. Rev. D.* **81** 024007 (*Preprint* 0909.0066)

[21] Cokelaer T and Pathak D 2009 *Classical and Quantum Gravity* **26** 045013 (*Preprint* 0903.4791)

[22] Peters P 1964 *Phys.Rev.* **136** B1224–B1232

[23] Wahlquist H 1987 *General Relativity and Gravitation* **19** 1101–1113 ISSN 1572-9532 URL https://doi.org/10.1007/BF00759146

[24] Yunes N, Arun K G, Berti E and Will C M 2009 *Phys. Rev. D* **80**(8) 084001 URL http://link.aps.org/doi/10.1103/PhysRevD.80.084001

[25] Tanay S, Haney M and Gopakumar A 2016 *Phys. Rev.* **D93** 064031 (*Preprint* 1602.03081)

[26] Tiwari S, Gopakumar A, Haney M and Hemantakumar P 2019 Phys. Rev. D **99** 124008 (*Preprint* 1905.07956)

[27] Moore B, Favata M, Arun K G and Mishra C K 2016 *Phys. Rev.* **D93** 124061 (*Preprint* 1605.00304)

[28] Huerta E, Kumar P, McWilliams S T, O'Shaughnessy R and Yunes N 2014 *Phys.Rev.* **D90** 084016 (*Preprint* 1408.3406)

[29] Klein A, Boetzel Y, Gopakumar A, Jetzer P and de Vittori L 2018 *ArXiv e-prints* (*Preprint* 1801.08542)

[30] Tai K S, McWilliams S T and Pretorius F 2014 *Phys. Rev.* **D90** 103001 (*Preprint* 1403.7754)

[31] Loutrel N and Yunes N 2017 *Classical and Quantum Gravity* **34** 135011 (*Preprint* 1702.01818)

[32] Loutrel N 2019 *arXiv e-prints* arXiv:1909.02143 (*Preprint* 1909.02143)

[33] Hinderer T and Babak S 2017 *Phys. Rev.* **D96** 104048 (*Preprint* 1707.08426)

[34] Cao Z and Han W B 2017 Phys. Rev. D **96** 044028 (*Preprint* 1708.00166)

[35] Liu X, Cao Z and Shao L 2019 *arXiv e-prints* arXiv:1910.00784 (*Preprint* 1910.00784)

[36] Chiaramello D and Nagar A 2020 *arXiv e-prints* arXiv:2001.11736 (*Preprint* 2001.11736)

[37] Boyle M, Hemberger D, Iozzo D A B, Lovelace G, Ossokine S, Pfeiffer H P, Scheel M A, Stein L C, Woodford C J, Zimmerman A B, Afshari N, Barkett K, Blackman J, Chatziioannou K, Chu T, Demos N, Deppe N, Field S E, Fischer N L, Foley E, Fong H, Garcia A, Giesler M, Hebert F, Hinder I, Katebi R, Khan H, Kidder L E, Kumar P, Kuper K, Lim H, Okounkova M, Ramirez T, Rodriguez S, Rüter H R, Schmidt P, Szilagyi B, Teukolsky S A, Varma V and Walker M 2019 *Classical and Quantum Gravity* **36** 195006 (*Preprint* `1904.04831`)

[38] Hinder I, Kidder L E and Pfeiffer H P 2018 *Phys. Rev. D* **98**(4) 044015 URL `https://link.aps.org/doi/10.1103/PhysRevD.98.044015`

[39] Huerta E A *et al.* 2018 *Phys. Rev.* **D97** 024031 (*Preprint* `1711.06276`)

[40] George D and Huerta E 2018 *Physics Letters B* **778** 64 – 70 ISSN 0370-2693 URL `http://www.sciencedirect.com/science/article/pii/S0370269317310390`

[41] Gondán L and Kocsis B 2019 ApJ **871** 178 (*Preprint* `1809.00672`)

[42] Gondán L, Kocsis B, Raffai P and Frei Z 2018 *The Astrophysical Journal* **855** 34 URL `https://doi.org/10.3847%2F1538-4357%2Faaad0e`

[43] Ma S and Yunes N 2019 *arXiv e-prints* arXiv:1908.07089 (*Preprint* `1908.07089`)

[44] Takátsy J, Bécsy B and Raffai P 2019 MNRAS **486** 570–581 (*Preprint* `1812.04012`)

[45] Nishizawa A, Berti E, Klein A and Sesana A 2016 Phys. Rev. D **94** 064020 (*Preprint* `1605.01341`)

[46] Nishizawa A, Sesana A, Berti E and Klein A 2017 MNRAS **465** 4375–4380 (*Preprint* `1606.09295`)

[47] LIGO Scientific Collaboration, Aasi J, Abbott B P, Abbott R, Abbott T, Abernathy M R, Ackley K, Adams C, Adams T, Addesso P and et al 2015 *Classical and Quantum Gravity* **32** 074001 (*Preprint* `1411.4547`)

[48] Acernese F *et al.* (VIRGO) 2015 *Class.Quant.Grav.* **32** 024001 (*Preprint* `1408.3978`)

[49] LIGO-India `http://www.gw-indigo.org`

[50] Aso Y, Michimura Y, Somiya K, Ando M, Miyakawa O *et al.* 2013 (*Preprint* `1306.6747`)

[51] Abbott, B P et al (LIGO Scientific Collaboration and Virgo Collaboration) 2016 *Phys. Rev. Lett.* **116**(6) 061102 URL `http://link.aps.org/doi/10.1103/PhysRevLett.116.061102`

[52] Abbott B P, Abbott R, Abbott T D, Abernathy M R, Acernese F, Ackley K, Adams C, Adams T, Addesso P, Adhikari R X and et al 2016 *Physical Review Letters* **116** 241103 (*Preprint* `1606.04855`)

[53] Abbott B P, Abbott R, Abbott T D, Acernese F, Ackley K, Adams C, Adams T, Addesso P, Adhikari R X, Adya V B and et al 2017 *Physical Review Letters* **118** 221101 (*Preprint* `1706.01812`)

[54] Abbott B P, Abbott R, Abbott T D, Acernese F, Ackley K, Adams C, Adams T, Addesso P, Adhikari R X, Adya V B and et al 2017 *Physical Review Letters* **119** 141101 (*Preprint* `1709.09660`)

[55] Abbott B P, Abbott R, Abbott T D, Acernese F, Ackley K, Adams C, Adams T, Addesso P, Adhikari R X, Adya V B and et al 2017 *Physical Review Letters* **119** 161101 (*Preprint* `1710.05832`)

[56] Abbott B P, Abbott R, Abbott T D, Acernese F, Ackley K, Adams C, Adams T, Addesso P, Adhikari R X, Adya V B and et al 2017 ApJ **851** L35 (*Preprint* `1711.05578`)

[57] Nishizawa A, Berti E, Klein A and Sesana A 2016 *Phys. Rev. D* **94**(6) 064020 URL `https://link.aps.org/doi/10.1103/PhysRevD.94.064020`

[58] Kowalska I, Bulik T, Belczynski K, Dominik M and Gondek-Rosinska D 2011 A&A **527** A70 (*Preprint* `1010.0511`)

[59] Seto N 2013 *Physical Review Letters* **111** 061106 (*Preprint* `1304.5151`)

[60] Antognini J M, Shappee B J, Thompson T A and Amaro-Seoane P 2013 *ArXiv e-prints* (*Preprint* `1308.5682`)

[61] Naoz S, Kocsis B, Loeb A and Yunes N 2013 *The Astrophysical Journal* **773** 187 (*Preprint* `1206.4316`)

[62] Antonini F, Murray N and Mikkola S 2014 *The Astrophysical Journal* **781** 45 (*Preprint* `1308.3674`)

[63] Blanchet L 2006 *Living Rev. Rel.* **9** 4

[64] O'Leary R M, Kocsis B and Loeb A 2009 MNRAS **395** 2127–2146 (*Preprint* `0807.2638`)

[65] Samsing J, MacLeod M and Ramirez-Ruiz E 2013 (*Preprint* `1308.2964`)

[66] Antonini F, Chatterjee S, Rodriguez C L, Morscher M, Pattabiraman B, Kalogera V and Rasio F A 2015 *ArXiv e-prints* (*Preprint* 1509.05080)

[67] Einstein Telescope www.et-gw.eu

[68] Chatziioannou K, Klein A, Yunes N and Cornish N 2017 Phys. Rev. D **95** 104004 (*Preprint* 1703.03967)

[69] Pierro V and Pinto I M 1996 *Nuovo Cimento B Serie* **111** 631–644

[70] Mikóczi B, Kocsis B, Forgács P and Vasúth M 2012 Phys. Rev. D **86** 104027 (*Preprint* 1206.5786)

[71] Mikóczi B, Forgács P and Vasúth M 2015 Phys. Rev. D **92** 044038 (*Preprint* 1502.00276)

[72] Moreno-Garrido C, Mediavilla E and Buitrago J 1995 MNRAS **274** 115–126

[73] Kovalevsky J 1967 *Introduction to Celestial Mechanics* (New York: Springer)

[74] Cutler C, Kennefick D and Poisson E 1994 *Phys. Rev.* **D50** 3816–3835

[75] Levin J and Perez-Giz G 2008 Phys. Rev. D **77** 103005 (*Preprint* 0802.0459)

[76] Komorowski P G, Valluri S R and Houde M 2009 *Classical and Quantum Gravity* **26** 085001 (*Preprint* 0903.3684)

[77] Abbott B P, Abbott R, Abbott T D, Abernathy M R, Ackley K, Adams C, Addesso P, Adhikari R X, Adya V B, Affeldt C and et al 2017 *Classical and Quantum Gravity* **34** 044001 (*Preprint* 1607.08697)

[78] Buonanno A, Iyer B R, Ochsner E, Pan Y and Sathyaprakash B S 2009 Phys. Rev. D **80** 084043 (*Preprint* 0907.0700)

[79] Turner M 1977 ApJ **216** 610–619

[80] Wen L 2003 *The Astrophysical Journal* **598** 419–430 (*Preprint* astro-ph/0211492)

[81] Droz S, Knapp D J, Poisson E and Owen B J 1999 *Phys.Rev.* **D59** 124016 (*Preprint* gr-qc/9901076)

[82] Damour T, Iyer B R and Sathyaprakash B S 2000 Phys. Rev. D **62** 084036 (*Preprint* gr-qc/0001023)

[83] Arun K, Blanchet L, Iyer B R and Qusailah M S 2008 *Phys.Rev.* **D77** 064034 (*Preprint* 0711.0250)

[84] Arun K, Blanchet L, Iyer B R and Qusailah M S 2008 *Phys.Rev.* **D77** 064035 (*Preprint* 0711.0302)

[85] Arun K G, Blanchet L, Iyer B R and Sinha S 2009 *Phys.Rev.* **D80** 124018 (*Preprint* 0908.3854)

[86] Loutrel N and Yunes N 2017 *Classical and Quantum Gravity* **34** 044003 (*Preprint* 1607.05409)

[87] Boetzel Y, Susobhanan A, Gopakumar A, Klein A and Jetzer P 2017 Phys. Rev. D **96** 044011 (*Preprint* 1707.02088)

[88] Yunes N and Pretorius F 2009 *Phys.Rev.* **D80** 122003 (*Preprint* 0909.3328)

[89] Loutrel N, Yunes N and Pretorius F 2014 Phys. Rev. D **90** 104010 (*Preprint* 1404.0092)

[90] Huerta E A, Moore C J, Kumar P, George D, Chua A J K, Haas R, Wessel E, Johnson D, Glennon D, Rebei A, Holgado A M, Gair J R and Pfeiffer H P 2018 Phys. Rev. D **97** 024031 (*Preprint* 1711.06276)

[91] Bender C M and Orszag S A 1999 *Advanced mathematical methods for scientists and engineers 1, Asymptotic methods and perturbation theory* (New York: Springer)

[92] Porter E K 2007 Phys. Rev. D **76** 104002 (*Preprint* 0706.0114)

[93] Abbott B P, Abbott R, Abbott T D, Acernese F, Ackley K, Adams C, Adams T, Addesso P, Adhikari R X, Adya V B and et al 2017 *Physical Review Letters* **119** 161101 (*Preprint* 1710.05832)

[94] Abbott B P, Abbott R, Abbott T D, Acernese F, Ackley K, Adams C, Adams T, Addesso P, Adhikari R X, Adya V B and et al 2017 *Physical Review Letters* **119** 141101 (*Preprint* 1709.09660)

[95] Abbott B P, Abbott R, Abbott T D, Acernese F, Ackley K, Adams C, Adams T, Addesso P, Adhikari R X, Adya V B and et al 2017 ApJ **851** L35 (*Preprint* 1711.05578)

[96] Abbott B P, Abbott R, Abbott T D, Acernese F, Ackley K, Adams C, Adams T, Addesso P, Adhikari R X, Adya V B and et al 2017 *Physical Review Letters* **118** 221101 (*Preprint* 1706.01812)

[97] Abbott B P, Abbott R, Abbott T D, Abernathy M R, Acernese F, Ackley K, Adams C, Adams T, Addesso P, Adhikari R X and et al 2016 *Physical Review Letters* **116** 241103 (*Preprint* 1606.04855)

[98] Abbott B P, Abbott R, Abbott T D, Abernathy M R, Acernese F, Ackley K, Adams C, Adams T, Addesso P, Adhikari R X and et al 2016 *Physical Review Letters* **116** 061102 (*Preprint* 1602.03837)

[99] The LIGO Scientific Collaboration, the Virgo Collaboration, Abbott B P, Abbott R, Abbott T D, Abraham S, Acernese F, Ackley K, Adams C, Adhikari R X and et al 2019 *arXiv e-prints* arXiv:1905.03457 (*Preprint* 1905.03457)

[100] Rodriguez C L, Amaro-Seoane P, Chatterjee S, Kremer K, Rasio F A, Samsing J, Ye C S and Zevin M 2018 Phys. Rev. D **98** 123005 (*Preprint* 1811.04926)

[101] Antonini F, Toonen S and Hamers A S 2017 ApJ **841** 77 (*Preprint* 1703.06614)

[102] Tiwari S and Gopakumar A *in preparation*

[103] Moore B, Robson T, Loutrel N and Yunes N 2018 *Classical and Quantum Gravity* **35** 235006 (*Preprint* 1807.07163)

[104] Damour T, Gopakumar A and Iyer B R 2004 *Phys. Rev.* **D70** 064028 (*Preprint* gr-qc/0404128)

[105] Memmesheimer R M, Gopakumar A and Schaefer G 2004 *Phys.Rev.* **D70** 104011 (*Preprint* gr-qc/0407049)

[106] Gopakumar A and Iyer B R 2002 Phys. Rev. D **65** 084011 (*Preprint* gr-qc/0110100)

[107] Press W H, Teukolsky S A, Vetterling W T and Flannery B P 2007 *Numerical Recipes 3rd Edition: The Art of Scientific Computing* 3rd ed (New York, NY, USA: Cambridge University Press) ISBN 0521880688, 9780521880688

[108] Ahnert K and Mulansky M 2011 *AIP Conference Proceedings 1389, 1586*

[109] Mikkola S 1987 *Celestial mechanics* **40** 329–334 ISSN 1572-9478 URL https://doi.org/10.1007/BF01235850

[110] Tessmer M and Gopakumar A 2007 MNRAS **374** 721–728 (*Preprint* gr-qc/0610139)

[111] Frigo M and Johnson S G 2005 *Proceedings of the IEEE* **93** 216–231 special issue on "Program Generation, Optimization, and Platform Adaptation"

[112] Pierro V, Pinto I M, Spallicci A D, Laserra E and Recano F 2001 MNRAS **325** 358–372 (*Preprint* gr-qc/0005044)

[113] Yunes N and Berti E 2008 Phys. Rev. D **77** 124006 (*Preprint* 0803.1853)

[114] Boetzel Y, Kant Mishra C, Faye G, Gopakumar A and Iyer B R 2019 *arXiv e-prints* arXiv:1904.11814 (*Preprint* 1904.11814)

[115] Ebersold M, Boetzel Y, Faye G, Mishra C K, Iyer B R and Jetzer P 2019 *arXiv e-prints* arXiv:1906.06263 (*Preprint* 1906.06263)

[116] The LIGO Scientific Collaboration and the Virgo Collaboration 2020 *arXiv e-prints* arXiv:2001.01761 (*Preprint* 2001.01761)

[117] The LIGO Scientific Collaboration and the Virgo Collaboration 2018 *arXiv e-prints* arXiv:1811.12940 (*Preprint* 1811.12940)

[118] Huerta E A, Kumar P, McWilliams S T, O'Shaughnessy R and Yunes N 2014 Phys. Rev. D **90** 084016 (*Preprint* 1408.3406)

[119] Moore B and Yunes N 2019 *Classical and Quantum Gravity* **36** 185003 (*Preprint* 1903.05203)

[120] Tanay S, Klein A, Berti E and Nishizawa A 2019 Phys. Rev. D **100** 064006 (*Preprint* 1905.08811)

[121] Hinder I, Kidder L E and Pfeiffer H P 2018 *Phys. Rev.* **D98** 044015 (*Preprint* 1709.02007)

[122] Huerta E A *et al.* 2017 *Phys. Rev.* **D95** 024038 (*Preprint* 1609.05933)

[123] Huerta E A *et al.* 2019 *Phys. Rev.* **D100** 064003 (*Preprint* 1901.07038)

[124] Romero-Shaw I M, Lasky P D and Thrane E 2019 *arXiv e-prints* arXiv:1909.05466 (*Preprint* 1909.05466)

[125] LIGO Scientific Collaboration, Virgo Collaboration and Salemi F 2019 *arXiv e-prints* arXiv:1907.09384 (*Preprint* 1907.09384)

[126] Nitz A H, Lenon A and Brown D A 2019 (*Preprint* 1912.05464)

[127] Antonini F and Perets H B 2012 *The Astrophysical Journal* **757** 27 (*Preprint* 1203.2938)

[128] Fang X, Thompson T A and Hirata C M 2019 ApJ **875** 75 (*Preprint* 1901.05092)

[129] Gilks W, Richardson S and Spiegelhalter D 1995 *Markov Chain Monte Carlo in Practice* Chapman & Hall/CRC Interdisciplinary Statistics (Taylor & Francis) ISBN 9780412055515 URL http://books.google.com/books?id=TRXrMWY_i2IC

[130] Di Matteo Tiziana K A C N 2019 *Black Hole Formation and Growth* (Springer-Verlag Berlin Heidelberg) ISBN 1861-7980

[131] Cho H S 2015 *Class. Quant. Grav.* **32** 235007 (*Preprint* 1502.04399)

[132] Yunes N and Siemens X 2013 *Living Reviews in Relativity* **16** URL http://www.livingreviews.org/lrr-2013-9

[133] Will C M 2006 *Living Reviews in Relativity* **9** (*Preprint* gr-qc/0510072) URL http://www.livingreviews.org/lrr-2006-3

[134] LIGO Scientific and Virgo Collaborations 2016 Phys. Rev. Lett. **116** 221101 (*Preprint* 1602.03841)

[135] LIGO Scientific Collaboration and the Virgo Collaboration 2019 Phys. Rev. D **100** 104036 (*Preprint* 1903.04467)

[136] LIGO Scientific Collaboration and Virgo Collaboration 2019 Phys. Rev. Lett. **123** 011102 (*Preprint* 1811.00364)

[137] Pan H P, Lin C Y, Cao Z and Yo H J 2019 *arXiv e-prints* arXiv:1912.04455 (*Preprint* 1912.04455)

[138] Ma S, Cao Z, Lin C Y, Pan H P and Yo H J 2017 Phys. Rev. D **96** 084046 (*Preprint* 1710.02965)

[139] Moore B and Yunes N 2020 *Classical and Quantum Gravity* URL http://iopscience.iop.org/10.1088/1361-6382/ab7963

[140] Yagi K 2013 *International Journal of Modern Physics D* **22** 1341013 (*Preprint* 1302.2388)

[141] Yagi K and Tanaka T 2010 Phys. Rev. D **81** 064008 (*Preprint* 0906.4269)

[142] Nair R, Perkins S, Silva H O and Yunes N 2019 Phys. Rev. Lett. **123** 191101

[143] Bertotti B, Iess L and Tortora P 2003 *Nature* **425** 374

[144] Yunes N, Yagi K and Pretorius F 2016 *Phys. Rev.* **D94** 084002 (*Preprint* 1603.08955)

[145] Will C M and Zaglauer H W 1989 *Astrophys.J.* **346** 366

[146] Finn L S 1999 *arXiv e-prints* gr-qc/9903107 (*Preprint* gr-qc/9903107)

[147] The LIGO Scientific Collaboration and the Virgo Collaboration 2019 *arXiv e-prints* arXiv:1903.04467 (*Preprint* 1903.04467)

[148] Gregory P 2005 *Bayesian Logical Data Analysis for the Physical Sciences* (New York, NY, USA: Cambridge University Press) ISBN 052184150X

[149] Green P J 1995 *Biometrika* **82** 711–732

[150] Akmal A, Pandharipande V R and Ravenhall D G 1998 Phys. Rev. C **58** 1804–1828 (*Preprint* `nucl-th/9804027`)

[151] Eardley D M 1975 ApJ **196** L59–L62

[152] Hawking S 1972 *Commun.Math.Phys.* **25** 167–171

[153] Yagi K, Stein L C, Yunes N and Tanaka T 2012 *Phys. Rev.* **D85** 064022 (*Preprint* `1110.5950`)

[154] Drasco S, Flanagan É É and Hughes S A 2005 *Classical and Quantum Gravity* **22** S801–S846 (*Preprint* `gr-qc/0505075`)

[155] Cornish N J and Littenberg T B 2015 *Classical and Quantum Gravity* **32** 135012 (*Preprint* `1410.3835`)